New Applications of the Gauge/Gravity Duality

Daniel Fernández

NEW APPLICATIONS OF THE GAUGE/GRAVITY DUALITY

DANIEL FERNÁNDEZ
Departament de Física Fonamental
Universitat de Barcelona

June 2013

Universitat de Barcelona

Programa de Doctorado en Física

NEW APPLICATIONS OF THE GAUGE/GRAVITY DUALITY

A dissertation submitted to the University of Barcelona
for the degree of Doctor of Philosophy

I Certify that this thesis was prepared under my supervision.

I Certify that this thesis was prepared under my tutoring.

David Mateos
ICREA Research Professor

Enric Verdaguer
Research Professor

at the Departament de Física Fonamental
Barcelona, June 2013

A mis padres.

Preface

The purpose of this thesis is to put forth and present a series of new applications of the gauge/string duality to areas of high energy physics and condensed matter physics. After having dwelt into the concepts behind this conjecture, I have come to realize the breakthrough it was for theoretical physics and its usefulness for very diverse fields. The contributions showcased in this thesis amount to the ever growing recollection of evidence that supports it. Indeed, even though it was proposed only sixteen years ago, the duality has already become a broad and extensive field of its own, so that explaining all its ramifications would have taken too much space and time. When writing the Introduction to this thesis, I have tried to select those points that are involved in the successive chapters.

Most of the work contained in this thesis addresses the study of the quark gluon plasma, a state of matter that might allow to be approximated by simple gravitational descriptions and is, at the same time, accessible by experiment. This constitutes a great advantage, since it gives the possibility of testing the qualitative predictions that can be derived from the calculations in holography. Chapter 2 is devoted to one of such predictions: that a heavy quark moving sufficiently fast through a quark-gluon plasma may lose energy by Cherenkov-radiating mesons. Special emphasis is given to the fact that this effect takes place in all strongly coupled, large-N_c plasmas with a gravity dual. Phenomenological implications for heavy-ion collision experiments are also discussed. This chapter contains [1] and [2].

Chapter 3 makes extensive use of a IIB supergravity solution dual to a spatially anisotropic finite-temperature $\mathcal{N} = 4$ super Yang-Mills plasma. Motivation comes from the fact that the quark gluon plasma created in heavy-ion collisions is anisotropic. The analysis focuses on three important observables of the plasma: Firstly, the drag force experienced by a massive quark propagating through the plasma is considered. The results show a generic misalignment of the gluon cloud trailing behind the quark, the quark velocity and the drag force itself whenever anisotropy is taken into account.

Secondly, a study of the jet quenching parameter of the plasma is presented for arbitrary orientations and arbitrary values of the anisotropy. Perhaps surprisingly, the anisotropic value can be larger or smaller than the isotropic one, and moreover, this depends on whether the comparison is made at equal temperatures or at equal entropy densities. Finally, the screening length for quarkonium mesons in the anisotropic plasma is computed. The most important result is that not only can the temperature cause the dissociation of mesons, but anisotropy itself, even at zero temperature, may be responsible for it. This chapter encloses [3], [4] and [5].

Chapter 4 deals with an entirely different field of application of the duality: The holographic description of condensed matter physics. I have come to reckon that this field is very well suited for inspecting the predictions of the correspondence, since there is a great variety of systems that can be studied. Here anisotropic p-wave superfluids are brought into focus, and a gravitational model is used to perform a complete analysis of their transport phenomena in the superfluid phase. The thermoelectric, piezoelectric and flexoelectric effects are thoroughly studied. The results reproduce characteristic features of both superfluids and superconductors. In particular, the viscosities of the fluid deviate from the universal value, as is expected in an anisotropic condensed phase. An additional viscosity coefficient, associated to the difference in normal stresses and not previously considered in the holographic context, is also computed. This chapter is composed of [6].

Chapter 5 contains some conclusions and possible future directions.

And finally, in order to comply with the University rules, I have added chapter 6, written in Spanish. It consists of a summary of all the previous chapters of the thesis.

List of publications within this thesis

[1] J. Casalderrey-Solana, D. Fernandez, and D. Mateos,
“A New Mechanism of Quark Energy Loss,”

Phys. Rev. Lett. **104** (2010) 172301, `arXiv:0912.3717 [hep-ph]`.

[2] J. Casalderrey-Solana, D. Fernandez, and D. Mateos,
“Cherenkov mesons as in-medium quark energy loss,”

JHEP **1011** (2010) 091, `arXiv:1009.5937 [hep-th]`.

[3] M. Chernicoff, D. Fernandez, D. Mateos and D. Trancanelli,
“Drag force in a strongly coupled anisotropic plasma,”

JHEP **1208** (2012) 100, `arXiv:1202.3696 [hep-th]`.

[4] M. Chernicoff, D. Fernandez, D. Mateos and D. Trancanelli,
“Jet quenching in a strongly coupled anisotropic plasma,”

JHEP **1208** (2012) 041, `arXiv:1203.0561 [hep-th]`.

[5] M. Chernicoff, D. Fernandez, D. Mateos and D. Trancanelli,
“Quarkonium dissociation by anisotropy,”

JHEP **1301** (2013) 170, `arXiv:1208.2672 [hep-th]`.

[6] J. Erdmenger, D. Fernandez, and H. Zeller,
“New Transport Properties of Anisotropic Holographic Superfluids,”

JHEP **1304** (2013) 049, `arXiv:1212.4838 [hep-th]`.

Acknowledgements

I would like to thank my supervisor, David Mateos, for his wise guidance during the last four years. He has been an excellent advisor. He didn't know me when I started, and yet he took me up with deep enthusiasm. We have worked together in fascinating projects and he has helped me every time I needed it, always treating me with respect and patience. In the end, this thesis represents a beginning, and beginnings can be hard. It's easy to give in to despair and lose the motivation you had before starting. David has always been encouraging me, sometimes even without realizing it. So most of all, I'm thankful to him because his faith in me taught me to have faith in myself.

I would also like to thank Johanna Erdmenger for making my visit to MPI possible, and for a wonderful collaboration. She was always approachable and nice to me. Thanks to her, the time I spent in Munich was an amazing academical experience. I'd also like to thank David, Hansjoerg, Migael, Patrick, Sebastian, Sophia, Srdjan and Stephan for making it also a great personal experience. We had so much fun together!

I'm also grateful to Luis Lehner, for his warm hospitality at PI. He helped me so much during my time there, being completely patient and supportive to me. I would thank Alex Buchel for some conversations, and Marcelo Ponce for his help. From this time, I'd like to thank Anton, Damián, Federico, Maeve, Natacha, Nima, Stephen and Yigit for the enjoyable times we had together.

I'm thankful to Jorge Casalderrey for his help during my first collaboration. It was really valuable to me. I would also thank Mariano Chernicoff for so many and so helpful discussions. I hope we'll have new chances of collaboration in the future. And finally, to Diego Trancanelli for useful discussions via email. I look forward to meeting him in person.

I thank as well all the professors and postdocs in my department for their help. Specially Roberto Emparan and Tomeu Fiol for their continuous support, and Enric Verdaguer for agreeing to be the tutor of my thesis. Also Domenec Espriu and Josep M. Pons for useful discussions, and Pablo Cámara, Joaquim Gomis, Javier Tarrío and Yuko Urakawa. I would also thank Oleg Bulashenko, Jaume Garriga and Oscar Iglesias for help regarding the courses for which I've been teaching assistant. I would like to thank Tim Hollowood for a wonderful course.

Also Cristina Manuel and Paul Townsend for helpful discussions, and Juan Luis Mañes for his orientation after finishing my undergraduate, and for allowing me to be teaching assistant in Bilbao's TAE. I thank Joan Camps as well, for his orientation and assistance in times of need.

I should also acknowledge the Spanish Ministry of Education for their financial support during this time, and the fellow members of D-Recerca and the FJI for defending and standing by scientific funding.

Personally, there is so many people to whom I'm grateful. I would like to start with my dear friends from Barcelona: Adriana, Alejandro, Blai, Carmen, Ivan, Marina, Markus and Luis; with whom I've shared so many unforgettable moments. I'm also thankful to the students with whom I've shared my office: Hicham, Luce and Mario. You've been an amazing company to me. And to all the other members of the Amazing Physics Club: Aldo, Blai, Genís, Guillem, Nidal, Noela, Patricia and Wilke for the most engaging discussions, as well as to Héctor, Toño and Simon for helping me get through the master's studies.

And here's to my best friends in Bilbao, Gontzal and Iñaki, for whom I raise my cup, and the rest of the crew: Ander, Argoitz, Juaro and Sheila. To my friends from the physics degree: Alex, Eli, Erik, Irene, Iván, Javi, Maider, María, Miguel, Nerea and Txema. The times we spent studying were made easy when we were together. To the friends I made during my time in Finland, Juanchi and Mireia, those nights were warmer thanks to them. To my dear friends from Zamora, for whom I'd wish summer never to end: Enrique, Félix, Gabi, Lete and Mauro. To Jonatan, whose strength inspires me beyond what he can imagine. And to my remaining friends from high school, who are so valuable to me, Íñigo and Sandra. Finally, a very special mention is for my beloved Naiara, who shall be forever in my heart.

I'm also thankful for having been born in such a perfect family. Starting with my aunts and cousins, who have all my love. My dear sister Patricia, for all the beautiful moments we have shared and because I value his affection like a treasure. She is more extraordinary than she can even see in herself. And lastly, my deepest gratitude is for my parents. I could not have wished for a brighter light to guide my path in life. They have taught me to be a good person, and so many things I wouldn't even know where to start with. I admire and love them so much that this thesis is dedicated to them.

Agradecimientos

Quiero dar las gracias a mi supervisor, David Mateos, por sus sabias orientaciones durante los últimos cuatro años. Ha sido un director de tesis excelente. Cuando empecé, él no me conocía y sin embargo me acogió con entusiasmo. Hemos trabajado juntos en proyectos fascinantes y me ha ayudado siempre que lo he necesitado, siempre tratándome con respeto y con paciencia. En definitiva, esta tesis representa un comienzo, y los comienzos pueden ser duros. Es fácil ceder a la desesperanza y perder la motivación que tenías antes de haber empezado. David siempre me ha animado, a veces incluso sin darse cuenta. Así que, por encima de todo, le estoy agradecido porque la confianza que depositó en mí me ha hecho tener confianza en mí mismo.

También querría agradecer a Johanna Erdmenger que mi visita al MPI se hiciera realidad, y por una magnífica colaboración. Siempre ha sido accesible y simpática conmigo. Gracias a ella, el tiempo que pasé en Múnich fue una gran experiencia académica. También doy las gracias a David, Hansjoerg, Migael, Patrick, Sebastian, Sophia, Srdjan y Stephan por hacer que fuera también una gran experiencia personal. Nos divertimos mucho juntos!

También le estoy agradecido a Luis Lehner, por su amable hospitalidad en PI. Me ayudó mucho durante el tiempo que pasé allí, siendo completamente paciente y comprensivo hacia mí. Agradecería a Alex Buchel por algunas conversaciones, y a Marcelo Ponce por su ayuda. De esta temporada, querría dar las gracias a Anton, Damián, Federico, Maeve, Natacha, Nima, Stephen y Yigit por los buenos momentos que pasamos.

Le agradezco a Jorge casalderrey su ayuda durante mi primera colaboración. Fue algo realmente valioso para mí. También le daría las gracias a Mariano Chernicoff, por tantas conversaciones que fueron tan útiles. Espero que podamos volver a colaborar en un futuro. Y finalmente, a Diego Trancanelli por fructíferas conversaciones por email. Espero poder conocerle pronto en persona.

Agradezco asimismo la ayuda de los profesores y postdocs de mi departamento. Especialmente a Roberto Emparan y Tomeu Fiol por su continuo apoyo, y a Enric Verdaguer por acceder a ser el tutor de mi tesis. También a Domenec Espriu y Josep M. Pons por útiles discusiones y a Pablo Cámara, Joaquim Gomis, Javier Tarrío y Yuko Urakawa. También les

daría las gracias a Oleg Bulashenko, Jaume Garriga y Oscar Iglesias por su ayuda con los cursos en los que he sido profesor asistente. A Tim Hollowood le agradezco que nos diera un excelente curso. A Cristina Manuel y Paul Townsend les agradezco algunas discusiones y a Juan Luis Mañes por su orientación tras acabar la carrera, y por permitirme ser profesor asistente en el TAE de Bilbao. Le doy las gracias a Joan Camps también, por darme su orientación y ayuda cuando lo he necesitado.

También debería agradecer al Ministerio de Educación por la beca que he disfrutado durante este tiempo, y a los compañeros de D-Recerca y la FJI por defender y luchar por la financiación de la Ciencia.

A nivel personal, hay mucha gente a la que estoy agradecido. Querría empezar por mis queridos amigos de Barcelona: Adriana, Alejandro, Blai, Carmen, Ivan, Marina, Markus y Luis; con quienes he compartido tantos momentos inolvidables. También doy las gracias a los estudiantes con quienes he compartido mi despacho: Hicham, Luce y Mario. Habéis sido una compañía estupenda. Y al resto de miembros del *Amazing Physics Club*: Aldo, Blai, Genís, Guillem, Nidal, Noela, Patricia y Wilke por las discusiones más atrapantes, así como a Héctor, Toño y Simon por ayudarme a superar mis estudios del máster.

Y esta va por mis mejores amigos de Bilbao, Gontzal e Iñaki, por quienes alzo mi copa, y el resto de la cuadrilla: Ander, Argoitz, Juaro y Sheila. Por mis amigos de la carrera de Física: Alex, Eli, Erik, Irene, Iván, Javi, Maider, María, Miguel, Nerea y Txema. Los ratos que pasamos estudiando eran más llevaderos cuando estábamos juntos. Por los amigos que hice en Finlandia, Juanchi y Mireia, pues aquellas noches eran menos frías gracias a ellos. Por mis queridos amigos de Zamora, por quienes desearía que el Verano no acabase nunca: Enrique, Félix, Gabi, Lete y Mauro. Por Jonatan, cuya fuerza me inspira más allá de lo que él se imagina. Y por los amigos que me quedan del instituto, que son tan valiosos para mí, Íñigo y Sandra. Finalmente, una mención muy especial es para mi amada Naiara, que estará por siempre en mi corazón.

También estoy agradecido por haber nacido en una familia tan perfecta. Empezando por mis tías y primos, que tienen todo mi cariño. Mi querida hermana, por todos los bellos momentos que hemos compartido y por el tesoro que supone para mí tener su cariño. Es más extraordinaria de lo que ella misma es capaz de ver. Y para acabar, mi más profunda gratitud es para mis padres. No podría haber deseado una luz más brillante que me mostrase el camino en mi vida. Ellos me han enseñado a ser una buena persona, y tantas cosas que no sabría ni por dónde empezar. Los admiro y quiero tanto que a ellos queda dedicada esta tesis.

Contents

“The scientist does not study nature because it is useful; he studies it because he delights in it, and he delights in it because it is beautiful.”
— Henri Poincaré

“Imagination is more important than knowledge. For knowledge is limited, whereas imagination embraces the entire world.”
— Albert Einstein

“A straight line may be the shortest distance between two points, but it is by no means the most interesting.”
— The Doctor

Chapter 1

Introduction

1 The gauge/string duality

Much literature has been written on the field of AdS/CFT [1–3][1]. There is no doubt that it has represented a major advance in our understanding of string theory and quantum gravity, and a powerful toolkit for studying strongly-coupled quantum field theories. In general terms, what is known as the gauge/string duality is a conjectured equivalence between certain conformal field theories and certain gravitational theories in asymptotically Anti de Sitter spacetimes. It was originally stated as a specific equivalence between $\mathcal{N} = 4$ $SU(N_c)$ SYM theory and type IIB string theory on $AdS_5 \times S^5$.

In this case, the gauge theory is the maximally supersymmetric gauge theory in $(3+1)$ dimensions. Its field content includes a gauge field A_μ, six real scalars ϕ^i and four Weyl fermions χ_a; all of them in the adjoint representation of the gauge group. On the other hand, the metric of the gravitational theory is

$$ds^2 = \frac{r^2}{R^2}\eta_{\mu\nu}dx^\mu dx^\nu + \frac{R^2}{r^2}\left(dr^2 + r^2 d\Omega_5^2\right) \ , \tag{1.1}$$

where $\eta_{\mu\nu}$ is the four-dimensional Minkowski metric, $x^\mu = (t, \vec{x})$ are cartesian coordinates, $r \in (0, \infty)$ is the radial coordinate and $d\Omega_5^2$ contains the angle coordinates that parametrize a unit five-sphere. The parameter R is a constant known as the AdS radius. This metric covers the “Poincaré patch” of a global AdS spacetime. Each radial slice of the AdS_5 part is isometric to four-dimensional Minkowski spacetime, this is why x^μ are identified as the coordinates of the gauge theory. It is sometimes convenient to rewrite (1.1) using an alternative radial coordinate $z = R^2/r$, so that

$$ds^2 = \frac{R^2}{z^2}\left(\eta_{\mu\nu}dx^\mu dx^\nu + dz^2 + z^2 d\Omega_5^2\right) \tag{1.2}$$

is the metric describing the geometry.

As $r \to \infty$, or $z \to 0$, we approach the so-called boundary of the spacetime. Since the prefactor R^2/z^2 also approaches infinity there, this must be understood as a conformal boundary. According to the conjecture, the Yang-Mills theory lives on the boundary of AdS_5, so that it is simply called “the boundary theory”. In a broader portrayal, this would only be a limit of the more general description that is outlined in the next section.

1.1 The boundary theory and its RG flow

The duality can be interpreted as a geometrization of the renormalization group (RG) flow of a quantum field theory (QFT). Let us review the basics behind the concept of RG flow. Generically, QFTs are defined with a short-distance cutoff ϵ. The theory loses its validity below this cutoff, in the sense that phenomena occurring at characteristic lengthscales comparable to or smaller than ϵ are not accurately described by the theory. A convenient outcome of the existence of ϵ is that it provides a scale, so that the physics can then be organized in terms of length scales (which in turn can be understood as energy scales), since degrees of freedom at widely separated scales do not interact with each other.

---

[1] See [4, 5] for reviews, and [6] for a review with applications to QCD.

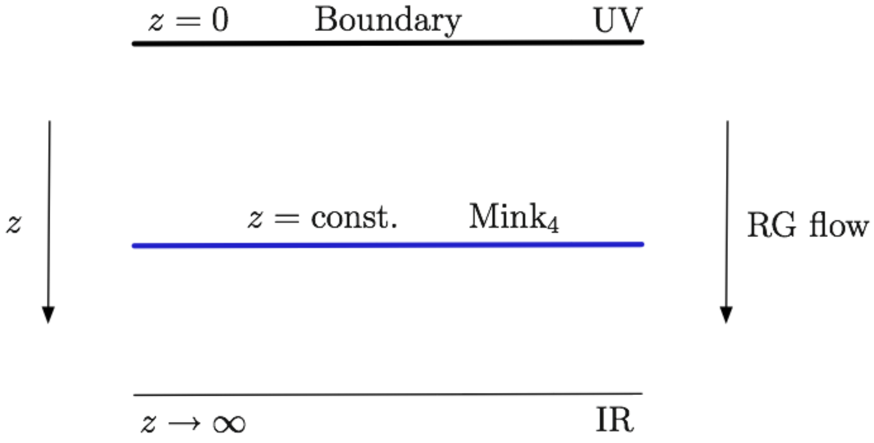

Figure 1. A schematic picture of the geometry of AdS_5.

That is, if one is interested in studying phenomena at a length scale $z \gg \epsilon$, there is no need to go straight to the theory as defined at scale ϵ, which could result in a very complicated calculation. It is actually more convenient to integrate out the short-distance degrees of freedom and work with an effective theory at length scale z. By following this procedure for every scale z, we end up with a continuous family of effective theories labeled by the scale z, which defines the RG evolution of the theory.

Now, given a QFT defined in $(3+1)$-dimensional Minkowski spacetime, the family of effective field theories may be visualized as a single theory in a (4+1)-dimensional spacetime (commonly referred to as the bulk), with the RG scale z playing the role of coordinate of the spatial extra dimension [7]. In order to establish such a higher dimensional characterization, we would need to develop a coherent description, by merging this continuous family of theories. For it to be consistent, there are some properties that have to be required from the 5-dimensional theory, in particular, all the physics in the region $z > z'$ (that is, below the Minkowski plane at z') should be describable by the effective theory of the original system defined precisely at the RG scale z'. As a consequence, the whole 5-dimensional description (region $z > 0$) has the same number of degrees of freedom as the 4-dimensional boundary theory. This picture is schematically shown in Fig. 1. Note, however, that the higher dimensional theory is not guaranteed to be *local* in the z direction.

Such a description was suggested from the holographic principle [8, 9], an interesting idea that has been extensively studied. According to it, a theory of quantum gravity in a region of space can be described by a non-gravitational theory living at the boundary of that region.

Note that we have adopted $z = 0$ as the boundary, where the bare QFT (with no cutoff) lives. A small cutoff corresponds to a slice $z = \epsilon$ that is close to this boundary, and there is where the short-distance effective theory lives.

1.2 The extra dimension as an energy scale

Going back to the case of the metric (1.2) we asserted that the boundary must be understood in the conformal sense. This is due to the presence of the factor R^2/z^2, which causes the length scales along the gauge theory directions in the bulk to be related to their counterparts in the gauge theory by a z-dependent rescaling. The same applies to the energy scale, given that it is a quantity conjugate to time. The rescalings of these quantities are as

$$d_{\text{bulk}} = \frac{R}{z} d, \qquad E_{\text{bulk}} = \frac{z}{R} E, \tag{1.3}$$

where d, E are respectively the characteristic length and energy of a process in the gauge theory and $d_{\text{bulk}}, E_{\text{bulk}}$ are the corresponding proper size and energy of the corresponding process occurring in the bulk theory. Thus, note that two physical process taking place in the bulk with the same proper energy but at different radial positions are translated in the gauge theory description as processes with different characteristic energies, for they would scale as $E \sim 1/z$. An analogous deliberation applies to the length scale, which scales as $d \sim z$.

With this argument we are coming back to Sec. 1.1. Indeed, the identification between the radial z-direction of the bulk and the energy scale of the boundary theory is made precise by arguing that z has to be identified with a geometrized direction of the RG flow of the gauge theory. In short,

$$\begin{array}{rcccccc} \text{UV limit} & / & E \to \infty & / & z \to 0 & / & \text{near boundary} \\ \text{IR limit} & / & E \to 0 & / & z \to \infty & / & \text{near horizon} \end{array}$$

where “horizon” refers to the core of the bulk, located at $r = 0$, or $z \to \infty$. The reason for the name is that usually the spacetime is cut off by an event horizon at a finite radial distance r_0, so that z does not actually extend all the way to infinity, but it ends at a finite value z_0. More precisely, this happens whenever we consider a confining theory with a mass gap or at finite temperature. If there exist excitations or arbitrarily low energy, this is reflected in the bulk by a geometry extending up to $z \to \infty$, but a mass gap m or a temperature T provide an IR cutoff at $z_0 \sim 1/m$ or $z_0 \sim 1/T$ respectively.

1.3 Relations between parameters

Once we have reached this point let us state that the details regarding how the duality is constructed can be lengthy and are beyond the scope of this chapter. As an introduction to the work developed in this thesis, we will concentrate on laying down those aspects of the topic that are related to, or used in, the research results that are contained in the following chapters.

An important point is the set of parameters that characterize the theories that are being discussed. $\mathcal{N} = 4$ SYM theory is scale-invariant and contains only two parameters: the Yang-Mills coupling $g_{\text{YM}} = g$, and the number of colors, N_{c}. On the other hand, type IIB string theory is characterized by the string coupling g_s and length ℓ_s. Equivalently, one could consider Newton’s constant G and the curvature radius R, which is the parameter for the metric of the maximally symmetric spacetime $AdS_5 \times S^5$.

The relations are derived in the following way. First, the ten-dimensional Newton's constant in IIB Supergravity is given by

$$16\pi G = (2\pi)^7 \, g_s^2 \ell_s^8 \,, \tag{1.4}$$

and a stack of $N_{\rm c}$ D3-branes can act as source for the solution (1.1), so that the parameter R is given by

$$R^4 = 4\pi g_s N_{\rm c} \ell_s^4 \,. \tag{1.5}$$

One can then consider the spectrum of massless fields excited on the branes by the open string modes. It turns out that this spectrum, and their low energy effective action, coincides precisely with those of $\mathcal{N} = 4$ SYM theory with gauge group $U(N_{\rm c})$ in $(3+1)$-dimensions. This is, of course, a very important ingredient for the construction of the duality. What matters at this stage is that one can derive a relation between the Yang-Mills coupling constant and the string coupling, namely

$$g^2 = 4\pi g_s \,. \tag{1.6}$$

Recalling now that $G \sim \ell_p^8$, with ℓ_p the Planck length, relations (1.4 - 1.6) imply

$$\frac{\ell_p^8}{R^8} \propto \frac{1}{N_{\rm c}^2} \,, \qquad \frac{\ell_s^2}{R^2} \propto \frac{1}{\sqrt{\lambda}} \,, \tag{1.7}$$

where $\lambda = g^2 N_{\rm c}$ is known as the 't Hooft coupling and we are omitting numerical factors only. As stated above, we are interested in considering the gauge/gravity limit, for simplicity since the full IIB string theory is very complicated. In other words, the regime of interest is the limit of classical supergravity, an approximation valid for large curvature radii compared to the planck and string scales, so that both the stringy nature of the string theory and its quantum nature are suppressed. That is,

$$\frac{\ell_p^8}{R^8} \ll 1 \,, \qquad \frac{\ell_s^2}{R^2} \ll 1 \,. \tag{1.8}$$

From the relations (1.7), it follows that this limit corresponds to

$$N_{\rm c} \gg 1 \,, \qquad \lambda \gg 1 \,. \tag{1.9}$$

This is usually referred to as the strong coupling, large $N_{\rm c}$ limit of the correspondence.

2 The field/operator correspondence

After having identified the parameters on both sides of the duality, we consider the map between their spectra of solutions. An intuition for this comes from the fact that the string coupling constant g_s is not really a parameter of the supergravity theory, but it is given by the expectation value of the dilaton field Φ, as in $g_s = e^{\Phi}$. Consequently, g_s is a function of space and time. When making contact with the boundary theory, one may take it as a constant, by selecting its asymptotic value at infinity (that is, at the AdS boundary, ∂AdS), so that $g_s = e^{\Phi_\infty}$.

Since g_s is related to the gauge theory coupling constant g, this means that changing the value of g corresponds to changing the asymptotic value of the dilaton field. This observation is extended to suggest the idea that deforming the theory with an additional contribution to a coupling constant corresponds to modifying a bulk field in ∂AdS. More precisely, given the deformation

$$S \to S + \int d^4x \; \phi(x)\mathcal{O}(x) \; , \tag{2.1}$$

where $\mathcal{O}(x)$ is a local gauge invariant operator and $\phi(x)$ a point-dependent coupling which is usually called source. Note that in the particular case in which $\phi(x)$ is a constant, the deformation above amounts to simply changing the coupling of the operator $\mathcal{O}(x)$, which is what we were considering above. Extrapolating the previous idea, we conceive that for each possible *source* $\phi(x)$ (rather than to each coupling) and for each possible local gauge invariant operator $\mathcal{O}(x)$, there corresponds a dual bulk field $\Phi(x,z)$; and vice versa. This bulk field must be so that its asymptotic value at the boundary is identified with the source, in the same way that e^{Φ_∞} was identified with the coupling g. That is,

$$\phi(x) = \left.\Phi\right|_{\partial AdS}(x) = \lim_{z\to 0} \Phi(x,z) \; . \tag{2.2}$$

This one-to-one map between the bulk fields and the local gauge invariant operators of the dual gauge theory is known as the field/operator correspondence.

2.1 Global and local symmetries

The symmetries on both sides of the correspondence can also be identified. The $\mathcal{N} = 4$ SYM theory is a conformal theory, and is invariant under the symmetry group $\mathrm{Conf}(1,3)\times SO(6)$, where $\mathrm{Conf}(1,3)$ is the full conformal group (containing, among others, the dilatation symmetry) and $SO(6)$ is the R-symmetry under which the ϕ^i fields transform as a vector. On the other hand, the string side of the correspondence is invariant under the group of diffeomorphism-induced gauge transformations. The subgroup of these consisiting of large gauge transformations that leave the asymptotic form of the metric invariant is precisely $SO(2.4) \times SO(6)$, where $SO(2,4)$ corresponds to the isometry group of the AdS_5 part and is isomorphic to $\mathrm{Conf}(1,3)$.

Thus, the global symmetry groups on both sides of the correspondence agree. A simple and specific example is the dilatation symmetry of Minkowski spacetime, which in AdS_5 is realized as the transformation $\{(t,\vec{x}) \to \Lambda(t,\vec{x}), z \to \lambda z\}$, which indeed leaves the metric (1.2) invariant. Similarly, the four special conformal transformations are realized as isometries of AdS_5, only that in a slightly more involved way.

The conclusion of the analysis of symmetries is that the global symmetries are the same on both sides of the duality, but it is important to note that on the gravity side the global symmetries arise as large gauge transformations. In this sense, there is a correspondence between global symmetries in the gauge theory and gauge symmetries in the string theory. This is an important feature in any gauge/gravity duality.

2.2 Important examples

In general, given an operator in a gauge theory, there is no systematic recipe to identify the dual field. There is an exception, however, that applies for a very important set of operators: the conserved currents associated to global symmetries. Given what was briefly described in the previous section, it is natural to make the identification with dynamical gauge fields, associated to the corresponding gauge symmetries of the dual theory.

For example, in the case of the $\mathcal{N} = 4$ SYM theory, a current associated to a $U(1)$ subgroup of the $SO(6)$ symmetry, $J^\mu(x)$, is coupled to a source $A_\mu(x)$ via the term

$$\int d^4x \; A_\mu(x) J^\mu(x) \; . \tag{2.3}$$

Here $A_\mu(x)$ can be thought of as an external background field and, according to the field-operator correspondence, it is given by the boundary value of a dynamical gauge field $A_\mu(x, z)$ in the bulk.

Another important example of conserved currents are those contained in the energy-momentum tensor operator $\mathcal{T}^{\mu\nu}(x)$, associated to translational invariance. The source that couples to this operator can be interpreted as an external spacetime metric deformation. Thus, the coupling term is

$$\int d^4x \; g_{\mu\nu}(x) \mathcal{T}^{\mu\nu}(x) \; . \tag{2.4}$$

Following the same discussion, this source is given by the boundary value of a dynamical gauge field, in this case the bulk metric $g_{\mu\nu}(x, z)$. An important consequence of this argument is that the dual of any gauge theory in which the energy-momentum tensor is conserved must involve dynamical gravity.

2.3 The normalizable modes

In order to illustrate further details regarding the field/operator correspondence, we consider the specific example of a massive bulk scalar field Φ, dual to some scalar operator $\mathcal{O}$ in the four-dimensional boundary theory. The bulk action for this field is

$$S = -\frac{1}{2} \int dz \; d^4x \; \sqrt{-g} \left[g^{MN} \partial_M \Phi \, \partial_N \Phi + m^2 \Phi^2 \right] + \ldots \tag{2.5}$$

where the dots stand for higher order terms, supressed by positive powers of $1/N_\mathrm{c}$, that will be omitted.

The equation of motion for $\Phi(z, x)$ can be solved asymptotically, so that generically near the boundary it can be written as

$$\Phi(z, k) \approx A(k) \, z^{4-\Delta} + B(k) \, z^{\Delta} \qquad \text{as } z \to 0 \, , \tag{2.6}$$

where $\Delta = 2 + \sqrt{m^2 R^2 + 4}$, and the integration functions A and B depend on k under the requirement that the solution be regular for all $z > 0$. Note that the exponents are real provided that

$$m^2 R^2 \geq -4 \; . \tag{2.7}$$

It can be shown that this is a requirement for the stability of the theory. For values of m^2 in the range $m^2R^2 < -4$, there exist modes that grow exponentially in time and the theory is unstable [11–13]. Thus, a negative mass-squared is allowed for a stable solution, provided that it is not "too negative". Equation (2.7) is what is called the Breitenlohner-Freedman (BF) bound, applied to this example. It turns out that in the stable region $-4 \leq m^2R^2 < -3$, both terms in (2.6) are normalizable. We will not comment further on this case, and focus on the region $m^2R^2 \geq -3$.

In this case, the first term of (2.6) is non-normalizable whereas the second term is normalizable and, consequently, does not affect the leading boundary behavior. Note that the normalizability is with respect to the inner product

$$(\Phi_1, \Phi_2) = -i \int_{\Sigma_t} dz\, d\vec{x}\, \sqrt{-g}\, g^{tt} (\Phi_1^* \partial_t \Phi_2 - \Phi_2 \partial_t \Phi_1^*)\,, \tag{2.8}$$

where Σ_t is a constant-t slice. It was already motivated at the beginning of this section that the boundary value of Φ has to be identified with the source of the corresponding boundary operator $\mathcal{O}$. The boundary behavior of (2.6) is controlled by the non-normalizable term $A(x)$. Therefore, its presence corresponds to the deformation

$$S_{\text{bdry}} \to S_{\text{bdry}} + \int d^4x\, A(x)\mathcal{O}(x)\,. \tag{2.9}$$

Thus, the non-normalizable term determines the boundary theory lagrangian. And we see that eq. (2.2) is not strictly valid in this case; it must be generalized so that for $m \neq 0$ we have

$$\phi(x) = \Phi|_{\partial AdS}(x) = \lim_{z\to 0} z^{\Delta-4}\Phi(x,z)\,. \tag{2.10}$$

The normalizable modes are also significant. Note that the non-normalizable solutions are not elements of the Hilbert space of the bulk theory, but the normalizable modes are. In order to build the Fock space and compute the bulk Green's functions, one would need to expand Φ in terms of a basis of normalizable solutions. Now, we claim that the bulk and boundary theories are dual, that is, equivalent. Such an equivalence implies that their respective Hilbert spaces must be identified. As a consequence, the normalizable modes should be identified with states of the boundary theory. This identification is a very important feature of the duality, for it allows to find the spectrum of low-energy excitations of strongly coupled gauge theories.

Furthermore, it can be shown [14] that the coefficient $B(x)$ of the normalizable term in (2.6) can be identified with the expectation value of the operator $\mathcal{O}$ in the presence of the source $\phi(x) = A(x)$,

$$\langle \mathcal{O}(x) \rangle_{A(x)} = 2(\Delta - 2)B(x)\,. \tag{2.11}$$

In the particular case of a purely normalizable solution (that is, when $A(x) = 0$), this equation yields the expectation value of the operator in the undeformed theory.

Thus we have completed the basic description of how normalizable and non-normalizable modes of a bulk field are interpreted in the boundary theory [15, 16].

3 Generalizations of the duality

In addition to the one between $\mathcal{N} = 4$ $SU(N_{\rm c})$ SYM theory and type IIB string theory on $AdS_5 \times S^5$, there are many other gauge/string dualities. Some are in different spacetime dimensions [17], others have fewer supersymmetries and there are theories which are not scale invariant too (in particular confining theories [18–21]). In general, the dual geometry in these cases is more complicated than pure AdS.

Here we will comment on the most commonly used generalizations of the mentioned well-known example.

3.1 Temperature and chemical potential

The solution (1.1) constitutes an extremal one, belonging to a family of solutions parametrized by their temperature T. The generalized solution comes about by exciting the D3-branes that source the metric, which in this case are sorrounded by an event horizon, thus becoming black branes. Note that the black brane is the only metric with AdS asymptotic boundary conditions, translationally-invariant along all the boundary directions while rotationally-invariant along the boundary spatial directions; and with a temperature that satisfies all laws of thermodynamics.

The solution is given by

$$ds^2 = \frac{r^2}{R^2}\left(-f(r)\,dt^2 + dx_1^2 + dx_2^2 + dx_3^2\right) + \frac{R^2}{r^2}\left(\frac{dr^2}{f(r)} + r^2 d\Omega_5^2\right) , \tag{3.1}$$

where $f(r) = 1 - r_0^4/r^4$. Equivalently, in terms of the z coordinate, (1.2) is generalized to

$$ds^2 = \frac{R^2}{z^2}\left(-f(z)\,dt^2 + dx_1^2 + dx_2^2 + dx_3^2 + \frac{dz^2}{f(z)} + z^2 d\Omega_5^2\right) , \tag{3.2}$$

where $f(z) = 1 - z^4/z_0^4$. The horizon of the black brane is located at $r = r_0$ (or $z = z_0$), and it extends along the three spatial directions $\vec{x}$ of the dual gauge theory. The Hawking temperature associated to this horizon is related to these parameters by $r_0 \propto \frac{1}{z_0} \propto T$, and is identified with the temperature of the $\mathcal{N} = 4$ SYM theory at finite temperature.

The Hawking temperature is calculated by demanding that the Euclidean continuation of the metric (obtained by the replacement $t \to -it_{\rm E}$) be regular at $z = z_0$ [22]. This requires that $t_{\rm E}$ be periodically identified with a period $\beta = 1/T = \pi z_0$. Since $t_{\rm E}$ corresponds precisely to the Euclidean time coordinate of the boundary theory, the identification of temperatures is natural.

On the other hand, a chemical potential μ can also be turned on. For a boundary theory with a $U(1)$ global symmetry, as is the case of $\mathcal{N} = 4$ SYM theory, we are referring to the chemical potential of the corresponding $U(1)$ charge. Following the arguments presented in Sec. 2, this requires that the bulk field A_μ (the one dual to the boundary current J_μ) satisfy the boundary condition

$$\lim_{z\to 0} A_t = \mu \, . \tag{3.3}$$

If finite temperature is also considered, this condition is complemented with the requirement that A_μ be regular at the horizon. In this case, the black hole is charged, since there is a finite radial electric field in the bulk.

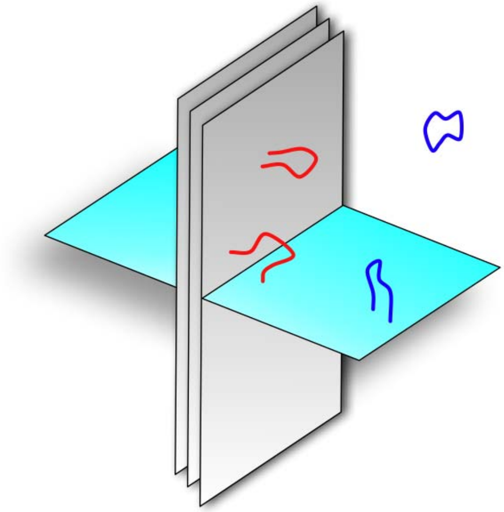

Figure 2. Schematic depiction of open strings and probe D-branes ($g_{\rm s}N_{\rm c} \ll 1$ regime).

3.2 Fundamental matter

As mentioned in Sec. 1, all the field content of $\mathcal{N} = 4$ SYM transforms in the adjoint representation of the gauge group. But matter in the fundamental representation can also be added. This is desirable, since in QCD the quarks transform in the fundamental representation and they play a most important role. In order to construct holographic models more closely related to QCD, we need to introduce matter degrees of freedom in the fundamental representation.

First, let us recall that fundamental matter fields (let us call them simply quarks) have $N_{\rm c}$ degrees of freedom, as opposed to the $N_{\rm c}^2$ carried by the adjoint matter ones (the gluons), so to include loops in their Feynman diagrams would lead to $1/N_{\rm c}$ suppressions. For instance, in a theory with $N_{\rm f}$ flavors, the single-quark loop planar diagram contribution to the vacuum amplitude scales as $N_{\rm f}N_{\rm c}$ rather than as $N_{\rm c}^2$. Then, in the large $N_{\rm c}$ limit, while keeping $N_{\rm f}$ finite, the contribution from quark loops is suppressed by factors of $N_{\rm f}/N_{\rm c}$.

Also in this limit, Feynman diagrams with quark loops can be classified in a topological expansion of two-dimensional Riemann surfaces with boundaries (as opposed to diagrams without quarks, which have no boundaries). Each boundary is identified with a quark loop. On the string side, these diagrams are formulated as worldsheets containing both closed and open strings, with boundaries corresponding to the worldlines of the endpoints of the open strings. These open strings must be attached to D-branes, therefore the introduction of quark degrees of freedom must correspond to introducing additional D-branes, so that these open strings can be present in the theory. Since they only need to act as supporting surfaces for their endpoints, they can be regarded as probe D-branes. Indeed, if there are $N_{\rm f}$ of them, provided that $N_{\rm c} \gg N_{\rm f}$, their gravitational backreaction can be neglected.

The field/operator correspondence relates the closed string fields living in the bulk to gauge-invariant operators built out of adjoint matter and gauge fields only, like $\mathcal{O} = \mathrm{Tr}\, F^2$. This is a way of saying that closed strings are dual to states such as glueballs (in confining models). On the other hand, open string fields are dual to meson-like operators like $\mathcal{O} = \bar{q}q$. The picture (see Fig. 2) devised by this correspondence is that the two endpoints of an open string, which must lie on the D-brane probe worldsheets, are respectively dual to a quark and an antiquark.

Thus we come to the conclusion that the introduction of gauge theory quarks must correspond to the introduction of Dp-brane probes in the string description, where the dimension p can be a subject of discussion that will not be addressed here, other than saying that it has to be $p > 3$. The open string sector includes three types of open strings:
i) with both ends on the D3-branes, which give rise to the $\mathcal{N} = 4$ SYM multiplet in the adjoint of $SU(N_{\mathrm{c}})$. The coupling constant for these degrees of freedom is simply the one in (1.6), which is dimensionless, so they remain interacting at low energies.
ii) with both ends on the Dp-branes. In this case, the coupling constant has dimensions of $(\mathrm{length})^{p-3}$. If $p > 3$, this implies that these strings become non-interacting at low energies.
iii) with one endpoint on the D3-branes and the other one on the Dp-branes. These degrees of freedom transform in the fundamental representation of the gauge group on the D3-branes, and in the fundamental representation of the gauge group on the Dp-branes as well; which means that they transform in the bifundamental representation of $SU(N_{\mathrm{c}}) \times SU(N_{\mathrm{f}})$. They interact with the other types of strings with strengths given by the corresponding coupling constants on the D3-branes and on the Dp-branes.

At low energies, when $g_{\mathrm{s}} N_{\mathrm{c}} \ll 1$, the system yields two decoupled sectors. The first sector is free (non-interacting) and consists of closed strings, propagating on the ten-dimensional spacetime, and p-p open strings, propagating on the worldvolume of the N_{f} Dp-branes. The second sector is interacting and consists of the 3-3 strings coupled to the 3-p strings. The gauge group $SU(N_{\mathrm{f}})$ becomes a global symmetry group because the effective coupling on the Dp-branes vanishes. This is the origin of the flavor symmetry expected in the presence of N_{f} equal mass quark species in the gauge theory.

On the other hand, if $g_{\mathrm{s}} N_{\mathrm{c}} \gg 1$, the D3-branes may be replaced by their backreaction on spacetime, to consider the closed string description, which is now complemented with the Dp-brane probes living in this geometry. The excitations of the system consist of closed strings and p-p open strings, propagating in two regions that decouple in the low-energy limit: the asymptotically flat region, where strings become non-interacting, and the $AdS_5 \times S^5$ throat, where strings remain interacting because of the gravitational redshift (see Fig. 3).

In any of the two cases, the low energy limit contains a free sector of closed and p-p open strings. These free sectors are identified and conjectured to provide dual descriptions of the same physics. That is, $\mathcal{N} = 4$ SYM coupled to N_{f} fundamental degrees of freedom is dual to type IIB closed strings in $AdS_5 \times S^5$ coupled to open strings living on the worldvolume of N_{f} Dp-brane probes.

Nevertheless, note that the leading contribution of the fundamental matter is always of relative order $N_{\mathrm{f}}/N_{\mathrm{c}}$ with respect to the contribution of the gluons. This does not

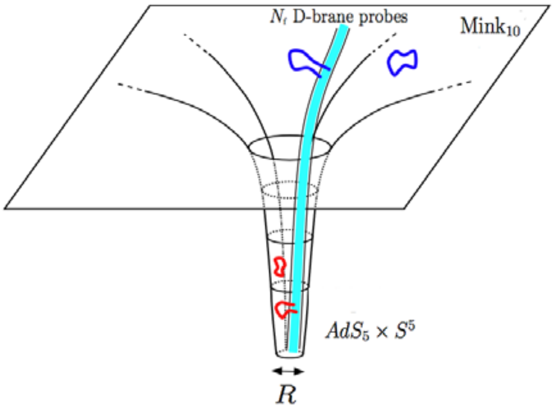

Figure 3. Excitations of the system in the $g_s N_c \gg 1$ regime.

mean that in the large N_c limit the quarks have to be completely ignored. When taking $N_c \to \infty$, the ratio N_f/N_c can be kept finite so that any observable can be calculated as a double expansion in $1/N_c^2$ and N_f/N_c, so that the relevant contribution from the quarks is captured. Indeed, in this thesis it will be shown that quarks can act as probes of dynamics dominated by adjoint matter, in order to answer questions regarding the effect of heavy quarks in the plasma: jet quenching, meson radiation, ...

4 Making the duality precise

The duality conjecture is made precise by postulating that the Euclidean partition functions of the two theories are identified [2, 3] as

$$Z_{\text{CFT}}\left[\phi(x)\right] = Z_{\text{string}}\left[\Phi|_{\partial AdS}\left(x\right)\right] . \tag{4.1}$$

An important point that must be taken into account is that the gravitational side has as many degrees of freedom as its dual. This is the concept that makes the holographic principle conceivable, and it also makes it possible to parametrize the degrees of freedom of the theory in terms of boundary variables. This is the reason why Z_{string} is expressed in terms of the boundary conditions $\Phi|_{\partial AdS}(x)$. Also, because of the previous identification (2.2), the variables appearing on both functionals in this equation are the same. In fact, the most general form of Z_{CFT} includes a source for each gauge-invariant operator of the theory. The Φ fields constitute (the duals of) the collection consisting of all these sources.

Of course, Z_{string} is in general difficult to compute. But in the classical gravity limit (1.8), it is greatly simplified as the exponential of the renormalized on-shell classical action of the supergravity limit of the theory (that is, the classical action evaluated on a solution of the equations of motion $\Phi_c^{(E)}$),

$$Z_{\text{string}}[\phi] \simeq \exp\left(S^{(\text{ren})}\left[\Phi_c^{(E)}\right]\right) . \tag{4.2}$$

where the superindex (E) stands for Euclidean. Note that we have absorbed the usual minus sign into the definition of the Euclidean action. The boundary conditions for the solution relate it to the $\phi(x)$ fields appearing on the left hand side of (4.1),

$$\lim_{z\to 0} z^{\Delta-4}\,\Phi_c^{(E)}(z,x)=\phi(x)\,, \tag{4.3}$$

which are complemented by the requirement of regularity everywhere in the bulk.

The renormalization of the action is an important detail of this calculation. Typically, there are contributions given by boundary-evaluated terms, the lack of which makes the on-shell classical value of the action divergent [3]. The divergence removal procedure is called "holographic renormalization" and is now a well understood topic (see [23] for a review).

The classical gravity limit is attained if one considers the strong coupling, large N_c limit. Since the classical gravitational action is proportional to $1/G$, which scales as $G\sim 1/N_c^2$ (see subsec. 1.3), then the action scales as $S^{(\mathrm{ren})}[\Phi_c^{(E)}]\sim N_c^2$. This is what one would expect for a theory with N_c^2 degrees of freedom for its fields, such as $SU(N_c)$ SYM theory in the large N_c limit. Quantum corrections would be included as an expansion in powers of $1/\sqrt{\lambda}$ and $1/N_c$.

4.1 The physics of correlation functions

Eq. (4.1), with (4.2), makes it possible to compute connected correlation functions of the gauge theory simply from functional derivatives of the on-shell classical gravity action with respect to the associated sources, as in

$$\langle\mathcal{O}(x_1)\ldots\mathcal{O}(x_n)\rangle=\left.\frac{\delta^n S^{(\mathrm{ren})}[\Phi_c^{(E)}]}{\delta\phi(x_1)\ldots\delta\phi(x_n)}\right|_{\phi=0}\,. \tag{4.4}$$

This is an important tool that is extensively used in many AdS/CFT models. A particular case for this formula takes us back to (2.11), which can be derived from

$$\langle\mathcal{O}(x)\rangle_\phi=\frac{\delta S^{(\mathrm{ren})}[\Phi_c^{(E)}]}{\delta\phi(x)}=\lim_{z\to 0} z^{4-\Delta}\frac{\delta S^{(\mathrm{ren})}[\Phi_c^{(E)}]}{\delta\Phi_c^{(E)}(z,x)}\,, \tag{4.5}$$

where (4.3) has been taken into account.

A very important application of this formula applies when considering $\mathcal{O}(x)=\mathcal{T}^{\mu\nu}(x)$. As outlined in (2.4), in this case the dual field is the metric $\Phi(x)=g_{\mu\nu}(x)$, which is an operator of dimension $\Delta=d$. Thus, (4.5) results in

$$\langle\mathcal{T}^{\mu\nu}(x)\rangle=\lim_{z\to 0}\frac{\delta S^{(\mathrm{ren})}[g^{(E)}]}{\delta g_{\mu\nu}^{(E)}(x,z)}\,. \tag{4.6}$$

Note that $\mathcal{T}^{\mu\nu}$ is a tensor density, for the actual tensor we have

$$\langle T^{\mu\nu}(x)\rangle=\lim_{z\to 0}\frac{2}{\sqrt{-g^{(E)}(x,z)}}\frac{\delta S^{(\mathrm{ren})}[g^{(E)}]}{\delta g_{\mu\nu}^{(E)}(x,z)}\,, \tag{4.7}$$

which is recognized as the usual definition of the stress-energy tensor of a classical field theory [24] (except for the limit $z \to 0$).

It is usual practice to follow the analogy with classical mechanics and identify the derivative on the right hand side of (4.5) as the canonical momentum Π_c conjugate to $\Phi_c^{(E)}$ evaluated on the classical solution. This Π_c is calculated as the variation of the action with respect to the time derivative of the field, but, in this analogy, this concept of momentum is generalized to considering the variation with respect to the boundary value of the field, this boundary not necessarily being a constant-time surface. In the present case, of course, the boundary would be a constant-z source. Thus, the renormalized momentum is defined as

$$\Pi_c^{(\text{ren})}(z,x) = \frac{\delta S^{(\text{ren})}[\Phi_c^{(E)}]}{\delta \Phi_c^{(E)}(z,x)}\,, \tag{4.8}$$

so (4.5) becomes

$$\langle \mathcal{O}(x)\rangle_\phi = \lim_{z\to 0} z^{4-\Delta}\Pi_c^{(\text{ren})}(z,x)\,. \tag{4.9}$$

In the example of section 2.3, (2.5), the momentum corresponding to the bulk scalar field is

$$\Pi = -g^{zz}\sqrt{-g}\,\partial_z\Phi\,, \tag{4.10}$$

and by performing this calculation, it can be shown that this implies (2.11), where $A(x)$ is $\phi(x)$.

4.2 Green's functions

Consider now two different observables, $\mathcal{O}_1$ and $\mathcal{O}_2$. Retarded Green's functions are defined as two-point Lorentzian correlation functions:

$$G_R^{\mathcal{O}_1\mathcal{O}_2}(\omega,\vec{k}) = -i\int d^3x\,dt\,e^{-i\omega t - i\vec{k}\cdot\vec{x}}\,\theta(t)\langle[\mathcal{O}_1(t,\vec{x}),\mathcal{O}_2(0,0)]\rangle\,, \tag{4.11}$$

where $\theta(t)$ is the Heaviside step function. It is convenient to consider a time-dependent perturbation in the action, reflected by the addition to the Hamiltonian of a term composed of the second operator and its source,

$$\delta H(t) = \int d^3x\,\phi_2(t,\vec{x})\mathcal{O}_2(x)\;. \tag{4.12}$$

The expectation value of the first operator is given by

$$\langle \mathcal{O}_1(t,\vec{x})\rangle = \operatorname{Tr}\rho_0(t)\,\mathcal{O}_1(\vec{x}) \tag{4.13}$$

where $\rho(t)$ is the time-dependent density matrix associated to the unperturbed hamiltonian H_0. This expected value can also be calculated from a derivative, as in (4.5), but here it is more convenient to consider this relation and go to the interaction picture, in which the time dependence due to $\delta H(t)$ is absorbed into the operators $\mathcal{O}_1$ and $\mathcal{O}_2$, so that

$$\langle \mathcal{O}_1(t,\vec{x})\rangle = \operatorname{Tr}\rho_0\,U^{-1}(t)\,\mathcal{O}_1(t,\vec{x})\,U(t)\;, \tag{4.14}$$

where $\rho_0 = e^{-H_0/T}$ and U is the usual time-ordered exponential

$$U(t) = T\, e^{-i\int^t dt' H(t')} \,. \tag{4.15}$$

Now adding the perturbation term (4.12) and expanding to first order in the perturbation of the Hamiltonian gives

$$\begin{aligned}\delta\langle \mathcal{O}_1(t,\vec{x})\rangle &= -i\,\mathrm{Tr}\,\rho_0 \int^t dt'\, \left[\mathcal{O}_1(t,\vec{x}), \delta H(t')\right] \\ &= -i\int^t d^3x'\, dt' \langle \left[\mathcal{O}_1(t,\vec{x}), \mathcal{O}_2(t',x')\right]\rangle \phi_2(t',\vec{x}')\,.\end{aligned} \tag{4.16}$$

Taking a Fourier's transform of (4.16), we can derive the characteristic relation of linear response theory, namely that the expectation value of an operator in momentum space is proportional to the corresponding source, assuming the former is a small perturbation around equilibrium. For instance, the appearance of an electric current triggered by an electric field is determined by the conductivity. Here we see that the constant of proportionality is actually the Green's function defined above:

$$\delta\langle \mathcal{O}_1(\omega,\vec{k})\rangle_{\phi_2} = G_R^{\mathcal{O}_1\mathcal{O}_2}(\omega,\vec{k})\,\phi_2(\omega,\vec{k})\,, \tag{4.17}$$

In the geometry dual to the field theory at equilibrium, there will be profiles for the various bulk fields involved, $\phi_A(x,z)$, with corresponding boundary values $\phi_{A\,(0)}(x)$. If we wish to perturb the boundary value, then in order to satisfy the bulk equations of motion we will need to perturb the entire bulk field,

$$\phi_A(x,z) \to \phi_A(x,z) + \delta\phi_A(x,z) e^{-i\omega t - i\vec{k}\cdot\vec{x}}\,. \tag{4.18}$$

The equation of motion for $\delta\phi_A(x,z)$ is obtained by substituting (4.18) into the bulk equations of motion and linearizing.

In general, there will be couplings between different operators, but for simplicity let's consider a particularly simple case in which both operators are the same, $\mathcal{O}_1 = \mathcal{O}_2 = \mathcal{O}$. Then, in Euclidean signature, we can define

$$\delta\langle \mathcal{O}(\omega_E,\vec{k})\rangle_{\phi} = G_E(\omega_E,\vec{k})\,\phi(\omega_E,\vec{k})\,, \tag{4.19}$$

where ω_E denotes Euclidean frequency. In the case of (2.5), this yields

$$G_E(\omega_E,\vec{k}) = \frac{\langle \mathcal{O}(\omega_E,\vec{k})\rangle_\phi}{\phi(\omega_E,\vec{k})} = \lim_{z\to 0} z^{2(4-\Delta)} \frac{\Pi_c^{(\mathrm{ren})}}{\Phi_c^{(E)}} = 2(\Delta-2)\frac{B(\omega_E,\vec{k})}{A(\omega_E,\vec{k})}\,. \tag{4.20}$$

Note that $G_E(\omega_E,\vec{k})$ possesses a pole precisely at those frequencies for which $A(\omega_E,\vec{k})$ vanishes. As a consequence, each pole of the Green's function corresponds to a normalizable solution of the equations of motion. This is a one-to-one correspondence, related to the one outlined below (2.10).

There is a reason why we give the definition (4.4) in Euclidean signature: This equation in Lorentzian signature is not directly applicable to obtain correlators. The complications arise because a Lorentzian black hole spacetime contains an event horizon, and it is mandatory to impose an appropriate boundary condition at the horizon when solving the classical equations of motion, in addition to imposing them at the spatial boundary. Besides, the resulting correlation function should be time-ordered, which leads to some subtleties.

However, it all amounts to an appropriate analytic continuation:

$$G_E(\omega_E, \vec{k}) = G_R(i\,\omega_E, \vec{k}) \qquad \text{for } \ \omega_E > 0\,, \tag{4.21}$$

$$G_R(\omega, \vec{k}) = G_E(-i(\omega + i\,\epsilon), \vec{k})\,. \tag{4.22}$$

So if the Euclidean correlation functions G_E are known exactly, the retarded ones can be obtained very simply. However, it is often the case that the Euclidean functions can only be obtained numerically, and then the analytic continuation becomes difficult. Therefore, it is advisable to compute the correlation functions directly in Lorentzian signature. There exists a prescription [25–27] that allows to do so very easily. The idea is to analytically continue the equations of motion to Lorentzian signature (4.22) and require the solution to obey the in-falling boundary condition at the future event horizon of the black brane metric,

$$\Phi_c(t, \vec{x}) \sim e^{-i\,\omega\,(t-z)}\,. \tag{4.23}$$

This ensures that the retarded correlator is causal and only propagates information forward in time. Intuitively, information can fall into the black hole horizon but not come out[2] (at the classical level). It can be verified that the analytic continuation of $\Phi_c^{(E)}(\omega_E, \vec{k})$,

$$\Phi_c(\omega, \vec{k}) = \Phi_c^{(E)}(-i(\omega + i\epsilon), \vec{k})\,, \tag{4.24}$$

satisfies this condition.

5 Wilson Loops

Wilson loops are are very important observables in any gauge theory because they are non-local, contain information about the non-perturbative physics and have applications to many physical phenomena, such as confinement and thermal phase transitions. Their expectation value is defined as

$$W^r(\mathcal{C}) = \mathrm{Tr}\,\mathcal{P}\exp\left[i\int_{\mathcal{C}} dx^\mu\, A_\mu(x)\right]\,, \tag{5.1}$$

where $\mathcal{P}$ denotes path ordering, $\int_{\mathcal{C}}$ denotes a line integral along a closed path $\mathcal{C}$, r denotes the representation of the symmetry group (usually $r = F$ or A, that is, fundamental or adjoint) and $A_\mu(x) = A_\mu^a(x)\,T^a$ is the vector potential expressed in terms of the generators T^a of the corresponding representation.

In the strong coupling limit, Wilson loops can be computed easily using the gravity description of the theory, since they have a dual portrayal in terms of a string worldsheet.

---

[2] Note that if we were to calculate the advanced correlator, as opposed to the retarded one, we would require the solution to obey the *out-going* boundary condition at the horizon.

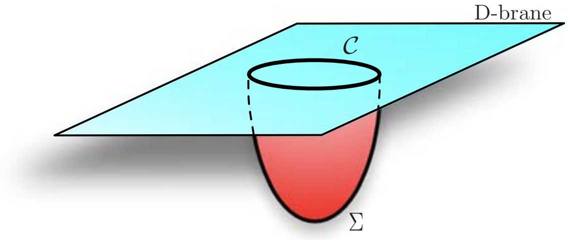

Figure 4. String worldsheet Σ associated to a Wilson loop $\mathcal{C}$.

For this purpose, it is useful to think of the loop $\mathcal{C}$ as the path followed by a fundamental matter field (a quark). As explained in Sec. 3.2, the endpoint of an open string, dual to the quark, lies on a D-brane. Therefore, the boundary of its worldsheet, $\partial\Sigma$, must coincide with the path traversed by the quark, $\mathcal{C}$ (see Fig. 4). On the other hand, the expectation value of the Wilson loop operator (5.1) is basically the partition function (or amplitude) of the quark traversing $\mathcal{C}$. This suggests to identify $W^r(\mathcal{C})$ with the partition function of the dual string worldsheet Σ [28, 29],

$$\langle W(\mathcal{C})\rangle = Z_{\text{string}}[\partial\Sigma = \mathcal{C}]\,. \tag{5.2}$$

The radial position at which the string is attached to the brane is proportional to the quark mass. For simplicity, we can focus on the large quark mass limit, so that the quark is non-dynamical. In this case, we can imagine the probe D-brane placed on the AdS boundary, so that the boundary $\partial\Sigma$ also lies on the boundary of AdS.

However, the string endpoint couples to the gauge field A_μ as well as to the scalar fields on the D-brane ϕ^i. They both get excited when the string pulls on the brane. This suggests that the amplitude of the quark should include also the scalar fields. Let us consider $\mathcal{N}=4$ SYM theory as an example. In this case, (5.1) is generalized to

$$W(\mathcal{C}) = \frac{1}{N_{\rm c}}\mathrm{Tr}\,\mathcal{P}\exp\left[i\oint_{\mathcal{C}} ds\,\left(A_\mu \dot{x}^\mu + \vec{n}\cdot\vec{\phi}\sqrt{\dot{x}^2}\right)\right]\,. \tag{5.3}$$

The dual description of the $W^r(\mathcal{C})$ of (5.1) is the same as that of (5.3), except that Neumann boundary conditions (instead of Dirichlet) must be used on the string worldsheet along the S^5 directions [30]. As a consequence, the strong coupling results to leading order are the same for (5.1) and (5.3). They only differ at the next order in the $1/\sqrt{\lambda}$ expansion.

Moreover, in the strong coupling, large $N_{\rm c}$ limit, the string partition function is greatly simplified because it is given by the exponential of the classical string action, as seen in (4.2). Therefore we have, in Lorentzian signature:

$$Z_{\text{string}}[\partial\Sigma = \mathcal{C}] = e^{iS(\mathcal{C})} \quad \Rightarrow \quad \langle W(\mathcal{C})\rangle = e^{iS(\mathcal{C})}\,, \tag{5.4}$$

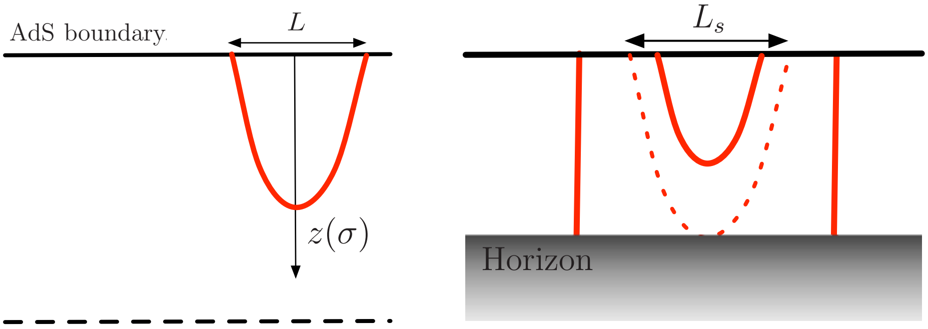

Figure 5. String associated with a quark-antiquark pair in vacuum (left) and in a plasma with temperature $T > 0$ (right).

where the classical action $S(\mathcal{C})$ is obtained by extremizing the Nambu-Goto action for the string worldsheet, under the condition that it ends on the curve $\mathcal{C}$. Intuitively, the reason why this limit is required is that a) strong coupling (large λ) ensures that the string tension is sufficiently large to neglect fluctuations on it, and b) large N_c sends the string coupling to zero, so we can ignore the possibility of loops of string breaking off from the worldsheet. Under this conditions, the worldsheet just hangs down from the contour $\mathcal{C}$ taking the shape corresponding to its classical configuration. Note that it is remarkable that a calculation of a Wilson loop in a strongly interacting gauge theory may simplify to a classical mechanics problem not more difficult than finding a catenary curve.

In many cases, the qualitative behavior of the Wilson loop can be explained by gross features of the bulk geometry. One of the clearest examples is that of a rectangular loop at zero or finite temperature. Consider $\mathcal{C}$ sitting at a constant position on the S^5 with a rectangular shape, so that the long side extends along the time direction (length $\mathcal{T}$) and the short side along the x_1-direction (length L), so that $\mathcal{T} \gg L$. This can be thought of as a static quark-antiquark pair separated by a distance L.

In a pure AdS spacetime (1.2), since there are no scales, the calculation must result in a potential energy between the pair with a dependence $V(L) \propto 1/L$. But if we introduce temperature as in (3.2), there exists a critical value of the separation, L_s, beyond which the preferred configuration takes on a different shape. As can be seen in Fig. 5, in this case there is a horizon, and at some separation the lowest part of the string touches the horizon. Above (and at) this separation the energy of the string gets minimized by splitting into two disjoint independent strings, each of which falls through the horizon. The transition value is called *screening length* and in this case it is determined by the temperature, which is the only scale of the problem, so $L_\mathrm{s} \sim 1/T$. When $L = L_\mathrm{s}$, the lowest point of the connected configuration is close but still somewhat above the horizon.

Once $L > L_\mathrm{s}$, the quark-antiquark separation can be increased further at no additional energy cost (because the strings become independent of each other). Thus, the potential must become a constant because the quark and antiquark are completely screened by the plasma between them. This description is a simple model for what happens in the

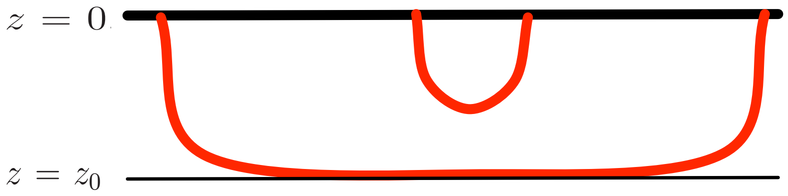

Figure 6. String associated with a quark-antiquark pair in a confining theory.

deconfined phase of QCD with the mesons that survive deconfinement, and it illustrates that, even though $\mathcal{N} = 4$ SYM at $T = 0$ is very different from QCD at $T = 0$, $\mathcal{N} = 4$ SYM at $T \neq 0$ can work as an approximation to QCD at $T > T_c$. This is a fact that will be employed to motivate many of the calculations on this thesis.

Now let us consider a spacetime metric corresponding to a confining theory [18]:

$$ds^2 = \frac{R^2}{z^2}\left(-dt^2 + dx_1^2 + dx_2^2 + f(z)dx_3^2\right) + \frac{R^2}{z^2 f(z)}dz^2 \,, \tag{5.5}$$

where $f(z) = 1 - z^4/z_0^4$. The crucial difference with respect to pure AdS is that this spacetime ends smoothly at a finite value $z = z_0$, which introduces a scale in the theory; and with respect to the finite temperature metric is that the string has no place to end, so in order to minimize its energy it tends to drop down to z_0 and to run parallel there, as pictured in Fig. 6. Beyond some critical value of the separation, so that $L \gg z_0$, we can expect the potential to be $V(L) \sim L$ because increasing further the separation does not make the string sag deeper, but it adds more and more string at the same depth z_0, which costs an energy that increases linearly with the separation. The lengthscale z_0 in this gravitational description corresponds to the mass gap of the gauge theory, $M \propto 1/z_0$, that only exists in the confining phase.

6 Quantum criticality and superconductors

Quantum critical theories arise at continuous phase transitions at zero temperature, caused by non-analyticities in the ground state of a system as a function of some order parameter, such as pressure or an applied magnetic field. The quantum critical point may or may not be the zero temperature limit of a finite temperature phase transition. A generic feature of quantum critical points is that they have a spacetime scale invariance that provides a strong connection to simple versions of the AdS/CFT correspondence. Furthermore, the absence of weakly coupled quasiparticles often makes them difficult to study using traditional methods. Outside of the AdS/CFT, there are no models of strongly coupled quantum criticality in which analytic results for processes such as transport can be obtained.

Typically, as the continuous quantum critical point is approached, the energy of fluctuations about the ground state (energy gap) vanishes and the coherence length (that is, the

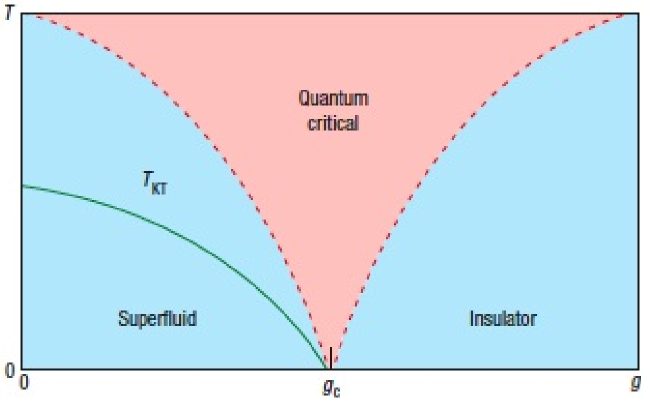

Figure 7. Typical phase diagram near a quantum critical point.

characteristic lengthscale) diverges with specific scaling properties. The quantum critical theory itself is scale invariant, and in regions of the phase diagram away from the point at which the energy gap vanishes, the quantum critical points dominate the behavior of the system. For instance, in regions where the deformation away from criticality due to an energy scale Δ is less important than the deformation due to a finite temperature T (that is, where $\Delta < T$), the system can actually be described by the fnite temperature quantum critical theory. This leads to the counterintuitive fact that the imprint of the zero temperature critical point grows as temperature is increased (see Fig. 7).

As outlined in Sec. 1.2, the gauge/gravity duality geometrizes the field theory energy scale. Most commonly, the theory is defined either with a UV cutoff or via a UV fixed point which depicts a theory valid at all scales. At the fixed point itself, the theory is scale invariant, and that makes it the simplest place to start for the gravitational dual. The framework of the gravitational dual is expected to be applicable to strongly coupled condensed matter systems in the vicinity of quantum phase transitions. Examples of systems that display quantum criticality and that can be subject to holographic models are the Wilson-Fisher fixed point and the spinon-photon interaction in quantum magnets. Typically the critical theory is strongly coupled and so any action we write down to describe the theory will not be directly useful for the analytic computation of many quantities of interest. Indeed, this is the motivation for turning to gravitational models.

Specially important are those systems that display induced symmetry breaking phase transitions. These are generically known as superconductors or superfluids, because of features that arise as consequences of that symmetry breaking. In the simplest superconducting systems, we have a global $U(1)$ symmetry which is spontaneously broken at the phase transition. This breaking results in a massless Goldstone boson φ, which transforms under $U(1)$ by the shift $\varphi \to \varphi + \Lambda$. Gauge invariance of the theory in an electromagnetic background A_μ means that the renormalized classical action can be written as

$$S^{(\text{ren})} = \int d^d x \sqrt{-g} \mathcal{F}[A_\mu - \partial_\mu \varphi] \tag{6.1}$$

for some function $\mathcal{F}$. Stability of the theory in the absence of Goldstone mode excitations or background fields implies that $\mathcal{F}$ must have a minimum at $A_\mu = \partial_\mu \varphi$. Following (4.5), the expected value of the current operator associated to the gauge field, J^μ, is calculated as

$$J^\mu = \frac{\delta S^{(\mathrm{ren})}}{\delta A_\mu(x)}\bigg|_{A_\mu = \partial_\mu\varphi + \delta A_\mu} = \mathcal{F}''[0]\,\delta A^\mu\,. \tag{6.2}$$

In the gauge with $\delta A_t = 0$, the electric field in Fourier space is just $\delta E_\mu = i\,\omega\,\delta A_\mu$. Therefore,

$$J_\mu = -\frac{i\,\mathcal{F}''[0]}{\omega}\,\delta E_\mu = \sigma(\omega)\,\delta E_\mu\,, \tag{6.3}$$

where $\sigma(\omega)$ is the conductivity, divergent as $\omega \to \infty$.

Beyond this generic simple model, one needs a microscopic theory to determine how the symmetry breaking condensate forms in the material. Most traditional theories, BCS theory being the canonical example, introduce charged quasiparticles that are paired into bosonic operators by a gluing interaction mediated by another quasiparticle such as phonons. The composite charged operator can then be shown to condense. One motivation for developing holographic models of superconductivity is to have a microscopic description of superconductivity out of first principles, rather than effective models, in which there are no quasiparticles whatsoever. Instead, there is a strongly coupled theory in which a charged operator condenses below a critical temperature.

High-T_c and p-wave superconductors are being accommodated into the gravitational framework [32]. There are many gravitational backgrounds that one may consider for the dual theory, the simplest one being (3.2), which corresponds to a scale invariant theory at finite temperature. But this one will not describe superconductivity, since all nonzero temperatures are equivalent. In order to have a critical temperature T_c, another scale must be introduced. The simplest way to do so is to work at finite chemical potential, as in (3.3). By dimensional analysis, this allows $T_c \propto \mu$. For instance, a chemical potential appears when describing cuprate superconductors, as a measure of the doping away from critical doping [33].

The normal state of the system is generically dual to the solution (3.2), which is unstable to the formation of a charged condensate (i.e. a non-vanishing expectation value $\langle \mathcal{O} \rangle$ for the operator dual to a bulk scalar field) if $T \ll \mu$. In order for this to happen, in this regime the spacetime should be unstable against perturbations of the bulk field, so that it acquires a non-zero solution spontaneously. Note that it is highly unusual from a weakly coupled perspective that a theory with charged bosons can be stable against condensation at zero temperature in the presence of a chemical potential.

In a broader sense, theories with gravitational duals are well defined, albeit exotic, theories against which the arsenal of condensed matter concepts can be tested. As opposed to other approaches, it is important to keep in mind that we can ask questions about currents and parameters, but not about "electrons" or "phonons", that is, we cannot resort to weak coupling language. The fact that the holographic approach provides explicit examples of theories without a quasiparticle description in which computations are, nevertheless, feasible is one of the reasons why AdS/CFT turns out to be very useful in the field of strongly coupled condensed matter physics. Another one is that, although the holographic duals may have unfamiliar points, they also display features that are expected to be universal for all strongly coupled theories with a gravity dual, so that we can use their qualitative predictions to test our expectations and guide us in refining our assumptions.

7 Potential of the holographic approach

If the numerical agreement between the theoretical predictions and experimental results is used as the only justification for it, there is clearly an uncertainty when it comes to evaluating the applicability of the gauge/string duality to heavy ion phenomenology or to condensed matter systems. However, the possibility of gaining insight into problems that cannot be addressed within the available theoretical technology outside of string theory is inherently valuable. Within the gauge/string correspondence, it has been possible to formulate and solve many problems in a large class of quantum field theories. In particular, strongly coupled $\mathcal{N} = 4$ SYM theory at large N_c turns out to provide a simple model for the strongly coupled plasma being produced and probed in heavy ion collisions, in addition to a fairly natural description of superconductivity.

Another important role played by the duality is being a testing ground for pre-established ideas and a source of new ones, in those regimes beyond the guidance of perturbation theory. For example, holographic calculations have given support to the possibility that heavy quarkonium mesons survive deconfinement. In this thesis, we focus on the qualitatively new ideas suggested by the duality: The in-medium energy loss of heavy quarks via Cherenkov emission of mesons (Chapter 1); and the non-trivial dependence on anisotropy of several observables of the plasma, such as screening lengths or the jet quenching parameter (Chapter 2), as well as its effect over transport coefficients of p-wave superfluids (Chapter 3). Even though it is true that a critical mind must be kept when trying to extract definitive conclusions from any holographic calculation, it is beyond a doubt that within their range of applicability they have provided useful computable models where direct means have failed to do so.

Thus, it is hoped that these new applications of the gauge/gravity duality will continue to make an important contribution to our understanding of fundamental open problems in high energy and condensed matter physics.

References

[1] J. M. Maldacena, "The large N limit of superconformal field theories and supergravity," *Adv. Theor. Math. Phys.* **2** (1998) 231–252, `arXiv:hep-th/9711200`.

[2] S. S. Gubser, I. R. Klebanov, and A. M. Polyakov, "Gauge theory correlators from non-critical string theory," *Phys. Lett.* **B428** (1998) 105–114, `arXiv:hep-th/9802109`.

[3] E. Witten, "Anti-de Sitter space and holography," *Adv. Theor. Math. Phys.* **2** (1998) 253–291, `arXiv:hep-th/9802150`.

[4] J. M. Maldacena, "Lectures on AdS/CFT," `arXiv:hep-th/0309246`.

[5] J. Polchinski, "Introduction to Gauge/Gravity Duality," `arXiv:1010.6134 [hep-th]`.

[6] J. Casalderrey-Solana, H. Liu, D. Mateos, K. Rajagopal and U. A. Wiedemann, "Gauge/String Duality, Hot QCD and Heavy Ion Collisions," `arXiv:1101.0618 [hep-th]`.

[7] A. M. Polyakov, "The wall of the cave," *Int. J. Mod. Phys.* **A14** (1999) 645–658, `arXiv:hep-th/9809057`.

[8] G. 't Hooft, "Dimensional reduction in quantum gravity," `arXiv:gr-qc/9310026`. , gr-qc/9310026.

[9] L. Susskind, "The World as a hologram," *J. Math. Phys.* **36** (1995) 6377–6396, `arXiv:hep-th/9409089`.

[10] A. W. Peet and J. Polchinski, "UV/IR relations in AdS dynamics," *Phys. Rev.* **D59** (1999) 065011, `arXiv:hep-th/9809022`.

[11] P. Breitenlohner and D. Z. Freedman, "Positive Energy in anti-De Sitter Backgrounds and Gauged Extended Supergravity," *Phys. Lett.* **B115** (1982) 197.

[12] P. Breitenlohner and D. Z. Freedman, "Stability in Gauged Extended Supergravity," *Ann. Phys.* **144** (1982) 249.

[13] L. Mezincescu and P. K. Townsend, "Stability at a Local Maximum in Higher Dimensional Anti-de Sitter Space and Applications to Supergravity," *Ann. Phys.* **160** (1985) 406.

[14] I. R. Klebanov and E. Witten, "AdS/CFT correspondence and symmetry breaking," *Nucl. Phys.* **B556** (1999) 89–114, `arXiv:hep-th/9905104`.

[15] V. Balasubramanian, P. Kraus, and A. E. Lawrence, "Bulk vs. boundary dynamics in anti-de Sitter spacetime," *Phys. Rev.* **D59** (1999) 046003, `arXiv:hep-th/9805171`.

[16] V. Balasubramanian, P. Kraus, A. E. Lawrence, and S. P. Trivedi, "Holographic probes of anti-de Sitter space-times," *Phys. Rev.* **D59** (1999) 104021, `arXiv:hep-th/9808017`.

[17] O. Aharony, S. S. Gubser, J. M. Maldacena, H. Ooguri, and Y. Oz, "Large N field theories, string theory and gravity," *Phys. Rept.* **323** (2000) 183–386, `arXiv:hep-th/9905111`.

[18] E. Witten, "Anti-de Sitter space, thermal phase transition, and confinement in gauge theories," *Adv. Theor. Math. Phys.* **2** (1998) 505–532, `arXiv:hep-th/9803131`.

[19] J. Polchinski and M. J. Strassler, "The string dual of a confining four-dimensional gauge theory," `arXiv:hep-th/0003136`.

[20] I. R. Klebanov and M. J. Strassler, "Supergravity and a confining gauge theory: Duality cascades and chiSB-resolution of naked singularities," *JHEP* **08** (2000) 052, `arXiv:hep-th/0007191`.

[21] J. M. Maldacena and C. Nunez, "Towards the large N limit of pure N = 1 super Yang Mills," *Phys. Rev. Lett.* **86** (2001) 588–591, `arXiv:hep-th/0008001`.

[22] G. W. Gibbons and S. W. Hawking, "Action Integrals and Partition Functions in Quantum Gravity," *Phys. Rev.* **D15** (1977) 2752–2756.

[23] K. Skenderis, "Lecture notes on holographic renormalization," *Class. Quant. Grav.* **19** (2002) 5849–5876, `arXiv:hep-th/0209067`.

[24] L. D. Landau and E. M. Lifshitz, "Course Theoretical Physics. Vol. 2: The Classical Theory of Fields,". , Elsevier (1975).

[25] D. T. Son and A. O. Starinets, "Minkowski-space correlators in AdS/CFT correspondence: Recipe and applications," *JHEP* **09** (2002) 042, `arXiv:hep-th/0205051`.

[26] N. Iqbal and H. Liu, "Universality of the hydrodynamic limit in AdS/CFT and the membrane paradigm," *Phys.Rev.* **D79** (2009) 025023, `arXiv:0809.3808 [hep-th]`.

[27] N. Iqbal and H. Liu, "Real-time response in AdS/CFT with application to spinors," *Fortsch. Phys.* **57** (2009) 367–384, `arXiv:0903.2596 [hep-th]`.

[28] J. M. Maldacena, "Wilson loops in large N field theories," *Phys. Rev. Lett.* **80** (1998) 4859–4862, `arXiv:hep-th/9803002`.

[29] S.-J. Rey and J.-T. Yee, "Macroscopic strings as heavy quarks in large N gauge theory and anti-de Sitter supergravity," *Eur. Phys. J.* **C22** (2001) 379–394, `arXiv:hep-th/9803001`.

[30] L. F. Alday and J. Maldacena, "Comments on gluon scattering amplitudes via AdS/CFT," *JHEP* **0711** (2007) 068, `arXiv:0710.1060 [hep-th]`.

[31] R. D. Parks, *Superconductivity*, Marcel Dekker Inc. (1969).

[32] V. Galitski and S. Sachdev "Paired electron pockets in the hole-doped cuprates," arXiv:0901.0005 [cond-mat.str-el].

[33] S. Sachdev, "Quantum magnetism and criticality," Nature Physics **4**, 173 (2008) [arXiv:0711.3015 [cond-mat.str-el]].

Chapter 2

Cherenkov emission of mesons: A universal prediction

This chapter contains the publications:

- J. Casalderrey-Solana, D. Fernandez, and D. Mateos,
“A New Mechanism of Quark Energy Loss,”

  Phys. Rev. Lett. **104** (2010) 172301, `arXiv:0912.3717 [hep-ph]`.

- J. Casalderrey-Solana, D. Fernandez, and D. Mateos,
“Cherenkov mesons as in-medium quark energy loss,”

  JHEP **1011** (2010) 091, `arXiv:1009.5937 [hep-th]`.

New Mechanism for Quark Energy Loss

Jorge Casalderrey-Solana,[1] Daniel Fernández,[2] and David Mateos[2,3]
[1] *Physics Department, Theory Unit, CERN, CH-1211 Genève 23, Switzerland*
[2] *Departament de Física Fonamental & Institut de Ciències del Cosmos, Universitat de Barcelona, Diagonal 647, E-08028 Barcelona, Spain*
[3] *Institució Catalana de Recerca i Estudis Avançats (ICREA), Lluís Companys 23, E-08010, Barcelona, Spain*
(Received 21 January 2010; published 30 April 2010)

We show that a heavy quark moving sufficiently fast through a quark-gluon plasma may lose energy by Cherenkov-radiating mesons. We demonstrate that this takes place in all strongly coupled, large-N_c plasmas with a gravity dual. The energy loss is exactly calculable in these models despite being an $\mathcal{O}(1/N_c)$ effect. We discuss implications for heavy-ion collision experiments.

DOI: 10.1103/PhysRevLett.104.172301 PACS numbers: 25.75.−q, 11.25.Tq

Introduction.—A remarkable conclusion from the Relativistic Heavy Ion Collider (RHIC) experiments [1] is that the quark-gluon plasma does not behave as a weakly coupled gas of quarks and gluons, but rather as a strongly coupled fluid [2]. This makes the study of the plasma a challenging task.

Experimentally, valuable information is obtained by analyzing the energy loss of energetic partons created in hard initial collisions. In order to use this information to learn about the plasma, a theoretical, quantitative understanding of the different mechanisms of parton energy loss is needed. Several such mechanisms have been previously studied, both in QCD itself [3] and in the context of the gauge-gravity duality [4].

In this Letter we will uncover a new mechanism whereby a sufficiently fast heavy quark traversing a strongly coupled plasma loses energy by Cherenkov-radiating in-medium mesons. We will first show that this takes place in all strongly coupled, large-N_c theories with a gravity dual. Next we will calculate the energy loss in a simple example. Finally, we will discuss possible implications for heavy-ion collision experiments.

Universality of the mechanism.—This follows from two universal properties of the gauge-gravity duality (in the limit $N_c, \lambda \to \infty$): (i) the fact that the gauge theory deconfined phase is described by a black hole (BH) geometry [5], and (ii) the fact that a finite number of quark flavors N_f is described by N_f D-brane probes [6]—see Fig. 1. In addition to the gauge theory directions, the gravity description always includes a radial direction which is dual to the gauge theory energy scale. The radial position of the horizon is proportional to the plasma temperature T. The D-branes extend in the radial direction down to a minimum value proportional to the (constituent) quark mass M_q.

For sufficiently large M_q/T, the D-branes sit outside the horizon [7–9]. In this phase, low-spin gauge theory mesons are described by small, normalizable fluctuations of scalar and vector fields propagating on the branes, whose spectrum is discrete and gapped. In particular, this means that sufficiently heavy mesons survive deconfinement, in agreement with lattice and potential model predictions for real-world QCD [10].

Let $\omega(q)$ be the in-medium dispersion relation (DR) for these mesons. As an illustrative example, the DR for vector mesons in the $D3/D7$ system is depicted in Fig. 2. As $q \to \infty$, the DR becomes linear: $\omega(q) \sim v_{\text{lim}} q$, with $v_{\text{lim}} < 1$. This subluminal limiting velocity, which is the same for all mesons, is easy to understand in the gravitational description [11]. Since highly energetic mesons are strongly attracted by the BH, their wave function is very concentrated at the bottom of the branes. Consequently, their velocity is limited by the local speed of light v_{lim} at this point (see Fig. 1). Because of the BH redshift, v_{lim} is lower than the speed of light at infinity. In the gauge theory this translates into the statement that v_{lim} is lower than the speed of light in the vacuum [12].

Consider now a heavy quark in the plasma. In the gravitational picture, this is described by a string that starts on the D-branes and falls through the horizon—see Fig. 1. In order to model a highly energetic quark we consider a string whose end point moves with an arbitrary velocity v at an arbitrary radial position r_0, where r_0 is inversely proportional to the size of the gluon cloud that dresses the quark [15].

Two simple observations now lead to the effect that we are interested in. The first one is that the string end point is charged under the scalar and vector fields on the branes. In the gauge theory, this corresponds to an effective quark-meson coupling (see Fig. 3) of order $\sim 1/\sqrt{N_c}$. The dynamics of the branes + string end point system is thus (a

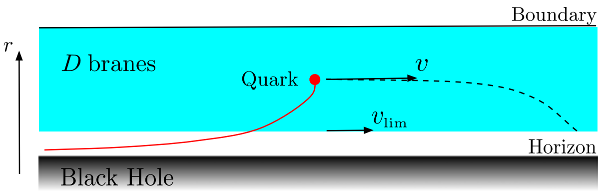

FIG. 1 (color online). D-branes and open string in a BH geometry.

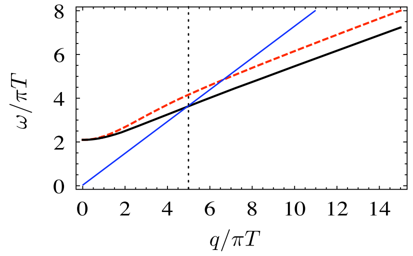

FIG. 2 (color online). DR for the transverse (black, continuous curve) and longitudinal (red, dashed curve) modes of a heavy vector meson with $v_{\rm lim} = 0.35$ in the $D3/D7$ system. The blue, continuous straight line corresponds to $\omega = vq$ with $v_{\rm lim} < v < 1$.

generalization of) that of classical electrodynamics in a medium in the presence of a fast-moving charge. The second observation is that the velocity of the quark may exceed the limiting velocity of the mesons, since the redshift at the position of the string end point is smaller than at the bottom of the branes. As in ordinary electrodynamics, if this happens then the string end point loses energy by Cherenkov radiating into the fields on the brane. In the gauge theory, this translates into the quark losing energy by Cherenkov-radiating scalar and vector mesons. The rate of energy loss is set by the square of the coupling, and is therefore of order $1/N_c$.

A quantitative example.—In this section we will calculate the rate of energy loss in four-dimensional, $SU(N_c)$, $\mathcal{N} = 4$ super-Yang-Mills (SYM) theory coupled to one quark flavour (but the result is valid for arbitrary N_f, see Discussion section). The dual description consists of a $D7$-brane probe in the supergravity background of N_c black $D3$-branes. Following [12] we write the induced metric on the $D7$-brane world volume as $ds^2 = L^2 ds^2(g)$ with

$$ds^2(g) = \frac{\rho^2}{2}\left[-\frac{f^2}{\tilde{f}}dt^2 + \tilde{f}dx_i^2\right] + \frac{(1+\dot{R}^2)}{\rho^2}dr^2 + \frac{r^2}{\rho^2}d\Omega_3^2, \tag{1}$$

where $\rho^2 = R^2 + r^2$, $f = 1 - 1/\rho^4$, $\tilde{f} = 1 + 1/\rho^4$, $\dot{R} = dR/dr$, and $x^\mu = \{t, x^i\}$ are the four gauge theory directions. $R(r)$ describes the $D7$-brane embedding, with $R(\infty) = 2M_q/\sqrt{\lambda}T$. The dimensionless coordinates above are related to their dimensionful counterparts (denoted with tildes) through $x^\mu = \pi T \tilde{x}^\mu$, $\{r, R, \rho\} = \{\tilde{r}, \tilde{R}, \tilde{\rho}\}/\pi L^2 T$.

The terms in the brane + string action relevant to our calculation are

$$S = -\int d^8\sigma\sqrt{-g}\,\frac{1}{4}F^{ab}F_{ab} - e\int d\tau A_a\frac{d\sigma^a}{d\tau}, \tag{2}$$

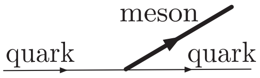

FIG. 3. Effective quark-meson coupling.

where $F_{ab} = \partial_{[a}A_{b]}$ and $\sigma^a = \{x^\mu, r, \Omega_3\}$. The first term comes from expanding the Dirac-Born-Infeld part of the $D7$-brane action to quadratic order in the gauge field. The metric g that enters this term is that in Eq. (1), which contains no factors of L; these have been absorbed in the definition of e in Eq. (3). The Wess-Zumino part of the $D7$-brane action will not contribute to our calculation. The second term in (2) is the minimal coupling of the end point of an open string, whose worldline is parametrized by $\sigma^a(\tau)$, to the gauge field on the branes. We have omitted a similar coupling to the scalar fields, which will be considered in [16]. The coupling constant in (2) is

$$e^2 = \frac{1}{T_{\rm D7}(2\pi l_s^2)^2 L^4} = \frac{8\pi^4}{N_c}, \tag{3}$$

where $T_{\rm D7} = 1/g_s(2\pi)^7\ell_s^8$ is the $D7$-brane tension. As expected, e is of order $1/\sqrt{N_c}$, which justifies our neglect of terms of order higher than quadratic in the action.

The second term in (2) may be written as $-e\int d^8\sigma A_a J^a$. For simplicity, we will assume that the quark moves with constant velocity along a straight line at constant radial and angular positions, so we write

$$J^a = \delta^{(3)}(\vec{x} - \vec{v}t)\delta(r - r_0)\delta^{(3)}(\Omega - \Omega_0)\times(1, \vec{v}, 0, \vec{0}). \tag{4}$$

In reality, r_0 and v will of course decrease with time because of the BH gravitational pull and the energy loss. However, for simplicity we will concentrate on the initial part of the trajectory (which is long provided the initial quark energy is large) for which r_0 and v are approximately constant [17]—see Fig. 1.

The rate of quark energy loss is given by minus the work per unit time done by the gauge field:

$$\frac{dE}{dt} = -e\int d^3x dr d\Omega_3 F_{0a}J^a = -ev^i F_{0i}(t, \vec{v}t, r_0, \Omega_0). \tag{5}$$

Since real-world QCD has no internal S^3, we focus on modes with no angular momentum on the S^3. These take the form $A_\mu(x^\nu, r)$, $A_r(x^\nu, r)$, $A_\Omega = 0$. We set $A_r = 0$ by a gauge choice. Further, we work with the Fourier-space components $A_\mu(\omega, q, r)$ and choose $\vec{q} = (q, 0, 0)$, $\vec{v} = v(\cos\theta, \sin\theta, 0)$. After integrating over the S^3, the relevant Fourier-space components of the current are

$$J^\mu = 2\pi\delta(\omega - qv\cos\theta)\delta(r - r_0)\times(1, \cos\theta, \sin\theta, 0). \tag{6}$$

With this choice the only transverse mode of the gauge field excited by the source is $\mathcal{A} = A_2$. The equation of motion for this mode is

$$\partial_r\left(\frac{fr^3\partial_r\mathcal{A}}{2\sqrt{1+\dot{R}^2}}\right) + \sqrt{1+\dot{R}^2}\,\frac{r^3}{\rho^4}\left(\frac{\omega^2\tilde{f}}{f} - \frac{q^2 f}{\tilde{f}}\right)\mathcal{A} = \tilde{e}\mathcal{J}, \tag{7}$$

where $\mathcal{J} = J^2$, $\tilde{e} = e/\Omega_3$, and $\Omega_3 = 2\pi^2$ is the volume of a unit S^3. We solve (7) by expanding $\mathcal{A}$ as

$$\mathcal{A}(\omega, q, r) = \sum_n \mathcal{A}_n(\omega, q)\xi_n(q, r) \tag{8}$$

in terms of a basis of normalizable eigenfunctions $\{\xi_n(q,r)\}$ in the radial direction. These are solutions of Eq. (7) with $\mathcal{J}=0$ with q-dependent eigenvalues $\omega=\omega_n(q)$, and satisfy the orthonormality relations

$$\int_0^\infty dr \frac{\tilde{f} r^3}{f \rho^4} \sqrt{1+\dot{R}^2}\, \xi_m \xi_n = \delta_{mn}. \tag{9}$$

Inserting the expansion (8) in (7), and using the eigenstate equation and the orthonormality relations, we find

$$[\omega^2 - \omega_n^2(q)]\mathcal{A}_n(\omega, q) = \tilde{e}\mathcal{J}_n(\omega, q), \tag{10}$$

where

$$\begin{aligned}\mathcal{J}_n(\omega, q) &= \int dr \mathcal{J}(\omega, q)\xi_n(q, r) \\ &= 2\pi\delta(\omega - qv\cos\theta)v\sin\theta\xi_n(q, r_0).\end{aligned} \tag{11}$$

Through the expansion (8) we have "Kaluza-Klein" reduced the five-dimensional gauge field to a discrete, infinite tower of independent four-dimensional gauge fields $\{\mathcal{A}_n(\omega, q)\}$. Each of these fields is characterized by a q-dependent radial "wave function" $\xi_n(q, r)$, as well as by a DR $\omega = \omega_n(q)$, and couples to the quark with an effective strength $e_{\rm eff}(q, r_0) = e\xi_n(q, r_0)$.

With retarded boundary conditions, as appropriate for the reaction to the quark's passage, Eq. (10) yields

$$\mathcal{A}_n(\omega, q) = \frac{\tilde{e}\mathcal{J}_n(\omega, q)}{(\omega + i\epsilon)^2 - \omega_n^2(q)}. \tag{12}$$

We now evaluate (5) to obtain the energy deposited on the nth transverse mode. We first express $F_{02}(t, \vec{v}t, r_0, \Omega_0)$ as an integral over its Fourier components. We then integrate over frequencies trivially because of the delta function in (11). Finally, we set $d^3q = 2\pi q^2 dq ds$, where $s = \cos\theta$, to arrive at

$$\begin{aligned}\frac{dE_n}{dt} &= -\frac{e^2 v}{\Omega_3}\int_0^\infty \frac{dq}{2\pi} q\xi_n^2(q, r_0)\int_{-1}^{1}\frac{ds}{2\pi i}\frac{s(1-s^2)}{(s+i\epsilon)^2 - s_n^2(q)} \\ &= \frac{e^2 v}{2\Omega_3}\int_0^\infty \frac{dq}{2\pi} q\xi_n^2(q, r_0)(1 - s_n^2(q))\Theta(1 - s_n^2(q)),\end{aligned} \tag{13}$$

where $s_n = v_n/v$ and $v_n(q) = \omega_n(q)/q$ is the phase velocity of the mode. The Heaviside function confirms the expected result: the quark only radiates into modes with phase velocity lower than v—those to the right of the dashed, vertical line in Fig. 2. The numerical result for $n = 0$ is plotted in Fig. 4. For fixed r_0, the energy loss increases monotonically with v up to the maximum allowed value of v—the local speed of light at r_0. As r_0 decreases, the characteristic momentum $q_{\rm char}$ of the modes contributing to the integral increases. As $r_0 \to 0$ these modes become increasingly peaked at small r, and $e_{\rm eff}(q_{\rm char}, r_0)$ and the energy loss diverge [16]. However, this mathematical divergence is removed by physical effects we have not taken into account. For example, for sufficiently large q the radial profile of the mesons becomes of order the string length and stringy effects become important [13]. Also, mesons acquire widths $\Gamma \propto q^2$ at large q [18] and can no longer be treated as well-defined quasiparticles. Finally, the approximation of a constant-v, constant-r_0 trajectory ceases to be valid whenever the energy loss rate becomes large.

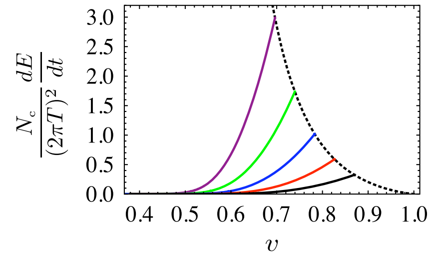

FIG. 4 (color online). Energy loss into $\mathcal{A}_{(n=0)}$ for an embedding with $R(\infty) = 1.32$. The continuous curves correspond to $r_0 = 0.86, 0.97, 1.10, 1.25, 1.45$. The dotted curve is defined by the end points of the constant-r_0 curves.

Phenomenology.—The Cherenkov radiation of mesons by quarks depends only on the qualitative features of the DR of Fig. 2, which are universal for all gauge theory plasmas with a dual gravity description [19]. Moreover, it is conceivable that they may also hold for QCD mesons such as the J/ψ or the Υ (see, e.g., the discussion in [14]). Here we will examine some qualitative consequences of this assumption for HIC experiments.

The energy lost into mesons would be reflected in a reduction of the heavy quark nuclear modification factor $R_{\rm AA}$ [21]. This would only occur for high enough quark velocities, thus yielding a very particular behavior of $R_{\rm AA}$. Note that the minimum quark velocity at which the reduction starts to occur may actually be higher than $v_{\rm lim}$, since the quark energy must be larger than the mass of the radiated meson. For example, for a charm quark to radiate a J/ψ meson this condition yields $v > 0.87$. In fact, our calculation applies strictly only in the limit of infinite quark energy, which suggests that it should be more relevant to HIC experiments at the Large Hadron Collider than at RHIC.

The radiated mesons would be preferentially emitted at a characteristic Cherenkov angle $\cos\theta_c = v_{\rm lim}/v$. Taking the gravity result as guidance, $v_{\rm lim}$ could be as low as $v_{\rm lim} = 0.35$ at the meson dissociation temperature [12], corresponding to an angle as large as $\theta_c \approx 1.21$ rad. This emission pattern is similar to the emission of sound waves by an energetic parton [22] in that both effects lead to a nontrivial angular structure. One important difference, however, is that the radiated heavy mesons would not thermalize and hence would not be part of a hydrodynamic shock wave. As in the Mach cone case, the meson emission pattern could be reflected in azimuthal dihadron correlations triggered by a high-p_T hadron. Because of surface bias, the energetic parton in the triggered direction is hardly modified, while the one propagating in the opposite direction moves through a significant amount of medium, emitting heavy mesons. Thus, under the above assumptions, the dihadron distribution with an associated J/ψ would have a ringlike structure peaked at an angle $\theta \approx \pi - \theta_c$.

Discussion.—Cherenkov emission of gluons in the context of heavy-ion collisions has been considered in [23], where the in-medium gluons are assumed to have spacelike DR. Although some of the underlying physics is similar, the mechanism we have discussed is different in two respects. First, the radiated particles are colorless mesons, not gluons. Second, the gauge-gravity duality provides a large class of completely explicit and calculable examples in which this mechanism is realized.

We have focused on the transverse modes of the gauge field. Since the vector mesons are massive, there is a similar energy loss into the longitudinal modes [16].

We calculated the energy deposited on the branes by the string end point. Since the branes sit outside the BH, this energy must stay on the branes (in the limit N_c, $\lambda \to \infty$). Because total conserved charges must agree, this energy is the same as the energy lost by the quark in the gauge theory. The Cherenkov angle θ_c is also the same, since it is determined by kinematics alone. In contrast, extracting unintegrated gauge theory quantities (e.g., the differential power spectrum) would require computing the boundary stress-energy tensor as in [24].

The validity of our results requires not just large N_c, but also strong coupling. In this regime the holographic mesons behave as elementary excitations, as opposed to composite bound states, up to energies of order $\sqrt{\lambda}T \gg T$ [7,12]. Despite the strong coupling requirement, our results might apply to asymptotically free theories as long as (i) they are sufficiently strongly coupled at the scale T, so that the in-medium meson DR shares the qualitative features of that in Fig. 2, and (ii) there is a nonzero quark-meson coupling in the medium.

The energy loss is N_f independent because (at leading order) the string end point couples directly to the gauge field on only one of the N_f *D*-branes. The $1/N_c$ scaling of the energy loss does not necessarily imply that the analogous effect (if present) is small in $N_c = 3$ real-world QCD, in particular, at high quark velocities. Furthermore, its characteristic geometry and velocity dependence may make it easily identifiable.

We close with a comment on the energy loss of heavy mesons. At $N_c \to \infty$, these mesons experience no drag [12,25]. At finite N_c, pointlike heavy mesons experience a drag of order $\mathcal{O}(1/N_c^2)$ [26]. Cherenkov radiation implies an $\mathcal{O}(1/N_c)$ drag for fast excited mesons describable as a long string with both end points on the *D*-branes [27], since each end point may radiate as an individual quark.

Acknowledgments. We thank M. Chernicoff, R. Emparan, B. Fiol, A. Guijosa, C. Manuel, A. Paredes, L. Patiño, and P. Townsend for discussions. We are supported by a Marie Curie PIEF-GA-2008-220207 (J. C. S.) and 2009SGR168, MEC FPA 2007-66665-C02 and CPAN CSD2007-00042 Consolider-Ingenio 2010 (D. F., D. M.).

[1] J. Adams *et al.* (STAR Collaboration), Nucl. Phys. **A757**, 102 (2005); K. Adcox *et al.* (PHENIX Collaboration), Nucl. Phys. **A757**, 184 (2005).

[2] E. Shuryak, Prog. Part. Nucl. Phys. **53**, 273 (2004); Nucl. Phys. **A750**, 64 (2005).

[3] M. Gyulassy *et al.*, arXiv:nucl-th/0302077; A. Kovner and U. A. Wiedemann, arXiv:hep-ph/0304151; J. Casalderrey-Solana and C. A. Salgado, Acta Phys. Pol. B **38**, 3731 (2007).

[4] C. P. Herzog *et al.*, J. High Energy Phys. 07 (2006) 013; H. Liu, K. Rajagopal, and U. A. Wiedemann, Phys. Rev. Lett. **97**, 182301 (2006); S. S. Gubser, Phys. Rev. D **74**, 126005 (2006); J. Casalderrey-Solana and D. Teaney, Phys. Rev. D **74**, 085012 (2006); M. Chernicoff and A. Guijosa, J. High Energy Phys. 06 (2008) 005.

[5] E. Witten, Adv. Theor. Math. Phys. **2**, 505 (1998).

[6] A. Karch and L. Randall, J. High Energy Phys. 06 (2001) 063; A. Karch and E. Katz, J. High Energy Phys. 06 (2002) 043.

[7] D. Mateos, R. C. Myers, and R. M. Thomson, Phys. Rev. Lett. **97**, 091601 (2006).

[8] J. Babington *et al.*, Phys. Rev. D **69**, 066007 (2004); I. Kirsch, Fortschr. Phys. **52**, 727 (2004); M. Kruczenski *et al.*, J. High Energy Phys. 05 (2004) 041.

[9] O. Aharony *et al.*, Ann. Phys. (N.Y.) **322**, 1420 (2007); A. Parnachev and D. A. Sahakyan, Phys. Rev. Lett. **97**, 111601 (2006).

[10] See, e.g., A. Bazavov *et al.*, arXiv:0904.1748, and references therein.

[11] As first noted in [12] and subsequently elaborated upon in [13]. For a discussion directly on the gauge theory side see, e.g., [14] and references therein.

[12] D. Mateos *et al.*, J. High Energy Phys. 05 (2007) 067.

[13] Q. J. Ejaz *et al.*, J. High Energy Phys. 04 (2008) 089.

[14] J. Casalderrey-Solana and D. Mateos, Phys. Rev. Lett. **102**, 192302 (2009).

[15] J. L. Hovdebo *et al.*, Int. J. Mod. Phys. A **20**, 3428 (2005).

[16] J. Casalderrey-Solana, D. Fernández, and D. Mateos (to be published).

[17] P. M. Chesler *et al.*, Phys. Rev. D **79**, 125015 (2009).

[18] T. Faulkner and H. Liu, Phys. Lett. B **673**, 161 (2009).

[19] Some implications have been discussed in [14,20].

[20] E. Iancu and A. H. Mueller, J. High Energy Phys. 02 (2010) 023.

[21] If light quarks can also radiate, the light hadron R_{AA} would also show this behavior.

[22] J. Casalderrey-Solana *et al.*, J. Phys. Conf. Ser. **27**, 22 (2005); Nucl. Phys. **A774**, 577 (2006).

[23] V. Koch, A. Majumder, and X. N. Wang, Phys. Rev. Lett. **96**, 172302 (2006); I. M. Dremin, Nucl. Phys. **A767**, 233 (2006).

[24] J. J. Friess *et al.*, Phys. Rev. D **75**, 106003 (2007); P. M. Chesler and L. G. Yaffe, Phys. Rev. D **78**, 045013 (2008).

[25] K. Peeters, M. Zamaklar, and J. Sonnenschein, Phys. Rev. D **74**, 106008 (2006); H. Liu, K. Rajagopal, and U. A. Wiedemann, Phys. Rev. Lett. **98**, 182301 (2007); M. Chernicoff *et al.*, J. High Energy Phys. 09 (2006) 068.

[26] K. Dusling *et al.*, J. High Energy Phys. 10 (2008) 098.

[27] Attached at points higher than the bottom of the branes.

Published for SISSA by Springer

Received: October 11, 2010
Accepted: October 27, 2010
Published: November 19, 2010

Cherenkov mesons as in-medium quark energy loss

Jorge Casalderrey-Solana,[a] **Daniel Fernández**[b] **and David Mateos**[b,c]

[a] *Physics Department, Theory Unit, CERN,*
CH-1211 Genève 23, Switzerland
[b] *Departament de Física Fonamental & Institut de Ciències del Cosmos (ICC),*
Universitat de Barcelona,
Martí i Franquès 1, E-08028 Barcelona, Spain
[c] *Institució Catalana de Recerca i Estudis Avançats (ICREA),*
Passeig Lluís Companys 23, E-08010, Barcelona, Spain

E-mail: jorge.casalderrey@cern.ch, daniel@correu.ffn.ub.es, dmateos@icrea.cat

Abstract: We recently showed that a heavy quark moving sufficiently fast through a quark-gluon plasma may lose energy by Cherenkov-radiating mesons [1]. Here we review our previous holographic calculation of the energy loss in $\mathcal{N} = 4$ Super Yang-Mills and extend it to longitudinal vector mesons and scalar mesons. We also discuss phenomenological implications for heavy-ion collision experiments. Although the Cherenkov energy loss is an $\mathcal{O}(1/N_c)$ effect, a ballpark estimate yields a value of dE/dx for $N_c = 3$ which is comparable to that of other mechanisms.

Keywords: Holography and quark-gluon plasmas, Gauge-gravity correspondence, 1/N Expansion

doi:10.1007/JHEP11(2010)091

Contents

1 Introduction

With the advent of the Large Hadron Collider (LHC) the field of heavy-ion collisions (HIC) enters a new era. The center-of-mass energy per nucleon in LHC collisions, $\sqrt{s_{\rm NN}} \simeq 5.5\,\text{TeV}$, is almost 30 times larger than that of the most energetic collisions at the Relativistic Heavy Ion Collider (RHIC). The highest temperature of the quark-gluon plasma (QGP) created in RHIC experiments is approximately $T_{\rm RHIC} \simeq 2T_{\rm c}$, with $T_{\rm c} \simeq 175\,\text{MeV}$ the deconfinement temperature of Quantum Chromodynamics (QCD). Despite the large increase in the collision energy, this is expected to lead only to a moderate increase in the plasma temperature at the LHC [2], i.e. $T_{\text{LHC}} \simeq (3-4)T_{\text{c}}$.[1] In contrast, high-energy partons originating from hard initial collisions will be copiously produced at the LHC. This will allow the study of quarks and gluons in the 100 GeV range, an order of magnitude larger than that at the RHIC.

Experimentally, extremely valuable information is obtained by analyzing the energy loss of these energetic partons as they travel through the QGP. In order to use this information to learn about the plasma, a theoretical, quantitative understanding of the different mechanisms of parton energy loss is needed. Several such mechanisms have been previously studied, both in QCD itself [3–5] and in the context of the gauge/gravity duality [6–10].

A remarkable conclusion from the RHIC experiments [11, 12] is that the QGP does not behave as a weakly coupled gas of quarks and gluons, but rather as a strongly coupled fluid [13, 14]. Because of the moderate increase in the temperature and the logarithmic running of the QCD coupling constant, a qualitatively rather similar behaviour may be expected for the QGP at the LHC. This makes it particularly important to understand mechanisms of parton energy loss that may operate at strong coupling. We recently uncovered one such mechanism [1] whereby a sufficiently fast heavy quark traversing a strongly coupled plasma loses energy by Cherenkov-radiating in-medium mesons.

The analysis in [1] showed that this mechanism takes place in all strongly coupled, large-N_{c} gauge theory plasmas with a gravity dual. The argument is so simple that we reproduce it in section 2 for completeness. This section emphasizes the universality of the mechanism, since no reference to a specific model is necessary.

Ref. [1] also performed a quantitative analysis in the simple example of a quark moving through the $\mathcal{N}=4$ super Yang-Mills (SYM) plasma. The quark Cherenkov-radiates both vector and scalar mesons. The rate of energy loss into the transverse modes of the vector mesons was calculated in [1], and again we reproduce it here for completeness. The vector mesons in question are massive, and thus they also possess a longitudinal mode. Here we extend the calculation of [1] and obtain the rate of energy loss into longitudinal vector mesons and scalar mesons. The result for the former is qualitatively similar to that for the transverse modes, whereas the result for scalar mesons displays some qualitative differences.

Ref. [1] presented a rather preliminary exploration of the potential implications of these results for HIC experiments. Here we elaborate on that discussion and extend it to include possible implications of the new results presented in this paper.

2 A universal mechanism of quark energy loss

The reason that the mechanism we are going to describe is universal is that it only relies on two universal features of the gauge/gravity duality:[2] (i) the fact that the deconfined phase of the gauge theory is described by a black hole geometry on the gravity side [15], and (ii) the fact that a finite number N_{f} of quark flavours is described by N_{f} D-brane probes [16, 17] — see figure 1.

---

[1] A rough estimate is obtained by assuming that the temperature scales as the fourth root of the energy density.

[2] In the limit $N_{\text{c}}, g^2_{\text{YM}}N_{\text{c}} \to \infty$.

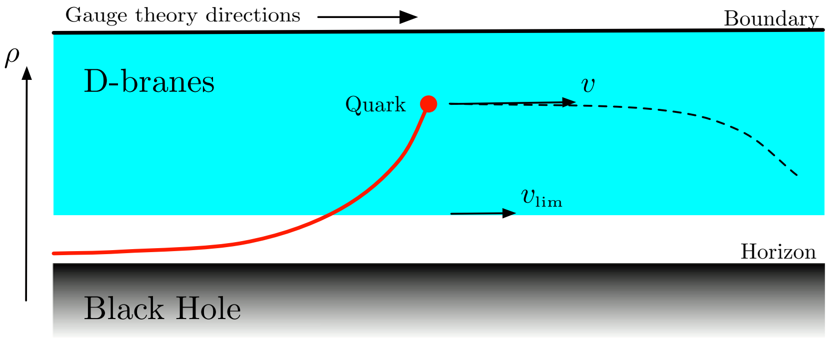

Figure 1. D-branes and an open string in a black hole geometry.

In addition to the gauge theory directions, the gravity description always includes a radial direction (denoted by ρ in figure 1) which is dual to the gauge theory energy scale. The radial position of the horizon is proportional to the plasma temperature T. The D-branes extend in the radial direction down to a minimum value proportional to the quark mass M_{q}.

As it is intuitively clear, for M_{q} sufficiently larger than T the D-branes sit completely outside the horizon [18–20, 22, 23].[3] In this phase, scalar and vector gauge theory mesons are described by small, normalizable fluctuations of scalar and vector fields propagating on the branes, whose low-energy dynamics is governed by a Maxwell-like theory. The spectrum of these fluctuations is discrete and gapped, which means that stable heavy meson states exist in the plasma. In other words, sufficiently heavy mesons survive deconfinement, in agreement with lattice and potential model predictions for QCD [25].

Consider now the in-medium dispersion relation $\omega(q)$ for these heavy mesons, where ω and q are the energy and the spatial three-momentum of the meson, respectively. As an illustrative example, the dispersion relations for vector and scalar mesons in the $\mathcal{N}=4$ SYM plasma[4] are depicted in figure 2.

As $q\to\infty$, the DR becomes linear: $\omega(q)\sim v_{\mathrm{lim}}q$, with $v_{\mathrm{lim}}<1$. This subluminal limiting velocity, which is the same for all mesons, can be easily understood in the gravitational description [19]. Since highly energetic mesons are strongly attracted by the gravitational pull of the black hole, their wave-function is very concentrated at the bottom of the branes. Consequently, their velocity is limited by the local speed of light at that point, v_{lim} (see figure 1). Because of the black hole redshift, v_{lim} is lower than the speed of light at infinity (i.e. at the boundary), which is normalised to unity. In the gauge theory this translates into the statement that v_{lim} is lower than the speed of light in the absence of a medium, namely in the vacuum. The reason is that the absence of a medium in the gauge theory corresponds to the absence of a black hole on the gravity side, in which case $v_{\mathrm{lim}}=1$ everywhere.

Imagine now a heavy quark in the plasma. In the gravitational picture, this is described by a string that starts on the D-branes and falls through the horizon — see figure 1. In

---

[3] In contrast, as the ratio M_{q}/T decreases, a first-order phase transition eventually occurs and a part of the branes falls through the horizon. See section 3.

[4] With quarks introduced as D7-branes; see below for details.

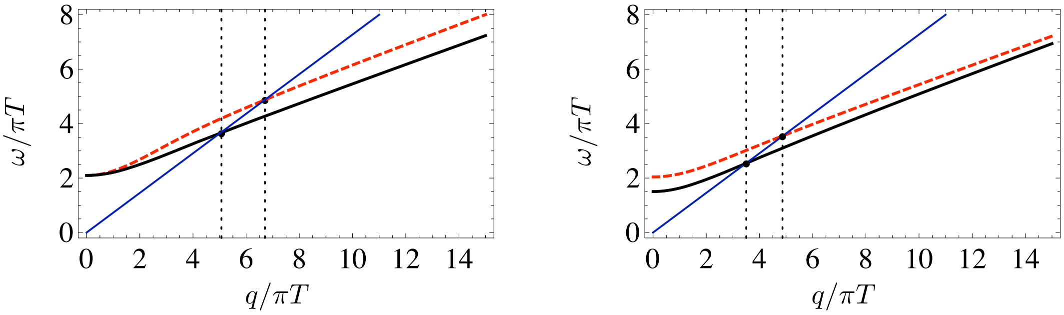

Figure 2. Left: dispersion relation for the transverse (black, continuous curve) and longitudinal (red, dashed curve) $n = 0$ modes of a heavy vector meson with $v_{\text{lim}} = 0.35$ in the $\mathcal{N} = 4$ SYM plasma. Right: analogous curves for a scalar (black, continuous curve) and pseudoscalar (red, dashed curve) meson. In both plots the blue, continuous straight lines correspond to $\omega = vq$ with $v_{\text{lim}} < v < 1$. The black, dotted, vertical lines mark the crossing points between the meson dispersion relations and the blue lines.

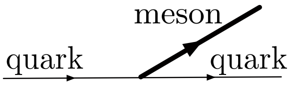

Figure 3. Effective quark-meson coupling.

order to model a highly energetic quark we consider a string whose endpoint moves with an arbitrary velocity v at an arbitrary radial position ρ_0. Roughly speaking, the interpretation of ρ_0 in the gauge theory is that of the inverse size of the gluon cloud that dresses the quark. This can be seen, for example, by holographically computing the profile of $\langle \text{Tr} F^2(x) \rangle$ around a static quark source dual to a string whose endpoint sits at $\rho = \rho_0$ [26].

Two simple observations now lead to the effect that we are interested in. The first one is that the string endpoint is charged under the scalar and vector fields on the branes. In the gauge theory, this corresponds to an effective quark-meson coupling (see figure 3) of order $e \sim 1/\sqrt{N_\text{c}}$. We will derive these facts rigorously below, but physically they can be understood very simply. The fields on the branes describe fluctuations around the branes equilibrium configuration. The string endpoint pulls on the branes and therefore excites (i.e. it is charged under) these fields. The branes tension is of order $1/g_s \sim N_\text{c}$, where g_s is the string coupling constant, whereas the string tension is N_c-independent. This means that the deformation of the branes caused by the string is of order $e^2 \sim 1/N_\text{c}$. We thus conclude that the dynamics of the 'branes+string endpoint' system is (a generalization of) that of classical electrodynamics in a medium in the presence of a fast-moving charge.

The second observation is that the velocity of the quark may exceed the limiting velocity of the mesons, since the redshift at the position of the string endpoint is smaller than at the bottom of the branes. As in ordinary electrodynamics, if this happens then the string endpoint loses energy by Cherenkov-radiating into the fields on the branes.[5] In the

---

[5] This can be viewed as a particular limit of string breaking — see section 7.

gauge theory, this translates into the quark losing energy by Cherenkov-radiating scalar and vector mesons. The rate of energy loss is set by the square of the coupling, and is therefore of order $1/N_{\rm c}$.

3 Quarks in the $\mathcal{N}=4$ SYM plasma

The four-dimensional $\mathcal{N}=4$ SYM theory with gauge group $SU(N_{\rm c})$ at non-zero temperature is dual to type IIB string theory on the gravitational background sourced by $N_{\rm c}$ black D3-branes. $N_{\rm f}$ quark flavours may be introduced in the gauge theory by adding D7-branes on the gravity side. The relative orientation of the 'colour' and 'flavour' branes is summarised by the array

$$\begin{array}{rcccccccccc} & 0 & 1 & 2 & 3 & 4 & 5 & 6 & 7 & 8 & 9 \\ N_{\rm c}\ \text{D3:} & \times & \times & \times & \times & & & & & & \\ N_{\rm f}\ \text{D7:} & \times & \times & \times & \times & \times & \times & \times & \times & & \end{array} \tag{3.1}$$

In the limit $N_{\rm f} \ll N_{\rm c}$ the backreaction of the D7-branes on the spacetime metric may be ignored and the D7-branes may be treated as probes in the gravitational background sourced by the D3-branes. Following [1, 19] we write the spacetime metric as $ds^2 = L^2 ds^2(G)$, where

$$ds^2(G) = \frac{\rho^2}{2}\left[-\frac{f^2}{\tilde{f}}dt^2 + \tilde{f}dx_i^2\right] + \frac{1}{\rho^2}\left[dr^2 + r^2 d\Omega_3^2 + dR^2 + R^2 d\vartheta^2\right] , \tag{3.2}$$

and

$$L^4 = 4\pi g_s N_{\rm c} \ell_s^4 , \qquad \rho^2 = R^2 + r^2 , \qquad f = 1 - 1/\rho^4 , \qquad \tilde{f} = 1 + 1/\rho^4 . \tag{3.3}$$

The four gauge theory directions are $x^\mu = \{t, \vec{x}\} = \{t, x^i\}$, and they are identified with the 0123-directions shared by both sets of branes in (3.1). The metric inside the second set of brackets in (3.2) is just the flat metric on $\mathbb{R}^6 = \mathbb{R}^4 \times \mathbb{R}^2$, which corresponds to the 456789-directions in (3.1), written in terms of two sets of spherical coordinates $\{r, \Omega_3\}$ and $\{R, \vartheta\}$. The coordinate ρ is the overall radial coordinate in $\mathbb{R}^6$. This splitting is convenient since the D7-branes extend along the $\{r, \Omega_3\}$-directions. All coordinates above are dimensionless, and they are related to their dimensionful counterparts (denoted with tildes) through

$$x^\mu = \pi T \, \tilde{x}^\mu , \qquad \{r, R, \rho\} = \frac{1}{\pi L^2 T}\{\tilde{r}, \tilde{R}, \tilde{\rho}\} . \tag{3.4}$$

In particular, this means that we are measuring energy and momentum in the gauge theory in units of πT. In addition, since the horizon of the metric (3.2) in dimensionless coordinates lies at $\rho_{\rm hor} = 1$, we see that the size of the horizon in physical units is proportional to the gauge theory temperature, i.e. $\tilde{\rho}_{\rm hor} \propto T$.

D7-brane embeddings. We now specialize to $N_{\rm f} = 1$; we will discuss the case $N_{\rm f} > 1$ in section 7. The action governing the dynamics of a D7-brane in the background sourced by D3-branes takes the form

$$S_{\rm D7} = -T_{\rm D7} \int d^8x \sqrt{-\det\left(g + 2\pi\ell_s^2 F\right)} + T_{\rm D7}\frac{\left(2\pi\ell_s^2\right)^2}{2}\int C_4 \wedge F \wedge F . \tag{3.5}$$

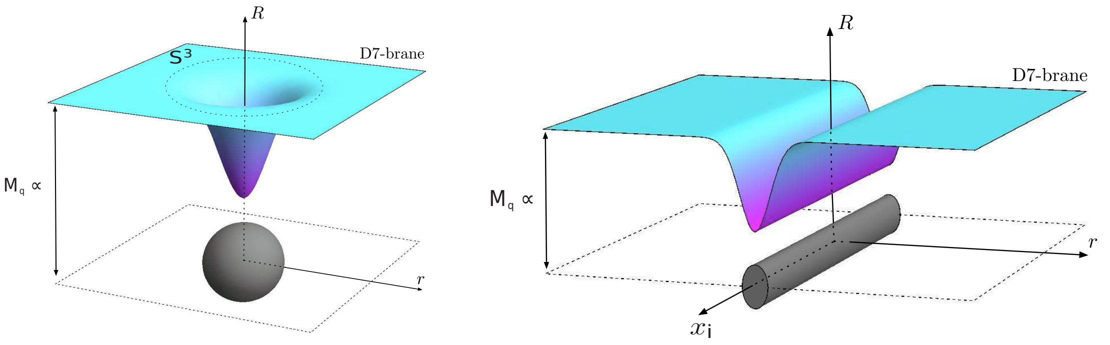

Figure 4. Minkowski-type D7-brane embedding showing the S^3 wrapped by the branes (left) and the gauge theory directions (right). The angular coordinate ϑ is suppressed in both cases. The asymptotic position of the brane is proportional to the quark mass $M_{\rm q}$, whereas the size of the black hole horizon (shown in dark grey) is proportional to the temperature T.

In this equation $T_{\rm D7} = 1/g_s(2\pi)^7\ell_s^8$ is the D7-brane tension, ℓ_s is the string length, x^a ($a = 0, \ldots, 7$) are intrinsic coordinates on the brane's worldvolume, g is the induced metric, $F = dA$ is the field-strength of the worldvolume U(1) gauge field A_a, and C_4 stands for the pull-back of the spacetime Ramond-Ramond four-form potential sourced by the D3-branes. As we will see below, the term in the action involving C_4 will not contribute to any of our calculations.

In order to describe the D7-brane embedding we use $x^a = \{x^\mu, r, \Omega_3\}$ as worldvolume coordinates. In other words, the brane extends along the gauge theory directions and the radial direction r, and it wraps an S^3 in the directions transverse to the D3-branes. Translational symmetry along x^μ and rotational symmetry along Ω_3 then imply that the embedding must be specified as $R = R(r)$ and $\vartheta = \vartheta(r)$. Since ϑ is also a symmetry direction, a consistent solution is obtained by choosing $\vartheta = \text{const}$. A typical D7-brane embedding with different sets of coordinates suppressed is shown in figure 4.

Under these circumstances the induced metric on the D7-brane takes the form $ds^2 = L^2 ds^2(g)$ with

$$ds^2(g) = \frac{\rho^2}{2}\left[-\frac{f^2}{\tilde f}dt^2 + \tilde f d\vec{x}^2\right] + \frac{(1+\dot R^2)}{\rho^2}dr^2 + \frac{r^2}{\rho^2}d\Omega_3^2\,, \tag{3.6}$$

where $\dot R = dR/dr$. The function $R(r)$ is determined by inserting (3.6) in (3.5), setting $F = 0$, and varying with respect to $R(r)$. The resulting Euler-Lagrange equation of motion is

$$\partial_r\left[r^3\left(1 - \frac{1}{(r^2+R^2)^4}\right)\frac{\dot R}{\sqrt{1+\dot R^2}}\right] = 8\frac{r^3 R}{(r^2+R^2)^5}\sqrt{1+\dot R^2}\,. \tag{3.7}$$

In the limit $r \to \infty$, this equation leads to the asymptotic behaviour

$$R(r) \simeq m + \frac{c}{r^2} + \cdots\,. \tag{3.8}$$

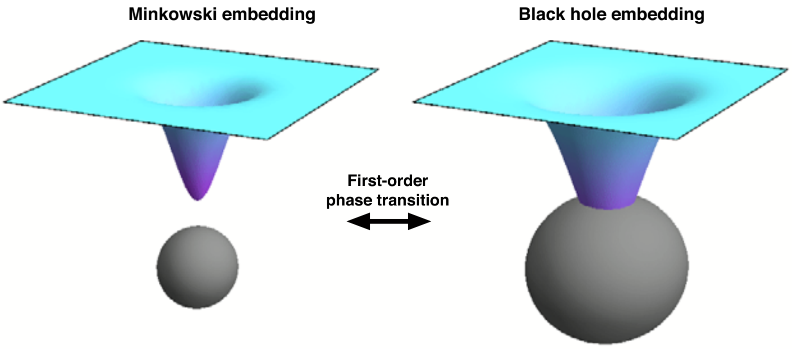

Figure 5. First-order phase transition between Minkowski and black-hole type embeddings.

Holography relates the dimensionless constants m and c to the quark mass and condensate as (see [19] for details)

$$M_\mathrm{q} = \frac{1}{2}\sqrt{\lambda}\, T\, m\,, \qquad \langle\bar{\psi}\psi\rangle = -\frac{1}{8}\sqrt{\lambda}\, N_\mathrm{f}\, N_\mathrm{c}\, T^3\, c\,, \tag{3.9}$$

where $\lambda = g_\mathrm{YM}^2 N_\mathrm{c} = 2\pi g_s N_\mathrm{c}$ is the 't Hooft coupling. An important point is that the constant m can also be written in terms of the mass M_mes of the lightest meson in the theory at zero temperature as [19]:

$$m = \frac{2M_\mathrm{q}}{\sqrt{\lambda}\, T} = \frac{M_\mathrm{mes}}{2\pi T}\,. \tag{3.10}$$

eq. (3.7) cannot be solved analytically, but numerical solutions for any value of the asymptotic brane position, $m = R(r \to \infty)$, can be easily found. The constants m and c correspond to the two solutions at infinity of the second-order equation of motion (3.7). These solutions are mathematically independent, but not physically: once m is specified, the requirement of regularity in the interior determines c. The physical solution is thus uniquely characterized by the value of m.[6] In the gauge theory this translates into the statement that once the quark mass (and the temperature) are specified, the dynamics determines the quark condensate.

Solutions of eq. (3.7) fall into two classes. For $m > 1.3$, i.e. for quark masses sufficiently larger than the temperature, the brane bends towards the horizon because of its gravitational pull, but the brane tension is able to compensate for this and the brane sits entirely outside the horizon, as in figure 4 and on the left-hand side of figure 5. In this case the brane embedding is of the so-called 'Minkowski' type [18, 19], and we will denote by $R_0 = R(r = 0)$ the radial position of the bottom of the branes. For Minkowski embeddings there is a one-to-one correspondence between m and R_0, and the lowest value $m = 1.3$ corresponds to $R_0 = 1.2$.

In contrast, for $m < 1.3$, the brane falls through the black hole horizon in a so-called 'black-hole embedding', since in this case the induced metric on the branes possesses a

---

[6] For thermodynamically stable embeddings. In the case of thermodynamically metastable or unstable embeddings, c may be multivalued [18, 19].

horizon — see figure 5. At $m = 1.3$ a first-order phase transition between the two phases occurs, as indicated in figure 5. As we will see below, in the Minkowski phase stable mesons exist, and their spectrum is discrete and gapped. In contrast, no stable mesons (in fact, no quasi-particles) exist in the black hole phase. For this reason, the phase transition above is interpreted in the gauge theory as a dissociation or 'melting' phase transition for mesons in the $\mathcal{N} = 4$ plasma [18, 19, 27].

The value $m = 1.3$ thus corresponds to the (stable) Minkowski-type brane that comes closest to the horizon, and therefore to the one for which the in-medium meson dispersion relation is most dramatically modified with respect to that in the vacuum. For this reason, we have chosen the embedding with $m = 1.3$ to illustrate some results in the sections below. Specifically, we see from eq. (3.6) that the local speed of light at the bottom of the brane is

$$v_{\mathrm{lim}} = \sqrt{-\frac{g_{00}}{g_{11}}}\Bigg|_{r=0} = \frac{f(R_0)}{\tilde{f}(R_0)}\,, \tag{3.11}$$

where we recall that $R_0 = R(r = 0)$. Since $m = 1.3$ corresponds to $R_0 = 1.2$, the formula above gives $v_{\mathrm{lim}} \simeq 0.35$, i.e. in this case the limiting velocity of mesons in the plasma is about 1/3 of that in the vacuum.

4 Meson dispersion relations in the $\mathcal{N} = 4$ SYM plasma

Despite the fact that the $\mathcal{N} = 4$ SYM theory is in a deconfined phase at any $T > 0$, stable quark-antiquark states exist for sufficiently large M_{q}/T, and the spectrum of these mesons is discrete and gapped. In particular, scalar and vector mesons in the gauge theory are dual to regular, normalizable modes of the scalar and vector fields on the D7-brane. Here we will review the dispersion relations for these modes, which we will need in order to compute the quark energy loss below. The dispersion relation for (some) vector mesons in the D3/D7 system appeared in [1], but no details were presented there. The dispersion relation for scalar mesons was first computed in [19] and then revisited in [28]. Here we will review the result in the geometric parametrization of [28], which is particularly suited for calculating the energy radiated into these modes by the quark.

4.1 Vector mesons

These are dual to regular, normalizable fluctuations of the worldvolume gauge field A. The $\mathcal{N} = 4$ SYM theory possesses an internal, global SO(6) symmetry that is broken down to SO(4) by the addition of quarks. In the string description, SO(6) is the isometry group of the spacetime metric (3.2), whereas SO(4) is the isometry group of the S^3 wrapped by the D7-branes. Under the preserved SO(4) symmetry, meson modes decompose into singlet and non-singlet modes. Since we are interested in using the $\mathcal{N} = 4$ SYM plasma as a toy model for the QCD plasma, and since QCD possesses no analog of the SO(4) symmetry, we will focus on singlet modes. The equation of motion for these modes receives no contribution from the second term in the action (3.5) [29], and therefore we will ignore this term in the following.

In conclusion, since we are interested in singlet modes, we only need to consider the first term in the action (3.5). In addition, since we are only interested in their dispersion relation (as opposed to higher-order couplings), it suffices to expand this term to quadratic order in F in the fixed worldvolume metric (3.6).[7] The result is

$$S_{\text{vector}} = -T_{\text{D7}} L^4 \left(2\pi l_s^2\right)^2 \int d^8x \sqrt{-g}\, \frac{1}{4} F^{ab} F_{ab}\,, \tag{4.1}$$

leading to the equation of motion

$$\sqrt{-g}\, \nabla_a F^{ab} = \partial_a (\sqrt{-g}\, F^{ab}) = 0\,. \tag{4.2}$$

The metric g that enters these expressions is that in eq. (3.6), which contains no factors of L; these have been explicitly included in the prefactor of (4.1).

Singlet modes take the form

$$A_\mu = A_\mu(x^\mu, r)\,, \qquad A_r = A_r(x^\mu, r)\,, \qquad A_{\Omega_3} = 0\,, \tag{4.3}$$

i.e. they have no components along the S^3 and depend only on r and the gauge theory directions. The equations of motion are further simplified by the gauge choice $A_r = 0$, which we will employ henceforth. In addition, we will work with the Fourier components of the gauge field defined through

$$A_\mu(t, x, r) = \int \frac{d\omega d^3q}{(2\pi)^4}\, A_\mu(\omega, q, r)\, e^{-i\omega t + iq\cdot x}\,, \tag{4.4}$$

where ω and q are the energy and the three-momentum of the meson, respectively. Finally, we choose the momentum to point along x^1 without loss of generality.

Under the conditions above, the equations of motion for the transverse modes A_2, A_3 decouple from each other and from those for the longitudinal mode A_0, A_1, so we will study them in turn.

Transverse modes. Let us collectively denote $\mathcal{A} = \{A_2, A_3\}$. Both modes obey identical equations of motion which take the form

$$\partial_r \left(\sqrt{g}\, g^{rr} g^{33}\, \partial_r \mathcal{A}\right) - \sqrt{g}\, g^{33} \left(g^{00}\omega^2 + g^{11} q^2\right) \mathcal{A} = 0\,. \tag{4.5}$$

Upon using (3.6) this becomes

$$\partial_r \left(\frac{f r^3}{2\sqrt{1+\dot{R}^2}}\, \partial_r \mathcal{A} \right) + \sqrt{1+\dot{R}^2}\, \frac{r^3}{\rho^4} \left(\frac{\omega^2 \tilde{f}}{f} - \frac{q^2 f}{\tilde{f}} \right) \mathcal{A} = 0\,. \tag{4.6}$$

Since we are interested in regular, normalizable solutions, we can expand $\mathcal{A}$ as

$$\mathcal{A}(\omega, q, r) = \sum_n \mathcal{A}_n(\omega, q)\, \xi_n(q, r) \tag{4.7}$$

---

[7] At higher orders gauge field fluctuations would mix with scalar fluctuations. Similarly, at higher orders singlet modes would generically mix with non-singlet modes.

in terms of a basis of regular, normalizable eigenfunctions $\{\xi_n(q,r)\}$ in the radial direction. These are solutions of eq. (4.6) with q-dependent eigenvalues $\omega = \omega_n(q)$, i.e. they obey the eigenstate equation

$$-\,\partial_r\left(\frac{f r^3}{2\sqrt{1+\dot{R}^2}}\,\partial_r\xi_n(q,r)\right)+\sqrt{1+\dot{R}^2}\,\frac{f r^3}{\tilde{f}\rho^4}\,q^2\,\xi_n(q,r)=\sqrt{1+\dot{R}^2}\,\frac{\tilde{f} r^3}{f\rho^4}\,\omega_n(q)^2\,\xi_n(q,r) \tag{4.8}$$

and satisfy the orthonormality relations

$$\int_0^\infty dr\,\frac{\tilde{f} r^3}{f\rho^4}\,\sqrt{1+\dot{R}^2}\,\xi_m(q,r)\xi_n(q,r)=\delta_{mn}\,. \tag{4.9}$$

As we will see in more detail below, the discreteness of the spectrum is guaranteed by the boundary conditions on the ξ_n: regularity at $r=0$ and normalizability at $r=\infty$. Inserting the expansion (4.7) in (4.6), and using the eigenstate equation (4.8) and the orthonormality relations (4.9), we find that each of the $\mathcal{A}_n(\omega,q)$ fields obeys an independent equation of the form

$$\left[\omega^2-\omega_n^2(q)\right]\mathcal{A}_n(\omega,q)=0\,. \tag{4.10}$$

Thus, through the expansion (4.7) we have 'Kaluza-Klein-reduced' the five-dimensional field $\mathcal{A}(\omega,q,r)$ to a discrete, infinite tower of independent four-dimensional fields $\{\mathcal{A}_n(\omega,q)\}$. Each of these fields is dual in the gauge theory to a transverse vector meson with dispersion relation $\omega=\omega_n(q)$, which is the physical meaning of the wave equation (4.10). In the gauge theory, each of the mesons in this infinite set is distinguished by its 'internal' quantum number n. In the string description, each value of n corresponds to a different, q-dependent radial 'wave-function' $\xi_n(q,r)$. As we will see below, this structure of mesons in the fifth dimension will play an important role in determining the strength with which each of them couples to a quark.

Given that the brane embedding $R(r)$ entering eq. (4.8) is only known numerically, the radial profiles must also be found numerically. The general solution of eq. (4.8) behaves as $\xi_n \sim a + b/r^2$ as $r\to 0$, and as $\xi_n \sim \tilde{a}+\tilde{b}/r^2$ as $r\to\infty$, for some constants $a,b,\tilde{a},\tilde{b}$. Regularity at $r=0$ requires $b=0$, whereas normalizability imposes the condition $\tilde{a}=0$. For fixed q, these two requirements are mutually compatible only for a discrete set of values of the energy, $\omega_n(q)$. This is the origin of the dispersion relation.

Figure 6 shows several numerically-obtained radial profiles of the first lowest-lying modes $\xi_n(q,r)$ for several values of q for a D7-brane embedding with $m=1.3$. The corresponding values of the energy, $\omega_n(q)$, are given by the dispersion relation curves in figures 2 and 7. As is familiar with solutions of Schrödinger-like equations, the nth solution possesses n zeros. More importantly, we see that the radial wave-functions for all these modes become concentrated around the bottom of the brane, $r\simeq 0$, as $q\to\infty$. Relatedly, we observe that the limiting velocity of all these modes agrees with the local speed of light at the bottom of the brane, eq. (3.11), as expected from the general argument in section 2.

Longitudinal modes. Eq. (4.2) with $b=0,1$ and r yields two second-order dynamical equations and a first-order constraint equation, respectively, in which the longitudinal

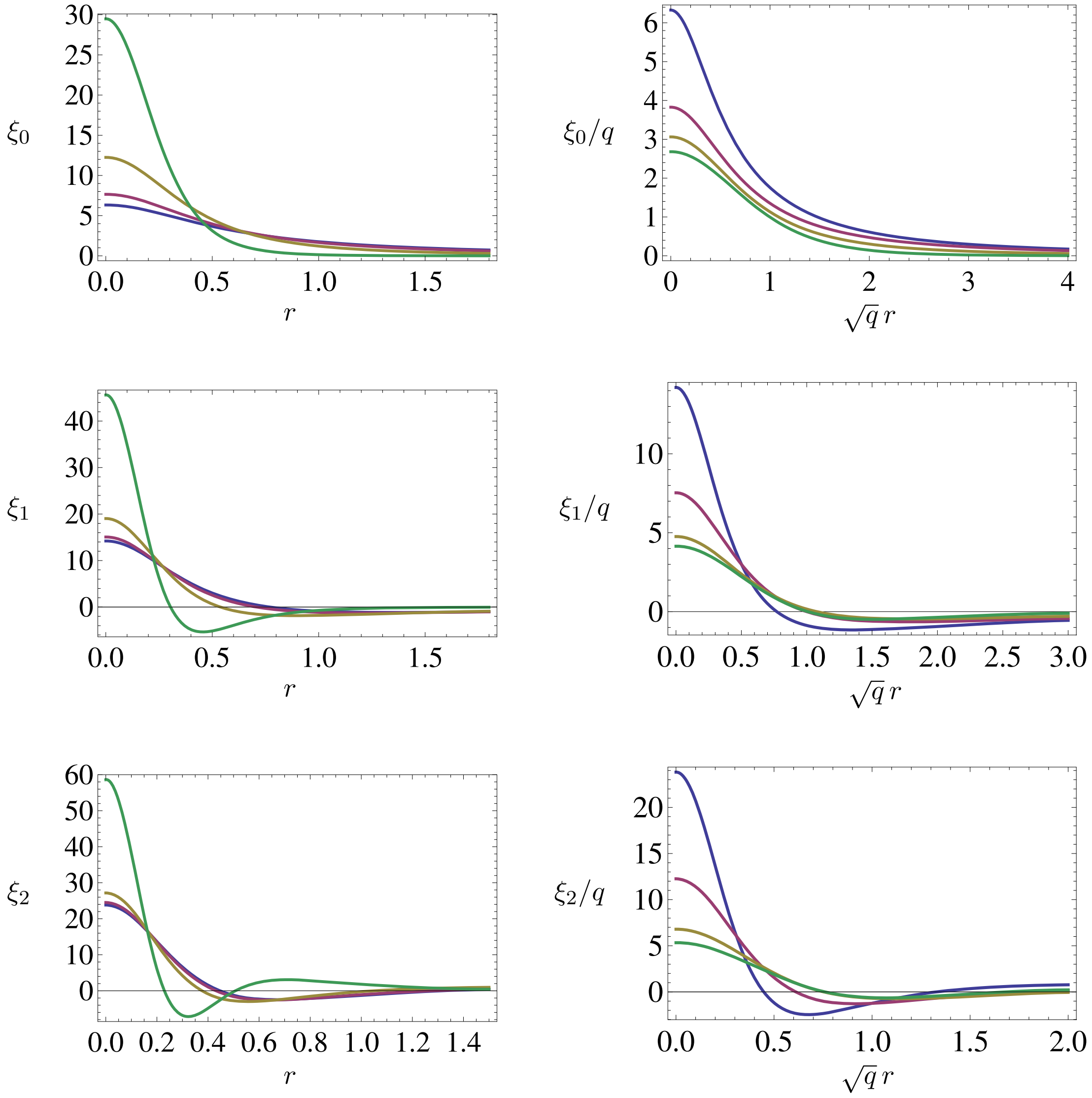

Figure 6. Normalized transverse vector meson radial profiles $\xi_n(q, r)$ for a D7-brane embedding with $m = 1.3$. The blue, violet, brown and green curves (i.e. bottom to top on the left, top to bottom on the right) correspond to $q = 1, 2, 4, 11$, respectively. The rescalings on the right-hand side correspond to those in appendix C. Note that the area under the curves is not unity because of the non-trivial measure in eq. (4.9).

components A_0 and A_1 are coupled to one another. Only two out of the three equations are independent, which we take to be

$$\partial_r \left(\sqrt{-g} g^{rr} g^{00} \partial_r A_0\right) + iq\sqrt{-g} g^{11} g^{00} E = 0 \,, \tag{4.11}$$

$$i\omega g^{00} \partial_r A_0 - iq g^{11} \partial_r A_1 = 0 \,, \tag{4.12}$$

where we have introduced the gauge-invariant electric field

$$E = F_{10} = iqA_0 + i\omega A_1 \,. \tag{4.13}$$

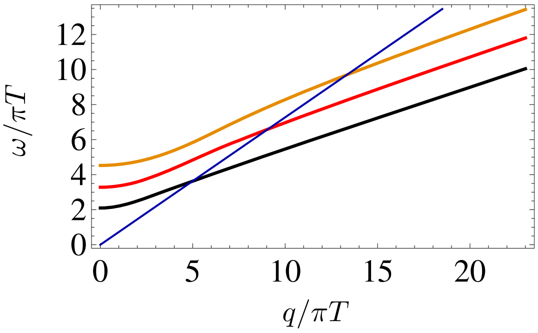

Figure 7. Dispersion relation for the first transverse modes ξ_n of a heavy vector meson with $v_{\rm lim} = 0.35$ in the $\mathcal{N} = 4$ SYM plasma. The curves correspond to $n = 0, 1, 2$ from bottom to top. The blue, continuous straight line corresponds to $\omega = vq$ with $v_{\rm lim} < v < 1$.

From these two equations, it is easy to see that E satisfies

$$-iq\,\partial_r\left(\frac{\sqrt{-g}\,g^{rr}g^{00}g^{11}}{q^2g^{11}+w^2g^{00}}\,\partial_r E\right)+iq\sqrt{-g}\,g^{11}g^{00}E=0\,. \tag{4.14}$$

In order to turn this into an eigenstate equation we introduce a new field Φ defined as

$$\Phi=\frac{\sqrt{-g}g^{rr}g^{00}g^{11}}{q^2g^{11}+w^2g^{00}}\,\partial_r E\,. \tag{4.15}$$

eq. (4.14) then implies the inverse relation

$$E=\frac{1}{\sqrt{-g}\,g^{11}g^{00}}\,\partial_r\Phi \tag{4.16}$$

which, when substituted back into (4.15), yields the equation of motion for Φ:

$$-\partial_r\left(\frac{1}{\sqrt{-g}\,g^{11}g^{00}}\,\partial_r\Phi\right)+\frac{q^2g^{11}+w^2g^{00}}{\sqrt{-g}\,g^{rr}g^{00}g^{11}}\,\Phi=0\,. \tag{4.17}$$

Inserting the explicit form of the metric functions, we arrive at

$$\partial_r\left(\frac{f\rho^4}{\tilde{f}r^3\sqrt{1+\dot{R}^2}}\,\partial_r\Phi\right)+2\frac{\sqrt{1+\dot{R}^2}}{fr^3}\left(w^2-\frac{f^2}{\tilde{f}^2}q^2\right)\Phi=0\,. \tag{4.18}$$

From this point onward, we proceed as in the case of transverse modes. We expand Φ as

$$\Phi(\omega,q,r)=\sum_n\Phi_n(\omega,q)\phi_n(q,r) \tag{4.19}$$

in terms of a basis of regular, normalizable eigenfunctions $\{\phi_n(q,r)\}$ in the radial direction. These are solutions of eq. (4.18) with q-dependent eigenvalues $\omega=\omega_n(q)$, and are subject to the orthonormality relations

$$\int_0^\infty dr\,2\frac{\sqrt{1+\dot{R}^2}}{fr^3}\phi_n(q,r)\phi_m(q,r)=\delta_{mn}\,. \tag{4.20}$$

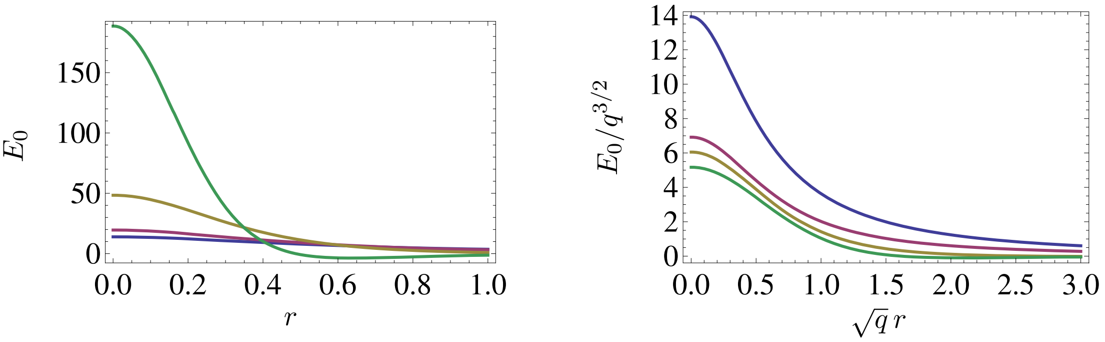

Figure 8. Electric field $E_0(q,r)$ of the normalized longitudinal vector meson radial profiles $\phi_0(q,r)$ for a D7-brane embedding with $m=1.3$. The blue, violet, brown and green curves (i.e. bottom to top on the left, top to bottom on the right) correspond to $q=1,2,4,11$, respectively. The rescalings on the right-hand side correspond to those in appendix C. Note that the area under the curves is not unity because of the non-trivial measure in eq. (4.20).

As in the case of transverse modes, the longitudinal modes $\Phi_n(\omega,q)$ obey the wave equation

$$\left[\omega^2-\omega_n^2(q)\right]\Phi_n(\omega,q)=0\,, \tag{4.21}$$

as appropriate for a four-dimensional field with dispersion relation $\omega=\omega_n(q)$. Again, through the expansion (4.19) we have Kaluza-Klein-reduced the five-dimensional field $\Phi(\omega,q,r)$ to a discrete, infinite tower of independent four-dimensional fields $\{\varphi_n(\omega,q)\}$, each of which is dual to a longitudinal vector meson in the gauge theory.

The general solution of eq. (4.18) behaves as $\phi_n\sim a+br^4$ as $r\to 0$, and as $\phi_n\sim\tilde{a}+\tilde{b}\log r$ as $r\to\infty$, for some constants $a,b,\tilde{a},\tilde{b}$. Normalizability with respect to (4.20) as $r\to 0$ requires that $a=0$, and regularity as $r\to\infty$ requires that $\tilde{b}=0$. As in the case of the transverse modes, for fixed q these two requirements are mutually compatible only for a discrete set of energies $\omega_n(q)$.

Figure 8 shows the electric field, eq. (4.16), of several numerically-obtained radial profiles of the lowest-lying mode $\phi_{n=0}(q,r)$ for several values of q. The corresponding values of the energy, $\omega_{n=0}(q)$, are given by the dispersion relation curve in figure 2. These results correspond again to a D7-brane embedding with asymptotic position $m=1.3$. We observe the same limiting velocity $v_{\text{lim}}=0.35$ given by the local speed of light at the bottom of the branes, eq. (3.11).

4.2 Scalar mesons

The scalar fields on the brane get excited by the string endpoint because the string tension pulls on the brane. A crucial feature is the fact that the boundary conditions at the string endpoint imply that the string must end orthogonally on the brane. (The unfamiliar reader can find a concise derivation in appendix A.) For this reason it is convenient to work with spacetime coordinates that locally parametrize the directions orthogonal to the brane. In the case of interest to us, the ϑ coordinate in (3.2) satisfies this requirement, since the vector field $\partial/\partial\vartheta$ is orthogonal to the fiducial D7-brane embedding at each point on the brane. However, the R coordinate does not meet this requirement, since $\partial/\partial R$ is in general not orthogonal to the brane due to the brane bending in the $r-R$ directions. We therefore follow [28] and work with two geometric coordinates X^A defined as follows. At each point on the brane, the two-dimensional space orthogonal to the brane is spanned by the unit vectors

$$V_1 \propto \frac{\partial}{\partial R} - \dot{R}(r)\frac{\partial}{\partial r}\,, \qquad V_2 \propto \frac{\partial}{\partial \vartheta}\,, \tag{4.22}$$

so a general vector orthogonal to the brane takes the form $U = X^A V_A$. For each vector U we shoot off a geodesic with unit affine parameter that at the brane has U as its tangent vector. The endpoint of this geodesic defines a point in a neighborhood of the brane. In this way we obtain a one-to-one correspondence (the so-called exponential map [30]) between the values of X^A and the points near the brane. In other words, X^A are the coordinates orthogonal to the brane that we were seeking, since on the brane we have $\partial/\partial X^A = V_A$ by construction. In particular, this implies that in these coordinates $G_{AB} = \delta_{AB}$ when evaluated precisely on the brane, where G is the spacetime metric (3.2). Note that in this section the ten dimensionless coordinates of spacetime are thus $\{x^a, X^A\}$, with $a = 0, \ldots, 7$ and $A = 1, 2$.

We chose the fiducial embedding of the brane to be given by $X^A = 0$, so that the X^A fields parametrize fluctuations around it. As shown in [28], to quadratic order in these fields the D7-brane action takes the simple form

$$S_{\text{scalar}} = -T_{\text{D7}} L^8 \int d^8x \sqrt{-g}\left[\frac{1}{2} g^{ab}\partial_a X^A \partial_b X^B G_{AB} + \frac{1}{2} m^2_{AB}(x) X^A X^B\right]\,, \tag{4.23}$$

where g is the induced metric (3.6) on the *fiducial* embedding of the brane, i.e. it is X^A-independent. As usual, this metric contains no factors of L, since this have been factored out explicitly in front of the action. The position-dependent mass matrix $m^2_{AB}(x)$ is diagonal and given in terms of geometric quantities as

$$\begin{aligned} m^2_{11} &= R_{11} + R_{2112} + 2R_{22} + {}^{(8)}R - R\,, \\ m^2_{22} &= -R_{22} + R_{2112}\,, \end{aligned} \tag{4.24}$$

where

$$R_{2112} = V_2^M V_1^N V_1^P V_2^Q R_{MNPQ}\,, \tag{4.25}$$

$$R_{11} = V_1^M V_1^N R_{MN}\,, \tag{4.26}$$

$$R_{22} = V_2^M V_2^N R_{MN}\,. \tag{4.27}$$

R_{MNPQ} and R_{MN} are, respectively, the Riemann and the Ricci tensors of the ten-dimensional spacetime metric G, R is the corresponding Ricci scalar, and ${}^{(8)}R$ is the Ricci scalar of the eight-dimensional induced metric on the brane g. Again none of these quantities contains any factors of L.

Using the fact that $G_{AB} = \delta_{AB}$ the action (4.23) leads to the equation of motion

$$\sqrt{-g}\,\nabla^2 X^A - \sqrt{-g}\,m^2 X^A = \partial_a\left(\sqrt{-g}\,\partial^a X^A\right) - \sqrt{-g}\,m^2 X^A = 0\,, \tag{4.28}$$

where $m = m_{11}$ or m_{22} as appropriate. Following the vector meson case, we focus on the zero-mode of X^A on the S^3, and work with its Fourier components $X^A(\omega, q, r)$, for which the equation of motion is

$$\partial_r \left(\sqrt{-g}\, g^{rr} \partial_r X^A \right) - \sqrt{-g} \left(g^{00}\omega^2 + g^{11} q^2 + m^2 \right) X^A = 0\,, \tag{4.29}$$

which upon substitution of the metric functions becomes

$$\partial_r \left(\frac{f \tilde{f} r^3 \rho^2}{\sqrt{1+\dot{R}^2}} \partial_r X^A \right) + f \tilde{f} r^3 \sqrt{1+\dot{R}^2} \left(\frac{2\tilde{f}}{\rho^2 f^2} \omega^2 - \frac{2}{\rho^2 \tilde{f}} q^2 - m^2 \right) X^A = 0\,. \tag{4.30}$$

As usual, we expand X^A as

$$X^A(\omega, q, r) = \sum_n X^A_n(\omega, k)\, \varphi^A_n(k, r) \tag{4.31}$$

in terms of a basis of normalizable eigenfunctions $\{\varphi^A_n(k, r)\}$ in the radial direction. These are solutions of eq. (4.30) with q-dependent eigenvalues $\omega = \omega^A_n(k)$, and are subject to the orthonormality relations

$$\int_0^\infty dr\, \frac{2\tilde{f}^2 r^3 \sqrt{1+\dot{R}^2}}{\rho^2 f}\, \varphi^A_m(q, r) \varphi^A_n(q, r) = \delta_{mn}\,. \tag{4.32}$$

Inserting the expansion (4.31) in (4.30), and using the orthonormality relations (4.32), we find that each of the $X^A_n(\omega, q)$ fields obeys

$$\left[\omega^2 - \omega^2_{nA}(q) \right] X^A_n(\omega, q) = 0\,, \tag{4.33}$$

as expected. As explained in [22], the modes $X^A_n(\omega, q)$ with $A = 1, 2$ correspond in the gauge theory to scalar and *pseudo*scalar mesons, respectively.

Both masses (for $A = 1, 2$) in eq. (4.30) behave as $m^2 \simeq -3 - m^2/r^2 + \cdots$ for $r \to \infty$ and $m^2 \simeq -c_1 + c_2 r^2 + \cdots$ for $r \to 0$, where $c_{1,2}$ are positive constants. It follows that the two independent solutions for X^A behave as $1/r$ and $1/r^3$ for $r \to \infty$ and as r^0 and $1/r^2$ for $r \to 0$. Thus in this case normalizability requires that $X^A \sim 1/r^3$ for $r \to \infty$ and regularity requires that $X^A \sim r^0$ for $r \to 0$. As in the case of vector modes, for fixed q these two requirements are compatible with each other only for a discrete set of energies $\omega^A_n(q)$.

Figure 9 shows several numerically-obtained radial profiles of the lowest-lying mode $\varphi_{n=0}(q, r)$ for several values of q. The corresponding values of the energy, $\omega_{n=0}(q)$, are given by the dispersion relation curves in figure 2. These results correspond again to a D7-brane embedding with asymptotic position $m = 1.3$. We observe the same limiting velocity $v_{\rm lim} = 0.35$ given by the local speed of light at the bottom of the brane, eq. (3.11).

5 Quark energy loss in the $\mathcal{N} = 4$ SYM plasma

We now turn to the main topic of this paper, namely the rate at which a heavy quark traversing the $\mathcal{N} = 4$ SYM plasma loses energy by Cherenkov-radiating mesons. As we

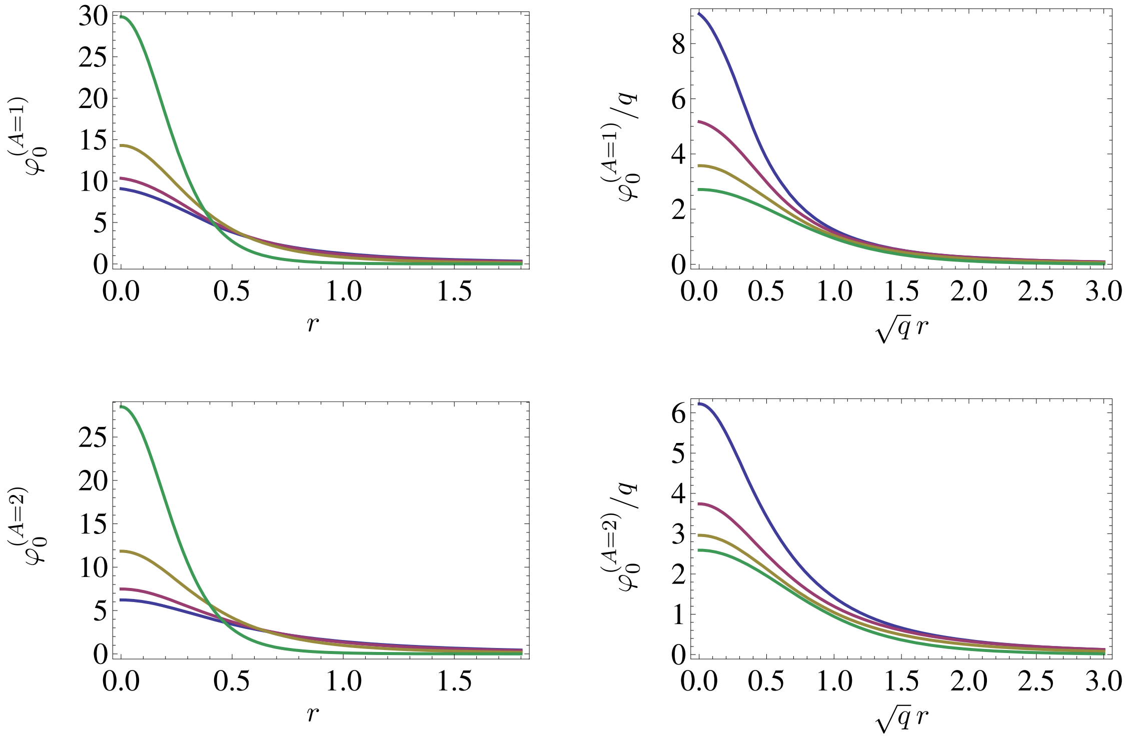

Figure 9. Normalized scalar (top plots) and pseudoscalar (bottom plots) meson radial profiles $\varphi_n(q, r)$ for a D7-brane embedding with $m = 1.3$. The blue, violet, brown and green curves (i.e. bottom to top on the left, top to bottom on the right) correspond to $q = 1, 2, 4, 11$, respectively. The rescalings on the right-hand side correspond to those in appendix C. Note that the area under the curves is not unity because of the non-trivial measure in eq. (4.32).

will see in detail below, the quark acts a source for the brane stress-energy tensor, defined as

$$T_{ab} = -\frac{2}{\sqrt{-g}}\frac{\delta S_{\rm D7}}{\delta g^{ab}} \,. \tag{5.1}$$

This leads to its non-conservation, $\nabla^a T_{ab} \neq 0$, where ∇ is the covariant derivative defined by the eight-dimensional worldvolume metric g. Under these circumstances the energy per unit time deposited on the brane by the quark is given by

$$\frac{dE}{dt} = -\int d^7x\,\sqrt{-g}\,\nabla^a T_{a0} \,, \tag{5.2}$$

where the integral is taken over the brane's worldspace. For the reader's convenience, a short derivation of this formula is provided in appendix B. Our task below will be to evaluate this formula for the cases of vector and scalar mesons.

5.1 Energy loss into vector mesons

The endpoint of an open string attached to the brane couples to the worldvolume gauge field, so the action (4.1) is modified in the presence of the quark to

$$S_{\rm vector} = -T_{\rm D7} L^4 \left(2\pi l_s^2\right)^2 \int d^8x \sqrt{-g}\,\frac{1}{4} F^{ab} F_{ab} - \int d\tau A_a \frac{dx^a}{d\tau} \,, \tag{5.3}$$

where, as usual, the worldvolume metric g contains no factors of L. The second term is the familiar coupling between an Abelian gauge field and a charged particle moving along a worldline parametrized as $x^a(\tau)$.[8] In order to work with a canonically normalized gauge field we rescale $A \to eA$ with

$$e^2 = \frac{1}{T_{\mathrm{D7}}\,(2\pi l_s^2)^2\,L^4} = \frac{8\pi^4}{N_{\mathrm{c}}}\,, \tag{5.4}$$

so that the action becomes

$$S_{\mathrm{vector}} = -\int d^8x\sqrt{-g}\,\frac{1}{4}F^{ab}F_{ab} - e\int d^8x\, A_a J^a\,, \tag{5.5}$$

where $J^a = \delta^{(7)}(x - x(\tau))\,\dot{x}^a$. As anticipated in section 2, the coupling e between the quark and the vector mesons is of order $1/\sqrt{N_{\mathrm{c}}}$, which justifies our neglect of terms of order higher than quadratic in the action.

Using the definition (5.1), the contribution from the gauge field to the brane's stress-energy tensor is easily calculated to be

$$T_{ab} = F_{ac}F_b{}^c - \frac{1}{4}g_{ab}F^2\,. \tag{5.6}$$

In the presence of the string endpoint, the equation of motion (4.2) for the gauge field is modified to

$$\sqrt{-g}\,\nabla_a F^{ab} = \partial_a(\sqrt{-g}\,F^{ab}) = eJ^b\,, \tag{5.7}$$

which implies the non-conservation of the stress-energy tensor

$$\sqrt{-g}\,\nabla^a T_{ab} = eF_{ba}J^a\,. \tag{5.8}$$

Inserting this into the general formula (5.2) yields the rate at which the quark deposits energy into the gauge field:

$$\frac{dE_{\mathrm{vector}}}{dt} = -e\int d^3x dr d\Omega_3\, F_{0a}J^a\,. \tag{5.9}$$

This formula has the simple interpretation of minus the work done on the quark by the gauge field. In order to evaluate it, we need to specify the quark trajectory. For simplicity, we will assume that the quark moves with constant velocity along a straight line at constant radial and angular positions, so we write

$$J^a = \delta^{(3)}(\vec{x} - \vec{v}t)\,\delta(r - r_0)\,\delta^{(3)}(\Omega - \Omega_0) \times (1, \vec{v}, 0, \vec{0})\,. \tag{5.10}$$

In reality, r_0 and v will of course decrease with time because of the black hole gravitational pull and the energy loss. However, we will concentrate on the initial part of the trajectory

---

[8] The relative normalization between the two terms in the action can be confirmed by noting that it ensures that supersymmetric BIon-like excitations on a D7-brane in flat space have tension $1/2\pi\ell_s^2$, as in [31, 32].

(which is long provided the initial quark energy is large) for which r_0 and v are approximately constant [33] — see figure 1. The delta-functions in (5.10) allow us to perform the integral in (5.9) and obtain

$$\frac{dE_{\text{vector}}}{dt} = -ev^i F_{0i}(t, \vec{v}t, r_0, \Omega_0)\,. \tag{5.11}$$

We thus see that we need to compute the electric field sourced by the string endpoint at the location of the string endpoint itself. To do so, we will solve the equation of motion (5.7) by expanding the gauge field in normalizable modes in the radial direction, as in section 4. Note that the fact that the quark is localized on the S^3 means that it will radiate both into S^3 singlets and non-singlets. A simple group theory argument shows that these two types of contributions can be calculated separately and independently at the quadratic level at which we are working. For the reasons explained in section 4, we will only calculate the energy loss into singlet modes, whose form in Fourier-space we recall to be:

$$A_\mu = A_\mu(\omega, q, r)\,, \qquad A_r = 0\,, \qquad A_{\Omega_3} = 0\,. \tag{5.12}$$

Without loss of generality, we choose $\vec{q} = (q, 0, 0)$ and $\vec{v} = (v\cos\theta, v\sin\theta, 0)$. After integrating over the S^3, the relevant Fourier-space components of the current are then

$$J^\mu = 2\pi\delta(\omega - qv\cos\theta)\,\delta(r - r_0) \times (1, v\cos\theta, v\sin\theta, 0)\,. \tag{5.13}$$

We are now ready to compute the energy loss into the transverse and longitudinal modes of the gauge field.

Transverse modes. With the choice above the only transverse mode of the gauge field excited by the source is $\mathcal{A} = A_2$, which couples to $\mathcal{J} = J^2$. The equation of motion (4.6) for this mode now becomes

$$\partial_r \left(\frac{f r^3\, \partial_r \mathcal{A}}{2\sqrt{1+\dot{R}^2}} \right) + \sqrt{1+\dot{R}^2}\,\frac{r^3}{\rho^4} \left(\frac{\omega^2 \tilde{f}}{f} - \frac{q^2 f}{\tilde{f}} \right) \mathcal{A} = \tilde{e}\mathcal{J}\,, \tag{5.14}$$

where $\tilde{e} = e/\Omega_3$ and the volume factor $\Omega_3 = 2\pi^2$ comes from integration over the S^3. We now follow section 4 and solve (5.14) by expanding $\mathcal{A}$ as in (4.7), where the radial eigenfunctions $\{\xi_n(q,r)\}$ satisfy exactly the same properties as in that section. In this case, inserting the expansion (4.7) in (5.14), and using the eigenstate equation and the orthonormality relations, we find that eq. (4.10) becomes

$$\left[\omega^2 - \omega_n^2(q)\right] \mathcal{A}_n(\omega, q) = \tilde{e}\mathcal{J}_n(\omega, q)\,, \tag{5.15}$$

where

$$\mathcal{J}_n(\omega, q) = \int dr\, \mathcal{J}(\omega, q)\xi_n(q, r) = 2\pi\delta\left(\omega - qv\cos\theta\right) v\sin\theta\, \xi_n(q, r_0)\,. \tag{5.16}$$

An important fact implied by eqs. (5.15)-(5.16) is that each of the four-dimensional meson modes $\mathcal{A}_n(\omega, q)$ couples to the quark with an effective strength proportional to the value of ξ_n at the location of the quark:

$$e_{\text{eff}}(q, r_0) = e\,\xi_n(q, r_0)\,. \tag{5.17}$$

The intuition behind this is that the radial profiles $\xi_n(q,r)$ roughly play the role of a 'wave function' in the fifth dimension for the corresponding meson mode $\mathcal{A}_n(\omega,q)$. This fact will play an important role below.

With retarded boundary conditions, as appropriate for the reaction to the quark's passage, the solution of eq. (5.15) is

$$\mathcal{A}_n(\omega,q) = \frac{\tilde{e}\mathcal{J}_n(\omega,q)}{(\omega+i\epsilon)^2-\omega_n^2(q)}\,. \tag{5.18}$$

In order to evaluate the energy loss (5.11), we first express $F_{02}(t,\vec{v}t,r_0,\Omega_0)$ as an integral over its Fourier components:[9]

$$\begin{aligned}\frac{dE_{\rm trans}}{dt} &= -ev^2\partial_t A_2(t,\vec{v}t,r_0,\Omega_0)\\ &= \int\frac{d\omega d^3q}{(2\pi)^4}(-ev\sin\theta)(-i\omega)\,\mathcal{A}(\omega,q,r_0)\;e^{-i\omega t}e^{iq\cdot x}\big|_{\vec{x}=\vec{v}t}\,.\end{aligned} \tag{5.19}$$

Inserting the expansion (4.7) we obtain

$$\frac{dE_{\rm trans}}{dt} = \sum_n\int\frac{d\omega d^3q}{(2\pi)^4}\,(ev\sin\theta)(i\omega)\,\mathcal{A}_n(\omega,q)\xi_n(q,r_0)\,e^{-i\omega t}e^{itq\cdot v}\,. \tag{5.20}$$

Substituting the solution (5.18) for $\mathcal{A}_n$ and using the delta-function in (5.16) to integrate over frequencies, we arrive at

$$\frac{dE_{\rm trans}}{dt} = \sum_n\int\frac{d^3q}{(2\pi)^3}\,(ev\sin\theta)(iqv\cos\theta)\,\frac{\tilde{e}v\sin\theta}{(qv\cos\theta+i\epsilon)^2-\omega_n^2(q)}\,\xi_n^2(q,r_0)\,. \tag{5.21}$$

Note that the two exponentials have cancelled out upon setting $\omega = qv\cos\theta$. In order to integrate over momenta we set $d^3q = 2\pi q^2\,dqdz$, where $z=\cos\theta$, so that the integral above becomes

$$\frac{dE_{\rm trans}}{dt} = \sum_n -\frac{e^2v}{\Omega_3}\int_0^\infty\frac{dq}{2\pi}\,q\,\xi_n^2(q,r_0)\int_{-1}^1\frac{dz}{2\pi i}\,\frac{z(1-z^2)}{(z+i\epsilon)^2-z_n^2(q)}\,, \tag{5.22}$$

where $z_n(q)=v_n(q)/v$, and $v_n(q)=\omega_n(q)/q$ is the phase velocity of the n-th mode. The integral over z can be performed in the complex plane by considering the contour shown in figure 10. The integral of interest corresponds to the integral over the segment Γ_1. In the limit $\epsilon\to 0$, this coincides with the integral over Γ_2, and the contribution from the vertical sides of the contour vanishes. Thus in this limit the integral over z in (5.22) equals 1/2 times the contour integral of figure 10. Now consider the poles of the integrand, which lie at $z=\pm z_n - i\epsilon$. If $v<v_n(q)$ then $z_n(q)>1$ and the poles lie outside the contour, so the integral vanishes. In contrast, if $v>v_n(q)$, then both poles lie inside the contour and they yield identical contributions equal to $(1-z_n^2)$. Taking into consideration the extra minus sign coming from the orientation of the contour, the final result is thus

$$\frac{dE_{\rm trans}}{dt} = \sum_n\frac{e^2v}{2\Omega_3}\int_0^\infty\frac{dq}{2\pi}\,q\,\xi_n^2(q,r_0)\left(1-\frac{v_n^2(q)}{v^2}\right)\Theta\left(1-\frac{v_n^2(q)}{v^2}\right)\,. \tag{5.23}$$

---

[9] Note that the singlet mode is independent of the S^3 position Ω_0 of the string endpoint.

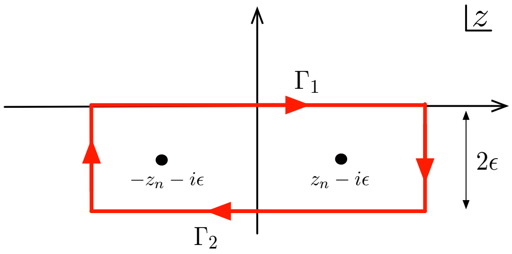

Figure 10. Contour in the complex plane used to evaluate the z-integral in eq. (5.22).

We see that the energy loss is a discrete sum over all mesons, as well as an integral over all the momentum modes of each meson into which the quark is allowed to radiate. As expected for Cherenkov radiation, this can only happen if the velocity v of the quark exceeds the phase velocity of the corresponding momentum mode, $v_n(q)$. For example, in the case of transverse vector mesons, the quark can only emit momentum modes to the right of the dashed, vertical line in figure 2. This cut-off is implemented by the Heaviside function in eq. (5.23).

Since the radial profiles $\xi_n(q, r_0)$ and the dispersion relations $v_n(q)$ entering eq. (5.23) are only known numerically, the energy loss must also be evaluated numerically. The result for the $n = 0$ term in the sum is plotted in figure 11. As one may expect, for fixed r_0 the energy loss increases monotonically with v up to the maximum allowed value of v, the local speed of light at r_0. In other words, a quark sitting at a fixed radial position radiates more the higher its velocity is. As r_0 decreases, the limiting velocity of the quark approaches that of the mesons from above. Therefore the quark and the meson dispersion relation curves cross at a higher momentum, i.e. the vertical dashed line in figure 2 moves to the right. This means that the characteristic momentum $q_{\rm char}$ of the modes contributing to the integral in (5.23) increases. As $r_0 \to 0$ these modes become increasingly peaked at small r (see figure 6(left)), and their effective couplings to the quark $e_{\rm eff}(q_{\rm char}, r_0)$ diverge. This explains why the energy loss at the maximum allowed value of the velocity diverges as $r_0 \to 0$. As we will discuss in section 7, however, this mathematical divergence is removed by physical effects that we have not taken into account.

Longitudinal modes. In the presence of the source eq. (4.11) becomes

$$\partial_r \left(\sqrt{-g} g^{rr} g^{00} \partial_r A_0\right) + iq\sqrt{-g} g^{11} g^{00} E = \tilde{e} J^0 \,. \tag{5.24}$$

eq. (4.12) remains unchanged, and together with the eq. above it yields

$$-\, iq\, \partial_r \left(\frac{\sqrt{-g}\, g^{rr} g^{00} g^{11}}{q^2 g^{11} + w^2 g^{00}}\, \partial_r E \right) + iq\sqrt{-g}\, g^{11} g^{00} E = \tilde{e} J^0 \,. \tag{5.25}$$

We now introduce a new field Φ defined as in eq. (4.15), but in this case the inverse relation (4.16) is modified by the source:

$$E = \frac{1}{\sqrt{-g}\, g^{11} g^{00}}\, \partial_r \Phi + \frac{1}{iq\, \sqrt{-g}\, g^{11} g^{00}}\, \tilde{e} J^0 \,. \tag{5.26}$$

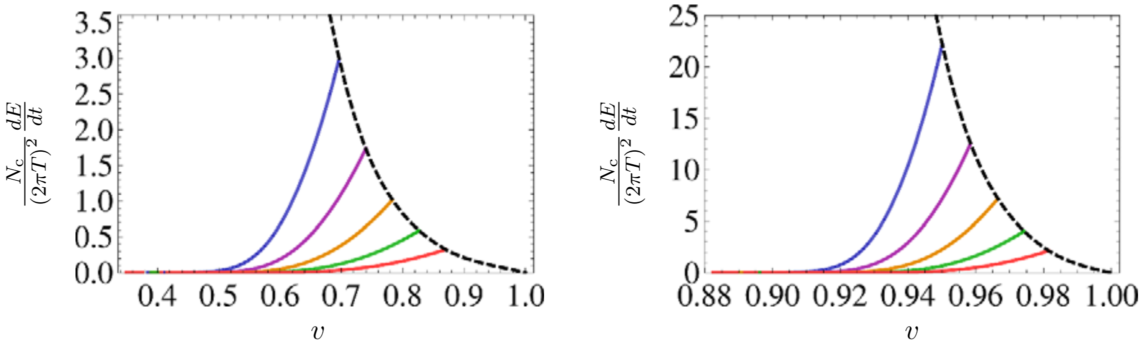

Figure 11. Energy loss into the transverse vector mode $\mathcal{A}_{(n=0)}$ for an embedding with $m = 1.32, R_0 = 1.2$ (left) and $m = 2.0, R_0 = 2.0$ (right). The continuous curves correspond (from top to bottom) to $r_0 = 0.86, 0.97, 1.10, 1.25, 1.45$ (left) and to $r_0 = 1.50, 1.69, 1.91, 2.18, 2.52$ (right). The dotted curve is defined by the endpoints of the constant-r_0 curves.

Substituting back into eq. (4.15) we find the new equation of motion for Φ:

$$-\,\partial_r\left(\frac{1}{\sqrt{-g}\,g^{11}g^{00}}\,\partial_r\Phi\right)+\frac{q^2g^{11}+w^2g^{00}}{\sqrt{-g}\,g^{rr}g^{00}g^{11}}\,\Phi=\frac{1}{iq}\partial_r\left(\frac{1}{\sqrt{-g}\,g^{11}g^{00}}\,\tilde{e}J^0\right)\,. \tag{5.27}$$

Inserting the explicit form of the metric functions, we finally arrive at

$$\partial_r\left(\frac{f\rho^4}{\tilde{f}r^3\sqrt{1+\dot{R}^2}}\,\partial_r\Phi\right)+2\frac{\sqrt{1+\dot{R}^2}}{fr^3}\left(w^2-\frac{f^2}{\tilde{f}^2}q^2\right)\Phi=-\frac{1}{iq}\partial_r\left(\frac{f\rho^4}{\tilde{f}r^3\sqrt{1+\dot{R}^2}}\,\tilde{e}J^0\right)\,. \tag{5.28}$$

We now follow section 4 and solve (5.28) by expanding Φ as in (4.19), where the radial eigenfunctions $\{\phi_n(q,r)\}$ satisfy exactly the same properties as in that section. In this case, inserting the expansion (4.19) in (5.28), and using the eigenstate equation and the orthonormality relations, we find that eq. (4.21) becomes

$$\left[\omega^2-\omega_n^2(q)\right]\Phi_n(\omega,q)=\tilde{e}J_n^0(\omega,q)\,, \tag{5.29}$$

whose solution with retarded boundary conditions is

$$\Phi_n(\omega,q)=\frac{\tilde{e}J_n^0(\omega,q)}{(\omega+i\epsilon)^2-\omega_n^2(q)}\,. \tag{5.30}$$

The coefficients J_n^0 are given (after integration by parts) by

$$J_n^0(\omega,q)=\int_0^\infty dr\,\frac{1}{iq}\frac{f\rho^4}{\tilde{f}r^3\sqrt{1+\dot{R}^2}}\,J^0(\omega,q)\,\partial_r\phi_n(q,r)=\frac{2\pi}{iq}\delta(\omega-qv\cos\theta)\mathcal{F}_n(q,r_0)\,, \tag{5.31}$$

with

$$\mathcal{F}_n(q,r)=-\frac{1}{\sqrt{-g}\,g^{11}g^{00}}\,\partial_r\phi_n(q,r)=\frac{f\rho^4}{\tilde{f}r^3\sqrt{1+\dot{R}^2}}\,\partial_r\phi_n(q,r)\,. \tag{5.32}$$

Note that the coefficients $\mathcal{F}_n$ appear in the expansion of the electric field (5.26), i.e.

$$E(\omega,q,r)=-\sum_n\Phi_n(\omega,q)\mathcal{F}_n(q,r)+\frac{1}{iq\,\sqrt{-g}\,g^{11}g^{00}}\,\tilde{e}J^0(\omega,q,r)\,. \tag{5.33}$$

As in the case of transverse modes, we see from eq. (5.29) that the effective coupling between a longitudinal meson $\Phi_n(\omega, q)$ and the quark is determined by the radial wave function of the meson, in this case

$$e_{\text{eff}}(q, r_0) = e\, \mathcal{F}_n(q, r_0)\,. \tag{5.34}$$

Our task now is to compute the rate of energy loss into longitudinal meson modes. For this purpose, eq. (5.11) instructs us to evaluate the electric field at the location of the quark. If we naively do so using the expression (5.26) for E then the second term gives a divergent result, since $J^0(r_0) \propto \delta(0)$. However, this divergence is unphysical: if one replaces the delta-function by a smooth charge distribution, then the integral over space in (5.9) vanishes. Indeed, suppose that the current (5.13) is replaced by

$$J^a = \varrho^{(3)}(\vec{x} - \vec{v}t, r, \Omega) \times (1, \vec{v}, 0, \vec{0})\,, \tag{5.35}$$

where ϱ is a smooth function. Then in Fourier space

$$J^a = 2\pi\, \delta(\omega - \vec{q}\cdot\vec{v})\, \varrho^{(3)}(\vec{q}, r, \Omega) \times (1, \vec{v}, 0, \vec{0}) \tag{5.36}$$

and the energy loss (5.9) is

$$\begin{aligned} \frac{dE}{dt} &= -e \int dr d\Omega \int d^3x\, E(t, \vec{x}, r, \Omega) \cdot J(t, \vec{x}, r, \Omega) \\ &= -e \int dr d\Omega \int \frac{d\omega d\tilde{\omega}}{(2\pi)^2} e^{-i\omega t - i\tilde{\omega} t} \int \frac{d^3q}{(2\pi)^3} z\, E(\tilde{\omega}, -\vec{q}, r, \Omega)\, J^1(\omega, \vec{q}, r, \Omega)\,, \end{aligned} \tag{5.37}$$

where as usual $z = \cos\theta$ is the relative angle between $\vec{q}$ and $\vec{v}$ and $d^3q = 2\pi q^2\, dqdz$. If we substitute the term in E that is proportional to J^0 we see that the integrand is proportional to

$$\frac{1}{iq}\, \delta(\tilde{\omega} + qvz)\, \delta(\omega - qvz)\, \varrho(-\vec{q}, r, \Omega)\, \varrho(\vec{q}, r, \Omega)\, z\,. \tag{5.38}$$

This is odd under $\vec{q} \to -\vec{q}$ (since ω and $\tilde{\omega}$ are dummy variables) and therefore the integral over z vanishes.

We therefore conclude that we can neglect the second term in (5.33) in order to evaluate (5.11). Following the previous section we have

$$\begin{aligned} \frac{dE_{\text{long}}}{dt} &= ev^1 E(t, \vec{v}t, r_0, \Omega_0) \\ &= \sum_n - \int \frac{d\omega d^3q}{(2\pi)^4} (ev\cos\theta)\, \Phi_n(\omega, q) \mathcal{F}_n(q, r_0)\, e^{-i\omega t} e^{itq\cdot v} \\ &= \sum_n - \int \frac{d^3q}{(2\pi)^3} (ev\cos\theta)\, \frac{\tilde{e}}{iq}\, \frac{1}{(qv\cos\theta + i\epsilon)^2 - \omega_n^2(q)}\, \mathcal{F}_n^2(q, r_0) \\ &= \sum_n - \frac{e^2}{\Omega_3 v} \int_0^\infty \frac{dq}{2\pi}\, \frac{1}{q}\, \mathcal{F}_n^2(q, r_0) \int_{-1}^1 \frac{dz}{2\pi i}\, \frac{z}{(z + i\epsilon)^2 - z_n^2(q)}\,. \end{aligned} \tag{5.39}$$

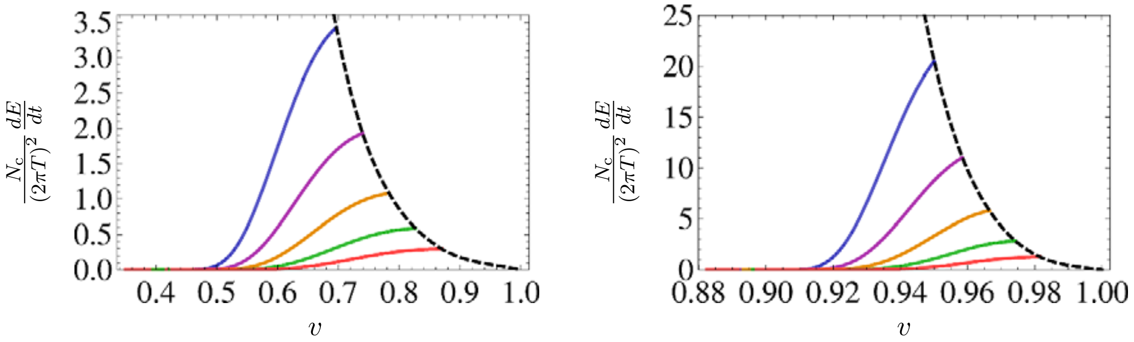

Figure 12. Energy loss into the longitudinal vector mode $\Phi_{(n=0)}$ for an embedding with $m = 1.32, R_0 = 1.2$ (left) and $m = 2.0, R_0 = 2.0$ (right). The continuous curves correspond (from top to bottom) to $r_0 = 0.86, 0.97, 1.10, 1.25, 1.45$ (left) and to $r_0 = 1.50, 1.69, 1.91, 2.18, 2.52$ (right). The dotted curve is defined by the endpoints of the constant-r_0 curves.

The z-integral can be evaluated using the same contour of figure 10. In this case each pole contributes -1/2, so the final result is

$$\frac{dE_{\rm long}}{dt} = \sum_n \frac{e^2}{2\Omega_3 v} \int_0^\infty \frac{dq}{2\pi}\, \frac{1}{q}\, \mathcal{F}_n^2(q, r_0)\, \Theta\left(1 - \frac{v_n^2(q)}{v^2}\right) . \tag{5.40}$$

The energy loss into the $n = 0$ mode is shown in figure 12. The same comments as in the case of transverse modes apply here.

5.2 Energy loss into scalar mesons

The endpoint of an open string attached to the brane couples to the worldvolume scalar fields, so in the presence of the quark the action (4.23) is modified to

$$\begin{aligned} S_{\rm scalar} = & -T_{\rm D7} L^8 \int d^8x \sqrt{-g} \left[\frac{1}{2} g^{ab} \partial_a X^A \partial_b X^B G_{AB} + \frac{1}{2} m^2_{AB}(x) X^A X^B \right] \\ & - \frac{L^2}{2\pi \ell_s^2} \int d\tau \sqrt{-\dot{x}^2}\, G_{AB}\, X^A n^B \, , \end{aligned} \tag{5.41}$$

where $\dot{x}^2 = g_{ab} \dot{x}^a \dot{x}^b$ and n^A is the unit vector that is tangent to the string and orthogonal to the brane at the string endpoint. As usual, in the last term we have explicitly factored out the L-dependence associated to the spacetime metric (3.2). The square-root factor in the last term is necessary to make the integrand a scalar density on the worldline of the string endpoint, which is contained in the brane's worldvolume. We emphasize that the indices of $\dot{x}^a$ are not contracted with the gauge theory metric η_{ab} but with the D7-brane metric g_{ab}. The relative normalization between the two lines in (5.41) can be confirmed as described in footnote 8. As explained in appendix A, the boundary condition at the string endpoint implies that the string ends orthogonally on the brane. The unit normal in the last term of the action (5.41) means that the string couples to the scalar that parametrizes the direction along which the string pulls on the brane, as one may intuitively expect.

In order to work with canonically normalized fields we rescale $X^A \to \sqrt{T_{\mathrm{D7}}L^8}\, X^A$ so that the action becomes

$$S_{\text{scalar}} = -\int d^8x\sqrt{-g}\left[\frac{1}{2}g^{ab}\partial_a X^A \partial_b X^B G_{AB} + \frac{1}{2}m^2_{AB}(x) X^A X^B\right] - e\int d^8x\, J_A X^A\,, \quad (5.42)$$

where $J_A = \delta^{(7)}(x - x(\tau))\sqrt{-\dot{x}^2}\, G_{AB}\, n^B$ and e is the same coupling constant defined in (5.4). Since the scalars do not interact with each other, they give independent contributions to the stress tensor of the brane. Using the definition (5.1), the contribution from either scalar field is easily found to be

$$T_{ab} = \nabla_a X \nabla_b X - \frac{1}{2}g_{ab}\left[(\nabla X)^2 + m^2 X^2\right] + X^2\,\frac{\delta m^2}{\delta g^{ab}}\,. \quad (5.43)$$

For ease of notation, in this equation we have dropped the superindex 'A' on the scalar, and we will continue to do so below. The last term originates from the non-trivial dependence of the scalar masses (4.24) on the metric. Fortunately, we will see that we do not need to evaluate this term explicitly in order to compute the divergence of the stress-tensor.

In the presence of the string endpoint, the equation of motion (4.28) for the scalars is modified to

$$\sqrt{-g}\left(\nabla^2 - m^2\right) X = eJ\,. \quad (5.44)$$

Using this, the divergence of the stress tensor takes the form

$$\sqrt{-g}\,\nabla^a T_{ab} = J\,\nabla_b X - X^2\,\nabla_b m + \nabla^a\left(X^2\,\frac{\delta m^2}{\delta g^{ab}}\right)\,. \quad (5.45)$$

The second term on the right-hand side is due to the possible spacetime dependence of the scalar masses $m(x)$, but it vanishes identically for the case of interest here, $b = 0$, because of the time-translation invariance of the theory. The last term on the right-hand side vanishes when evaluated on a solution of the equations of motion, even in the presence of the source J. To see this, recall that the stress tensor must be identically conserved in the absence of the source because of the diffeomorphism invariance of the brane's worldvolume theory. This means, in particular, that when $J = 0$ we have

$$X\,\nabla^a\left(\frac{\delta m^2}{\delta g^{a0}}\right) + 2\left(\frac{\delta m^2}{\delta g^{a0}}\right)\nabla^a X = 0\,. \quad (5.46)$$

The key point now is that this equation is linear in X. Since the solution in the presence of the source is a linear supersposition of solutions of the source-less equation, linearity of (5.46) implies that this expression also vanishes for solutions of eq. (5.44) with $J \neq 0$. We thus conclude that (the time component of) the non-conservation of the stress-tensor in the scalar sector takes the form

$$\sqrt{-g}\,\nabla^a T_{a0} = J\,\nabla_0 X\,. \quad (5.47)$$

As in the case of vector mesons, we consider a rectilinear quark motion with constant velocity, in which case

$$J = \sqrt{-\dot{x}^2(r_0)}\,\delta^{(3)}(\vec{x} - \vec{v}t)\,\delta(r - r_0)\,\delta^{(3)}(\Omega - \Omega_0)\,. \quad (5.48)$$

Note that, although the velocity v is the quark velocity as seen by a gauge theory observer, the prefactor above is not just $\sqrt{1-v^2}$ but depends non-trivially on the quark position in the radial direction through

$$\sqrt{-\dot{x}^2(r_0)} = \sqrt{-g_{00}(r_0) - g_{11}(r_0)v^2} \,. \tag{5.49}$$

Because of the black hole redshift, for fixed r_0 this factor vanishes before v reaches the speed of light, i.e. at $v < 1$. As we will see, this fact is responsible for a qualitative difference between the energy radiated into scalar and into vector mesons.

Following section 4.2, we focus on the zero-mode of X on the S^3, and work with its Fourier components $X(\omega, q, r)$, for which the equation of motion takes the form

$$\partial_r \left(\sqrt{-g}\, g^{rr} \partial_r X\right) - \sqrt{-g}\left(g^{00}\omega^2 + g^{11}q^2 + m^2\right) X = \tilde{e} J \,, \tag{5.50}$$

where the relevant Fourier-space components of the source are

$$J = \sqrt{-\dot{x}^2(r_0)}\, 2\pi\delta(\omega - qv\cos\theta)\, \delta(r - r_0) \,, \tag{5.51}$$

and as usual $\tilde{e} = e/\Omega_3$. We solve (5.50) by expanding X as in eq. (4.30). In the presence of the source, the equation obeyed by the X_n mode is

$$\left[\omega^2 - \omega_n^2(q)\right] X_n(\omega, q) = \tilde{e} J_n(\omega, q) \,, \tag{5.52}$$

where

$$J_n(\omega, q) = \int dr J(\omega, q) \varphi_n(q, r) = \sqrt{-\dot{x}^2(r_0)}\, 2\pi\delta(\omega - qv\cos\theta) \varphi_n(q, r_0) \,. \tag{5.53}$$

With retarded boundary conditions, as appropriate for the reaction to the quark's passage, eq. (5.52) yields

$$X_n(\omega, q) = \frac{\tilde{e} J_n(\omega, q)}{(\omega + i\epsilon)^2 - \omega_n^2(q)} \,. \tag{5.54}$$

As in the case of vector modes, we see from eq. (5.52) that the effective coupling between a scalar meson $X_n(\omega, q)$ and the quark is determined by the radial wave function of the meson, in this case

$$e_{\text{eff}}(q, r_0) = e\, \sqrt{-\dot{x}^2(r_0)}\, \varphi_n(q, r_0) \,. \tag{5.55}$$

We are now ready to compute the rate of energy deposition into scalar mesons. From eqs. (5.2) and (5.47) we have

$$\frac{dE_{\text{scalar}}}{dt} = -e \int d^3x dr d\Omega_3\, \dot{X} J = -e\sqrt{-\dot{x}^2(r_0)}\, \dot{X}(t, \vec{v}t, r_0, \Omega_0) \,. \tag{5.56}$$

Following the steps of the vector meson case we find:

$$\begin{aligned}
\frac{dE_{\text{scalar}}}{dt} &= \sum_n -e\sqrt{-\dot{x}^2(r_0)} \int \frac{d\omega d^3q}{(2\pi)^4} \left(-i\omega\right) X_n(\omega, q) \varphi_n(q, r_0)\, e^{-i\omega t} e^{itq\cdot v} \\
&= \sum_n -e\left[-\dot{x}^2(r_0)\right] \int \frac{d^3q}{(2\pi)^3} \left(-iqv\cos\theta\right) \frac{\tilde{e}}{(qv\cos\theta + i\epsilon)^2 - \omega_n^2(q)}\, \varphi_n^2(q, r_0) \\
&= \sum_n -\frac{e^2}{\Omega_3 v} \left[-\dot{x}^2(r_0)\right] \int_0^\infty \frac{dq}{2\pi}\, q\, \varphi_n^2(q, r_0) \int_{-1}^1 \frac{dz}{2\pi i} \frac{z}{(z + i\epsilon)^2 - z_n^2(q)} \\
&= \sum_n \frac{e^2}{2\Omega_3 v} \left[-\dot{x}^2(r_0)\right] \int_0^\infty \frac{dq}{2\pi}\, q\, \varphi_n^2(q, r_0)\, \Theta\left(1 - \frac{v_n^2(q)}{v^2}\right) \,.
\end{aligned} \tag{5.57}$$

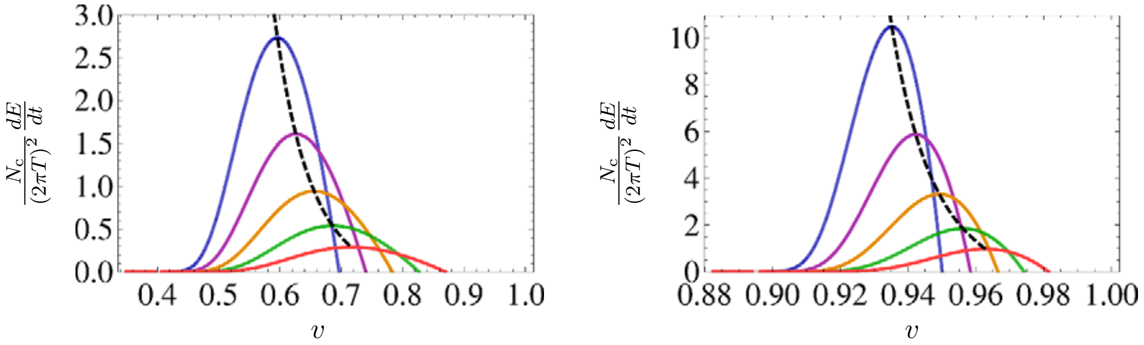

Figure 13. Energy loss into the scalar mode $\varphi^{(A=1)}_{(n=0)}$ for an embedding with $m = 1.32, R_0 = 1.2$ (left) and $m = 2.0, R_0 = 2.0$ (right). The continuous curves correspond (from top to bottom) to $r_0 = 0.86, 0.97, 1.10, 1.25, 1.45$ (left) and to $r_0 = 1.50, 1.69, 1.91, 2.18, 2.52$ (right). The dotted curve is defined by the maxima of the constant-r_0 curves.

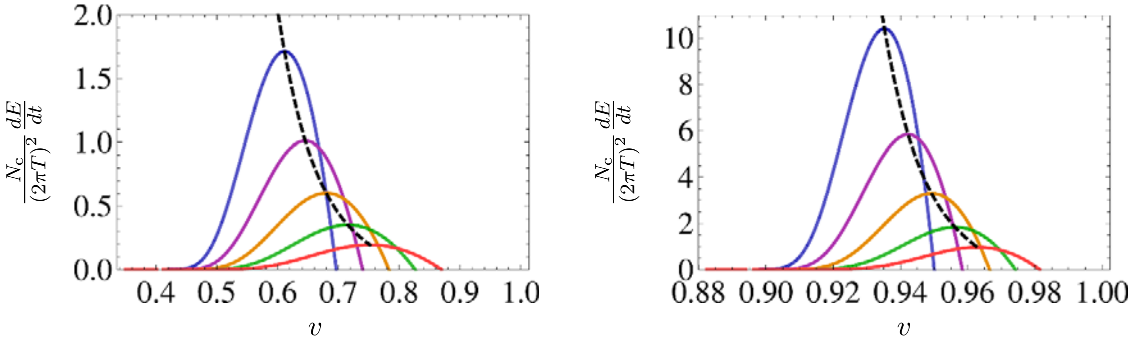

Figure 14. Energy loss into the pseudoscalar mode $\varphi^{(A=2)}_{(n=0)}$ for an embedding with $m = 1.32, R_0 = 1.2$ (left-hand side plots) and $m = 2.0, R_0 = 2.0$ (right-hand side plots). The continuous curves correspond (from top to bottom) to $r_0 = 0.86, 0.97, 1.10, 1.25, 1.45$ (left) and to $r_0 = 1.50, 1.69, 1.91, 2.18, 2.52$ (right). The dotted curve is defined by the maxima of the constant-r_0 curves.

The result for the energy loss into the lowest-lying scalar and pseudoscalar modes is shown in figures 13 and 14. The main difference with respect to the case of vector mesons is the fact that the constant-r_0 curves do not rise monotonically as v increases, but instead they vanish when v reaches the local speed of light at r_0. The reason for this is of course the factor in eq. (5.49).

6 Phenomenological implications for HIC experiments

As is clear from our general discussion in section 2, the mechanism of Cherenkov energy loss depends only on two qualitative properties encoded in the dispersion relations of figure 2: the fact that heavy mesons remain bound in the gauge theory plasma, and the fact that their limiting velocity in the plasma is subluminal. Both properties can be motivated in QCD irrespectively of whether or not a string dual of QCD exists. The first property is suggested by the fact that sufficiently heavy mesons are smaller than the screening length in the plasma [34], and is supported by calculations of both the static quark-antiquark potential [35–39] and of Minkowski-space spectral functions in lattice-regularized QCD [40–

45].[10] The second property, which goes back to ref. [47], is suggested by the fact that moving mesons see a boosted, higher energy density that will melt them if they move sufficiently fast [48–51].[11]

Rigorously verifying these two properties in QCD is not presently feasible. For this reason it is reassuring that, as we explained in section 2, they are both realized in all gauge theory plasmas with a gravity dual in the large-N_c, strong coupling limit. In this section we will assume that the two properties are also realized in the QGP and extract some phenomenological consequences that might be observable in heavy ion collisions.[12] Since the heavier the meson the more perturbative its properties become, we expect that our conclusions are more likely to be applicable to the charmonium rather than to the bottomonium sector.

An interesting feature of the energy loss by Cherenkov radiation is that, unlike other energy-loss mechanisms, it is largely independent of the details of the quark excited state, such as the precise features of the gluon cloud around the quark, etc. In the gravity description these details would be encoded in the precise profile of the entire string, but the Cherenkov emission only depends on the trajectory of the string endpoint. This leads to a dramatic simplification which, with the further approximation of rectilinear uniform motion, reduces the parameters controlling the energy loss to two simple ones: the string endpoint velocity v and its radial position r_0. The former is just the velocity of the quark in the gauge theory, whereas the second roughly measures the size of the gluon cloud that dresses the quark [26]. In order to obtain a ballpark estimate of the magnitude of the energy loss, we will assume that in a typical collision quarks are produced with order-one values of r_0. Under these circumstances the energy loss is of order unity in units of $(2\pi T)^2/N_c$, which for a temperature range of $T = 200 - 400$ MeV and $N_c = 3$ leads to $dE/dx \approx 2 - 8$ GeV/fm. This is is of the same order of magnitude as other mechanisms of energy loss in the plasma; for example, the BDMPS radiative energy loss $dE/dx = \alpha_s C_F \hat{q} L/2$ yields values of $dE/dx = 7 - 40\,\mathrm{GeV/fm}$ for $\hat{q} = 1 - 5\,\mathrm{GeV}^2/\mathrm{fm}$, $\alpha_s = 0.3$ and $L \approx 6$ fm. Since our gravity calculation is strictly valid only in the infinite-quark energy limit (because of the linear trajectory approximation), we expect that our estimate is more likely to be applicable to highly energetic quarks at LHC rather than to those at RHIC.

Even if in the QGP the magnitude of Cherenkov energy loss turns out to be subdominant with respect to other mechanisms, its velocity dependence and its geometric features may still make it identifiable. Indeed, Cherenkov energy loss would only occur for quarks moving at velocities $v > v_{\mathrm{lim}}$, with v_{lim} the limiting velocity of the corresponding meson in the plasma. The presence of such a velocity threshold is the defining characteristic of Cherenkov energy loss. The precise velocity at which the mechanism starts to operate may actually be higher than v_{lim} in some cases, since the additional requirement that the energy

---

[10] In some models light mesons also remain bound above T_c by Coulomb-like forces [46].

[11] An alternative possibility would be that meson states with q above some upper bound cease to exist. In any event, our conclusions rely on meson states existing (with a sufficiently narrow width) only up to some moderate q for which $q \gtrsim \omega(q)$.

[12] Implications for photon production have been discussed in [52], and for deep inelastic scattering in [53].

of the quark be equal or larger than the in-medium mass of the meson must also be met. A related conclusion of our calculation in the $\mathcal{N} = 4$ model is that the energy loss decreases as the velocity of the quark approaches the speed of light. This is in fact a universal feature of all plasmas with a gravity dual. The reason is that the quark velocity can approach unity only in the limit $r_0 \to \infty$, in which the effective couplings (5.17), (5.34) and (5.55) between the quark and the mesons vanish because the meson radial wave functions are normalizable. In fact, in the case of scalar mesons the energy loss ceases completely at some subluminal velocity at which (5.49) vanishes. If these properties also hold in QCD then Cherenkov energy loss may be identifiable because it only operates in a limited range of quark velocities.

Cherenkov mesons would be radiated at a characteristic angle $\cos\theta_c = v_{\rm lim}/v$ with respect to the emitting quark, where v is the velocity of the quark. Taking the gravity result as guidance, $v_{\rm lim}$ could be as low as $v_{\rm lim} = 0.35$ at the meson dissociation temperature [19], corresponding to an angle as large as $\theta_{\rm c} \approx 1.21$ rad. This would result in an excess of heavy mesons associated to high-energy quarks passing through the plasma. Our estimate of the energy loss suggests that the number of emitted J/ψ's, for example, could range from one to three per fm. This emission pattern is similar to the emission of sound waves by an energetic parton [54] in that both effects lead to a non-trivial angular structure. One important difference, however, is that the radiated heavy mesons would not thermalize and hence would not be part of a hydrodynamic shock wave. As in the Mach cone case, the meson emission pattern could be reflected in azimuthal dihadron correlations triggered by a high-$p_{\rm T}$ hadron. Due to surface bias, the energetic parton in the triggered direction is hardly modified, while the one propagating in the opposite direction moves through a significant amount of medium, emitting heavy mesons. Thus, under the above assumptions, the dihadron distribution with an associated J/ψ would have a ring-like structure peaked at an angle $\theta \approx \pi - \theta_{\rm c}$.

A final observation is that Cherenkov energy loss also has a non-trivial temperature dependence, since it requires that there are meson-like states in the plasma, and therefore it does not take place at temperatures above the meson dissociation temperature. Similarly, it is reasonable to assume that it does not occur at temperatures below T_c, since in this case we do not expect the meson dispersion relation to become spacelike.[13] Under these circumstances, the Cherenkov mechanism is only effective over a limited range of temperatures $T_c < T < T_{\rm diss}$ which, if $T_{\rm diss} \gtrsim 1.2 T_c$ as in [55], is a narrow interval. As was pointed out in [56], a mechanism of energy loss which is confined to a narrow range of temperatures in the vicinity of T_c concentrates the emission of energetic probes to a very narrow layer on the collision geometry and is able to explain v_2-data at high p_T at RHIC [57, 58]. Provided that the meson dissociation temperature $T_{\rm diss}$ is not much larger than T_c, the radiation of Cherenkov mesons is one such mechanism.

---

[13] This assumption is certainly correct for plasmas with a gravity dual, since the corresponding geometry does not include a black hole horizon if $T < T_c$.

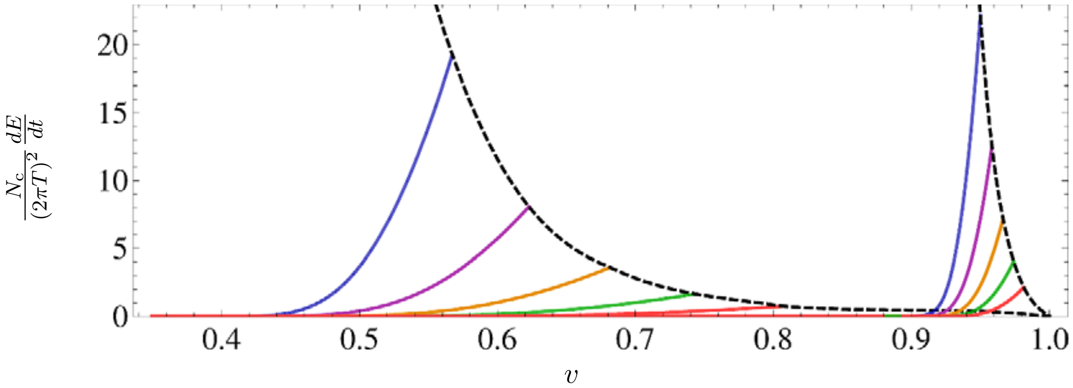

Figure 15. Energy loss into the transverse vector mode $\mathcal{A}_{(n=0)}$ for an embedding with $m = 1.32, R_0 = 1.2$ (left-hand side curves) and $m = 2.0, R_0 = 2.0$ (right-hand side curves). The continuous curves correspond (from top to bottom) to $r_0 = 0.58, 0.70, 0.83, 0.98, 1.18$ (left-hand side) and to $r_0 = 1.50, 1.69, 1.91, 2.18, 2.52$ (right-hand side). The dotted curve is defined by the endpoints of the constant-r_0 curves.

7 Discussion

Cherenkov emission of mesons [59–71] and gluons [72, 73] in QCD has been considered before. Although some of the underlying physics is similar, the mechanism we have discussed is different in several respects. First, it operates in the QGP, as opposed to in a hadronic medium as in [59–71], and the radiated particles are colourless mesons, as opposed to gluons as in [72, 73]. Second, the gauge/string duality provides a large class of completely explicit examples (although none of them includes QCD) in which this mechanism is realized and in which the energy loss can be calculated without further model assumptions.

Figures 11, 12, 13 and 14 show the rate of energy deposition into vector and scalar modes on the brane. All these figures share the property that the energy loss diverges as $1/r_0^6$ (as shown analytically in appendix D) in the limit $r_0 \to 0$. However, this mathematical divergence is removed by physical effects we have not taken into account. For example, for sufficiently large q the radial profile of the mesons becomes of order the string length and stringy effects become important [28]. Also, mesons acquire widths $\Gamma \propto q^2$ at large q [74] and can no longer be treated as well defined quasiparticles. Finally, the approximation of a constant-v, constant-r_0 trajectory ceases to be valid whenever the energy loss rate becomes large.

Figures 11, 12, 13 and 14 also illustrate the simple dependence of the energy loss on the ratio $m \propto M_q/T$. Increasing m decreases the redshift at the bottom of the branes, and therefore increases the limiting velocity of mesons, v_{lim}, at which quark energy loss via Cherenkov emission starts to operate. This means that the energy loss becomes concentrated on a narrower range of velocities, closer to unity, as m is increased, but the structure of the curves is roughly the same up to a rescaling. This can be seen in the figures above by comparing the energy loss for $m = 1.2$ (left-hand side) and $m = 2.0$ (right-hand side). The concentration of energy loss on a narrower velocity interval is also illustrated in figures 15 and 16, where the result for both values of m is shown simultaneously on the same plot (for the transverse vector and scalar modes).

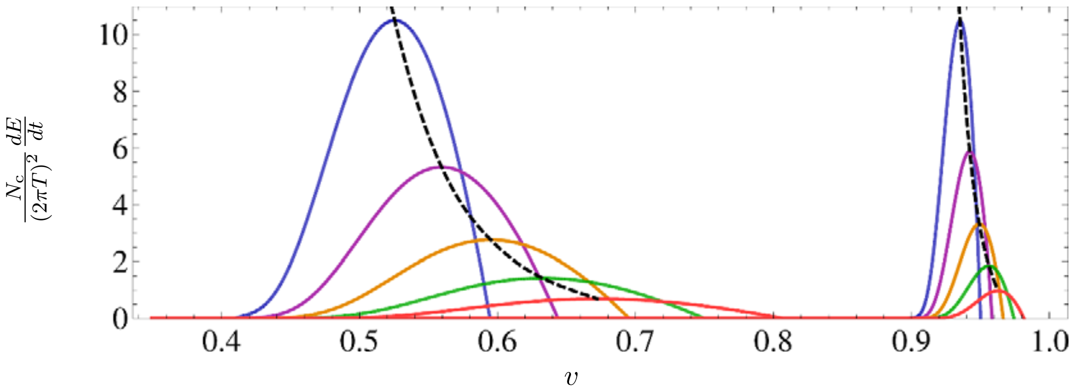

Figure 16. Energy loss into the scalar mode $\varphi^{(A=1)}_{(n=0)}$ for an embedding with $m = 1.32, R_0 = 1.2$ (left-hand side curves) and $m = 2.0, R_0 = 2.0$ (right-hand side curves). The continuous curves correspond (from top to bottom) to $r_0 = 0.64, 0.74, 0.86, 1.00, 1.18$ (left-hand side) and to $r_0 = 1.50, 1.69, 1.91, 2.18, 2.52$ (right-hand side). The dotted curve is defined by the maxima of the constant-r_0 curves.

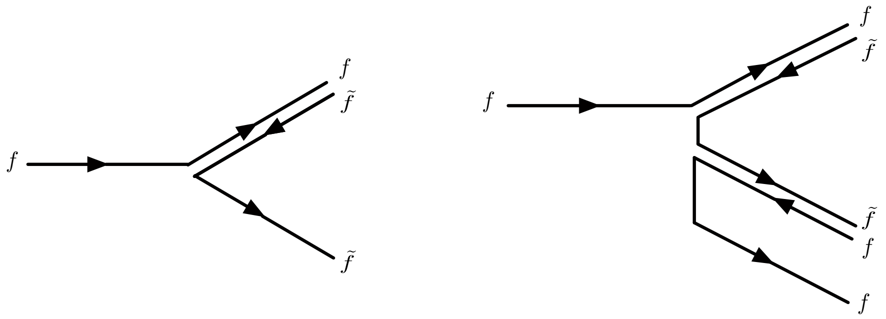

Figure 17. Meson emissions by a quark in a theory with multiple flavours.

In this paper we have concentrated on the case $N_f = 1$, i.e. we have assumed the presence of a single heavy flavour. Consider now a theory with multiple heavy quarks, such as QCD with c and b quarks, for example. In the string description this corresponds to a situation with $N_f > 1$ D-branes. If all quarks have identical masses (and R-symmetry quantum numbers) then the D-branes are all coincident and their worldvolume theory is described by a non-Abelian U(N_f) theory, corresponding to the fact that mesons $m^{f\tilde{f}}$ come in multiplets that transform in the adjoint representation of U(N_f). A quark with flavour f then may emit any of the N_f mesons with flavour $f\tilde{f}$, with $\tilde{f} = 1, \ldots, N_f$. Under these circumstances the energy loss is enhanced by a power of N_f.[14] Note that if the resulting meson has $\tilde{f} \neq f$ then the quark must change flavour $f \to \tilde{f}$ in the emission process, as shown in figure 17(left). A process in which the quark does not change flavour is also possible, as shown in figure 17(right), but this requires the emission of at least two mesons and is therefore further suppressed at large N_c.

---

[14] This corrects the corresponding statement in ref. [1].

Consider now the opposite situation, more analogous to QCD, in which the heavy quarks have different masses, so that the D-branes in the string description do not overlap. This is depicted in figures 18, 19 and 20, which show the string description of the emission processes of figures 17(left) and 17(right), respectively. Figures 18 and 19 correspond to emissions with $\tilde{f} \neq f$, whereas figure 20 describes the emission of an ff-meson. In this geometric picture the necessity of a two-meson emission in the case $\tilde{f} \neq f$ in order to preserve the quark flavour is due to the fact that the string must break twice in order to stay attached to the same brane — see figure 19. Since string breaking is suppressed at large N_c, this process is subleading with respect to one-meson emission. In any case, since an open string must always have its endpoints attached to a brane, the emission of one or multiple mesons with $\tilde{f} \neq f$ by a quark of flavour f requires a tunneling process in which the string fluctuates and touches the $\tilde{f}$-brane, as shown in figures 18 and 19. The amplitude for this process can be studied semiclassically provided the distance between the two branes is sufficiently large compared to ℓ_s, but it is far from straightforward to calculate [75, 76]. In addition, in the present context the calculation would require a precise specification of the string profile. On general grounds, however, one may expect the amplitude to be exponentially suppressed, since it requires a large string fluctuation that is classically forbidden. Note that the same exponential suppression applies to the emission of a large ff-meson by an f-quark, as shown in figure 20. This is the reason why we neglected this process in our calculation of energy loss. More precisely, our calculation can be seen as accounting for this process in the limit in which the size of the emitted meson is so small that it requires quantization of the resulting string. In this limit there is no exponential suppression, and the emitted string must be described as a field propagating on the brane.

We close with a comment on a possible extension of our work. In this paper we have focused on the energy loss of quarks attached to branes that sit outside the horizon in a Minkowski embedding. It would be interesting to study the energy loss in the case of black hole embeddings, which describe light quarks. In this case no stable quark-antiquark bound states exist in the plasma, which in the string description corresponds to the fact that excitations on the brane are characterized by quasinormal modes with complex frequencies. It would be interesting to explore whether the emission of quasinormal modes could also lead to a significant energy loss.

Acknowledgments

We thank Mariano Chernicoff, David d'Enterria, Roberto Emparan, Bartomeu Fiol, Alberto Guijosa, Cristina Manuel, Angel Paredes, Robert Myers, Leonardo Patiño, Amit Sever and Paul Townsend for discussions. We are supported by a Marie Curie Intra-European Fellowship PIEF-GA-2008-220207 (JCS) and by 2009-SGR-168, MEC FPA 2007-66665-C02 and CPAN CSD2007-00042 Consolider-Ingenio 2010 (DF, DM).

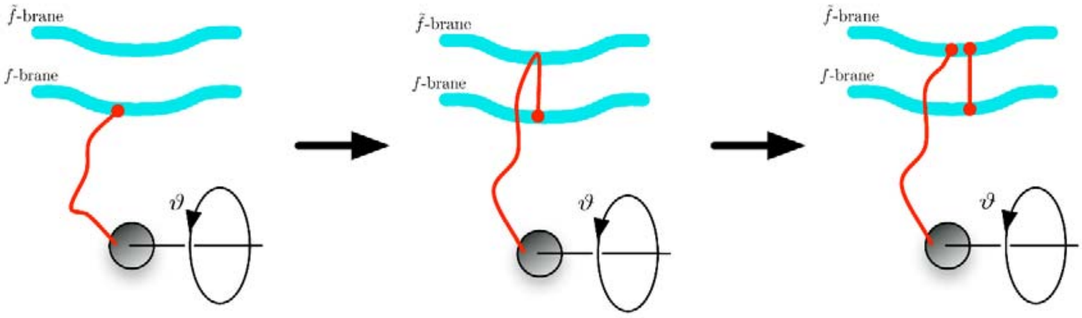

Figure 18. String description of the emission of an $f\tilde{f}$-meson with $\tilde{f} \neq f$. The quark changes flavour in the process.

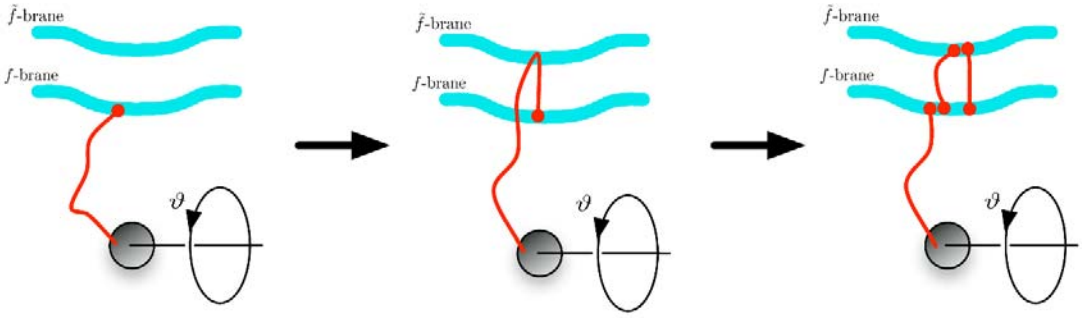

Figure 19. String description of the emission of two mesons with $\tilde{f} \neq f$. The quark does not change flavour in the process.

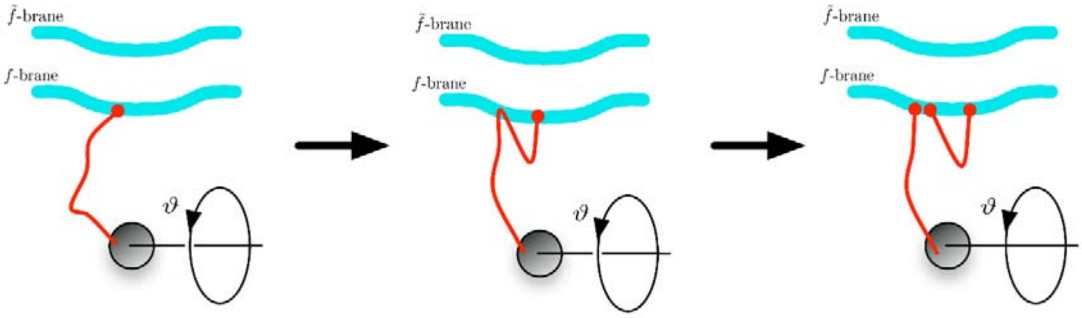

Figure 20. String description of the emission of an ff-meson by an f-quark. The quark does not change flavour in the process.

A Boundary conditions at the string endpoint

The action for the string may be written as

$$S = -T_{\text{string}} \int d\tau d\sigma \sqrt{-g}\, \frac{1}{2}\, g^{\alpha\beta} \partial_\alpha X^M \partial_\beta X^N G_{MN}\,. \tag{A.1}$$

In this form of the action g is an *independent* worldsheet metric and $X^M(\tau, \sigma)$ specify the embedding in spacetime of the string worldsheet. Since g appears undifferentiated, it can be eliminated from the action through its equation of motion. This equation implies that

$$g_{\alpha\beta} = \partial_\alpha X^M \partial_\beta X^N G_{MN} \,, \tag{A.2}$$

i.e. that g is the induced metric on the worldsheet. Substituting this into the action one obtains the familiar Nambu-Goto action

$$S = -\frac{T_{\rm string}}{2} \int d\tau d\sigma \sqrt{-g} \,. \tag{A.3}$$

An alternative way to proceed, which is more convenient to elucidate the boundary conditions at the string endpoint, is to choose the so-called conformal gauge. This means that one uses the reparametrization invariance of the string action to ensure that the worldsheet metric is conformally flat, i.e that $g_{\alpha\beta} = \Omega^2(\tau, \sigma)\eta_{\alpha\beta}$. (In addition, Weyl invariance may be used to ensure that $\Omega = 1$.) In this gauge the action becomes

$$S = -T_{\rm string} \int d\tau d\sigma \frac{1}{2} \eta^{\alpha\beta} \partial_\alpha X^M \partial_\beta X^N G_{MN} \,. \tag{A.4}$$

Variation of this action with respect to the embedding coordinates yields a bulk term proportional to the equation of motion, $\eta^{\alpha\beta}\partial_\alpha\partial_\beta X^M = 0$, plus the boundary term

$$- T_{\rm string} \int d\tau \left[X^{M\prime} \delta X^N G_{MN} \right]_{\rm bdry} \,, \tag{A.5}$$

which is integrated over the string boundary. The equation of motion must be supplemented by the constraints associated to the gauge fixing of g, which take the form

$$\begin{aligned} \dot{X} \cdot X' &\equiv G_{MN} \dot{X}^M X^{N\prime} = 0 \,, \\ \dot{X}^2 + X'^2 &\equiv G_{MN} \left(\dot{X}^M \dot{X}^N + X^{M\prime} X^{N\prime} \right) = 0 \,. \end{aligned} \tag{A.6}$$

The boundary conditions follow from the requirement that the boundary term vanish. This may be achieved by imposing either a Neumann boundary condition, $X^{M\prime}|_{\rm bdry} = 0$, or a Dirichlet boundary condition, $\delta X^M|_{\rm bdry} = 0$. If all coordinates satisfy Neumann boundary conditions, then the second constraint immediately implies that $\dot{X}^2|_{\rm bdry} = 0$, namely the familiar condition that the endpoint moves at the speed of light. Suppose however that the string is attached to a Dp-brane, and let the first $p+1$ coordinates X^a be coordinates along the brane directions, and X^A be coordinates orthogonal to the brane. Then by definition we must choose Neumann boundary conditions for X^a and Dirichlet boundary conditions for X^A:

$$X^{a\prime}|_{\rm bdry} = 0 \,, \qquad \dot{X}^A|_{\rm bdry} = 0 \,. \tag{A.7}$$

The Neumann boundary condition on X^a implies that the string ends orthogonally on the brane, since the vector tangent to the string at its endpoint, $X^{M\prime}|_{\rm bdry} = 0$, has no components along the brane. Substituting both boundary conditions on the second constraint equation one finds that

$$\dot{X^a}^2 |_{\rm bdry} = - \, {X^{A\prime}}^2 |_{\rm bdry} \leq 0 \,, \tag{A.8}$$

which means that the endpoint moves along the brane at a speed lower than or equal to the local speed of light.

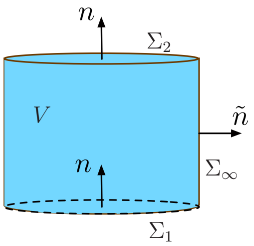

Figure 21. Brane's worldvolume, to which Stokes' theorem is applied.

B Energy loss formula

A charge can be defined for each of the isometries of the brane's worldvolume metric (3.6). For concreteness, in this section we will focus on the four-momentum associated to translations in the gauge theory, which is generated by the set of Killing vector fields $k_\mu = \partial_\mu$.

Let Σ be a spacelike 7-surface in the brane's worldvolume, which we take to be a $t=$ const. surface, and $n = \partial_t/\sqrt{-g_{00}}$ the future-pointing unit normal to Σ. The momenta are then given by

$$P_\mu = \int_\Sigma d^7x\,\sqrt{g_{\rm sp}}\,n^a\,T_{ab}\,k^b_\mu = \int_\Sigma d^7x\,\sqrt{g_{\rm sp}}\,n^a\,T_{a\mu}\,, \tag{B.1}$$

where $g_{\rm sp}$ is the spatial metric on Σ. Since the time-space off-diagonal components of g vanish we have that

$$g^{00} = 1/g_{00}\,, \qquad \sqrt{-g} = \sqrt{-g_{00}}\sqrt{g_{\rm sp}}\,. \tag{B.2}$$

Using these relations P_μ may be rewritten as

$$P_\mu = \int_\Sigma d^7x\,\sqrt{g_{\rm sp}}\,\frac{1}{\sqrt{-g_{00}}}\,T_{0\mu} = -\int_\Sigma d^7x\,\sqrt{-g}\,T^0{}_\mu\,. \tag{B.3}$$

For $\mu = 0$, these formulas give the energy on the brane:

$$E = P_0 = \int_\Sigma d^7x\,\sqrt{g_{\rm sp}}\,\frac{1}{\sqrt{-g_{00}}}\,T_{00} = -\int_\Sigma d^7x\,\sqrt{-g}\,T^0{}_0 \geq 0\,. \tag{B.4}$$

Note that this is non-negative because $T_{00} \geq 0$.[15]

Consider now the brane's worldvolume V as shown in figure 21. Σ_1 and Σ_2 are spacelike hypersurfaces at times t_1 and t_2, respectively, and Σ_∞ is a timelike hypersurface at spatial infinity. Applying Stokes' theorem we then have

$$\int_V \sqrt{-g}\,\nabla^a T_{a\mu} = \int_{\Sigma_2} \sqrt{g_{\rm sp}}\,n^a_{(1)} T_{a\mu} + \int_{\Sigma_1} \sqrt{g_{\rm sp}}\,n^a_{(2)} T_{a\mu} + \int_{\Sigma_\infty} \sqrt{g_{\rm sp}}\,n^a_{(\infty)} T_{a\mu}\,. \tag{B.5}$$

The unit normals must be taken inward-pointing if they are time-like, and outward-

---

[15] For example, in flat space eq. (5.6) gives $T_{00} = E^2/2 + B^2/2 \geq 0$, where $E_i = F_{i0}$, $E^i = F^i{}_0$, $E^2 = E_i E^i$, and $2B^2 = F_{ij}F^{ij}$.

pointing if they are space-like. Therefore we have $n^a_{(1)} = -n^a_{(2)} = n$ and $n^a_{(\infty)} = \tilde{n}$, so eq. (B.5) with $\mu = 0$ yields

$$E_2 - E_1 + F_\infty = -\int_V \sqrt{-g}\,\nabla^a T_{a0}\,, \tag{B.6}$$

where $E_{1,2}$ is the energy contained in $\Sigma_{1,2}$ and $F_\infty = -\int_{\Sigma_\infty} \sqrt{g_{\rm sp}}\,\tilde{n}^a T_{a0}$ is the energy flux that has escaped through Σ_∞ between t_1 and t_2.[16] The left-hand side of eq. (B.6) is the total energy deposited on the brane by the source. Since $\int_V = \int dt d^7x$, if t_1 and t_2 are innitesimally close we obtain

$$\frac{dE}{dt} = -\int d^7x\sqrt{-g}\,\nabla^a T_{a0}\,. \tag{B.7}$$

C High-momentum radial wave functions

As shown (on the left-hand side of) figures 6, 8, and 9, the high-momentum radial profiles of the different modes are concentrated near the tip of the brane ($r = 0$). In this region of high q and small r it is possible to find analytic expressions for the radial profiles [28]. In this appendix we shortly review this computation and extend it to vector modes.

Following [28] we introduce the coordinate z which fulfills

$$\frac{dz}{dr} = \sqrt{\frac{g_{rr}}{-g_{00}}} = \sqrt{\frac{2\tilde{f}(1+\dot{R}^2)}{\rho^4 f^2}}\,. \tag{C.1}$$

In terms of this new coordinate, the different modes $\Psi^\alpha = \{\phi_1, \phi_2, \mathcal{A}, \Phi\}$ satisfy a differential equation of the generic form

$$\partial_z\left[a^\alpha(z)\,\partial_z\Psi^\alpha\right] + a^\alpha(z)\left[\omega^2 - \frac{f^2}{\tilde{f}^2}q^2\right]\Psi^\alpha - b^\alpha(z)\,(m^\alpha)^2\Psi^\alpha = 0\,, \tag{C.2}$$

where $m^\alpha = \{m_{11},\, m_{22}, 0\,, 0\,\}$ and the different coefficient functions are given by

$$\begin{aligned} a^1 = a^2 &= -\sqrt{-g}\,g^{00}\,,\\ a^3 &= -\sqrt{-g}\,g^{00}g^{11}\,,\\ a^4 &= -g_{11}g_{00}/\sqrt{-g}\,,\\ b^1 = b^2 &= \sqrt{-g}\,. \end{aligned} \tag{C.3}$$

Via the simple rescaling $\psi^\alpha = \sqrt{a^\alpha}\,\Psi^\alpha$, the set of eqs. (C.2) can be written in the Schrödinger form

$$-\,\partial_z^2\,\psi^\alpha + V^\alpha\,\psi^\alpha = \omega^2\psi^\alpha\,, \tag{C.4}$$

where the potential is given by

$$V^\alpha(z,q) = q^2\,\frac{f^2}{\tilde{f}^2} + \frac{\partial_z^2\left(\sqrt{a^\alpha}\right)}{\sqrt{a^\alpha}} + \frac{b^\alpha}{a^\alpha}(m^\alpha)^2\,. \tag{C.5}$$

---

[16] The minus sign in the definition of the flux comes from the fact that the energy current in the a-direction is given by $-T_{a0}$, as can be seen from the continuity equation. For example, in flat space in the absence of sources the continuity equation $\partial^a T_{a0} = 0$ yields $\partial_0 T_{00} - \partial_i T_{i0} = 0$.

This potential is a complicated function of z which is only known numerically because it depends non-trivially on the brane embedding. However, since the radial profiles are concentrated near the tip of the brane, we focus on the small-z expansion of the potential (C.5). In the limit $z \to 0$, eq. (C.1) reduces to[17]

$$z = \frac{\sqrt{2(R_0^4+1)}}{R_0^4-1}\, r\,, \tag{C.6}$$

and the small-z potential is given by

$$V^\alpha(z,q) = \left(\frac{3}{4} + \ell^\alpha(\ell^\alpha+2)\right)\frac{1}{z^2} + v_{\rm lim}^2 q^2 + \frac{1}{4} z^2 q^2 \Omega^2\,, \tag{C.7}$$

where $\ell^\alpha = \{0,0,0,1\}$, $v_{\rm lim}$ is the meson limiting velocity (3.11), and

$$\Omega^2 = \frac{16 R_0^2 (R_0^4-1)^2 (1+R_0^8)}{(1+R_0^4)^5}\,. \tag{C.8}$$

As claimed, this potential has a minimum at $z \propto 1/\sqrt{q}$ which means that, at least for the lowest modes, the wave functions are concentrated at small z. Different meson excitations correspond to different states of the four-dimensional harmonic oscillator (C.7). The eigenfunctions and eigenvalues are given by

$$\omega_n^2 = v_{\rm lim}^2 q^2 + q\Omega(2n+2+\ell^\alpha)\,, \tag{C.9}$$

$$\psi_n^\alpha = \mathcal{N}^\alpha z^{\frac{3}{2}+\ell^\alpha} L_n^{(\ell^\alpha+1)}\left(\frac{1}{2}\Omega q z^2\right) \exp\left(-\frac{1}{4}\Omega q z^2\right)\,, \tag{C.10}$$

where $L_n^{\ell+1}$ is the generalized Laguerre polynomial and $\mathcal{N}^\alpha$ are normalization constants determined by the requirements

$$\int dz\, \psi_n^\alpha(z)\, \psi_m^\alpha(z) = \delta_{mn}\,. \tag{C.11}$$

These normalization conditions coincide with those in eqs. (4.9), (4.20) and (4.32).

For future use, we provide explicit expressions for the lowest excitations, which correspond to $n=0$. The normalization constants are given by

$$\mathcal{N}^\alpha = \frac{(q\Omega)^{1+\frac{\ell^\alpha}{2}}}{\sqrt{2}^{1+\ell^\alpha}\sqrt{(1+\ell^\alpha)!}}\,, \tag{C.12}$$

and the radial wave functions take the form

$$\Psi_0^\alpha = \beta^\alpha \mathcal{N}^\alpha z^{4\ell^\alpha} \exp\left(-\frac{1}{4}\Omega q z^2\right)\,, \tag{C.13}$$

---

[17] To derive this expression we have used the small-r expansion of the embedding, $R(r) = R_0 + r^2/\big(R_0(R_0^8-1)\big)$.

where $\beta^\alpha = \lim_{r\to 0} \sqrt{a^\alpha}$:

$$\beta^1 = \beta^2 = \frac{2^{3/2} R_0^3}{\left(R_0^4 - 1\right)^{3/2}} , \tag{C.14}$$

$$\beta^3 = \frac{2R_0^2 \left(1 + R_0^4\right)^{1/2}}{\left(R_0^4 - 1\right)^{3/2}} , \tag{C.15}$$

$$\beta^4 = \frac{\left(R_0^4 - 1\right)^{3/2}}{2R_0^2 \left(1 + R_0^4\right)^{1/2}} . \tag{C.16}$$

D Energy loss at small r_0

As the quark position approaches the tip of the branes, $r_0 \to 0^+$, the maximum velocity of the quark approaches the meson limiting velocity $v_{\rm lim}$ from above. As a consequence, the quark and meson dispersion relations cross at $q_0 \gg T$. In figure 2 this means that the dotted vertical lines move to the right. For a fixed r_0 the smallest value of the crossing point, $q_0^{\rm min}$, is attained at the maximal velocity of the quark, $v_{\rm max}$. Using the high-momentum dispersion relation (C.9), the crossing momentum at an arbitrary quark velocity v is determined by the condition

$$v_{\rm lim} q_0 + \left(1 + n + \frac{\ell^\alpha}{2}\right) \frac{\Omega}{v_{\rm lim}} = v q_0 , \tag{D.1}$$

which leads to

$$q_0 = \left(1 + n + \frac{\ell^\alpha}{2}\right) \frac{\Omega}{v_{\rm lim}} \frac{1}{v - v_{\rm lim}} . \tag{D.2}$$

The maximal velocity for a quark at r_0 is

$$v_{\rm max}(z_0) = \sqrt{-\frac{g_{00}}{g_{ii}}}\Bigg|_{r_0} \approx v_{\rm lim} + z_0^2 \frac{\Omega^2}{8 v_{\rm lim}} , \tag{D.3}$$

where we have expanded to leading order in r_0 and used the definition (C.6) of z. Substituting this value of v in eq. (D.2) we find that the minimum crossing point is

$$q_0^{\rm min} = \left(1 + n + \frac{\ell^\alpha}{2}\right) \frac{8}{\Omega z_0^2} . \tag{D.4}$$

Thus, the energy loss can be reliably computed with the approximate solutions of appendix C. Since the energy-loss formulas are different for each mode, we will address them separately. Furthermore, we will focus on the lowest state of each mode.

D.1 Scalar mesons

Since in the high-momentum, small-r region both scalar modes have the same radial profile, the energy loss into scalar mesons in this limit will also be the same. Expanding the energy loss formula (5.57) and using the radial profiles (C.13) we obtain

$$\frac{dE_{\rm scalar}}{dt} = \frac{e^2}{2\Omega_3} \left[\frac{v_{\rm max}^2(z_0) - v^2}{v}\right] \left[\frac{1 + R_0^4}{2R_0^2}\right] \left(\beta^1\right)^2 \frac{\Omega^2}{2} \int_{q_0^{\rm min}}^{\infty} \frac{dq}{2\pi} q^3 \exp\left(-\frac{1}{2}\Omega q z_0^2\right) . \tag{D.5}$$

After integration, this yields

$$\frac{dE_{\text{scalar}}}{dt} = \frac{e^2}{4\pi\Omega_3}\frac{\left(1+R_0^4\right)^2\left(\beta^1\right)^2}{2R_0^2}\left[\frac{v_{\max}^2(z_0)-v^2}{v}\right]\times \\ \left[\frac{48+24\Omega q_0^{\min}z_0^2+6\Omega^2(q_0^{\min})^2z_0^4+\Omega^3(q_0^{\min})^3z_0^6}{\Omega^2z_0^8}\right]\exp\left(-\frac{1}{2}\Omega q_0^{\min}z_0^2\right). \tag{D.6}$$

As expected on general grounds, and in agreement with figures 13 and 14, we see that the energy loss vanishes both for $v \to v_{\max}$ and for $v \to v_{\lim}$. The former is due to the fact that the factor (5.49) vanishes in this limit. The latter is implemented by the fact that $q_0^{\min}$ diverges as $v \to v_{\lim}$, which in turn is a manifestation of the Heaviside theta function in eq. (5.57). As reflected in figures 13 and 14, the maximum energy loss occurs at some intermediate velocity such that $v_{\lim} < v_{\text{int}} < v_{\max}$. Although v_{int} is not easy to compute, we know that $v_{\max} - v_{\lim} \propto z_0^2$. It then follows that also $v_{\max} - v_{\text{int}} \propto z_0^2$ and therefore that the maximum energy loss diverges as $1/z_0^6$.

D.2 Transverse vector mesons

The energy lost into these modes is given by eq. (5.23) which, utilizing (C.13), leads to

$$\frac{dE_{\text{trans}}}{dt} = \frac{e^2v}{2\Omega_3}\left(\beta^3\right)^2\frac{\Omega^2}{2}\int_{q_0^{\min}}^{\infty}\frac{dq}{2\pi}q^3\exp\left(-\frac{1}{2}\Omega q z_0^2\right)\left(1-\frac{v_{\lim}^2}{v^2}-\frac{2\Omega}{qv^2}\right). \tag{D.7}$$

Unlike for scalar meson emission, it is easy to see that in this case the energy loss is a monotonically growing function of the velocity. Thus, the maximum value of the energy loss is attained for $v = v_{\max}$ and, to leading order in z_0, it is given by

$$\frac{dE_{\text{trans}}}{dt} = \frac{e^2}{4\pi\Omega_3}\left(\beta^3\right)^2\frac{76\,\exp(-4)}{v_{\lim}z_0^6}. \tag{D.8}$$

This shows the same divergence for small r_0 as in the case of scalar modes.

D.3 Longitudinal vector mesons

Inserting (C.13) into the expression for energy loss (5.40), and to leading order in z_0 we obtain

$$\frac{dE_{\text{long}}}{dt} = \frac{e^2}{2\Omega_3}\frac{2\Omega^3}{v}\frac{1}{(\beta^4)^2}\int_{q_0^{\min}}^{\infty}\frac{dq}{2\pi}q^2\left(1-\frac{1}{8}\Omega q z_0^2\right)^2\exp\left(-\frac{1}{2}\Omega q z_0^2\right). \tag{D.9}$$

As in the transverse vector case, the maximum energy loss is attained at $v = v_{\max}$. Using (D.4) and setting $\ell^\alpha = 1$ (see the definition below eq. (C.7)) the maximum energy loss is

$$\frac{dE_{\text{long}}}{dt} = \frac{e^2}{4\pi\Omega_3}\frac{1}{(\beta^4)^2}\frac{632\exp(-6)}{v_{\lim}\,z_0^6}. \tag{D.10}$$

Again, this diverges with the same power of z_0 as in the cases of transverse and scalar modes. Note also that since $\beta^4 = 1/\beta^3$ and the numerical factors in eqs. (D.10) and (D.8) are similar, we find that in this limit the energy lost into transverse and longitudinal vector modes is comparable.

Finally, we may comment on the mass dependence of the energy lost into vector mesons. The maximal energy loss is proportional to

$$\left.\frac{dE}{dt}\right|_{\text{max}} \propto \frac{R_0^4\left(R_0^4-1\right)^2}{\left(R_0^4+1\right)}\frac{1}{r_0^6}\,. \tag{D.11}$$

The fact that this is a growing function of R_0 means that the energy loss increases if the quark mass is increased while keeping all other parameters such as r_0, v, etc. fixed. However, this should not be necessarily taken as an indication that Cherenkov energy loss in a real HIC experiment increases as the quark mass increases, because the 'preferred' or 'mean' values of these parameters with which a quark is produced may themselves depend on the quark mass.

E Low-temperature limit

As $T \to 0$ with all other scales fixed, the redshift at the bottom of the branes decreases, and so the limiting velocity of mesons, v_{lim}, approaches unity. In turn, this means that the momentum $q_0(T)$ at which Cherenkov radiation turns on diverges as $T \to 0$, much in the same way as in the case $r_0 \to 0$ studied above. The purpose of this section is to estimate $q_0(T)$ in the low-temperature limit. As we will see, the product $q_0(T)\,T^2$ remains finite as $T \to 0$, which makes this limit harder to study than the $r_0 \to 0$ limit.

As $T \to 0$ with fixed quark mass, the parameter $m \propto M_{\text{q}}/T$ controlling the asymptotic position of the branes, $R(r \to \infty) = m$, diverges. For this reason it is convenient to introduce rescaled coordinates

$$\hat{x}^\mu = \frac{x^\mu}{\sqrt{\epsilon}}\,, \qquad \{\hat{r}, \hat{R}, \hat{\rho}\} = \sqrt{\epsilon}\{r, R, \rho\}\,, \tag{E.1}$$

where $\epsilon \equiv 1/m^2$ and we are interested in the limit $\epsilon \to 0$. The rescaling of the x-coordinates is chosen so that the induced metric on the D7-brane takes the same form as that in (3.6), i.e. $ds^2 = L^2 ds^2(g)$ with

$$ds^2(g) = \frac{\hat{\rho}^2}{2}\left[-\frac{f^2}{\tilde{f}}d\hat{t}^2 + \tilde{f}\,d\hat{\vec{x}}^2\right] + \frac{(1+\dot{\hat{R}}^2)}{\hat{\rho}^2}d\hat{r}^2 + \frac{\hat{r}^2}{\hat{\rho}^2}d\Omega_3^2\,, \tag{E.2}$$

where now

$$f(\hat{\rho}) = 1 - \frac{\epsilon^2}{\hat{\rho}^4}\,, \qquad \tilde{f}(\hat{\rho}) = 1 + \frac{\epsilon^2}{\hat{\rho}^4}\,. \tag{E.3}$$

In this new set of coordinates the horizon is located at $\hat{\rho}_{\text{hor}} = \sqrt{\epsilon}$, whereas $\hat{R}(\hat{r} \to \infty) = 1$. In fact, in the limit $\epsilon \to 0$ the gravitational pull of the black hole becomes very small and the brane bends very little. Inserting the ansatz $\hat{R}(\hat{r}) = 1 + \delta\hat{R}(\hat{r})$ in eq. (3.7) and linearizing in $\delta\hat{R}$ one finds that $\delta\hat{R} = \mathcal{O}(\epsilon^4)$. Since we will work to order ϵ^2 we will neglect this correction. Furthermore, it is easy to see that the equations of motion for the transverse (4.6), longitudinal (4.18) and scalar (4.30) modes are unmodified by the rescaling (E.1) provided we rescale the momentum in a consistent way, i.e. $\{\hat{\omega}, \hat{q}\} = \sqrt{\epsilon}\{\omega, q\}$, so that we leave the product $(\omega t - \vec{q}\cdot\vec{x})$ invariant. For ease of notation, in the following we will omit the hat symbol.

Following appendix C, eqs. (4.6), (4.18) and (4.30) can be rewritten in the Schrödinger form (C.4). The potential (C.5) is in general a complicated function, but it simplifies in the limit $\epsilon \to 0$. Indeed, in this case eq. (C.1) can be integrated explicitly with the result

$$z(r) = \sqrt{2}\arctan r + \frac{3}{8\sqrt{2}}\left(3\arctan r + \frac{r(5+3r^2)}{(1+r^2)^2}\right)\epsilon^2 + \mathcal{O}(\epsilon^4)\,, \tag{E.4}$$

so that $z_{\max} \equiv z(r\to\infty) \simeq \pi/\sqrt{2}$. The potential can then be written as

$$V^\alpha(z,q) = V_1(z)q^2 + V_2^\alpha(z)\,, \tag{E.5}$$

where

$$V_1(z) = 1 - 4\cos^4\left(\frac{z}{\sqrt{2}}\right)\epsilon^2 + g(z)\epsilon^4 + \mathcal{O}(\epsilon^6)\,, \tag{E.6}$$

$$V_2^\alpha(z) = \frac{\mathrm{A}^\alpha\cos^2\left(\sqrt{2}z\right) + \mathrm{B}^\alpha\cos\left(\sqrt{2}z\right) + \mathrm{C}^\alpha}{2\sin^2\left(\sqrt{2}z\right)} + \frac{(m^\alpha)^2}{1+\cos\left(\sqrt{2}z\right)} + h(z)\epsilon^2 + \mathcal{O}(\epsilon^4)\,, \tag{E.7}$$

with $\mathrm{A}^\alpha = \{0,0,1,1\}$, $\mathrm{B}^\alpha = \{-6,-6,0,8\}$ and $\mathrm{C}^\alpha = \{9,9,2,6\}$. The functions $g(z)$ and $h(z)$ are smooth and bound, and their explicit form will not be needed.

Before proceeding further let us clarify one point. In the limit $z \to z_{\max}$, $V_2^4(z)$ shows a negative divergence. This is related to the fact that the radial profile $\Psi^4(r) = \Phi(r)$ does not vanish near the boundary. This may seem counterintuitive, since generically one expects a 'confining' potential near the boundary (the AdS 'box') which is partly responsible for the discreteness of the spectrum. However, note that the physical electric field E is related to Φ through eq. (4.16), which may be written as $E = a^4(z)\partial_z\Phi$. In the limit $r\to\infty$, the factor $f^2/\tilde{f}^2$ in eq. (C.2) approaches 1, so one can differentiate this equation with $\alpha = 4$ and use the fact that $a^4(z) = 1/a^3(z)$ to show that the asymptotic form of the equation for E is identical to that for the transverse mode $\Psi^3 = \mathcal{A}$.

Let us now return to the potential (E.5). As explained above, we are interested in the limit $\epsilon \to 0$ and $q \geq q_0(\epsilon) \to \infty$. In particular, we wish to determine whether in this limit the product ϵq_0 goes to zero, remains finite, or diverges. We will establish that the product remains finite by showing that the other two possibilities lead to a contradiction.

Consider first the possibility that $\epsilon q_0 \to \infty$ as $\epsilon \to 0$. Then the potential takes the form

$$V^\alpha(z,q) - q^2 \simeq \frac{\mathrm{A}^\alpha\cos^2\left(\sqrt{2}z\right) + \mathrm{B}^\alpha\cos\left(\sqrt{2}z\right) + \mathrm{C}^\alpha}{2\sin^2\left(\sqrt{2}z\right)} + \frac{(m^\alpha)^2}{1+\cos\left(\sqrt{2}z\right)} - 4\cos^4\left(\frac{z}{\sqrt{2}}\right)\epsilon^2 q^2\,, \tag{E.8}$$

where the last term dominates everywhere except near the endpoints $z = 0$ and $z_{\max}$, at which the order-one part of the potential, given by the first two terms on the right-hand side, diverges. As an illustration, figure 22 shows the potential for the $\alpha = 3$ - mode for several values of ϵq. We see that the potential develops a minimum at a small value of z as ϵq becomes large. This allows us to consider an expansion for small z in order to obtain

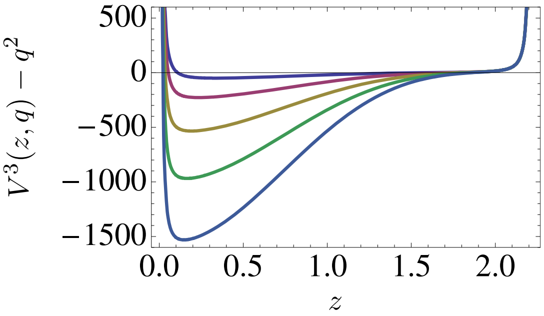

Figure 22. Potential for $\alpha = 3$, in the limit $\epsilon \to 0$, $q \to \infty$ and ϵq fixed. From top to bottom the curves correspond to $\epsilon q = 4, 8, 12, 16, 20$.

the energy levels associated to the potential. In this way we reproduce the result (C.9), approximated for $\epsilon \to 0$. For example, in the case $\alpha = 3$ and $n = 0$ the dispersion relation takes the form:

$$\omega(q) = \left(1 - 2\epsilon^2\right) q + \frac{2}{\sqrt{5}q}\sqrt{1 + 20q^2\epsilon^2} + \mathcal{O}(\epsilon^2)\,. \tag{E.9}$$

The value of q_0 is determined by the condition $\omega(q_0) = vq_0$, where v is the quark velocity, which depends on the quark position through

$$v(r_0) = 1 - \frac{2\epsilon^2}{\rho_0^4} + \mathcal{O}(\epsilon^4)\,. \tag{E.10}$$

The result is

$$\epsilon q_0 = \left[-10 + \sqrt{5}\frac{\sqrt{20 + r_0^2(2 + r_0^2)\left(40 + 21r_0^2(2 + r_0^2)\right)}}{(1 + r_0^2)^2}\right]^{-1/2}\,. \tag{E.11}$$

This expression is not parametrically large for any value of r_0 except in the limit $r_0 \to 0$, which was considered above and is unrelated to the zero-temperature limit under consideration here. In particular, for small r_0 eq. (E.11) yields $\epsilon q_0 = 1/{r_0}^2 + 3/2 + \mathcal{O}(r_0^2)$, whereas for large r_0 one finds $\epsilon q_0 = 2.01 + 1.99/r_0^4 + \mathcal{O}(1/r_0^6)$. We therefore conclude that $\epsilon q_0(\epsilon)$ remains finite as $\epsilon \to 0$, in contradiction with our initial assumption that $\epsilon q_0(\epsilon) \to \infty$ in this limit.

Consider now the opposite possibility, i.e. that $\epsilon q_0 \to 0$ as $\epsilon \to 0$. In this case the last term in the potential (E.8) is small and the energy levels can be determined using perturbation theory with the result

$$\omega_n^2(q) = q^2 + \lambda_n - w_n\epsilon^2 q^2 + \mathcal{O}(\epsilon^4 q^4)\,. \tag{E.12}$$

Here, λ_n are the eigenvalues of the problem in the absence of the perturbation, and $-\omega_n$ is the (negative) first-order correction given by the expectation value of the perturbation in the n-th eigenstate, $\langle n| -4\cos^4(z/\sqrt{2})|n\rangle$. The key point is that λ_n and w_n are independent of ϵ and q. In order to find the crossing point, we need to solve $\omega_n^2(q_0) = v^2 q_0^2$. Since the minimum possible value of q_0 corresponds to the maximum quark velocity, $v = 1$, we find

$$\epsilon q_0 \simeq \sqrt{\frac{\lambda_n}{w_n}} \,, \tag{E.13}$$

which is in contradiction with our initial assumption that $\epsilon q_0 \to 0$.

We therefore conclude that the combination

$$\epsilon \hat{q} = \epsilon \sqrt{\epsilon} q = \frac{1}{m^3} \frac{\tilde{q}}{\pi T} = \left(\frac{\sqrt{\lambda} T}{2 M_{\rm q}} \right)^3 \frac{\tilde{q}}{\pi T} = \left(\frac{2\pi T}{M_{\rm mes}} \right)^3 \frac{\tilde{q}}{\pi T} \tag{E.14}$$

remains finite in the limit $T \to 0$, where we have reinstated the hat and we recall that $\tilde{q}$ is the physical, dimensionful momentum. We see that in this limit $\tilde{q}(T)\, T^2 \sim M_{\rm q}^3 / \lambda^{3/2} \sim M_{\rm mes}^3$, which remains finite in the low-temperature limit, as we anticipated. This means that the relevant potential in this limit is (E.8), where all terms are of the same order. This makes the problem harder than that associated to the limit $r_0 \to 0$, and we have been unable to find analytic expressions for the corresponding eigenfunctions and eigenvalues.

References

[1] J. Casalderrey-Solana, D. Fernández and D. Mateos, *A New Mechanism of Quark Energy Loss*, *Phys. Rev. Lett.* **104** (2010) 172301 [`arXiv:0912.3717`] [SPIRES].

[2] N. Armesto, (ed.) et al., *Heavy Ion Collisions at the LHC — Last Call for Predictions*, *J. Phys.* **G 35** (2008) 054001 [`arXiv:0711.0974`] [SPIRES].

[3] M. Gyulassy, I. Vitev, X.-N. Wang and B.-W. Zhang, *Jet quenching and radiative energy loss in dense nuclear matter*, `nucl-th/0302077` [SPIRES].

[4] A. Kovner and U.A. Wiedemann, *Gluon radiation and parton energy loss*, `hep-ph/0304151` [SPIRES].

[5] J. Casalderrey-Solana and C.A. Salgado, *Introductory lectures on jet quenching in heavy ion collisions*, *Acta Phys. Polon.* **B 38** (2007) 3731 [`arXiv:0712.3443`] [SPIRES].

[6] C.P. Herzog, A. Karch, P. Kovtun, C. Kozcaz and L.G. Yaffe, *Energy loss of a heavy quark moving through $N = 4$ supersymmetric Yang-Mills plasma*, *JHEP* **07** (2006) 013 [`hep-th/0605158`] [SPIRES].

[7] H. Liu, K. Rajagopal and U.A. Wiedemann, *Calculating the jet quenching parameter from AdS/CFT*, *Phys. Rev. Lett.* **97** (2006) 182301 [`hep-ph/0605178`] [SPIRES].

[8] S.S. Gubser, *Drag force in AdS/CFT*, *Phys. Rev.* **D 74** (2006) 126005 [`hep-th/0605182`] [SPIRES].

[9] J. Casalderrey-Solana and D. Teaney, *Heavy quark diffusion in strongly coupled $\mathcal{N} = 4$ Yang-Mills*, *Phys. Rev.* **D 74** (2006) 085012 [`hep-ph/0605199`] [SPIRES].

[10] M. Chernicoff and A. Guijosa, *Acceleration, Energy Loss and Screening in Strongly-Coupled Gauge Theories*, *JHEP* **06** (2008) 005 [`arXiv:0803.3070`] [SPIRES].

[11] STAR collaboration, J. Adams et al., *Experimental and theoretical challenges in the search for the quark gluon plasma: The STAR collaboration's critical assessment of the evidence from RHIC collisions*, *Nucl. Phys.* **A 757** (2005) 102 [`nucl-ex/0501009`] [SPIRES].

[12] PHENIX collaboration, K. Adcox et al., *Formation of dense partonic matter in relativistic nucleus nucleus collisions at RHIC: Experimental evaluation by the PHENIX collaboration*, *Nucl. Phys.* **A 757** (2005) 184 [`nucl-ex/0410003`] [SPIRES].

[13] E. Shuryak, *Why does the quark gluon plasma at RHIC behave as a nearly ideal fluid?*, *Prog. Part. Nucl. Phys.* **53** (2004) 273 [`hep-ph/0312227`] [SPIRES].

[14] E.V. Shuryak, *What RHIC experiments and theory tell us about properties of quark-gluon plasma?*, *Nucl. Phys.* **A 750** (2005) 64 [`hep-ph/0405066`] [SPIRES].

[15] E. Witten, *Anti-de Sitter space, thermal phase transition and confinement in gauge theories*, *Adv. Theor. Math. Phys.* **2** (1998) 505 [`hep-th/9803131`] [SPIRES].

[16] A. Karch and L. Randall, *Open and closed string interpretation of SUSY CFT's on branes with boundaries*, *JHEP* **06** (2001) 063 [`hep-th/0105132`] [SPIRES].

[17] A. Karch and E. Katz, *Adding flavor to AdS/CFT*, *JHEP* **06** (2002) 043 [`hep-th/0205236`] [SPIRES].

[18] D. Mateos, R.C. Myers and R.M. Thomson, *Holographic phase transitions with fundamental matter*, *Phys. Rev. Lett.* **97** (2006) 091601 [`hep-th/0605046`] [SPIRES].

[19] D. Mateos, R.C. Myers and R.M. Thomson, *Thermodynamics of the brane*, *JHEP* **05** (2007) 067 [`hep-th/0701132`] [SPIRES].

[20] J. Babington, J. Erdmenger, N.J. Evans, Z. Guralnik and I. Kirsch, *Chiral symmetry breaking and pions in non-supersymmetric gauge/gravity duals*, *Phys. Rev.* **D 69** (2004) 066007 [`hep-th/0306018`] [SPIRES].

[21] I. Kirsch, *Generalizations of the AdS/CFT correspondence*, *Fortsch. Phys.* **52** (2004) 727 [`hep-th/0406274`] [SPIRES].

[22] M. Kruczenski, D. Mateos, R.C. Myers and D.J. Winters, *Towards a holographic dual of large-N_c QCD*, *JHEP* **05** (2004) 041 [`hep-th/0311270`] [SPIRES].

[23] O. Aharony, J. Sonnenschein and S. Yankielowicz, *A holographic model of deconfinement and chiral symmetry restoration*, *Annals Phys.* **322** (2007) 1420 [`hep-th/0604161`] [SPIRES].

[24] A. Parnachev and D.A. Sahakyan, *Chiral phase transition from string theory*, *Phys. Rev. Lett.* **97** (2006) 111601 [`hep-th/0604173`] [SPIRES].

[25] A. Bazavov, P. Petreczky and A. Velytsky, *Quarkonium at Finite Temperature*, `arXiv:0904.1748` [SPIRES].

[26] J.L. Hovdebo, M. Kruczenski, D. Mateos, R.C. Myers and D.J. Winters, *Holographic mesons: Adding flavor to the AdS/CFT duality*, *Int. J. Mod. Phys.* **A 20** (2005) 3428 [SPIRES].

[27] C. Hoyos-Badajoz, K. Landsteiner and S. Montero, *Holographic Meson Melting*, *JHEP* **04** (2007) 031 [`hep-th/0612169`] [SPIRES].

[28] Q.J. Ejaz, T. Faulkner, H. Liu, K. Rajagopal and U.A. Wiedemann, *A limiting velocity for quarkonium propagation in a strongly coupled plasma via AdS/CFT*, *JHEP* **04** (2008) 089 [`arXiv:0712.0590`] [SPIRES].

[29] M. Kruczenski, D. Mateos, R.C. Myers and D.J. Winters, *Meson spectroscopy in AdS/CFT with flavour*, *JHEP* **07** (2003) 049 [`hep-th/0304032`] [SPIRES].

[30] S. Kobayashi and K. Nomizu, *Foundations of Differential Geometry*, Volume I, Chapter 3, Wiley-Interscience (1963).

[31] C.G. Callan and J.M. Maldacena, *Brane dynamics from the Born-Infeld action*, *Nucl. Phys.* **B 513** (1998) 198 [`hep-th/9708147`] [SPIRES].

[32] G.W. Gibbons, *Born-Infeld particles and Dirichlet p-branes*, *Nucl. Phys.* **B 514** (1998) 603 [`hep-th/9709027`] [SPIRES].

[33] P.M. Chesler, K. Jensen, A. Karch and L.G. Yaffe, *Light quark energy loss in strongly-coupled* $N = 4$ *supersymmetric Yang-Mills plasma*, *Phys. Rev.* **D 79** (2009) 125015 [`arXiv:0810.1985`] [SPIRES].

[34] T. Matsui and H. Satz, *J/psi Suppression by Quark-Gluon Plasma Formation*, *Phys. Lett.* **B 178** (1986) 416 [SPIRES].

[35] O. Kaczmarek, F. Karsch, F. Zantow and P. Petreczky, *Static quark anti-quark free energy and the running coupling at finite temperature*, *Phys. Rev.* **D 70** (2004) 074505 [*Erratum ibid.* **D 72** (2005) 059903] [`hep-lat/0406036`] [SPIRES].

[36] P. Petreczky and K. Petrov, *Free energy of a static quark anti-quark pair and the renormalized Polyakov loop in three flavor QCD*, *Phys. Rev.* **D 70** (2004) 054503 [`hep-lat/0405009`] [SPIRES].

[37] O. Kaczmarek and F. Zantow, *Static quark anti-quark interactions in zero and finite temperature QCD. I: Heavy quark free energies, running coupling and quarkonium binding*, *Phys. Rev.* **D 71** (2005) 114510 [`hep-lat/0503017`] [SPIRES].

[38] A. Mócsy and P. Petreczky, *Can quarkonia survive deconfinement?*, *Phys. Rev.* **D 77** (2008) 014501 [`arXiv:0705.2559`] [SPIRES].

[39] A. Mócsy , *Potential Models for Quarkonia*, *Eur. Phys. J.* **C 61** (2009) 705 [`arXiv:0811.0337`] [SPIRES].

[40] M. Asakawa and T. Hatsuda, *J/ψ and η/c in the deconfined plasma from lattice QCD*, *Phys. Rev. Lett.* **92** (2004) 012001 [`hep-lat/0308034`] [SPIRES].

[41] S. Datta, F. Karsch, P. Petreczky and I. Wetzorke, *Behavior of charmonium systems after deconfinement*, *Phys. Rev.* **D 69** (2004) 094507 [`hep-lat/0312037`] [SPIRES].

[42] T. Hatsuda, *Hadrons above T_c*, *Int. J. Mod. Phys.* **A 21** (2006) 688 [`hep-ph/0509306`] [SPIRES].

[43] F. Karsch, D. Kharzeev and H. Satz, *Sequential charmonium dissociation*, *Phys. Lett.* **B 637** (2006) 75 [`hep-ph/0512239`] [SPIRES].

[44] H. Satz, *Quarkonium Binding and Dissociation: The Spectral Analysis of the QGP*, *Nucl. Phys.* **A 783** (2007) 249 [`hep-ph/0609197`] [SPIRES].

[45] M. Asakawa, T. Hatsuda and Y. Nakahara, *Hadronic spectral functions above the QCD phase transition*, *Nucl. Phys.* **A 715** (2003) 863 [*Nucl. Phys. Proc. Suppl.* **119** (2003) 481] [`hep-lat/0208059`] [SPIRES].

[46] E.V. Shuryak and I. Zahed, *Towards a theory of binary bound states in the quark gluon plasma*, *Phys. Rev.* **D 70** (2004) 054507 [`hep-ph/0403127`] [SPIRES].

[47] M.C. Chu and T. Matsui, *Dynamic Debye screening for a heavy quark-antiquark pair traversing a quark-gluon plasma*, *Phys. Rev.* **D 39** (1989) 1892 [SPIRES].

[48] K. Peeters, J. Sonnenschein and M. Zamaklar, *Holographic melting and related properties of mesons in a quark gluon plasma*, *Phys. Rev.* **D 74** (2006) 106008 [`hep-th/0606195`] [SPIRES].

[49] H. Liu, K. Rajagopal and U.A. Wiedemann, *An AdS/CFT calculation of screening in a hot wind*, *Phys. Rev. Lett.* **98** (2007) 182301 [`hep-ph/0607062`] [SPIRES].

[50] M. Chernicoff, J.A. Garcia and A. Guijosa, *The energy of a moving quark-antiquark pair in an $N = 4$ SYM plasma*, *JHEP* **09** (2006) 068 [`hep-th/0607089`] [SPIRES].

[51] Q.J. Ejaz, T. Faulkner, H. Liu, K. Rajagopal and U.A. Wiedemann, *A limiting velocity for quarkonium propagation in a strongly coupled plasma via AdS/CFT*, *JHEP* **04** (2008) 089 [`arXiv:0712.0590`] [SPIRES].

[52] J. Casalderrey-Solana and D. Mateos, *Prediction of a Photon Peak in Relativistic Heavy Ion Collisions*, *Phys. Rev. Lett.* **102** (2009) 192302 [`arXiv:0806.4172`] [SPIRES].

[53] E. Iancu and A.H. Mueller, *Light-like mesons and deep inelastic scattering in finite-temperature AdS/CFT with flavor*, *JHEP* **02** (2010) 023 [`arXiv:0912.2238`] [SPIRES].

[54] J. Casalderrey-Solana, E.V. Shuryak and D. Teaney, *Conical flow induced by quenched QCD jets*, *J. Phys. Conf. Ser.* **27** (2005) 22 [`hep-ph/0411315`] [SPIRES].

[55] A. Mócsy and P. Petreczky, *Can quarkonia survive deconfinement?*, *Phys. Rev.* **D 77** (2008) 014501 [`arXiv:0705.2559`] [SPIRES].

[56] J. Liao and E. Shuryak, *Angular Dependence of Jet Quenching Indicates Its Strong Enhancement Near the QCD Phase Transition*, *Phys. Rev. Lett.* **102** (2009) 202302 [`arXiv:0810.4116`] [SPIRES].

[57] PHENIX collaboration, S.S. Adler et al., *Detailed study of high-p_T neutral pion suppression and azimuthal anisotropy in Au + Au collisions at $\sqrt{s_{NN}} = 200\,GeV$*, *Phys. Rev.* **C 76** (2007) 034904 [`nucl-ex/0611007`] [SPIRES].

[58] STAR collaboration, J. Adams et al., *Azimuthal anisotropy and correlations at large transverse momenta in p + p and Au + Au collisions at $\sqrt{s_{NN}} = 200\,GeV$*, *Phys. Rev. Lett.* **93** (2004) 252301 [`nucl-ex/0407007`] [SPIRES].

[59] W.W. Wada, *Cerenkov Radiation Effect in Meson Theory*, *Phys. Rev.* **75** (1949) 981 [SPIRES].

[60] D.D. Ivanenko and V.A. Gurgenidze, *Radiation of the Superlight Type on the Passage of Charged Particles through Ferromagnetics*, *DAN SSSR* **67** (1949) 997.

[61] D.I. Blokhintsev and V.L. Indenbom, *Cherenkov's effect for the meson field*, *ZhETF* **20** (1950) 1123.

[62] G. Yekutieli, *On the radiation of mesons with a constant transverse momentum P_T in cosmic ray jets*, *Nuovo Cim.* **13** (1959) 446, 1306.

[63] W. Czyz, T. Ericson and S.L. Glashow, *A new model for multiple meson production at high energies*, *Nucl. Phys.* **13** (1959) 516.

[64] W. Czyz, S.L. Glashow, *Multiple production of mesons in pion-nucleon collisions*, *Nucl. Phys.* **20** (1960) 309.

[65] P. Smrz, *On mesonic Čerenkov radiation*, *Nucl. Phys.* **35** (1962) 165.

[66] D.B. Ion, *Mesonic Cerenkov-like Effect as Possible Mechanism of Meson Production in Hadronic Interactions*, DSc Thesis, Bucharest University (1971).

[67] D.B. Ion, *The classical theory of mesonic Cerenkov radiation in nuclear media*, *St. Cerc. Fiz.* **22** (1970) 125.

[68] D.B. Ion and F.G. Nichitiu, *A possible Cherenkov mechanism for single-pion production in hadron hadron interactions at high energies*, *Nucl. Phys.* **B 29** (1971) 547 [SPIRES].

[69] D.F. Zaretskii and V.V. Lomonosov, *Coherent production of pions in collisions of relativistic nucleons with nuclei*, *Sov. J. Nucl. Phys.* **26** (1977) 639.

[70] I.M. Dremin, *Coherent hadron radiation at ultrahigh-energies*, *JETP Lett.* **30** (1979) 140 [SPIRES].

[71] I.M. Dremin, *Coherent hadroproduction*, *Sov. J. Nucl. Phys.* **33** (1981) 726 [*Yad. Fiz.* **33** (1981) 1357] [SPIRES].

[72] V. Koch, A. Majumder and X.-N. Wang, *Cherenkov Radiation from Jets in Heavy-ion Collisions*, *Phys. Rev. Lett.* **96** (2006) 172302 [`nucl-th/0507063`] [SPIRES].

[73] I.M. Dremin, *Ring-like events: Cherenkov gluons or Mach waves?*, *Nucl. Phys.* **A 767** (2006) 233 [`hep-ph/0507167`] [SPIRES].

[74] T. Faulkner and H. Liu, *Meson widths from string worldsheet instantons*, *Phys. Lett.* **B 673** (2009) 161 [`arXiv:0807.0063`] [SPIRES].

[75] K. Peeters, J. Sonnenschein and M. Zamaklar, *Holographic decays of large-spin mesons*, *JHEP* **02** (2006) 009 [`hep-th/0511044`] [SPIRES].

[76] A.L. Cotrone, L. Martucci and W. Troost, *String splitting and strong coupling meson decay*, *Phys. Rev. Lett.* **96** (2006) 141601 [`hep-th/0511045`] [SPIRES].

Chapter 3

A study of anisotropy in strongly coupled plasmas

3.1 Drag force on a massive quark

This section contains the publication:

- M. Chernicoff, D. Fernandez, D. Mateos and D. Trancanelli, “Drag force in a strongly coupled anisotropic plasma,”

  JHEP **1208** (2012) 100, `arXiv:1202.3696 [hep-th]`.

Published for SISSA by Springer

Received: *July 17, 2012*
Accepted: *July 31, 2012*
Published: *August 21, 2012*

Drag force in a strongly coupled anisotropic plasma

Mariano Chernicoff,[a,b] **Daniel Fernández,**[a] **David Mateos**[a,c] **and Diego Trancanelli**[d,e]

[a] *Departament de Física Fonamental & Institut de Ciències del Cosmos (ICC),*
Universitat de Barcelona (UB),
Martí i Franquès 1, E-08028 Barcelona, Spain
[b] *Department of Applied Mathematics and Theoretical Physics, Centre for Mathematical Sciences,*
Wilberforce Road, Cambridge, CB3 0WA, U.K.
[c] *Institució Catalana de Recerca i Estudis Avançats (ICREA),*
Passeig Lluís Companys 23, E-08010, Barcelona, Spain
[d] *Department of Physics, University of Wisconsin,*
Madison, WI 53706, U.S.A.
[e] *Instituto de Física, Universidade de São Paulo,*
05314-970 São Paulo, Brazil

E-mail: `M.Chernicoff@damtp.cam.ac.uk`, `daniel@ffn.ub.edu`, `dmateos@icrea.cat`, `dtrancan@fma.if.usp.br`

Abstract: We calculate the drag force experienced by an infinitely massive quark propagating at constant velocity through an anisotropic, strongly coupled $\mathcal{N} = 4$ plasma by means of its gravity dual. We find that the gluon cloud trailing behind the quark is generally misaligned with the quark velocity, and that the latter is also misaligned with the force. The drag coefficient μ can be larger or smaller than the corresponding isotropic value depending on the velocity and the direction of motion. In the ultra-relativistic limit we find that generically $\mu \propto p$. We discuss the conditions under which this behaviour may extend to more general situations.

Keywords: Gauge-gravity correspondence, Holography and quark-gluon plasmas

ArXiv ePrint: 1202.3696

doi:10.1007/JHEP08(2012)100

Contents

1 Introduction

A remarkable conclusion from the experiments at the Relativistic Heavy Ion Collider (RHIC) [1, 2] and at the Large Hadron Collider (LHC) (see the contributions on elliptic flow at the LHC in [3]) is that the quark-gluon plasma (QGP) does not behave as a weakly coupled gas of quarks and gluons, but rather as a strongly coupled fluid [4, 5]. This renders perturbative methods inapplicable in general. The lattice formulation of Quantum Chromodynamics (QCD) is also of limited utility, since for example it is not well suited for studying real-time phenomena. This has provided a strong motivation for understanding the dynamics of strongly coupled non-Abelian plasmas through the gauge/string duality [6–8] (see [9] for a recent review of applications to the QGP).

For a period of time $\tau_{\rm out}$ immediately after the collision, the system thus created is far from equilibrium. After a time $\tau_{\rm iso} > \tau_{\rm out}$ the system becomes locally isotropic and a standard hydrodynamic description becomes applicable. It has been proposed than an intrinsically anisotropic hydrodynamical description can be used to describe the system at intermediate times $\tau_{\rm out} < \tau < \tau_{\rm iso}$ [10–18]. In this phase the plasma is assumed to have significantly unequal pressures in the longitudinal and transverse directions. The standard hydrodynamic description is a derivative expansion around equal pressures, and therefore it is not applicable in this regime. In contrast, the intrinsically anisotropic hydrodynamical description is a derivative expansion around an anisotropic state, and hence in this case the requirement that derivative corrections be small does not imply small pressure differences. In a real collision the degree of anisotropy will decrease with time, but for some purposes it is a good approximation to take it to be constant over an appropriate time scale.

Motivated by these considerations, in this paper we will investigate the effect of an intrinsic anisotropy on the drag force felt by an infinitely massive quark propagating through a strongly coupled plasma. For this purpose we will examine a string moving in a gravity solution [19, 20] dual to an anisotropic $\mathcal{N} = 4$ super Yang-Mills plasma. As we will review below, the plasma is held in anisotropic equilibrium by an external force. The gravity solution possesses an anisotropic horizon, it is completely regular on and outside the horizon, and it is solidly embedded in type IIB string theory. For these reasons it provides an ideal toy model in which questions about anisotropic effects at strong coupling can be addressed from first principles.

We will pay particular attention to the ultra-relativistic behavior of the drag force, which can be determined analytically. To avoid confusion, we emphasize from the beginning that our results correspond to sending the quark mass to infinity first, and then sending $v \to 1$. In particular, this means that in any future attempt to connect our results to the phenomenology of the QGP, this connection can only be made to the phenomenology of heavy quarks moving through the plasma.

Following the original calculations [21, 22] of the drag coefficient, the closely related diffusion coefficient was obtained independently in [23]. These seminal papers have been generalized and elaborated on in a vast number of subsequent contributions [24–41], including in particular comparisons with the corresponding weakly-coupled results [42–45], as well as extensive analyses of the energy-momentum tensor which provide a detailed picture of the directionality of energy flow away from the moving quark [46–53]. Examples of holographic studies of the drag force in the presence of anisotropies and/or inhomogeneities include [54, 55].

2 Gravity solution

The type IIB supergravity solution of [19, 20] in the string frame takes the form

$$ds^2 = \frac{L^2}{u^2}\left(-\mathcal{F}\mathcal{B}\,dt^2 + dx^2 + dy^2 + \mathcal{H}dz^2 + \frac{du^2}{\mathcal{F}}\right) + L^2 e^{\frac{1}{2}\phi} d\Omega_5^2, \tag{2.1}$$

$$\chi = az\,, \qquad \phi = \phi(u)\,, \tag{2.2}$$

where χ and ϕ are the axion and the dilaton, respectively, and (t, x, y, z) are the gauge theory coordinates. Since there is rotational invariance in the xy-directions, we will refer to these as the transverse directions, and to z as the longitudinal direction. $\mathcal{F}, \mathcal{B}$ and $\mathcal{H}$ are functions of the holographic radial coordinate u that were determined numerically in [19, 20]. Their form for two values of a/T is plotted in figure 1. The horizon lies at $u = u_{\rm H}$, where $\mathcal{F} = 0$, and the boundary at $u = 0$, where $\mathcal{F} = \mathcal{B} = \mathcal{H} = 1$ and $\phi = 0$. The metric near the boundary asymptotes to $AdS_5 \times S^5$. Note that the axion is linear in the z-coordinate. The proportionality constant a has dimensions of mass and is a measure of the anisotropy. The axion profile is dual in the gauge theory to a position-dependent theta parameter of the form $\theta \propto z$. This acts as an isotropy-breaking external source that forces the system into an anisotropic equilibrium state.

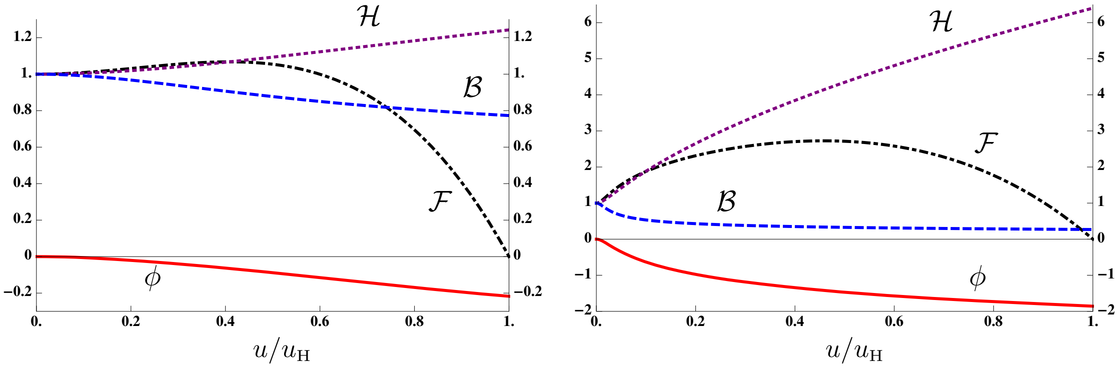

Figure 1. Metric functions for $a/T \simeq 4.4$ (left) and $a/T \simeq 86$ (right).

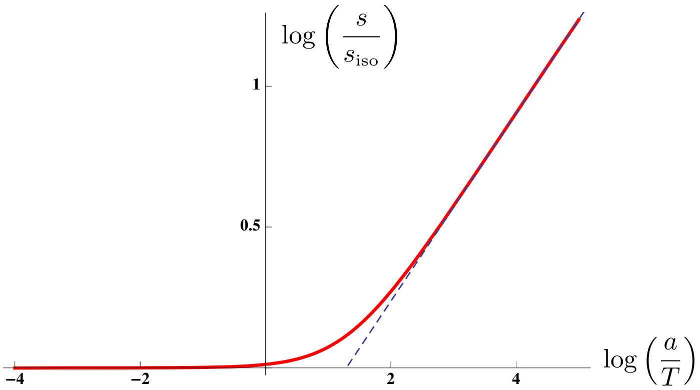

Figure 2. Log-log plot of the entropy density as a function of a/T, with $s_{\rm iso}$ defined as in eq. (2.4). The dashed blue line is a straight line with slope 1/3.

If $a = 0$ then the solution reduces to the isotropic black D3-brane solution dual to the isotropic $\mathcal{N} = 4$ theory at finite temperature. In this case

$$\mathcal{B} = \mathcal{H} = 1\,, \qquad \chi = \phi = 0\,, \qquad \mathcal{F} = 1 - \frac{u^4}{u_{\rm H}^4}\,, \qquad u_{\rm H} = \frac{1}{\pi T} \tag{2.3}$$

and the entropy density takes the form

$$s_{\rm iso} = \frac{\pi^2}{2} N_{\rm c}^2 T^3\,. \tag{2.4}$$

Figure 2 shows the entropy density of the anisotropic plasma as a function of the dimensionless ratio a/T, normalized to the entropy density of the isotropic plasma at the same temperature. At small a/T the entropy density scales as in the isotropic case, whereas at large a/T it scales as [19, 20, 56]

$$s = c_{\rm ent} N_{\rm c}^2 a^{1/3} T^{8/3}\,, \tag{2.5}$$

where $c_{\rm ent}$ is a constant that can be determined numerically.

A feature of the solution (2.2) that played an important role in the analysis of [19, 20] is the presence of a conformal anomaly. Its origin lies in the fact that diffeomorphism invariance in the radial direction u gets broken in the process of renormalization of the on-shell supergravity action. In the gauge theory this means that scale invariance is broken by the renormalization process. One manifestation of the anomaly is the fact that, unlike the entropy density, other thermodynamic quantities do not depend solely on the ratio a/T but on a and T separately. Fortunately, this will not be the case for our drag force, which will take the form $F(a,T) = T^2 f$ with f a function of the ratio a/T alone. The reason for this is that no regularization procedure is necessary for the computation of the drag force, and thus diffeomorphism invariance is preserved. We will also verify this analytically in certain limits, and numerically for general values of a and T.

3 Drag force

Extending the isotropic analysis of refs. [21, 22], in this section we will consider the drag force acting on an infinitely massive quark moving at constant velocity through the anisotropic $\mathcal{N}=4$ plasma described by (2.2). A simple model for this system is described by the equation of motion

$$\frac{d\vec{p}}{dt} = -\mu\vec{p} + \vec{F}\,, \tag{3.1}$$

where $\vec{p}$ is the quark's momentum, μ is a drag coefficient, and $\vec{F}$ is an external force. The necessary force to keep a steady motion is $\vec{F} = \mu\vec{p}$. An observation that will be important for us is that, in the case of an anisotropic medium, the drag coefficient is not just a number but a matrix. In our case we will see that this matrix is diagonal, $\mu = \mathrm{diag}(\mu_x, \mu_y, \mu_z)$ with $\mu_x = \mu_y \neq \mu_z$. Thus we should expect that the force and the momentum or the velocity of the quark will not be aligned in general, and indeed our calculations will reproduce this feature. We will also see that, unlike in [21, 22], the drag coefficient is momentum-dependent.

On the gravity side the quark is described by a string propagating in the background (2.2). The string action is

$$S = -\frac{1}{2\pi\alpha'}\int d^2\sigma\,\sqrt{-g} = \int d^2\sigma\,\mathcal{L}\,, \tag{3.2}$$

where g is the induced worldsheet metric. With the L^2 factor from the spacetime metric the Lagrangian scales as $L^2/2\pi\alpha' = \sqrt{\lambda}/2\pi$. We will set this factor to one in intermediate expressions, and we will reinstate it at the end. Denoting the spacetime coordinates collectively by X^M, the flow of spacetime momentum Π_M along the string is given by

$$\Pi_M = \frac{\partial\mathcal{L}}{\partial(\partial_\sigma X^M)}\,. \tag{3.3}$$

Physically, one can imagine that the external force on the quark needed to sustain steady motion may be exerted by attaching the endpoint of the string to a D7-brane and turning on a constant electric field $F_{MN} = \partial_{[M}A_{N]}$ on the brane. In other words, we add to the action (3.2) the boundary term

$$S_{\mathrm{bdry}} = -\int_{\partial\Sigma} d\tau A_N \partial_\tau X^N = -\frac{1}{2}\int_{\partial\Sigma} d\tau F_{MN} X^M \partial_\tau X^N\,. \tag{3.4}$$

Demanding that the boundary term arising from variation of the total action $S + S_{\rm bdry}$ vanish yields the boundary condition

$$\Pi_M + F_{MN}\partial_\tau X^N\big|_{\partial\Sigma} = 0\,. \tag{3.5}$$

We will now specify to the case of a quark moving steadily through the plasma. The string will not move along the sphere directions, so this part of the metric will play no role in the following. Also, given the rotational symmetry in the xy-directions, we will assume that $y = 0$. We fix the static gauge by identifying $(t, u) = (\sigma^0, \sigma^1)$ and consider a string embedding of the form

$$x(t,u) \to \Big(vt + x(u)\Big) \sin\varphi\,, \tag{3.6}$$

$$z(t,u) \to \Big(vt + z(u)\Big) \cos\varphi\,, \tag{3.7}$$

corresponding to a quark moving with velocity v in the xz-plane at an angle φ with the z-axis. Under these circumstances the Lagrangian takes the form

$$\mathcal{L} = -\left[\frac{\mathcal{B}\mathcal{F} + \sin^2\varphi\,(\mathcal{B}\mathcal{F}^2 x'^2 - v^2) + \mathcal{H}\cos^2\varphi\,\Big[\mathcal{B}\mathcal{F}^2 z'^2 - v^2 - \mathcal{F}v^2(x'-z')^2\sin^2\varphi\Big]}{\mathcal{F}u^4}\right]^{1/2}\,. \tag{3.8}$$

The rates at which energy and momentum flow down the string towards the horizon are then

$$\begin{aligned}
-\Pi_t &= \frac{1}{\mathcal{L}u^4}\,\mathcal{B}\mathcal{F}v\Big[x'\sin^2\varphi + \mathcal{H}z'\cos^2\varphi\Big]\,,\\
\Pi_x &= \frac{1}{\mathcal{L}u^4}\,\Big[\mathcal{B}\mathcal{F}\,x' + \mathcal{H}v^2(z'-x')\cos^2\varphi\Big]\sin\varphi\,,\\
\Pi_z &= \frac{1}{\mathcal{L}u^4}\,\mathcal{H}\Big[\mathcal{B}\mathcal{F}\,z' + v^2(x'-z')\sin^2\varphi\Big]\cos\varphi\,,
\end{aligned} \tag{3.9}$$

where $'$ denotes differentiation with respect to u, and the boundary conditions (3.5) become

$$\Pi_x = F_x\,, \qquad \Pi_z = F_z\,, \qquad -\Pi_t = F_x\,v\sin\varphi + F_z\,v\cos\varphi\,, \tag{3.10}$$

where (F_x, F_z) denote the components of the external force (the electric field). The first two equations are the statement that the external force exactly compensates for the momentum lost by the quark into the medium. The third equation is identically satisfied by virtue of (3.9), and it expresses the fact that the work done by the external force precisely equals the rate at which the quark deposits energy into the medium. As we will see below, the energy and the momentum flow from the boundary to the horizon (i.e. Π_x, Π_z and $-\Pi_t$) are positive provided the string trails behind the quark (i.e. if x', z' are negative), as we would expect on physical grounds. This can be easily seen by inspection in the simple cases of motion along the z-direction ($\varphi = 0$), for which

$$\Pi_z = -\frac{\mathcal{B}\mathcal{F}\mathcal{H}\,z'}{u^2\sqrt{\mathcal{B} - \frac{\mathcal{H}v^2}{\mathcal{F}} + \mathcal{B}\mathcal{F}\mathcal{H}\,z'^2}}\,, \qquad -\Pi_t = \Pi_z\,v\,, \qquad \Pi_x = 0\,, \tag{3.11}$$

and of motion along the x-direction ($\varphi = \pi/2$), for which

$$\Pi_x = -\frac{\mathcal{B}\mathcal{F}\, x'}{u^2\sqrt{\mathcal{B} - \frac{v^2}{\mathcal{F}} + \mathcal{B}\mathcal{F}\, x'^2}}\,, \qquad -\Pi_t = \Pi_x\, v\,, \qquad \Pi_z = 0\,. \tag{3.12}$$

We will now determine the string profile and the corresponding values of the energy and momentum flows for arbitrary v, φ. The first observation is that, generically, the string does not trail 'below' its endpoint's trajectory. In other words, $x(u) \neq z(u)$. Indeed, if $x(u) = z(u)$ then the ratio of the momenta would be given by

$$\frac{\Pi_x}{\Pi_z} = \frac{\tan\varphi}{H(u)}\,, \tag{3.13}$$

which would be a contradiction because the left-hand side is constant whereas the right-hand side is not. In order to determine the correct string profile we invert the relations (3.9) to find

$$x' = \pm\frac{\mathcal{H}v}{\mathcal{F}\sqrt{\mathcal{B}\mathcal{H}}}\frac{N_x}{\sqrt{N_xN_z - D}}\,, \qquad z' = \pm\frac{v}{\mathcal{F}\sqrt{\mathcal{B}\mathcal{H}}}\frac{N_z}{\sqrt{N_xN_z - D}}\,, \tag{3.14}$$

where

$$N_x = -\Pi_x(\mathcal{B}\mathcal{F}\csc\varphi - v^2\sin\varphi) + \Pi_z v^2\cos\varphi\,, \tag{3.15}$$

$$N_z = -\Pi_z(\mathcal{B}\mathcal{F}\sec\varphi - \mathcal{H}v^2\cos\varphi) + \Pi_x\,\mathcal{H}v^2\sin\varphi\,, \tag{3.16}$$

$$D = \frac{\mathcal{B}\mathcal{F}\csc\varphi\sec\varphi}{u^4}\Big[\Pi_x\Pi_z u^4 - \mathcal{H}v^2\cos\varphi\sin\varphi\Big]\Big[\mathcal{B}\mathcal{F} - v^2\left(\mathcal{H}\cos^2\varphi + \sin^2\varphi\right)\Big]\,. \tag{3.17}$$

The factor $N_xN_z - D$ inside the square root in the denominator of (3.14) is positive at the boundary, where $\mathcal{B}, \mathcal{F}, \mathcal{H} \to 1$ and $u \to 0$, and also at the horizon, where $\mathcal{F} \to 0$, and generically it becomes negative in some region in between. In other words, it vanishes at two different values of u between the boundary and the horizon. To see this, consider the last factor in square brackets in (3.17). $\mathcal{B}\mathcal{F}$ ($\mathcal{H}$) is monotonically decreasing (increasing) from the boundary to the horizon, so this factor is positive at the boundary and negative at the horizon. Therefore there exists a critical value u_c in between such that

$$\mathcal{B}_c\,\mathcal{F}_c - v^2\left(\mathcal{H}_c\cos^2\varphi + \sin^2\varphi\right) = 0\,, \tag{3.18}$$

where $\mathcal{B}_c = \mathcal{B}(u_c)$, etc. At this point $D = 0$ and

$$N_xN_z\big|_{u_c} = -v^4\left(\mathcal{H}_c\,\Pi_x\cos\varphi - \Pi_z\sin\varphi\right)^2\,, \tag{3.19}$$

which is negative unless the momenta are related through

$$\frac{\Pi_x}{\Pi_z} = \frac{\tan\varphi}{\mathcal{H}_c}\,. \tag{3.20}$$

If this condition is not satisfied then $N_xN_z - D$ is negative in some interval $u_1 < u_c < u_2$ and vanishes at $u = u_1$ and at $u = u_2$. This type of solutions correspond to strings with two endpoints at the boundary. Here we wish to study isolated quarks, which are described by strings that extend all the way from the boundary to the horizon, so we must require that $N_x N_z - D$ is non-negative for all $0 < u < u_{\rm H}$. This is satisfied if and only if (3.20) holds and if the two zeros of D coincide with one another, i.e. if the first square bracket in (3.17) also vanishes at $u = u_c$. The latter condition, together with (3.20), allows us to solve for the two momenta independently with the final result:

$$\Pi_x = \frac{v \sin\varphi}{u_c^2}\,, \qquad \Pi_z = \mathcal{H}_c \frac{v \cos\varphi}{u_c^2}\,. \tag{3.21}$$

Under these circumstances the denominator in (3.14) is always real and positive except at u_c, where it vanishes. At this point the numerators also vanish and the functions x', z' are smooth and negative for all $0 < u < u_{\rm H}$ provided in (3.14) we choose the positive sign for $u < u_c$ and the negative sign for $u > u_c$.

In summary, we have obtained the force $\vec{F} = (\Pi_x, \Pi_z)$ that must be exerted on the quark in order to maintain its stationary motion,

$$\vec{F} = \frac{\sqrt{\lambda}}{2\pi} \frac{v}{u_c^2} \left(\sin\varphi, \mathcal{H}_c \cos\varphi\right), \tag{3.22}$$

in terms of the quark's velocity $\vec{v} = v(\sin\varphi, \cos\varphi)$. (In this equation we have reinstated the factor $L^2/2\pi\alpha'$.) The external force $\vec{F}$ is equal to minus the drag force exerted on the quark by the plasma, but in a slight abuse of language we will refer to $\vec{F}$ itself as the drag force. Note that $\vec{v}$ and $\vec{F}$ are not aligned with one another except in the isotropic case, for which $\mathcal{H}_c = 1$, or in the cases in which the velocity is aligned with one of the axes, in which $\varphi = 0, \pi/2$. Note also the force depends on the velocity both through the explicit factors of v and φ in eq. (3.22) and implicitly through the value of $\mathcal{H}_c$, which is a solution of the $\vec{v}$-dependent equation (3.18).

Substituting the result (3.21) in (3.14) we obtain the form of the string profile as a function of the velocity. The projection of this profile on the xz-plane has tangent vector $\vec{\tau} = (\tau_x, \tau_z) = (x' \sin\varphi, z' \cos\varphi)$. The angle φ_τ between this vector and the z-axis is

$$\tan\varphi_\tau = \frac{\tau_x}{\tau_z} = \epsilon \tan\varphi\,, \qquad \epsilon = 1 + \frac{\mathcal{B}\mathcal{F}(\mathcal{H} - \mathcal{H}_c)}{\mathcal{B}\mathcal{F}\mathcal{H}_c - \mathcal{B}_c\mathcal{F}_c\mathcal{H}}\,. \tag{3.23}$$

At the horizon we have $\mathcal{F} = 0$ and thus $\epsilon = 1$, which means that deep in the infrared the string aligns itself with the velocity. However, near the boundary $\mathcal{B}, \mathcal{H}, \mathcal{F} \to 1$ and thus

$$\epsilon \to 1 + \frac{1 - \mathcal{H}_c}{\mathcal{H}_c - \mathcal{B}_c\mathcal{F}_c}\,. \tag{3.24}$$

This is different from unity for generic φ, and so the string does not align itself with the velocity except if $\varphi = 0$ or $\varphi = \pi/2$. In these two special cases the entire string profile (not just the infrared part) aligns itself with the z- or the x-axis, respectively, because ϵ remains finite in these limits whereas $\tan\varphi \to 0, \infty$, respectively. Note also that the vector $\vec{\tau}$ is not aligned with the force $\vec{F}$ either, since $\epsilon \neq \mathcal{H}_c^{-1}$.

The formulas above reduce to the correct expressions in the isotropic limit (2.3). In this case eq. (3.18) yields

$$u_c^2 = u_{\rm H}^2 \sqrt{1 - v^2} = \frac{\sqrt{1 - v^2}}{\pi^2 T^2} \tag{3.25}$$

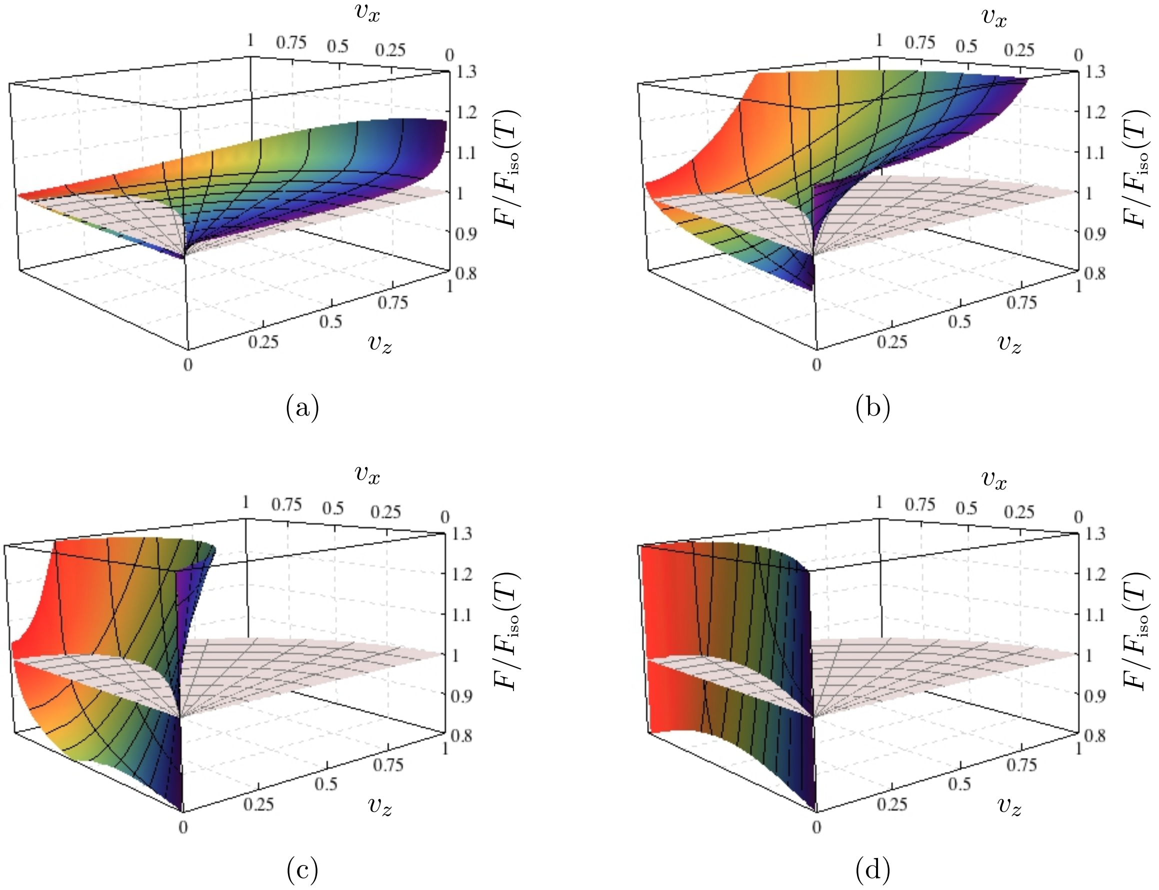

Figure 3. Drag force as a function of the quark velocity $(v_x, v_z) = v(\sin\varphi, \cos\varphi)$ for a quark moving through an anisotropic plasma with $a/T = 1.38\text{(a)}, 4.41\text{(b)}, 12.2\text{(c)}, 86\text{(d)}$. F is plotted in the appropriate units to facilitate comparison with the isotropic result (3.27) for a plasma at the same temperature.

and the force (3.22) becomes

$$\vec{F}_{\rm iso}(T) = F_{\rm iso}(T)(\sin\varphi, \cos\varphi) \tag{3.26}$$

with

$$F_{\rm iso}(T) = \frac{\pi}{2}\sqrt{\lambda}\,T^2\frac{v}{\sqrt{1-v^2}}\,, \tag{3.27}$$

as in [21, 22]. For later purposes it is useful to rewrite this result as

$$F_{\rm iso}(s) = \frac{\sqrt{\lambda}\,s^{2/3}}{(2\pi)^{1/3}N_{\rm c}^{4/3}}\,\frac{v}{\sqrt{1-v^2}} \tag{3.28}$$

in terms of the entropy density (2.4) of the isotropic $\mathcal{N}=4$ plasma.

4 Results

With the groundwork above in place, we can now proceed to state our results. Since for general a the metric functions in (2.2) are only known numerically, we have numerically deter-

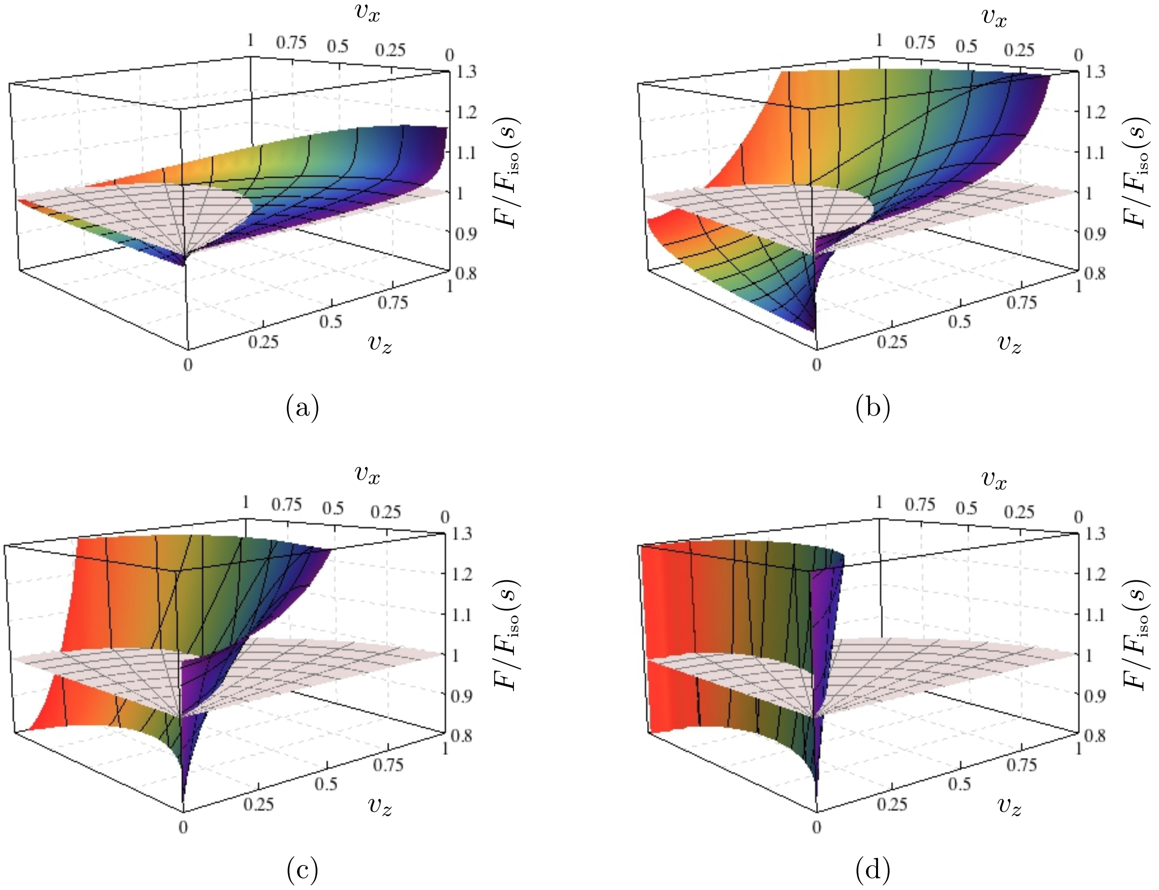

Figure 4. Drag force as a function of the quark velocity $(v_x, v_z) = v(\sin\varphi, \cos\varphi)$ for a quark moving through an anisotropic plasma with $aN_c^{2/3}/s^{1/3} = 0.80(\mathrm{a}), 2.47(\mathrm{b}), 6.24(\mathrm{c}), 35.5(\mathrm{d})$. F is plotted in the appropriate units to facilitate comparison with the isotropic result (3.28) for a plasma at the same entropy density.

mined the drag force as a function of the magnitude of the quark velocity v, of its direction φ, and of the anisotropy a measured in units of the temperature T or in units of the entropy density s. The reason for working with both a/T and $a/s^{1/3}$ is that we wish to compare the drag force in the anisotropic plasma to that in the isotropic plasma, and this can be done at least in two different ways: the two plasmas can be taken to have the same temperatures but different entropy densities, or the same entropy densities but different temperatures.

The drag force $F(v, \varphi, a/T)$ in units of the isotropic drag force in a plasma at the same temperature is shown in figure 3. The drag force $F(v, \varphi, a/s^{1/3})$ in units of the isotropic drag force in a plasma at the same entropy density is shown in figure 4. With a few exceptions, the results are qualitatively similar. In both cases we see that the anisotropic drag is larger than the isotropic drag except in a region near the x-axis. This region is more clearly shown in figure 5: the curves in that figure are the intersections between the two surfaces shown in each of the corresponding 3D plot in figures 3 or figures 4. Considering that the value of a/T varies by a factor of 62 between the top and the bottom curves in figure 5, we see that the region in question depends relatively mildly on the magnitude of the anisotropy.

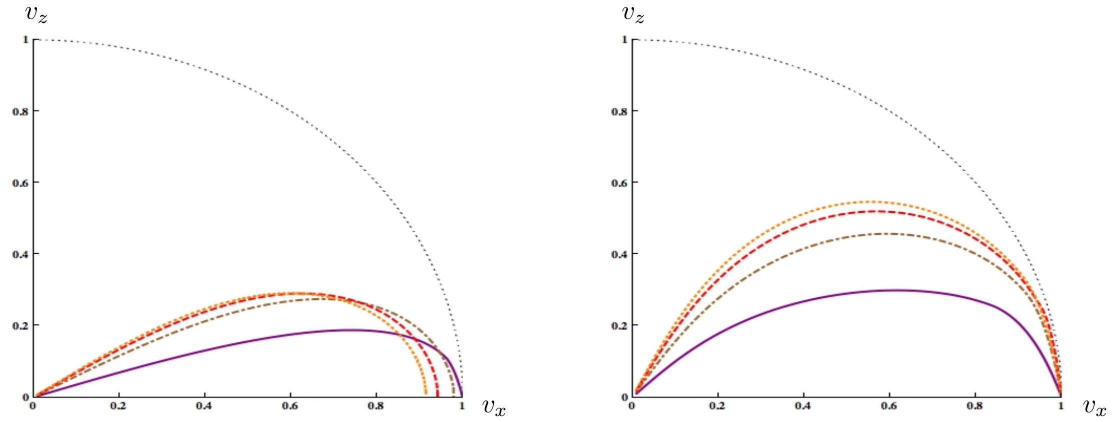

Figure 5. (Left) Values of the velocity at which the drag in an anisotropic plasma with (from top to bottom) $a/T = 1.38, 4.41, 12.2, 86$ equals the drag in an isotropic plasma at the same temperature. (Right) Values of the velocity at which the drag in an anisotropic plasma with (from top to bottom) $aN_c^{2/3}/s^{1/3} = 0.80, 2.47, 6.24, 35.5$ equals the drag in an isotropic plasma at the same entropy density. For a given value of a/T or $aN_c^{2/3}/s^{1/3}$, the anisotropic drag is larger (smaller) than the isotropic drag above (below) the corresponding curve.

For motion along the longitudinal z-direction, the anisotropic drag is greater than the isotropic drag for any value of v. For any direction of motion $\varphi \neq \pi/2$, the ratio $F_{\text{aniso}}/F_{\text{iso}}$ diverges as $1/\sqrt{1-v^2}$ in the ultra-relativistic limit $v \to 1$ irrespectively of whether the comparison is made at the same temperature or at the same entropy density, as we prove analytically in appendix A.[1] In other words, for motion not perfectly aligned with the transverse x-direction, the anisotropic drag becomes arbitrarily larger than the isotropic one as the ultra-relativistic limit is approached. This is most clearly illustrated in figure 6, which shows constant-φ slices of the (c) and (d) plots in figures 3 and figures 4. We will come back to this result in section 5.

The ratio $F_{\text{aniso}}/F_{\text{iso}}$ is always finite for motion along the transverse x-direction. (Incidentally, this implies that the limits $\varphi \to \pi/2$ and $v \to 1$ do not commute.) In this case we must distinguish between the comparisons at equal temperature or at equal entropy density. In the first case, our numerical results indicate that the anisotropic drag is smaller than the isotropic one for $0 \leq v < v_c$ and larger than the isotropic one for $v_c < v \leq 1$, and we have confirmed this analytically in the limits of small and large anisotropies (see the appendices). The velocity v_c at which the transition takes place is $v_c \simeq 0.9$ for small anisotropies and it approaches 1 as the anisotropy increases.

In the second case our numerical results indicate that the anisotropic drag is smaller than the isotropic one for all $v \in [0, 1]$ provided $a/s^{1/3}$ is small enough. In the opposite limit, $a/s^{1/3} \gg 1$, the anisotropic drag stays smaller than the isotropic one for small velocities and becomes larger above some critical velocity. We have confirmed this analytically in the appendices. For a fixed v, the angle with respect to the z-direction beyond which

---

[1] We recall that we first send the quark mass to infinity and then $v \to 1$. See the penultimate paragraph of section 1.

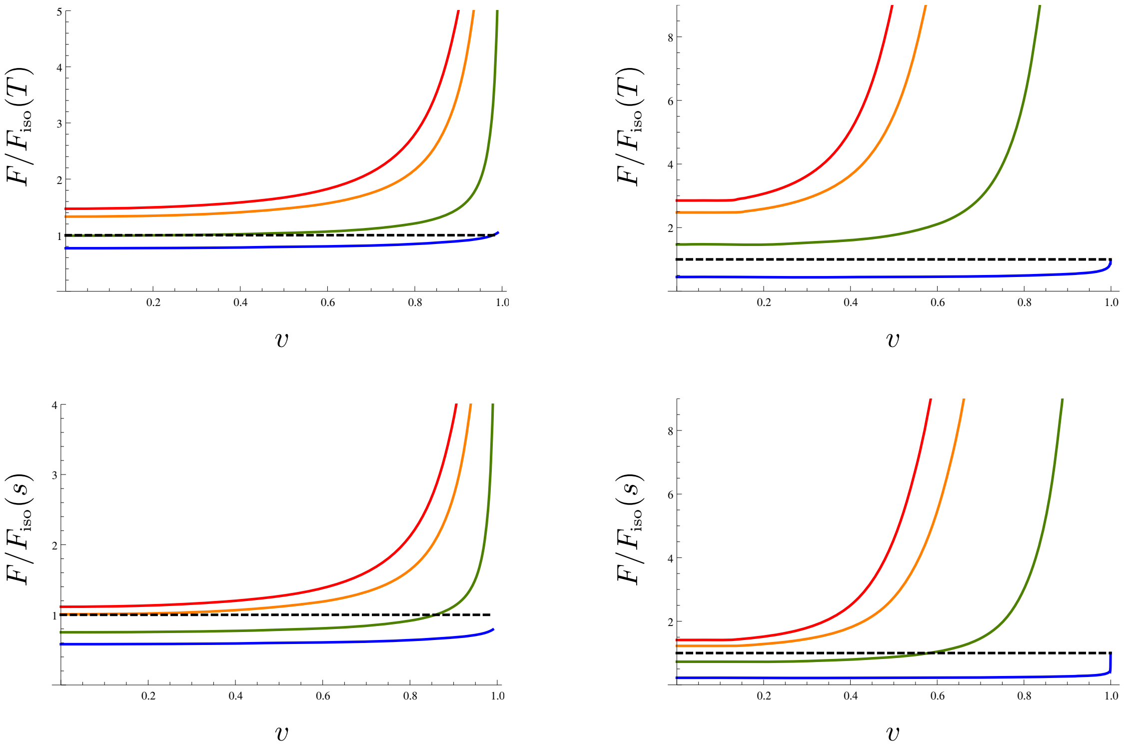

Figure 6. Drag force as a function of the velocity for a quark moving through an anisotropic plasma with $a/T = 12.2$, or equivalently $aN_c^{2/3}/s^{1/3} = 6.24$, (left column) and $a/T = 86$, or equivalently $aN_c^{2/3}/s^{1/3} = 35.5$, (right column) along four different directions lying at angles (curves from top to bottom) $\varphi = 0, \pi/6, \pi/3, \pi/2$ with respect to the longitudinal direction z. F is plotted in the appropriate units to facilitate comparison with the isotropic result for a plasma at the same temperature (top row) or at the same entropy density (bottom row). The isotropic result is given in eqs. (3.27) and (3.28).

the anisotropic drag may become smaller than the isotropic drag is shown in the constant-v slices of figure 7.

The dependence of the drag force on the anisotropy for fixed velocity is most clearly seen in figures 8 and figures 9, where the ratio $F/F_{\rm iso}$ is plotted for several values of v and φ.

In order to illustrate the geometric properties of the string solution, in figure 10 we have plotted the projection of the string profile onto the gauge theory directions. As anticipated, we see that the string curves in the xz-plane and (unless $\varphi = 0$ or $\pi/2$) only aligns itself with the velocity in the far infrared, i.e. at large u. The misalignment between the velocity $\vec{v}$, the drag force $\vec{F}$, and the tangent to the string profile at the string's endpoint $\vec{\tau}$ are shown in figure 11. We see that, generally speaking, the misalignment becomes larger for larger anisotropies. This is more clearly quantified in figures 12 and 13, where the angles with respect to the z-direction of the tangent vector to the string and of the force are shown as a function of the angle of the direction of motion. From figure 12 we see that the tangent vector to the string systematically 'lags behind' the direction of motion as the latter varies from being aligned with the z-direction to being aligned with the x-direction. Only in these

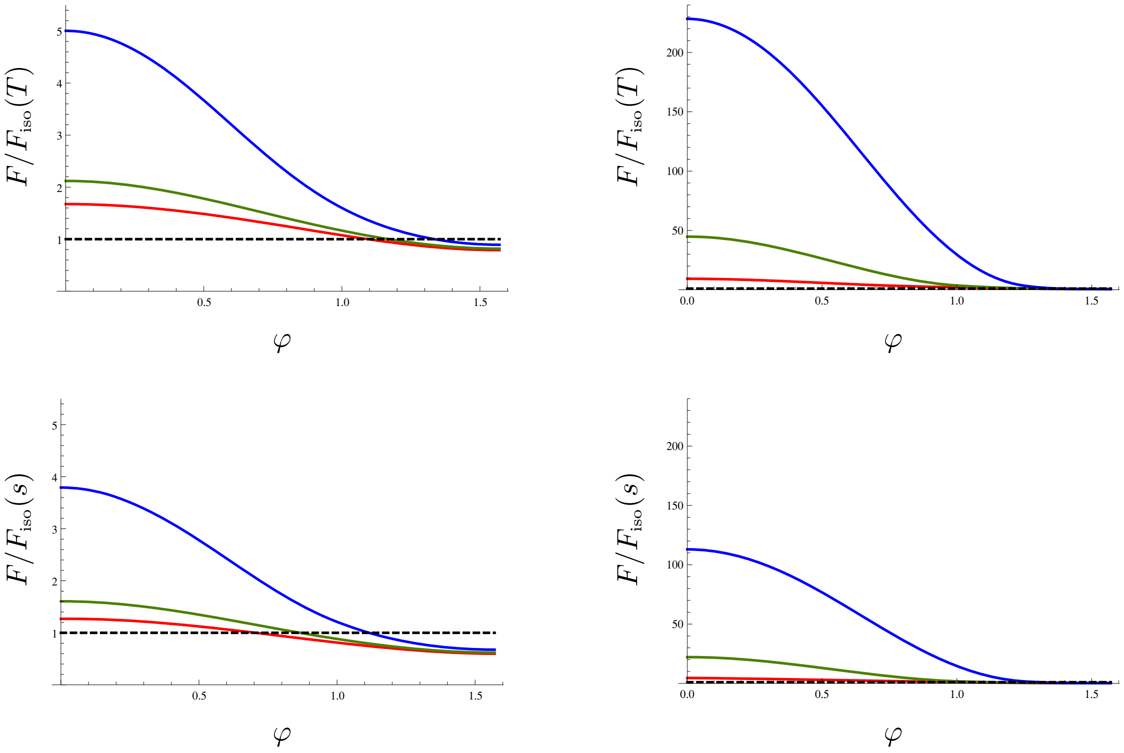

Figure 7. Drag force as a function of the direction of motion φ, measured with respect to the longitudinal direction z, for a quark moving through an anisotropic plasma with $a/T = 12.2$, or equivalently $aN_c^{2/3}/s^{1/3} = 6.24$, (left column) and $a/T = 86$, or equivalently $aN_c^{2/3}/s^{1/3} = 35.5$, (right column) at three different velocities (curves from top to bottom) $v = 0.9, 0.7, 0.5$. F is plotted in the appropriate units to facilitate comparison with the isotropic result for a plasma at the same temperature (top row) or at the same entropy density (bottom row). The isotropic result is given in eqs. (3.27) and (3.28).

two limits does the string profile align itself entirely with the velocity. Moreover, the larger the anisotropy the more the string 'wants' to stay aligned with the z-direction, changing direction quickly only as φ approaches $\pi/2$. From figure 13 we see that the behaviour of the force is similar, except that for sufficiently large anisotropies its direction does not vary monotonically with the direction of the velocity.

In order to gain an intuitive understanding of these geometric facts it is useful to think of the string in our anisotropic background (2.2) as a fishing string immersed in a river. Since the string provides a semiclassical description of the quark and its gluon cloud in the dual plasma, each of the statements below can be easily translated into gauge theory language. In the river analogy, the direction of the river's current provides the anisotropic direction, and the fact that the anisotropy function $\mathcal{H}(u)$ in (2.2) depends on the radial coordinate can be modeled by imagining that the magnitude of the current depends on the depth. Under these circumstances it is clear that the string will curve as it descends deeper and deeper, since pieces of the string at different depths experience different degrees of anisotropy. It is also clear that each bit of the string deposits momentum into the river

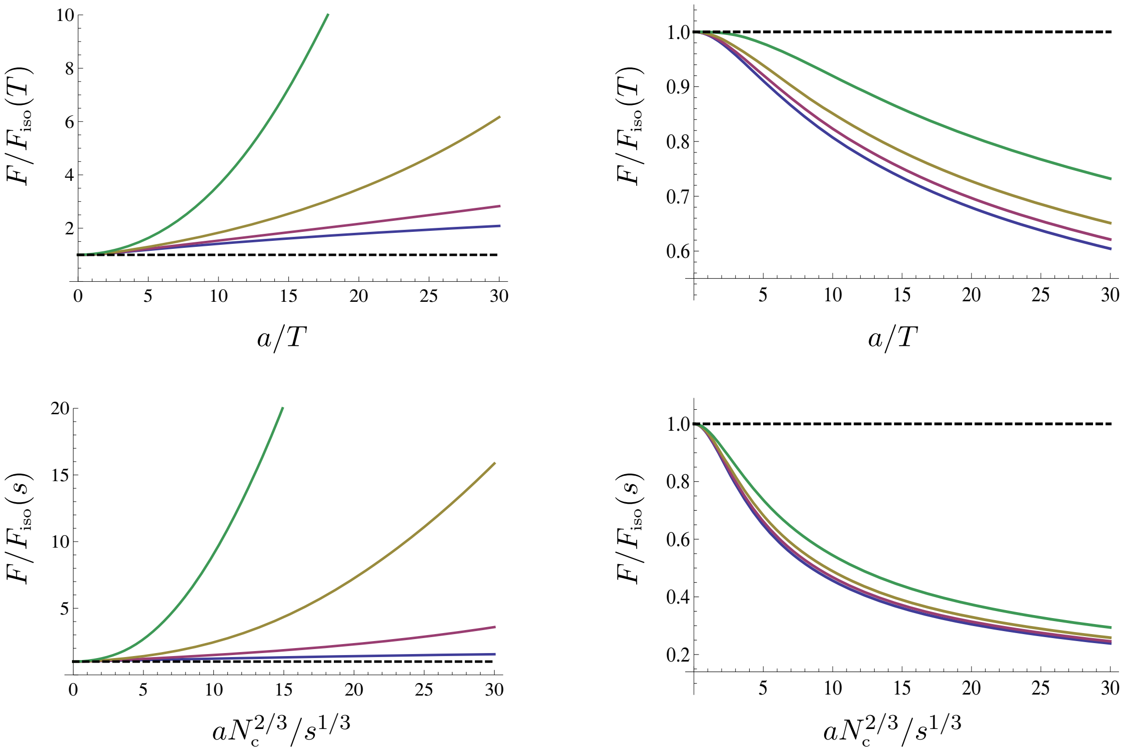

Figure 8. Drag force as a function of the anisotropy for a quark moving along the longitudinal z-direction, i.e. at $\varphi = 0$ (left column) or along the transverse x-direction, i.e. at $\varphi = \pi/2$ (right column), at four different velocities (curves from top to bottom) $v = 0.9, 0.7, 0.5, 0.25$. F and a are plotted in the appropriate units to facilitate comparison with the isotropic result for a plasma at the same temperature (top row) or at the same entropy density (bottom row). The isotropic result is given in eqs. (3.27) and (3.28).

in a different direction that depends on the bit's local orientation. The direction of the total (rate of) momentum deposition is a combination of all of these contributions, and this combination equals the external force. It is thus clear that the external force will not point in the same direction as the vector tangent to the string at a generic point, in particular at its endpoint. Finally, the fact that the string eventually aligns with the velocity deep in the infrared can be understood as a consequence of the fact that the string 'piles up' on top of the horizon of (2.2). In the river's analogy, this could perhaps be modeled by imagining that the current vanishes at the bottom of the river, and that the string piles up there. To understand this point, note that a constant-u slice of the metric (2.2) is locally isotropic, since the factor $\mathcal{H}(u)$ can be locally absorbed through a rescaling of the z-coordinate. For generic u this is irrelevant since the local isotropy is only experienced by an infinitesimal bit of string. However, an infinite length of string lies between $u_{\rm H}$ and $u_{\rm H} + \epsilon$ for any $\epsilon > 0$. Since this infinite piece of string experiences an effectively isotropic metric, it is not surprising that it aligns with the velocity of the quark, as it happens in the completely isotropic case [21, 22].

We stress that the heuristic analogy above is only meant to provide a somewhat intuitive understanding of the geometric features described by figures 10–13, which arise

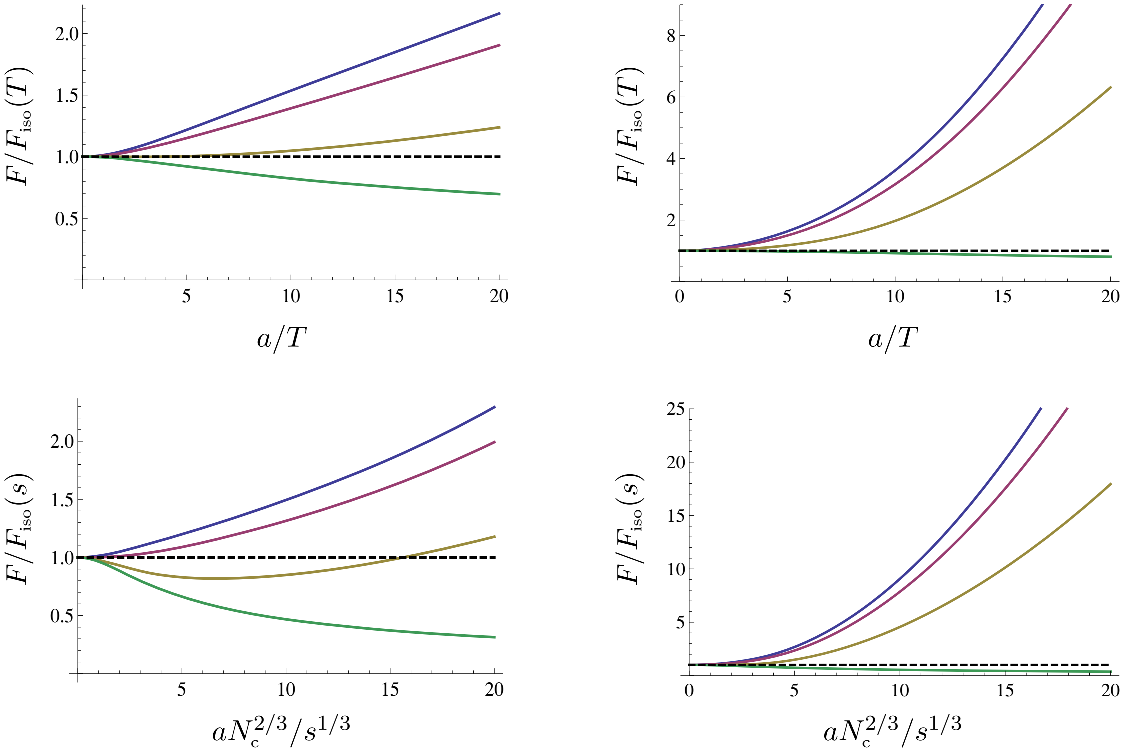

Figure 9. Drag force as a function of the anisotropy for a quark moving at $v = 0.5$ (left column) or at $v = 0.9$ (right column) along four different angles (curves from top to bottom) $\varphi = 0, \pi/6, \pi/3, \pi/2$ with respect to the longitudinal direction z. F and a are plotted in the appropriate units to facilitate comparison with the isotropic result for a plasma at the same temperature (top row) or at the same entropy density (bottom row). The isotropic result is given in eqs. (3.27) and (3.28).

rigorously from the minimization of the string action in our anisotropic background (2.2). In particular, we emphasize that, although it may seem counterintuitive at first sight, there is no reason to expect the tangent vector to the string, the velocity and the force to be mutually aligned in the presence of an anisotropic medium.

5 Discussion

We have analyzed the drag force exerted on an infinitely massive quark moving through an anisotropic $\mathcal{N} = 4$ super Yang-Mills plasma described by the metric (2.2). In this case the anisotropy is induced by a position-dependent theta term in the gauge theory, or equivalently by a position-dependent axion on the gravity side. One may therefore wonder how sensitive the conclusions may be to the specific source of the anisotropy. In this respect it is useful to note that the gravity calculation involves only the coupling of the string to the background metric. This means that any anisotropy that gives rise to a qualitatively similar metric (and no Neveu-Schwarz B-field) will yield qualitatively similar results for the drag force irrespectively of the form of the rest of the supergravity fields.

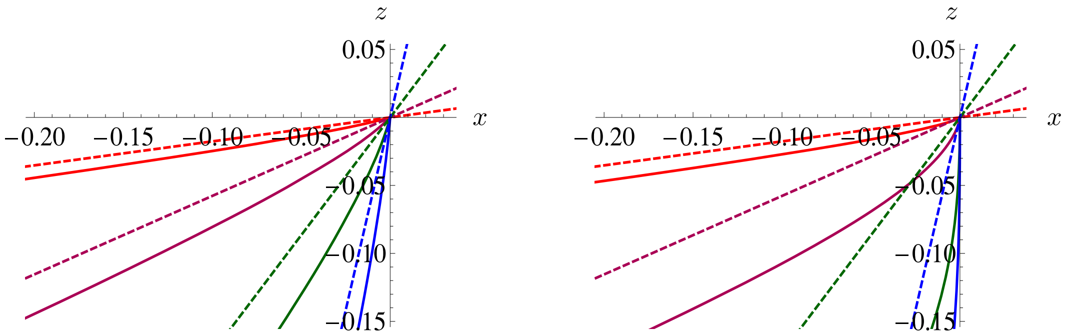

Figure 10. Projection of a $t = 0$ snapshot of the string profile (3.7) (continuous curves) onto the xz-plane for a quark moving with velocity $v = 0.7$ in four different directions (indicated by the dashed straight lines) that lie at angles (clockwise) $\varphi = \pi/18, \pi/6, \pi/3, 8\pi/18$ with respect to the z-direction. The quark moves through a plasma with anisotropy $a = 12.2\,T$ (left) and $a = 86\,T$ (right). The origin $(x, z) = (0, 0)$ corresponds to the string endpoint, which lies at the boundary $u = 0$. The coordinate u increases along the curves away from this point. The string curves in the xz-plane and (unless $\varphi = 0$ or $\pi/2$) only aligns itself with the velocity in the far infrared, i.e. at large u.

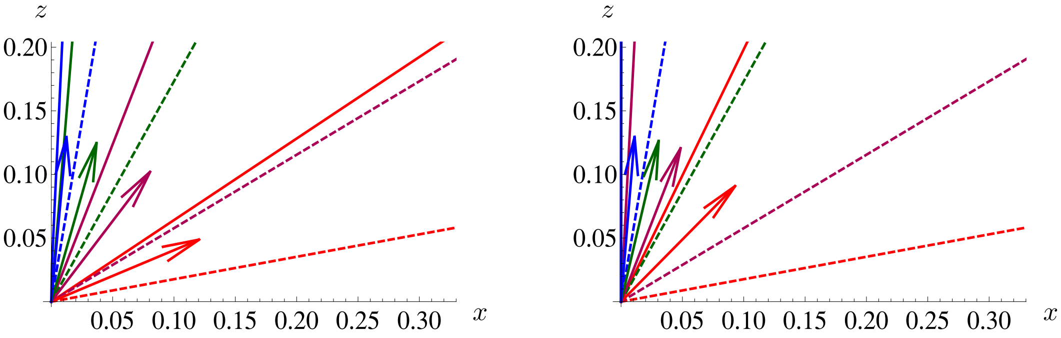

Figure 11. Generic misalignment between the direction of the quark velocity (dashed straight lines), the direction of the force (arrows) and the direction tangent to the string profile at its endpoint (continuous straight lines). The quark velocity is $v = 0.7$, its direction lies at angles (clockwise) $\varphi = \pi/18, \pi/6, \pi/3, 8\pi/18$ with respect to the z-direction, and the anisotropy is $a = 12.2\,T$ (left) and $a = 86\,T$ (right).

An example of a rather robust conclusion is the ultra-relativistic behaviour of the drag force.[2] We have seen that the anisotropic solution (2.2) yields a drag force that becomes arbitrarily larger than the isotropic one for all ultra-relativistic quarks except for those whose velocity is perfectly aligned with the transverse xy-plane. This follows from the fact that the near-boundary fall-off of the metric (2.2) takes the schematic form

$$g_{\mu\nu} = \frac{L^2}{u^2}\left(\eta_{\mu\nu} + u^2 g^{(2)}_{\mu\nu} + u^4 g^{(4)}_{\mu\nu} + \cdots\right) . \tag{5.1}$$

As v grows closer and closer to 1 the string worldsheet develops a horizon closer and closer to the AdS boundary at $u = 0$. As a consequence the physics in this limit is solely

---

[2] We recall that we first send the quark mass to infinity and then $v \to 1$. See the penultimate paragraph of section 1.

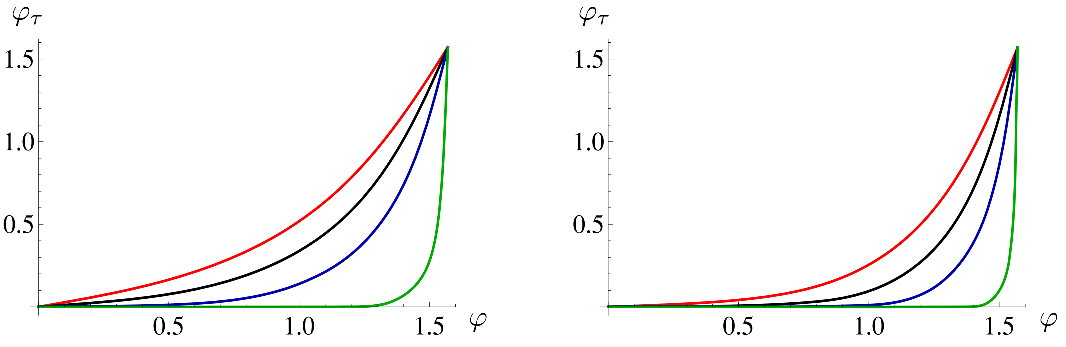

Figure 12. Tendency of the string to align itself with the longitudinal direction z for four different anisotropies (from top to bottom) $a/T = 12.2, 20.3, 42.6, 744$. The angle φ_τ is the angle between the z-axis and the tangent vector to the string at its endpoint, defined as in eq. (3.23). The angle φ is the angle between the z-axis and the velocity. The magnitude of the velocity is $v = 0.7$ (left) and $v = 0.9$ (right).

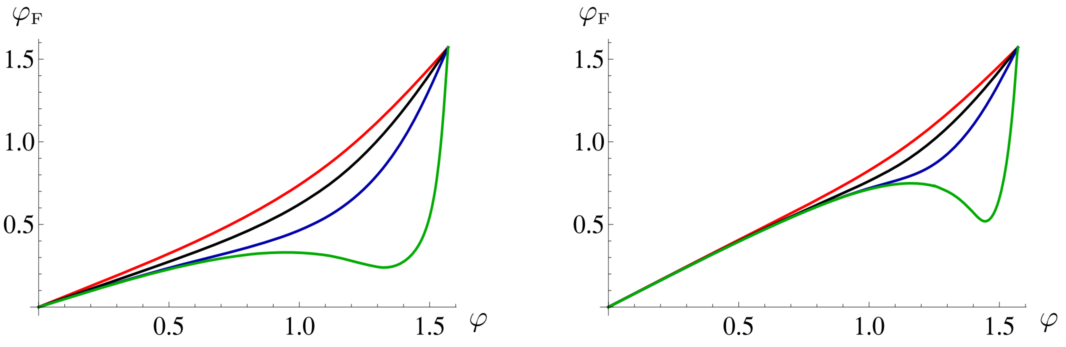

Figure 13. Correlation between the direction of the force, φ_{F}, and the direction of the velocity, φ (with both angles measured with respect to the longitudinal direction z), for four different anisotropies (from top to bottom) $a/T = 12.2, 20.3, 42.6, 744$. The magnitude of the velocity is $v = 0.7$ (left) and $v = 0.9$ (right).

controlled by the near-boundary behaviour of the metric. eq. (3.18) can then be solved using the asymptotic form (5.1) of the metric functions. Generically the solution to leading order is determined by the $\mathcal{O}(u^2)$-terms and yields $u_c^2 \propto 1 - v^2$. Substituting in (3.22) one gets $F \propto 1/(1 - v^2)$, or equivalently $F = \mu p$ with a momentum-dependent drag coefficient $\mu \propto p$. For example, we show in appendix A that the metric (2.2) yields a drag coefficient

$$\mu(p) \simeq \frac{\sqrt{\lambda}\, a^2 \cos^2 \varphi}{8\pi M^2}\, p \tag{5.2}$$

at large p, where M is the quark mass. In contrast, in the isotropic case of [21, 22] the $\mathcal{O}(u^2)$-terms in the metric are absent. This means that the solution of eq. (3.18) is $u_c^4 \propto 1 - v^2$ and hence that in this case the drag force in the ultra-relativistic limit has a softer divergence $F_{\text{iso}} \propto 1/\sqrt{1 - v^2}$. Rewriting this in terms of the momentum gives $F = \mu p$ with μ a momentum-independent constant in this case. For certain choices of the parameters (for example for $\varphi = \pi/2$ in our case) the $\mathcal{O}(u^2)$-terms in eq. (3.18) may vanish, in which case $F \propto 1/\sqrt{1 - v^2}$.

The above discussion makes it clear that the linear behaviour of the drag coefficient in the ultra-relavistic limit, $\mu \propto p$, depends solely on two features of the solution: The presence of the $g^{(2)}_{\mu\nu}$ term in the near-boundary expansion of the metric, and the fact that the metric (5.1) be non-boost-invariant at order u^2 (i.e. that $g^{(2)}_{\mu\nu}$ not be proportional to $\eta_{\mu\nu}$). The latter condition is necessary because otherwise there would be no solution for u_c at order u^2. Note that adding temperature to an otherwise boost-invariant metric will only affect $g^{(4)}_{\mu\nu}$, and thus this is not enough to make $g^{(2)}_{\mu\nu}$ non-boost-invariant. This conclusion is consistent with the fact that $g^{(2)}_{\mu\nu}$ is only a function of the external sources which the theory is coupled to.

Interesting backgrounds with non-zero $g^{(2)}_{\mu\nu}$ include bona fide string theory constructions, i.e. smooth supergravity solutions with a well known gauge theory dual, as well as 'ad hoc' backgrounds, i.e. backgrounds that do not solve supergravity equations but are phenomenologically motivated. An example in the first category is the supergravity flow [57–59] dual to the $\mathcal{N} = 2^*$ deformation of the $\mathcal{N} = 4$ super Yang-Mills theory by fermion (and scalar) masses. An example in the second category is the linear-dilaton background of refs. [60–62]. Both sets of examples have in common that, at zero temperature, conformal invariance is broken but the full Lorentz symmetry of the boundary theory is preserved. The breaking of conformality results in a momentum-dependent drag coefficient $\mu(p)$, as shown in [63] for the $\mathcal{N} = 2^*$ theory, and in [62, 64] for the linear-dilaton background. However, in both sets of examples $g^{(2)}_{\mu\nu}$ is boost-invariant, since this term (unlike $g^{(4)}_{\mu\nu}$) is unaffected by the further breaking of conformal symmetry that occurs at non-zero temperature. As a consequence, in the ultra-relativistic limit the drag-coefficient becomes momentum-independent and approaches a constant. Thus, as measured by this particular observable, one may regard the breaking of conformality in the anisotropic plasma of [19, 20] as more severe than in the backgrounds above.

Acknowledgments

It is a pleasure to thank Roberto Emparan, Tomeu Fiol, Alberto Güijosa, and specially Jorge Casalderrey-Solana and Ioannis Papadimitriou for discussions. MC is supported by a postdoctoral fellowship from Mexico's National Council of Science and Technology (CONACyT). We acknowledge financial support from 2009-SGR-168, MEC FPA2010-20807-C02-01, MEC FPA2010-20807-C02-02 and CPAN CSD2007-00042 Consolider-Ingenio 2010 (MC, DF and DM), and from DE-FG02-95ER40896 and CNPq (DT).

A Ultra-relativistic limit

In the limit $v \to 1$ the value of u_c that solves eq. (3.18) approaches the boundary, i.e. $u_c \to 0$. Therefore in this limit u_c can be determined from the near-boundary expansion of the metric functions, which takes the form:

$$\mathcal{F} = 1 + \frac{11\,a^2}{24} u^2 + \left(\mathcal{F}_4 + \frac{7\,a^4}{12} \log u \right) u^4 + O(u^6)\,,$$

$$\mathcal{B} = 1 - \frac{11\,a^2}{24}u^2 + \left(\mathcal{B}_4 - \frac{7\,a^4}{12}\log u\right) u^4 + O(u^6)\,,$$
$$\mathcal{H} = 1 + \frac{a^2}{4}u^2 - \left(\frac{2\,\mathcal{B}_4}{7} - \frac{5\,a^4}{4032} - \frac{a^4}{6}\log u\right) u^4 + O(u^6)\,, \tag{A.1}$$

The coefficients $\mathcal{B}_4, \mathcal{F}_4$ depend on a, T and are related to the energy and the pressures of the plasma eqs. (35) in [20]. They are not determined by the near-boundary analysis but must instead be read off from a full bulk solution.

We must solve (3.18) for u_c to leading order in $1-v^2$. For $\cos\varphi \neq 0$ we only need to consider the terms of $\mathcal{O}(u^2)$ in the metric functions, and the solution is

$$\frac{1}{u_c^2} = \frac{a^2\, v^2 \cos^2\varphi}{4(1-v^2)}\,. \qquad [\cos\varphi \neq 0] \tag{A.2}$$

Substituting into (3.22) we obtain the drag force

$$\vec{F} = \frac{\sqrt{\lambda}}{8\pi}\, a^2 \cos^2\varphi\, \frac{v^3}{1-v^2} (\sin\varphi, \cos\varphi)\,. \qquad [\cos\varphi \neq 0] \tag{A.3}$$

The divergence when $v \to 1$ contrasts with the softer behaviour (3.27)–(3.28) of the isotropic case. We conclude that for $\cos\varphi \neq 0$ the ratio $F_{\rm aniso}/F_{\rm iso}$ diverges in the limit $v \to 1$ as $1/\sqrt{1-v^2}$, in agreement with our numerical results displayed in figure 6. Note that this is true even if the two plasmas have different temperatures and/or different entropy densities, since in the anisotropic case F diverges as $1/(1-v^2)$ irrespectively of the temperature or the entropy density.

The previous analysis shows that the limits $v \to 1$ and $\varphi \to \pi/2$ do not commute. This is because if we first set $\cos\varphi = 0$ then the terms of order u^2 cancel out in eq. (3.18) and we must go to order u^4. The solution in this case is

$$\frac{1}{u_c^2} = \frac{T^2}{\sqrt{1-v^2}} \sqrt{\frac{121}{576}\frac{a^4}{T^4} - \frac{\mathcal{B}_4 + \mathcal{F}_4}{T^4}}\,, \qquad [\cos\varphi = 0] \tag{A.4}$$

which yields the drag force

$$F_x = \frac{\sqrt{\lambda}\,T^2}{2\pi} \frac{v}{\sqrt{1-v^2}} \sqrt{\frac{121}{576}\frac{a^4}{T^4} - \frac{\mathcal{B}_4 + \mathcal{F}_4}{T^4}}\,. \qquad [\cos\varphi = 0] \tag{A.5}$$

This result is valid for any value of a/T, large or small, and it implies that the ratio $F_{\rm aniso}/F_{\rm iso}$ is finite in the limit $v \to 1$ and given by

$$\frac{F_x}{F_{\rm iso}} = \frac{1}{\pi^2} \sqrt{\frac{121 a^4}{576 T^4} - \left(\frac{\mathcal{F}_4 + \mathcal{B}_4}{T^4}\right)}\,. \qquad [\cos\varphi = 0] \tag{A.6}$$

This result is valid for any a, large or small (as long as the motion is exactly aligned with the x-direction). In order to proceed further we need analytic expressions for the coefficients $\mathcal{F}_4, \mathcal{B}_4$. These are known in the limiting cases of small and large a/T. In the first case they are given in eq. (175) of [20]:

$$\begin{aligned}
\mathcal{F}_4 &= -\pi^4 T^4 - \frac{9\pi^2 T^2}{16} a^2 - \left[\frac{101}{384} - \frac{7}{12}\log\left(\frac{2\pi T}{a}\right) - \frac{7}{12}\log\left(\frac{a}{\Lambda}\right)\right] a^4 + O(a^6)\,, \\
\mathcal{B}_4 &= \frac{7\pi^2 T^2}{16} a^2 + \left[\frac{593}{1152} - \frac{7}{12}\log\left(\frac{2\pi T}{a}\right) - \frac{7}{12}\log\left(\frac{a}{\Lambda}\right)\right] a^4 + O(a^6)\,,
\end{aligned} \tag{A.7}$$

where Λ is a reference scale related to the conformal anomaly. Substituting into (A.6) we find

$$\frac{F_x}{F_{\mathrm{iso}}} = 1 + \frac{a^2}{16\pi^2 T^2} + \mathcal{O}\left(\frac{a^4}{T^4}\right) . \qquad [\cos\varphi = 0, \text{small } a/T] \tag{A.8}$$

Note that the dependence on the reference scale Λ has cancelled out in this result, as expected from the discussion in the last paragraph of section 2. The result (A.8) shows that the drag force on an ultra-relativistic quark moving along the transverse directions in an anisotropic plasma with small a/T is greater than the drag in an isotropic plasma at the same temperature, in agreement with our numerical results. In order to make this comparison at equal entropy densities we use the fact that the entropy density at small a/T is given by (see eq. (174) in [20])

$$s = \frac{\pi^2 N_{\mathrm{c}}^2 T^3}{2} + \frac{N_{\mathrm{c}}^2 T}{16} a^2 + O\left(\frac{a^4}{T}\right) . \tag{A.9}$$

Inverting this relation,

$$T = \left(\frac{2}{N_{\mathrm{c}}^2 \pi^2}\right)^{1/3} s^{1/3} \left[1 - \frac{1}{24}\left(\frac{N_{\mathrm{c}}^2}{2\pi}\right)^{2/3} \frac{a^2}{s^{2/3}} + O\left(\frac{a^4}{s^{4/3}}\right)\right] , \tag{A.10}$$

substituting in (A.5) and taking the ratio with (3.28) we arrive at

$$\frac{F_x}{F_{\mathrm{iso}}} = 1 - \frac{1}{48}\left(\frac{N_{\mathrm{c}}^2}{2\pi}\right)^{2/3} \frac{a^2}{s^{2/3}} + \mathcal{O}\left(\frac{a^4}{s^{4/3}}\right) . \qquad [\cos\varphi = 0, \text{small } a^3/s] \tag{A.11}$$

We see that, in contrast to the case of equal temperatures, the drag in the anisotropic plasma is smaller if the comparison is made at equal entropy densities, again in agreement with our numerical results.

In the limit of large a/T the coefficients $\mathcal{F}_4, \mathcal{B}_4$ can be obtained by combining eqs. (35), (89) and (90) of [20]. The result is

$$\mathcal{F}_4 = \frac{1}{132}\left[132 a^4 c_{\mathrm{int}} + 77 a^4 \log\left(\frac{a}{\Lambda}\right) - 348 c_{\mathrm{ent}} \pi^2 a^{1/3} T^{11/3} + \cdots\right] , \tag{A.12}$$

$$\mathcal{B}_4 = \frac{1}{6336}\left[-6336 a^4 c_{\mathrm{int}} + 1331 a^4 - 3696 a^4 \log\left(\frac{a}{\Lambda}\right) + 4032 c_{\mathrm{ent}} \pi^2 a^{1/3} T^{11/3} + \cdots\right] , \tag{A.13}$$

where c_{int} in an integration constant and c_{ent} is the constant introduced in (2.5). Following the same procedure as in the small-a case we find that the ratio at equal temperatures is

$$\frac{F_x}{F_{\mathrm{iso}}} = \frac{\sqrt{2 c_{\mathrm{ent}}}}{\pi} \frac{a^{1/3}}{T^{1/3}} + \cdots , \qquad [\cos\varphi = 0, \text{large } a/T] \tag{A.14}$$

where the dots stand for subleading terms in the large a/T limit, and at equal entropy densities it is

$$\frac{F_x}{F_{\rm iso}} = \frac{1}{2^{1/6}\pi^{1/3}c_{\rm ent}^{3/16}}\left(\frac{s}{N_{\rm c}^2}\right)^{1/48}\frac{1}{a^{1/16}}+\cdots\,, \qquad [\cos\varphi=0, \text{large } a^3/s] \tag{A.15}$$

We conclude that at large anisotropies the ultra-relativistic drag in the anisotropic case is always greater than the isotropic drag.

B Small-anisotropy limit

For small values of a/T analytic expressions for the metric functions can be found [19, 20] by perturbing around the isotropic case. The result is

$$\mathcal{F}(u) = 1-\frac{u^4}{u_{\rm H}^4}+a^2\mathcal{F}_2(u)+\mathcal{O}(a^4)\,, \tag{B.1}$$

$$\mathcal{B}(u) = 1+a^2\mathcal{B}_2(u)+\mathcal{O}(a^4)\,, \tag{B.2}$$

$$\log\mathcal{H}(u) = \frac{a^2u_{\rm H}^2}{4}\log\left[1+\frac{u^2}{u_{\rm H}^2}\right]+\mathcal{O}(a^4)\,, \tag{B.3}$$

where

$$\mathcal{F}_2(u) = \frac{1}{24u_{\rm H}^2}\left[8u^2(u_{\rm H}^2-u^2)-10u^4\log 2+3u_{\rm H}^4+7u^4\log\left(1+\frac{u^2}{u_{\rm H}^2}\right)\right]\,, \tag{B.4}$$

$$\mathcal{B}_2(u) = -\frac{u_{\rm H}^2}{24}\left[\frac{10u^2}{u_{\rm H}^2+u^2}+\log\left(1+\frac{u^2}{u_{\rm H}^2}\right)\right]\,. \tag{B.5}$$

Using these expressions in the general formulas of section 3 we obtain the correction to the isotropic result for the drag force at leading order in a/T. The result for the drag force along the longitudinal direction z is

$$F_z=F_{\rm iso}(T)\left[1+\left(\frac{a^2}{T^2}\right)\frac{1-v^2+\sqrt{1-v^2}+(1+v^2)\log\left(1+\sqrt{1-v^2}\right)}{24\pi^2(1-v^2)}+\mathcal{O}\left(\frac{a^4}{T^4}\right)\right]\,, \tag{B.6}$$

whereas for the transverse direction x it is

$$F_x=F_{\rm iso}(T)\left[1+\left(\frac{a^2}{T^2}\right)\frac{1-v^2+\sqrt{1-v^2}+(4v^2-5)\log\left(1+\sqrt{1-v^2}\right)}{24\pi^2(1-v^2)}+\mathcal{O}\left(\frac{a^4}{T^4}\right)\right]\,, \tag{B.7}$$

The $\mathcal{O}(a^2/T^2)$ correction in (B.6) is positive for $v\in[0,1]$, whereas that in (B.7) is negative for $0\leq v<v_c$ and positive for $v<v_c\leq 1$, where $v_c\simeq 0.9$. This means that, for small enough an anisotropy, the drag force along the longitudinal direction in the anisotropic plasma is always larger than the drag force in an isotropic plasma at the same temperature (but different entropy density). In the case of motion in the transverse direction the anisotropic drag is smaller than the isotropic drag for low v and larger for high v. This is in agreement with the numerical results of section 4.

In order to compare with an isotropic plasma at the same entropy density (but different temperature) we use the relation found in [20] for the entropy density of the anisotropic plasma:

$$s=\frac{\pi^2N_c^2T^3}{2}\left[1+\frac{a^2}{8\pi^2T^2}+\mathcal{O}\left(\frac{a^4}{T^4}\right)\right]. \tag{B.8}$$

Inverting this relation and substituting in (B.6) and (B.7) we get:

$$\begin{aligned}
F_z&=F_{\rm iso}(s)\left[1+\frac{a^2}{24}\left(\frac{N_c^2}{2\pi s}\right)^{2/3}\frac{\sqrt{1-v^2}-(1-v^2)+(1+v^2)\log(1+\sqrt{1-v^2})}{1-v^2}+\mathcal{O}\left(\frac{a^4}{s^{4/3}}\right)\right],\\
F_x&=F_{\rm iso}(s)\left[1+\frac{a^2}{24}\left(\frac{N_c^2}{2\pi s}\right)^{2/3}\frac{\sqrt{1-v^2}-(1-v^2)+(4v^2-5)\log(1+\sqrt{1-v^2})}{1-v^2}+\mathcal{O}\left(\frac{a^4}{s^{4/3}}\right)\right].
\end{aligned} \tag{B.9}$$

In this case the leading correction is positive for all v in z-direction and negative for all v in the x-direction. Again, this is in agreement with the numerical results of section 4.

References

[1] STAR collaboration, J. Adams et al., *Experimental and theoretical challenges in the search for the quark gluon plasma: the STAR collaboration's critical assessment of the evidence from RHIC collisions*, *Nucl. Phys.* **A 757** (2005) 102 [`nucl-ex/0501009`] [INSPIRE].

[2] PHENIX collaboration, K. Adcox et al., *Formation of dense partonic matter in relativistic nucleus-nucleus collisions at RHIC: experimental evaluation by the PHENIX collaboration*, *Nucl. Phys.* **A 757** (2005) 184 [`nucl-ex/0410003`] [INSPIRE].

[3] *Proceedings of the Quark Matter* 2011, *J. Phys.* **G 38** (2011) 120301.

[4] E. Shuryak, *Why does the quark gluon plasma at RHIC behave as a nearly ideal fluid?*, *Prog. Part. Nucl. Phys.* **53** (2004) 273 [`hep-ph/0312227`] [INSPIRE].

[5] E.V. Shuryak, *What RHIC experiments and theory tell us about properties of quark-gluon plasma?*, *Nucl. Phys.* **A 750** (2005) 64 [`hep-ph/0405066`] [INSPIRE].

[6] J.M. Maldacena, *The large-N limit of superconformal field theories and supergravity*, *Adv. Theor. Math. Phys.* **2** (1998) 231 [*Int. J. Theor. Phys.* **38** (1999) 1113] [`hep-th/9711200`] [INSPIRE].

[7] S. Gubser, I.R. Klebanov and A.M. Polyakov, *Gauge theory correlators from noncritical string theory*, *Phys. Lett.* **B 428** (1998) 105 [`hep-th/9802109`] [INSPIRE].

[8] E. Witten, *Anti-de Sitter space and holography*, *Adv. Theor. Math. Phys.* **2** (1998) 253 [`hep-th/9802150`] [INSPIRE].

[9] J. Casalderrey-Solana, H. Liu, D. Mateos, K. Rajagopal and U.A. Wiedemann, *Gauge/string duality, hot QCD and heavy ion collisions*, `arXiv:1101.0618` [INSPIRE].

[10] W. Florkowski, *Anisotropic fluid dynamics in the early stage of relativistic heavy-ion collisions*, *Phys. Lett.* **B 668** (2008) 32 [`arXiv:0806.2268`] [INSPIRE].

[11] W. Florkowski and R. Ryblewski, *Dynamics of anisotropic plasma at the early stages of relativistic heavy-ion collisions*, *Acta Phys. Polon.* **B 40** (2009) 2843 [`arXiv:0901.4653`] [INSPIRE].

[12] R. Ryblewski and W. Florkowski, *Early anisotropic hydrodynamics and the RHIC early-thermalization and HBT puzzles*, *Phys. Rev.* **C 82** (2010) 024903 [`arXiv:1004.1594`] [INSPIRE].

[13] W. Florkowski and R. Ryblewski, *Highly-anisotropic and strongly-dissipative hydrodynamics for early stages of relativistic heavy-ion collisions*, *Phys. Rev.* **C 83** (2011) 034907 [`arXiv:1007.0130`] [INSPIRE].

[14] M. Martinez and M. Strickland, *Dissipative dynamics of highly anisotropic systems*, *Nucl. Phys.* **A 848** (2010) 183 [`arXiv:1007.0889`] [INSPIRE].

[15] R. Ryblewski and W. Florkowski, *Non-boost-invariant motion of dissipative and highly anisotropic fluid*, *J. Phys.* **G 38** (2011) 015104 [`arXiv:1007.4662`] [INSPIRE].

[16] M. Martinez and M. Strickland, *Non-boost-invariant anisotropic dynamics*, *Nucl. Phys.* **A 856** (2011) 68 [`arXiv:1011.3056`] [INSPIRE].

[17] R. Ryblewski and W. Florkowski, *Highly anisotropic hydrodynamics — discussion of the model assumptions and forms of the initial conditions*, *Acta Phys. Polon.* **B 42** (2011) 115 [`arXiv:1011.6213`] [INSPIRE].

[18] R. Ryblewski and W. Florkowski, *Highly-anisotropic and strongly-dissipative hydrodynamics with transverse expansion*, *Eur. Phys. J.* **C 71** (2011) 1761 [`arXiv:1103.1260`] [INSPIRE].

[19] D. Mateos and D. Trancanelli, *The anisotropic $\mathcal{N} = 4$ super Yang-Mills plasma and its instabilities*, *Phys. Rev. Lett.* **107** (2011) 101601 [`arXiv:1105.3472`] [INSPIRE].

[20] D. Mateos and D. Trancanelli, *Thermodynamics and instabilities of a strongly coupled anisotropic plasma*, *JHEP* **07** (2011) 054 [`arXiv:1106.1637`] [INSPIRE].

[21] C. Herzog, A. Karch, P. Kovtun, C. Kozcaz and L. Yaffe, *Energy loss of a heavy quark moving through $\mathcal{N} = 4$ supersymmetric Yang-Mills plasma*, *JHEP* **07** (2006) 013 [`hep-th/0605158`] [INSPIRE].

[22] S.S. Gubser, *Drag force in AdS/CFT*, *Phys. Rev.* **D 74** (2006) 126005 [`hep-th/0605182`] [INSPIRE].

[23] J. Casalderrey-Solana and D. Teaney, *Heavy quark diffusion in strongly coupled $\mathcal{N} = 4$ Yang-Mills*, *Phys. Rev.* **D 74** (2006) 085012 [`hep-ph/0605199`] [INSPIRE].

[24] C.P. Herzog, *Energy loss of heavy quarks from asymptotically AdS geometries*, *JHEP* **09** (2006) 032 [`hep-th/0605191`] [INSPIRE].

[25] E. Caceres and A. Guijosa, *Drag force in charged $\mathcal{N} = 4$ SYM plasma*, *JHEP* **11** (2006) 077 [`hep-th/0605235`] [INSPIRE].

[26] S.-J. Sin and I. Zahed, *Ampere's law and energy loss in AdS/CFT duality*, *Phys. Lett.* **B 648** (2007) 318 [`hep-ph/0606049`] [INSPIRE].

[27] T. Matsuo, D. Tomino and W.-Y. Wen, *Drag force in SYM plasma with B field from AdS/CFT*, *JHEP* **10** (2006) 055 [`hep-th/0607178`] [INSPIRE].

[28] P. Talavera, *Drag force in a string model dual to large-N QCD*, *JHEP* **01** (2007) 086 [`hep-th/0610179`] [INSPIRE].

[29] E. Antonyan, *Friction coefficient for quarks in supergravity duals*, `hep-th/0611235` [INSPIRE].

[30] A. Karch and A. O'Bannon, *Metallic AdS/CFT*, *JHEP* **09** (2007) 024 [`arXiv:0705.3870`] [INSPIRE].

[31] C. Herzog and A. Vuorinen, *Spinning dragging strings*, *JHEP* **10** (2007) 087 [`arXiv:0708.0609`] [INSPIRE].

[32] M. Chernicoff and A. Guijosa, *Energy loss of gluons, baryons and k-quarks in an $\mathcal{N}=4$ SYM plasma*, *JHEP* **02** (2007) 084 [`hep-th/0611155`] [INSPIRE].

[33] S.S. Gubser, *Momentum fluctuations of heavy quarks in the gauge-string duality*, *Nucl. Phys.* **B 790** (2008) 175 [`hep-th/0612143`] [INSPIRE].

[34] J. Casalderrey-Solana and D. Teaney, *Transverse momentum broadening of a fast quark in a $\mathcal{N}=4$ Yang-Mills plasma*, *JHEP* **04** (2007) 039 [`hep-th/0701123`] [INSPIRE].

[35] G. Bertoldi, F. Bigazzi, A.L. Cotrone and J.D. Edelstein, *Holography and unquenched quark-gluon plasmas*, *Phys. Rev.* **D 76** (2007) 065007 [`hep-th/0702225`] [INSPIRE].

[36] K.B. Fadafan, *R^2 curvature-squared corrections on drag force*, *JHEP* **12** (2008) 051 [`arXiv:0803.2777`] [INSPIRE].

[37] M. Chernicoff and A. Guijosa, *Acceleration, energy loss and screening in strongly-coupled gauge theories*, *JHEP* **06** (2008) 005 [`arXiv:0803.3070`] [INSPIRE].

[38] K.B. Fadafan, *Charge effect and finite 't Hooft coupling correction on drag force and jet quenching parameter*, *Eur. Phys. J.* **C 68** (2010) 505 [`arXiv:0809.1336`] [INSPIRE].

[39] F. Bigazzi, A.L. Cotrone, J. Mas, A. Paredes, A.V. Ramallo and J. Tarrío, *D3-D7 quark-gluon plasmas*, *JHEP* **11** (2009) 117 [`arXiv:0909.2865`] [INSPIRE].

[40] K.B. Fadafan, *Heavy quarks in the presence of higher derivative corrections from AdS/CFT*, *Eur. Phys. J.* **C 71** (2011) 1799 [`arXiv:1102.2289`] [INSPIRE].

[41] A. Guijosa and J.F. Pedraza, *Early-time energy loss in a strongly-coupled SYM plasma*, *JHEP* **05** (2011) 108 [`arXiv:1102.4893`] [INSPIRE].

[42] P. Chesler and A. Vuorinen, *Heavy flavor diffusion in weakly coupled $\mathcal{N}=4$ super Yang-Mills theory*, *JHEP* **11** (2006) 037 [`hep-ph/0607148`] [INSPIRE].

[43] S.C. Huot, S. Jeon and G.D. Moore, *Shear viscosity in weakly coupled $\mathcal{N}=4$ super Yang-Mills theory compared to QCD*, *Phys. Rev. Lett.* **98** (2007) 172303 [`hep-ph/0608062`] [INSPIRE].

[44] J.-P. Blaizot, E. Iancu, U. Kraemmer and A. Rebhan, *Hard thermal loops and the entropy of supersymmetric Yang-Mills theories*, *JHEP* **06** (2007) 035 [`hep-ph/0611393`] [INSPIRE].

[45] W. Horowitz and M. Gyulassy, *Heavy quark jet tomography of Pb + Pb at LHC: AdS/CFT drag or pQCD energy loss?*, *Phys. Lett.* **B 666** (2008) 320 [`arXiv:0706.2336`] [INSPIRE].

[46] J.J. Friess, S.S. Gubser and G. Michalogiorgakis, *Dissipation from a heavy quark moving through script $\mathcal{N}=4$ super-Yang-Mills plasma*, *JHEP* **09** (2006) 072 [`hep-th/0605292`] [INSPIRE].

[47] Y.-H. Gao, W.-S. Xu and D.-F. Zeng, *Wake of color fields in charged $\mathcal{N}=4$ SYM plasmas*, `hep-th/0606266` [INSPIRE].

[48] J.J. Friess, S.S. Gubser, G. Michalogiorgakis and S.S. Pufu, *Stress tensor of a quark moving through $\mathcal{N}=4$ thermal plasma*, *Phys. Rev.* **D 75** (2007) 106003 [`hep-th/0607022`] [INSPIRE].

[49] A. Yarom, *High momentum behavior of a quark wake*, *Phys. Rev.* **D 75** (2007) 125010 [`hep-th/0702164`] [INSPIRE].

[50] A. Yarom, *Energy deposited by a quark moving in an $\mathcal{N} = 4$ super Yang-Mills plasma*, *Phys. Rev.* **D 75** (2007) 105023 [`hep-th/0703095`] [INSPIRE].

[51] P.M. Chesler and L.G. Yaffe, *Wake of a quark moving through a strongly coupled $\mathcal{N} = 4$ supersymmetric Yang-Mills plasma*, *Phys. Rev. Lett.* **99** (2007) 152001 [`arXiv:0706.0368`] [INSPIRE].

[52] S.S. Gubser, S.S. Pufu and A. Yarom, *Sonic booms and diffusion wakes generated by a heavy quark in thermal gauge-string duality*, *Phys. Rev. Lett.* **100** (2008) 012301 [`arXiv:0706.4307`] [INSPIRE].

[53] S.S. Gubser and A. Yarom, *Universality of the diffusion wake in the gauge-string duality*, *Phys. Rev.* **D 77** (2008) 066007 [`arXiv:0709.1089`] [INSPIRE].

[54] A. Nata Atmaja and K. Schalm, *Anisotropic drag force from 4D Kerr-AdS black hole*, *JHEP* **04** (2011) 070 [`arXiv:1012.3800`] [INSPIRE].

[55] K.L. Panigrahi and S. Roy, *Drag force in a hot non-relativistic, non-commutative Yang-Mills plasma*, *JHEP* **04** (2010) 003 [`arXiv:1001.2904`] [INSPIRE].

[56] T. Azeyanagi, W. Li and T. Takayanagi, *On string theory duals of Lifshitz-like fixed points*, *JHEP* **06** (2009) 084 [`arXiv:0905.0688`] [INSPIRE].

[57] D.Z. Freedman, S.S. Gubser, K. Pilch and N.P. Warner, *Renormalization group flows from holography-supersymmetry and a c-theorem*, *Adv. Theor. Math. Phys.* **3** (1999) 363 [`hep-th/9904017`] [INSPIRE].

[58] K. Pilch and N.P. Warner, *$\mathcal{N} = 2$ supersymmetric RG flows and the IIB dilaton*, *Nucl. Phys.* **B 594** (2001) 209 [`hep-th/0004063`] [INSPIRE].

[59] A. Buchel and J.T. Liu, *Thermodynamics of the $\mathcal{N} = 2^*$ flow*, *JHEP* **11** (2003) 031 [`hep-th/0305064`] [INSPIRE].

[60] A. Karch, E. Katz, D.T. Son and M.A. Stephanov, *Linear confinement and AdS/QCD*, *Phys. Rev.* **D 74** (2006) 015005 [`hep-ph/0602229`] [INSPIRE].

[61] C.P. Herzog, *Holographic prediction for the deconfinement temperature*, *Phys. Rev. Lett.* **98** (2007) 091601 [`hep-th/0608151`] [INSPIRE].

[62] E. Nakano, S. Teraguchi and W.-Y. Wen, *Drag force, jet quenching and an AdS/QCD model*, *Phys. Rev.* **D 75** (2007) 085016 [`hep-ph/0608274`] [INSPIRE].

[63] C. Hoyos, *Drag and jet quenching of heavy quarks in a strongly coupled script $\mathcal{N} = 2^*$ plasma*, *JHEP* **09** (2009) 068 [`arXiv:0907.5036`] [INSPIRE].

[64] H. Liu, K. Rajagopal and Y. Shi, *Robustness and infrared sensitivity of various observables in the application of AdS/CFT to heavy ion collisions*, *JHEP* **08** (2008) 048 [`arXiv:0803.3214`] [INSPIRE].

3.2 Jet quenching parameter

This section contains the publication:

- M. Chernicoff, D. Fernandez, D. Mateos and D. Trancanelli, "Jet quenching in a strongly coupled anisotropic plasma," *JHEP* **1208** (2012) 041, `arXiv:1203.0561 [hep-th]`.

Published for SISSA by Springer

Received: *July 17, 2012*
Accepted: *July 28, 2012*
Published: *August 7, 2012*

Jet quenching in a strongly coupled anisotropic plasma

Mariano Chernicoff,[a,b] **Daniel Fernández,**[a] **David Mateos**[a,c] **and Diego Trancanelli**[d,e]

[a] *Departament de Física Fonamental & Institut de Ciències del Cosmos (ICC),*
Universitat de Barcelona (UB), Martí i Franquès 1, E-08028 Barcelona, Spain
[b] *Department of Applied Mathematics and Theoretical Physics,*
Centre for Mathematical Sciences,
Wilberforce Road, Cambridge, CB3 0WA, U.K.
[c] *Institució Catalana de Recerca i Estudis Avançats (ICREA),*
Passeig Lluís Companys 23, E-08010, Barcelona, Spain
[d] *Department of Physics, University of Wisconsin,*
Madison, WI 53706, U.S.A.
[e] *Instituto de Física, Universidade de São Paulo,*
05314-970 São Paulo, Brazil

E-mail: `M.Chernicoff@damtp.cam.ac.uk`, `daniel@ffn.ub.edu`,
`dmateos@icrea.cat`, `dtrancan@fma.if.usp.br`

Abstract: The jet quenching parameter of an anisotropic plasma depends on the relative orientation between the anisotropic direction, the direction of motion of the parton, and the direction along which the momentum broadening is measured. We calculate the jet quenching parameter of an anisotropic, strongly coupled $\mathcal{N} = 4$ plasma by means of its gravity dual. We present the results for arbitrary orientations and arbitrary values of the anisotropy. The anisotropic value can be larger or smaller than the isotropic one, and this depends on whether the comparison is made at equal temperatures or at equal entropy densities. We compare our results to analogous calculations for the real-world quark-gluon plasma and find agreement in some cases and disagreement in others.

Keywords: Gauge-gravity correspondence, Holography and quark-gluon plasmas

ArXiv ePrint: 1203.0561

doi:10.1007/JHEP08(2012)041

Contents

---

1 Introduction

A remarkable conclusion from the experiments at the Relativistic Heavy Ion Collider (RHIC) [1, 2] and at the Large Hadron Collider (LHC) (see the contributions on elliptic flow at the LHC in [3]) is that the quark-gluon plasma (QGP) does not behave as a weakly coupled gas of quarks and gluons, but rather as a strongly coupled fluid [4, 5]. This renders perturbative methods inapplicable in general. The lattice formulation of Quantum Chromodynamics (QCD) is also of limited utility, since for example it is not well suited for studying real-time phenomena. This has provided a strong motivation for understanding the dynamics of strongly coupled non-Abelian plasmas through the gauge/string duality [6–8] (see [9] for a recent review of applications to the QGP).

For a period of time τ_{out} immediately after the collision, the system thus created is anisotropic and far from equilibrium. After a time $\tau_{\text{iso}} > \tau_{\text{out}}$ the system becomes locally isotropic. It has been proposed than an intrinsically anisotropic hydrodynamical description can be used to describe the system at intermediate times $\tau_{\text{out}} < \tau < \tau_{\text{iso}}$ [10–18]. In this phase the plasma is assumed to have significantly unequal pressures in the longitudinal and transverse directions. The standard hydrodynamic description is a derivative expansion around equal pressures, and therefore it is not applicable in this regime. In contrast, the intrinsically anisotropic hydrodynamical description is a derivative expansion around an anisotropic state, and hence in this case the requirement that derivative corrections be small does not imply small pressure differences. In a real collision the degree of anisotropy will decrease with time, but for some purposes it is a good approximation to take it to be constant over an appropriate time scale.

Motivated by these considerations, in this paper we will investigate the effect of an intrinsic anisotropy on the momentum broadening experienced by a fast parton moving through the plasma. For this purpose we will compute the jet quenching parameter for an ultra-relativistic quark propagating through an anisotropic $\mathcal{N} = 4$ super Yang-Mills

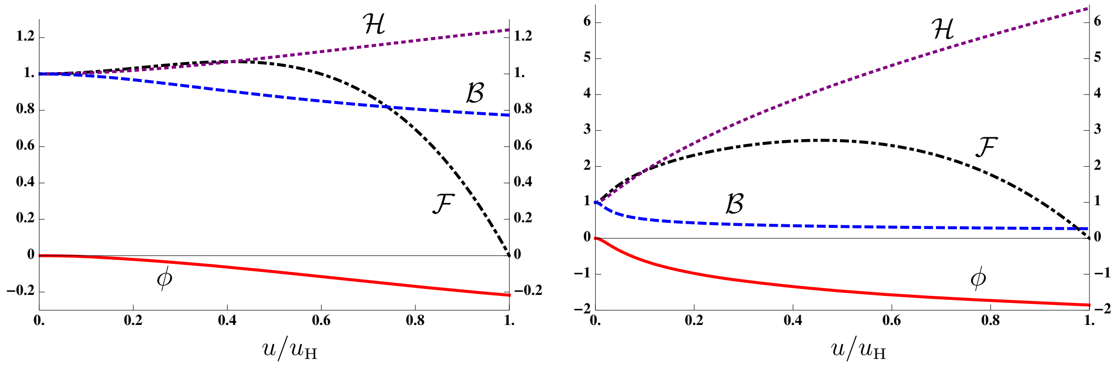

Figure 1. Metric functions for $a/T \simeq 4.4$ (left) and $a/T \simeq 86$ (right).

plasma by means of its gravity dual [19, 20]. As we will review below, the plasma is held in anisotropic equilibrium by an external force. The gravity solution possesses an anisotropic horizon, it is completely regular on and outside the horizon, and it is solidly embedded in type IIB string theory. For these reasons it provides an ideal toy model in which questions about anisotropic effects at strong coupling can be addressed from first principles.

Previous calculations of the jet quenching parameter in the presence of anisotropy in the context of the gauge/gravity correspondence include [21, 22]. While this paper was being typewritten we received [23], in which the jet quenching parameter along particular directions in the background of [19, 20] is studied in the limit of small anisotropy.

2 Gravity solution

The type IIB supergravity solution of [19, 20] in the string frame takes the form

$$ds^2 = \frac{L^2}{u^2}\left(-\mathcal{F}\mathcal{B}\,dt^2 + dx^2 + dy^2 + \mathcal{H}dz^2 + \frac{du^2}{\mathcal{F}}\right) + L^2 e^{\frac{1}{2}\phi} d\Omega_5^2, \tag{2.1}$$

$$\chi = az\,, \qquad \phi = \phi(u)\,, \tag{2.2}$$

where χ and ϕ are the axion and the dilaton, respectively, and (t,x,y,z) are the gauge theory coordinates. Since there is rotational invariance in the xy-directions, we will refer to these as the transverse directions, and to z as the longitudinal direction. $\mathcal{F},\mathcal{B}$ and $\mathcal{H}$ are functions of the holographic radial coordinate u that were determined numerically in [19, 20]. Their form for two values of a/T is plotted in figure 1. The horizon lies at $u = u_{\rm H}$, where $\mathcal{F} = 0$, and the boundary lies at $u = 0$, where $\mathcal{F} = \mathcal{B} = \mathcal{H} = 1$ and $\phi = 0$. The metric near the boundary asymptotes to $AdS_5 \times S^5$. Note that the axion is linear in the z-coordinate. The proportionality constant a has dimensions of mass and is a measure of the anisotropy. The axion profile is dual in the gauge theory to a position-dependent theta parameter that depends linearly on z. This acts as an isotropy-breaking external source that forces the system into an anisotropic equilibrium state.

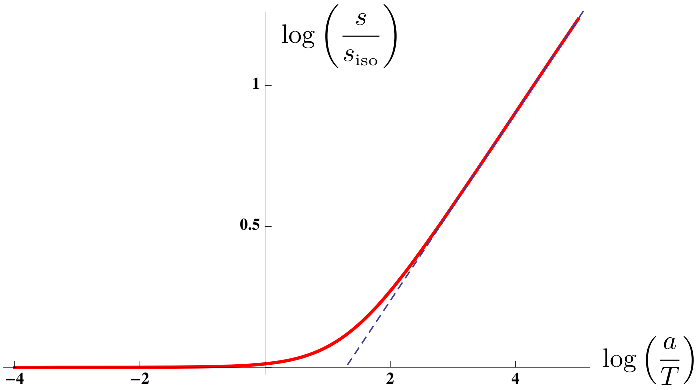

Figure 2. Log-log plot of the entropy density as a function of a/T, with s_{iso} defined as in eq. (2.4). The dashed blue line is a straight line with slope 1/3.

If $a = 0$ then the solution reduces to the isotropic black D3-brane solution dual to the isotropic $\mathcal{N} = 4$ theory at finite temperature. In this case

$$\mathcal{B} = \mathcal{H} = 1\,, \qquad \chi = \phi = 0\,, \qquad \mathcal{F} = 1 - \frac{u^4}{u_{\rm H}^4}\,, \qquad u_{\rm H} = \frac{1}{\pi T} \tag{2.3}$$

and the entropy density takes the form

$$s_{\text{iso}} = \frac{\pi^2}{2} N_{\rm c}^2 T^3\,. \tag{2.4}$$

figure 2 shows the entropy density of the anisotropic plasma as a function of the dimensionless ratio a/T, normalized to the entropy density of the isotropic plasma at the same temperature. At small a/T the entropy density scales as in the isotropic case, whereas at large a/T it scales as [19, 20, 24]

$$s = c_{\text{ent}} N_{\rm c}^2 a^{1/3} T^{8/3}\,, \tag{2.5}$$

where $c_{\text{ent}} \simeq 3.21$. The transition between the two behaviours takes place approximately around $a/T \simeq 3.7$.

A feature of the solution (2.2) that played an important role in the analysis of [19, 20] is the presence of a conformal anomaly. Its origin lies in the fact that diffeomorphism invariance in the radial direction u gets broken in the process of renormalization of the on-shell supergravity action. In the gauge theory this means that scale invariance is broken by the renormalization process. One manifestation of the anomaly is the fact that, unlike the entropy density, other thermodynamic quantities do not depend solely on the ratio a/T but on a and T separately. This will not be the case for the jet quenching parameter, which as we will see takes the form $\hat{q}(a, T) = T^3 f(a/T)$.

3 Jet quenching parameter

In this section we will calculate the jet quenching parameter $\hat{q}$ for an ultra-relativistic quark following the prescription of refs. [25–27]. This instructs us to consider the worldsheet of a

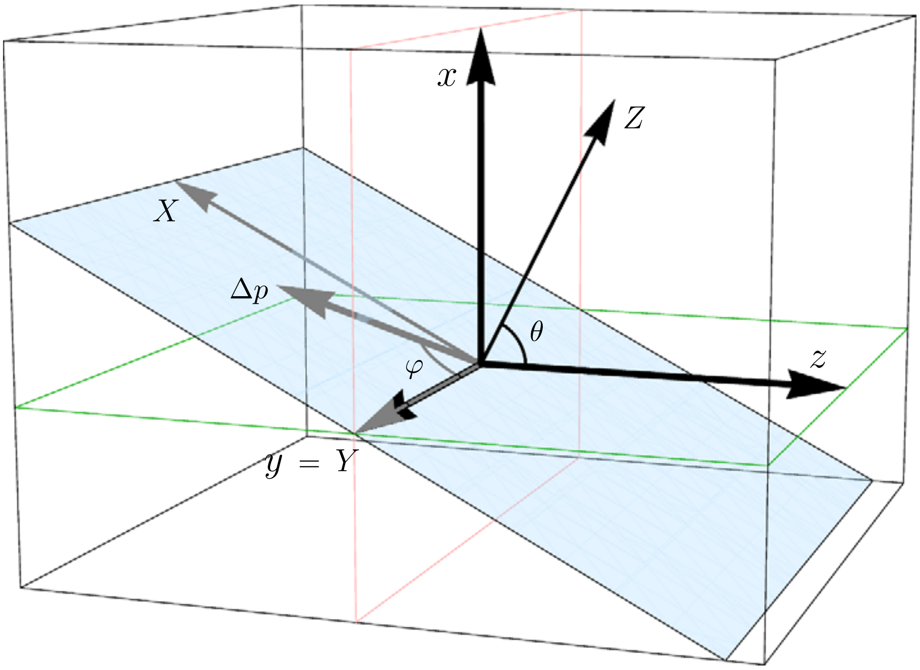

Figure 3. Relative orientation between the anisotropic direction z, the direction of motion of the quark Z, and the direction in which the momentum broadening is measured Δp. In the context of a heavy ion collision z would correspond to the longitudinal direction along the beam, and x, y to the directions in the transverse plane. The direction of motion lies in the xz-plane at an angle θ with respect to the z-axis. The momentum broadening takes place in any direction in the XY-plane orthogonal to Z. X lies within the xz-plane, whereas $y = Y$ is orthogonal to it. The angle in the XY-plane between the Y axis and the direction of the momentum broadening is φ.

string whose endpoints move at the speed of light along a given boundary direction and are separated a small distance ℓ along an orthogonal direction. The former is the direction of motion of the quark, and the latter is the direction along which the momentum broadening takes place. In the presence of anisotropy the jet quenching parameter depends on how these directions are oriented with respect to the longitudinal and transverse directions in the plasma. Recall that there is rotational symmetry in the xy-directions but not in the z-direction. In the context of a heavy ion collision z would correspond to the longitudinal, beam direction, and x, y to the directions in the transverse plane. Given the rotational symmetry in this plane, we will assume without loss of generality that the the direction of motion is contained in the xz-plane, and we will denote it by Z (see figure 3). We call θ the angle between this direction and the z-axis. The two independent orthogonal directions to Z can then be chosen so that one, which we denote by X, lies within the xz-plane, and the other one, Y, coincides with the y-axis. We denote as φ the polar angle in the XY-plane with respect to the Y-axis. The XYZ-coordinate system is obtained from the xyz-coordinate system by a rotation of angle θ around the $y = Y$ axis, as described by eq. (3.31) below. We will determine the jet quenching parameter associated to momentum broadening in an arbitrary direction in the XY-plane, and we will refer to it as $\hat{q}_{\theta,\varphi}$ in order to emphasize that it depends on the two angles defined above.

Now recall that $\hat{q}$ is the average momentum squared acquired by the quark after traveling through the medium a unit distance [28]. If we call p_φ the component of the momentum in the direction within the XY-plane specified by φ, then clearly

$$p_\varphi = p_Y \cos\varphi + p_X \sin\varphi\,. \tag{3.1}$$

Squaring and taking an average we obtain

$$\langle \Delta p_\varphi^2 \rangle = \cos^2\varphi \langle \Delta p_Y^2 \rangle + \sin^2\varphi \langle \Delta p_X^2 \rangle\,, \tag{3.2}$$

where we used the fact that $\langle \Delta p_Y \Delta p_X \rangle = 0$ given the symmetry under $Y \to -Y$. Rewritten in terms of the corresponding jet quenching parameters this becomes

$$\hat{q}_{\theta,\varphi} = \hat{q}_{\theta,0} \cos^2\varphi + \hat{q}_{\theta,\pi/2} \sin^2\varphi\,. \tag{3.3}$$

We will see that the gravity calculation reproduces this relation.

Rather than starting with the most general case, for pedagogical reasons we will first study two particular cases corresponding to motion along the longitudinal direction and motion contained within the transverse plane. The general case will be discussed in section 3.3.

3.1 Motion along the longitudinal direction

This case corresponds to $\theta = 0$ and is the simplest one because the momentum broadening takes place in the transverse xy-plane, which is rotationally symmetric. In particular, this means that the result is independent of φ, since $\hat{q}_{0,0} = \hat{q}_{0,\pi/2}$. In the context of heavy ion collisions, this case corresponds to motion of the parton along the beam direction.

It is convenient to carry out the calculation using the light cone coordinates

$$z^\pm = \frac{t \pm z}{\sqrt{2}}\,. \tag{3.4}$$

Ignoring the sphere part, which will play no role in the following, the metric (2.1) reads

$$\begin{aligned} ds^2 = \frac{L^2}{u^2}\bigg[&\frac{1}{2}(\mathcal{H} - \mathcal{F}\mathcal{B})(dz^+)^2 + \frac{1}{2}(\mathcal{H} - \mathcal{F}\mathcal{B})(dz^-)^2 \\ &-(\mathcal{H} + \mathcal{F}\mathcal{B})dz^+ dz^- + dx^2 + dy^2 + \frac{du^2}{\mathcal{F}}\bigg]\,. \end{aligned} \tag{3.5}$$

We consider a quark moving along z^-. Given the symmetry in the xy-plane we set $y = 0$ without loss of generality. We then fix the static gauge by identifying $(z^-, x) = (\tau, \sigma)$ and specify the string embedding through one function $u = u(x)$ subject to the boundary condition that $u(\pm\ell/2) = 0$. Under these circumstances the Nambu-Goto action

$$S = -\frac{1}{2\pi\alpha'} \int d\tau d\sigma \sqrt{-\det g_{\text{ind}}} \tag{3.6}$$

takes the form

$$S = 2i\frac{L^2}{2\pi\alpha'}\int dz^- \int_0^{\ell/2} dx\, \frac{1}{u^2}\sqrt{\frac{1}{2}\left(\mathcal{H}-\mathcal{F}\mathcal{B}\right)\left(1+\frac{u'^2}{\mathcal{F}}\right)}\,, \tag{3.7}$$

where the factor of 2 comes from the fact that the integral over x covers only one half of the string, and $u' = du/dx$. Note that the action is imaginary because the string worldsheet is spacelike, as expected in order for the jet quenching parameter to be real [26] (see also [9] for an extensive discussion). The fact that the Lagrangian does not depend on x explicitly leads to a conserved quantity Π_x and to the first-order equation

$$u'^2 = \frac{\mathcal{F}}{2\Pi_x^2 u^4}\left[\left(\mathcal{H}-\mathcal{F}\mathcal{B}\right) - 2\Pi_x^2 u^4\right]\,. \tag{3.8}$$

The turn-around point for the string is defined by $u' = 0$. The prescription for computing the jet quenching parameter instructs us to work in the limit $\ell \to 0$. As we will see below, this corresponds to the limit $\Pi_x \to 0$. In this case it is clear that the term inside the square brackets is positive. This follows from the fact that $\mathcal{H}$ ($\mathcal{F}\mathcal{B}$) is monotonically increasing (decreasing) from the boundary to the horizon, and that near the boundary $\mathcal{H}-\mathcal{F}\mathcal{B}$ scales as $a^2u^2/4$.

We thus see that in the limit of interest the string descends all the way into the bulk and turns around precisely at the black hole horizon, as in the isotropic case [25, 26]. As explained in [27], the string worldsheet must have this property in order to be dual to a gauge theory Wilson loop with the operator ordering required for the extraction of the jet quenching parameter. The reason is that this ordering can be implemented by thinking of the time coordinate t as a complex coordinate and requiring the worldlines of the quark and the antiquark to lie on the $\mathrm{Im}\, t = 0$ and $\mathrm{Im}\, t = -i\epsilon$ slices, respectively. In the black hole geometry (2.2) $\mathrm{Im}\, t$ is periodic with period $1/T$ and these two slices only meet at the horizon, irrespectively of whether $a = 0$ or $a \neq 0$. Therefore the string must descend from the boundary to the horizon on the (say) $\mathrm{Im}\, t = 0$ slice, turn around, and return to the boundary on the $\mathrm{Im}\, t = -i\epsilon$ slice. However, since the metric on these two slices is identical, the resulting string action is the same as that of a horizon-touching string worldsheet that lies entirely on a single slice, and which is dual to a Wilson loop with a different operator ordering. This is the reason why the subtlety identified in ref. [27] did not change the isotropic result of refs. [25, 26], which considered a single slice. Exactly the same equivalence applies in our anisotropic case, since all the string worldsheets that we will consider turn around precisely at the horizon. For this reason in what follows we will simply use the prescription from [25, 26].

Integrating equation (3.8) we obtain half the separation between the two endpoints of the string along the spatial side of the Wilson loop:

$$\frac{\ell}{2} = \sqrt{2}\,\Pi_x \int_0^{u_{\mathrm{H}}} du \frac{u^2}{\sqrt{\mathcal{F}}\sqrt{\left(\mathcal{H}-\mathcal{F}\mathcal{B}\right) - 2\Pi_x^2 u^4}}\,. \tag{3.9}$$

Note that, as anticipated above, $\ell \to 0$ as $\Pi_x \to 0$, and in this limit we have

$$\ell = 2\sqrt{2}\,\Pi_x \mathcal{I}_x + \mathcal{O}(\Pi_x^2) \tag{3.10}$$

with

$$\mathcal{I}_x \equiv \int_0^{u_{\rm H}} du \frac{u^2}{\sqrt{\mathcal{F}}\sqrt{\mathcal{H}-\mathcal{F}\mathcal{B}}} \tag{3.11}$$

a convergent integral.

To compute the jet quenching parameter we need to evaluate the on-shell action (3.7) on the solution (3.8). After changing the integration variable from x to u the result is

$$S = i\frac{\sqrt{\lambda}\,L^-}{\sqrt{2}\,\pi}\int_0^{u_{\rm H}} du \frac{(\mathcal{H}-\mathcal{F}\mathcal{B})}{u^2\sqrt{\mathcal{F}}\sqrt{(\mathcal{H}-\mathcal{F}\mathcal{B})-2\Pi_x^2 u^4}}\,, \tag{3.12}$$

where L^- is the long side of the Wilson loop. This action diverges due to the integration near $u=0$. This can be seen by expanding in powers of Π_x,

$$S = i\frac{\sqrt{\lambda}\,L^-}{\sqrt{2}\,\pi}\int_0^{u_{\rm H}} du \frac{\sqrt{\mathcal{H}-\mathcal{F}\mathcal{B}}}{u^2\sqrt{\mathcal{F}}} + i\frac{\sqrt{\lambda}\,L^-\ell^2}{8\sqrt{2}\,\pi\,\mathcal{I}_x} + \mathcal{O}(\ell^4)\,, \tag{3.13}$$

where we have used the relation (3.10). All terms of order ℓ^2 and higher are finite, whereas the first, ℓ-independent term diverges as $\log u$. This term can be renormalized away using several methods, including subtraction of the action of two disconnected strings [25, 26] or addition to the string action of a counterterm proportional to $\log u \int d\tau\sqrt{\gamma}$, where γ is the induced worldline metric on a constant-σ slice of the string worldsheet. The logarithm in this counterterm illustrates the fact that the renormalized string action is sensitive to the conformal anomaly in the gauge theory [19, 20]. However, the jet quenching parameter is given by the finite ℓ^2-term, whose extraction does not require any renormalization. It thus follows that $\hat{q}$ is insensitive to the presence of the anomaly, as anticipated in the Introduction. Using the prescription from [25, 26],

$$e^{i2S} = \langle W^A(C)\rangle = \exp\left[-\frac{L^-\ell^2}{4\sqrt{2}}\,\hat{q}\right]\,, \tag{3.14}$$

where S denotes the finite part of the action, we finally arrive at

$$\hat{q}_z \equiv \hat{q}_{0,\varphi} = \frac{\sqrt{\lambda}}{\pi\mathcal{I}_x}\,, \tag{3.15}$$

where the subscript in $\hat{q}_z$ reminds us of the direction of motion of the quark. Eq. (3.15) reduces to the correct result in the isotropic limit. In this case, using (2.3), we see that

$$\mathcal{I}_x = u_{\rm H}^2\int_0^{u_{\rm H}} du \frac{1}{\sqrt{1-u^4/u_{\rm H}^4}} = \frac{1}{\pi^3 T^3}\frac{\sqrt{\pi}\,\Gamma\left(\frac{5}{4}\right)}{\Gamma\left(\frac{3}{4}\right)}\,. \tag{3.16}$$

Substituting into (3.15) we reproduce the isotropic result [25, 26]

$$\hat{q}_{\rm iso}(T) = \frac{\pi^{3/2}\,\Gamma\left(\frac{3}{4}\right)}{\Gamma\left(\frac{5}{4}\right)}\sqrt{\lambda}\,T^3\,. \tag{3.17}$$

For later purposes it is useful to rewrite this in terms of the entropy density (2.4) as

$$\hat{q}_{\rm iso}(s) = \frac{2\Gamma\left(\frac{3}{4}\right)}{\sqrt{\pi}\,\Gamma\left(\frac{5}{4}\right)}\sqrt{\lambda}\,\frac{s}{N_{\rm c}^2}\,. \tag{3.18}$$

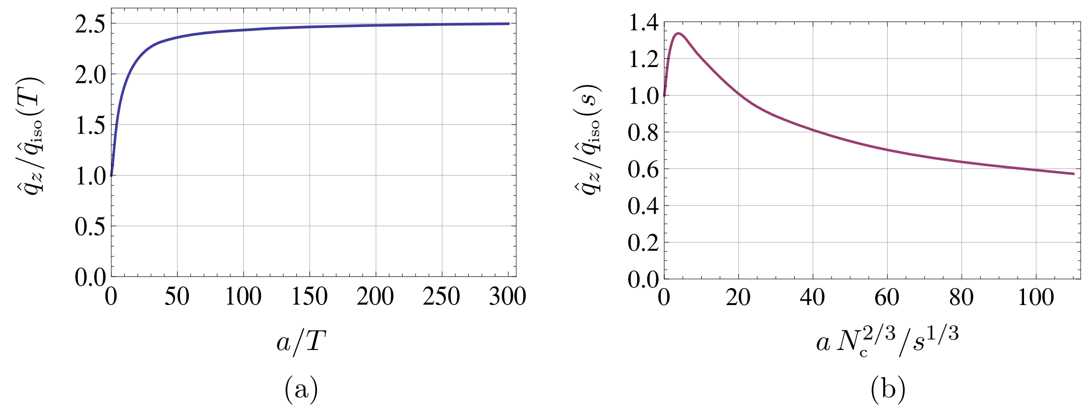

Figure 4. Jet quenching parameter for a quark moving along the longitudinal z-direction as a function of the anisotropy. $\hat{q}_z = \hat{q}_{0,\varphi}$ and a are plotted in the appropriate units to facilitate comparison with the isotropic result for a plasma at the same temperature (a), or at the same entropy density (b). The isotropic result is given in eqs. (3.17) and (3.18).

Since for general a the metric functions in (2.2) are only known numerically, we have numerically determined $\hat{q}_z$ as a function of the magnitude of the anisotropy a measured in units of the temperature or in units of the entropy density (see figure 4). The reason for working with both is that we wish to compare the jet quenching in the anisotropic plasma to that in the isotropic plasma, and this can be done at least in two different ways: the two plasmas can be taken to have the same temperatures but different entropy densities, or the same entropy densities but different temperatures.

3.2 Motion in the transverse plane

Given the rotational symmetry in the xy-plane, we will choose the direction of motion to be the x-direction. Thus this case corresponds to $\theta = \pi/2$ in the parametrization of figure 3. Since there is no symmetry between the y and z directions, in this case the result will depend on φ.

As in the previous example, it is convenient to work with adapted coordinates

$$x^{\pm} = \frac{t \pm x}{\sqrt{2}}\,, \tag{3.19}$$

in terms of which the metric takes the form

$$\begin{aligned} ds^2 = \frac{L^2}{u^2}\bigg[&\frac{1}{2}(1-\mathcal{F}\mathcal{B})(dx^+)^2 + \frac{1}{2}(1-\mathcal{F}\mathcal{B})(dx^-)^2 \\ &-(1+\mathcal{F}\mathcal{B})dx^+dx^- + dy^2 + \mathcal{H}dz^2 + \frac{du^2}{\mathcal{F}}\bigg]\,. \end{aligned} \tag{3.20}$$

In this case we choose the static gauge $(\tau, \sigma) = (x^-, u)$, set $x^+ =$ const., and specify the string projection in the yz-plane as

$$y \to \cos\varphi\, y(u)\,, \qquad z \to \sin\varphi\, z(u)\,. \tag{3.21}$$

Under these circumstances, the Nambu-Goto action (3.6) becomes

$$S = 2i\frac{L^2}{2\pi\alpha'}\int dx^- \int_0^{u_{\rm H}} du \frac{1}{u^2}\sqrt{\frac{1}{2}\left(1-\mathcal{F}\mathcal{B}\right)\left(\frac{1}{\mathcal{F}} + y'^2\cos^2\varphi + \mathcal{H}z'^2\sin^2\varphi\right)}\,, \tag{3.22}$$

where the primes denote differentiation with respect to u and the overall factor of 2 comes from the two branches of the string. We now follow the procedure in the previous section to obtain the jet quenching parameter. Since the Lagrangian does not depend on y, z explicitly we find that

$$y' = \frac{\sqrt{2\mathcal{H}}\, u^2\, \Pi_y}{\sqrt{\mathcal{F}}\sqrt{\mathcal{H}\left(1-\mathcal{F}\mathcal{B}\right) - 2u^4\left(\mathcal{H}\,\Pi_y^2\cos^2\varphi + \Pi_z^2\sin^2\varphi\right)}} \tag{3.23}$$

and

$$z' = \frac{\sqrt{2}\, u^2\, \Pi_z}{\sqrt{\mathcal{H}\mathcal{F}}\sqrt{\mathcal{H}\left(1-\mathcal{F}\mathcal{B}\right) - 2u^4\left(\mathcal{H}\,\Pi_y^2\cos^2\varphi + \Pi_z^2\sin^2\varphi\right)}}\,, \tag{3.24}$$

where Π_y and Π_z are conserved quantities (into which some factors of $\cos\varphi$ and $\sin\varphi$ have been absorbed). An argument analogous to that in section 3.1 shows that the denominators in these expressions only vanish at the horizon in the small-Π limit. By integrating these equations we obtain the separation between the two endpoints of the string. As in the previous section we will be interested in the limit $\Pi_y, \Pi_z \to 0$, so we work to lowest order in these quantities:

$$\ell = 2\sqrt{2}\,\Pi_y\,\mathcal{I}_{xy} + \mathcal{O}\left(\Pi^2\right)\,, \qquad \ell = 2\sqrt{2}\,\Pi_z\,\mathcal{I}_{xz} + \mathcal{O}\left(\Pi^2\right)\,, \tag{3.25}$$

with

$$\mathcal{I}_{xy} \equiv \int_0^{u_{\rm H}} du \frac{u^2}{\sqrt{\mathcal{F}(1-\mathcal{F}\mathcal{B})}}\,, \qquad \mathcal{I}_{xz} \equiv \int_0^{u_{\rm H}} du \frac{u^2}{\mathcal{H}\sqrt{\mathcal{F}(1-\mathcal{F}\mathcal{B})}} \tag{3.26}$$

convergent integrals. Substituting the solution (3.23)-(3.24) into the action (3.22), expanding in powers of Π and keeping only the term of order Π^2 we obtain

$$S = \frac{i\sqrt{\lambda}L^-}{\sqrt{2}\,\pi}\int_0^{u_{\rm H}} du \left(\frac{u^2\,\Pi_y^2\,\cos^2\varphi}{\sqrt{\mathcal{F}(1-\mathcal{F}\mathcal{B})}} + \frac{u^2\,\Pi_z^2\,\sin^2\varphi}{\mathcal{H}\sqrt{\mathcal{F}(1-\mathcal{F}\mathcal{B})}}\right)\,. \tag{3.27}$$

Using (3.25) and (3.26) the action becomes

$$S = \frac{i\sqrt{\lambda}L^-\ell^2}{8\sqrt{2}\,\pi}\left(\frac{\cos^2\varphi}{\mathcal{I}_{xy}} + \frac{\sin^2\varphi}{\mathcal{I}_{xz}}\right)\,, \tag{3.28}$$

so applying the prescription (3.14) and defining

$$\hat{q}_\perp \equiv \hat{q}_{\pi/2,0} = \frac{\sqrt{\lambda}}{\pi\mathcal{I}_{yx}}\,, \qquad \hat{q}_{\rm L} \equiv \hat{q}_{\pi/2,\pi/2} = \frac{\sqrt{\lambda}}{\pi\mathcal{I}_{yz}} \tag{3.29}$$

we finally arrive at

$$\hat{q}_{\pi/2,\varphi} = \hat{q}_\perp\cos^2\varphi + \hat{q}_{\rm L}\sin^2\varphi\,. \tag{3.30}$$

This is a particular case of the relation (3.3) anticipated above. In figure 5 we have plotted this result for several values of φ.

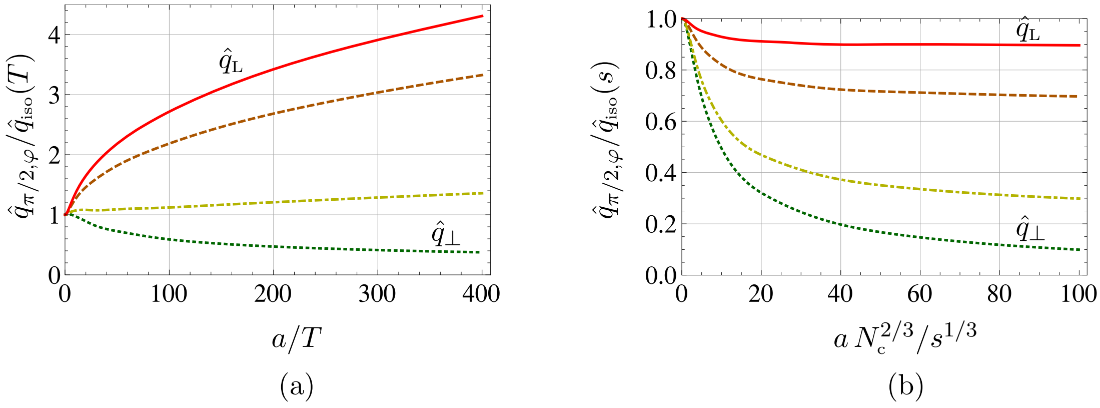

Figure 5. Jet quenching parameter $\hat{q}_{\pi/2,\varphi}$ associated to momentum broadening in the yz-plane for a quark moving along the transverse direction x. The direction in the yz-plane lies at an angle (from top to bottom) $\varphi = \pi/2, \pi/3, \pi/6, 0$ with respect to the y-axis (see figure 3). The top (bottom) curves correspond to momentum broadening along the longitudinal (transverse) direction. $\hat{q}_{\pi/2,\varphi}$ and a are plotted in the appropriate units to facilitate comparison with the isotropic result for a plasma at the same temperature (a), or at the same entropy density (b). The isotropic result is given in eqs. (3.17) and (3.18).

3.3 Arbitrary motion

We now consider an arbitrary motion within the xz-plane, as explained in figure 3. For this purpose we first define rotated coordinates X, Z through

$$\begin{aligned} z &= Z\cos\theta - X\sin\theta\,, \\ x &= Z\sin\theta + X\cos\theta\,, \\ y &= Y\,, \end{aligned} \tag{3.31}$$

and then we go to light-cone coordinates by setting

$$t = \frac{Z^- + Z^+}{\sqrt{2}}\,, \qquad Z = \frac{Z^- - Z^+}{\sqrt{2}}\,. \tag{3.32}$$

Recall that Z is the direction of motion. We thus fix the static gauge $Z^- = \tau$, $u = \sigma$, and seek a solution for the string embedding parametrized as

$$Z^+ = Z^+(u)\,, \qquad X \to X(u)\sin\varphi\,, \qquad Y \to Y(u)\cos\varphi\,. \tag{3.33}$$

With this choice φ is the polar angle in the plane orthogonal to Z between the direction of momentum broadening and the Y-axis. Note that we must allow for a non-constant embedding in the Z^+-direction in order to find a solution.

Starting from the ansatz above it is straightforward to obtain the Nambu-Goto action (3.6). However, the resulting expression is quite lengthy and we will not write it down explicitly. As in the previous sections, we can use the fact that the action does not depend explicitly on Z^+, X, and Y. This allows us to express the derivatives with respect to u of these embedding functions in terms of three constants of motion, which we call Π_+, Π_X, and Π_Y. We are only interested in the limit in which these quantities are small. In this limit we find

$$(z^+)' = c_{++}\Pi_+ + \frac{1}{\sin\varphi}c_{+X}\Pi_X + \mathcal{O}\left(\Pi^2\right) , \tag{3.34}$$

$$X' = \frac{1}{\sin\varphi}c_{X+}\Pi_+ + \frac{1}{\sin^2\varphi}c_{XX}\Pi_X + \mathcal{O}\left(\Pi^2\right) , \tag{3.35}$$

$$Y' = \frac{1}{\cos^2\varphi}c_{YY}\Pi_Y + \mathcal{O}\left(\Pi^2\right) , \tag{3.36}$$

with

$$c_{++} \equiv \frac{1}{\sqrt{2}}\frac{u^2(\mathcal{FB}(\cos^2\theta + \mathcal{H}\sin^2\theta) - \mathcal{H})}{\mathcal{FBH}\sqrt{\mathcal{F}(\sin^2\theta + \mathcal{H}\cos^2\theta - \mathcal{FB})}} , \tag{3.37}$$

$$c_{XX} \equiv \frac{\sqrt{2}\,u^2(\sin^2\theta + \mathcal{H}\cos^2\theta)}{\mathcal{H}\sqrt{\mathcal{F}(\sin^2\theta + \mathcal{H}\cos^2\theta - \mathcal{FB})}} , \tag{3.38}$$

$$c_{+X} = c_{X+} \equiv \frac{u^2(\mathcal{H}-1)\sin\theta\cos\theta}{\mathcal{H}\sqrt{\mathcal{F}(\sin^2\theta + \mathcal{H}\cos^2\theta - \mathcal{FB})}} , \tag{3.39}$$

$$c_{YY} \equiv \frac{\sqrt{2}\,u^2}{\sqrt{\mathcal{F}(\sin^2\theta + \mathcal{H}\cos^2\theta - \mathcal{FB})}} . \tag{3.40}$$

An argument analogous to that in section 3.1 shows that the denominators in these expressions only vanish at the horizon in the small-Π limit. The endpoints of the string are not separated in the z^+-direction, so we must have $\int dz^+ = 0$. Integrating (3.34) then gives

$$\Pi_+ = -\frac{1}{\sin\varphi}\frac{\int_0^{u_\mathrm{H}} du\, c_{+X}}{\int_0^{u_\mathrm{H}} du\, c_{++}}\Pi_X + \mathcal{O}\left(\Pi^2\right) . \tag{3.41}$$

This result can now be used in the integration of eq. (3.35) to obtain Π_X:

$$\Pi_X = \frac{\ell}{2}\frac{\sin^2\varphi\int_0^{u_\mathrm{H}} du\, c_{++}}{\left(\int_0^{u_\mathrm{H}} du\, c_{++}\right)\left(\int_0^{u_\mathrm{H}} du\, c_{XX}\right) - \left(\int_0^{u_\mathrm{H}} du\, c_{+X}\right)^2} + \mathcal{O}\left(\Pi^2\right) . \tag{3.42}$$

Similarly, integrating (3.36) yields

$$\Pi_Y = \frac{\ell}{2}\frac{\cos^2\varphi}{\int_0^{u_\mathrm{H}} du\, c_{YY}} + \mathcal{O}\left(\Pi^2\right) . \tag{3.43}$$

Inserting eqs. (3.34)–(3.36) into the action, expanding to quadratic order in the Π's and dropping the leading, Π-independent term we find

$$S = 2i\frac{\sqrt{\lambda}L^-}{4\pi}\int_0^{u_\mathrm{H}} du\left[c_{++}\Pi_+^2 + \frac{1}{\sin^2\varphi}c_{XX}\Pi_X^2 + \frac{2}{\sin\varphi}c_{+X}\Pi_+\Pi_X + \frac{1}{\cos^2\varphi}c_{YY}\Pi_Y^2\right] . \tag{3.44}$$

With the explicit expressions (3.41)–(3.43) this reduces to

$$S = 2i\frac{\sqrt{\lambda}L^-\ell^2}{16\pi}\left[P(\theta)\sin^2\varphi + Q(\theta)\cos^2\varphi\right] , \tag{3.45}$$

with

$$P(\theta) \equiv \frac{\int_0^{u_\mathrm{H}} du\, c_{++}}{\left(\int_0^{u_\mathrm{H}} du\, c_{++}\right)\left(\int_0^{u_\mathrm{H}} du\, c_{XX}\right) - \left(\int_0^{u_\mathrm{H}} du\, c_{+X}\right)^2}\,, \qquad Q(\theta) \equiv \frac{1}{\int_0^{u_\mathrm{H}} du\, c_{YY}}\,. \tag{3.46}$$

Using the prescription (3.14) we finally arrive at

$$\hat{q}_{\theta,\varphi} = \frac{\sqrt{2\lambda}}{\pi}\left[P(\theta)\sin^2\varphi + Q(\theta)\cos^2\varphi\right]. \tag{3.47}$$

We see that we have indeed derived the expected relation (3.3) with

$$\hat{q}_{\theta,0} = \frac{\sqrt{2\lambda}}{\pi}\,P(\theta)\,, \qquad \hat{q}_{\theta,\pi/2} = \frac{\sqrt{2\lambda}}{\pi}\,Q(\theta)\,. \tag{3.48}$$

Setting $\theta = 0$ in (3.47) we recover the previous result (3.30). In figure 6 we have plotted the result (3.47) for $\varphi = 0$ and $\varphi = \pi/2$ as a function of the ratios a/T and $aN_\mathrm{c}^{2/3}/s^{1/3}$ for different values of θ. In figures 7 and 8 we have plotted the result as a function of θ and φ for several values of a/T and $aN_\mathrm{c}^{2/3}/s^{1/3}$, respectively. Note that when $\theta = 0$ (motion along the longitudinal direction) the rotational symmetry in the xy-plane implies that the jet quenching parameter is independent of φ. For this reason the blue, dotted curves in figures 6(a)-(b) agree with the blue, solid curves in figures 6(c)-(d). The red, solid curves in figures 5 also agree with the red, dotted curves in figures 6(c)-(d), since they both correspond to $\theta = \varphi = \pi/2$. Similarly, the green, dotted curves in figures 5 agree with the green, solid curves in figures 6(a)-(b), since they both correspond to $\theta = \pi/2, \varphi = 0$.

4 Discussion

The momentum broadening of a highly relativistic parton moving through a non-Abelian plasma is described by the jet quenching parameter $\hat{q}$. We have considered an anisotropic $\mathcal{N} = 4$ SYM plasma in which the x, y directions are rotationally symmetric, but the z-direction is not. In the context of heavy ion collisions the latter would correspond to the beam direction, and the former to the transverse plane. The jet quenching parameter depends on the relative orientation between these directions on the one hand, and the direction of motion of the parton and the direction in which the momentum broadening is measured, on the other. This dependence can be parametrized by two angles (θ, φ), as shown in figure 3. We have determined the jet quenching parameter $\hat{q}_{\theta,\varphi}$ for the most general orientation and for any anisotropy. Our results are valid in the strong-coupling, large-N_c limit, since we have obtained them by means of the gravity dual [19, 20] of the anisotropic $\mathcal{N} = 4$ plasma. The anisotropy is induced by a position-dependent theta term in the gauge theory, or equivalently by a position-dependent axion on the gravity side. One may therefore wonder how sensitive the conclusions may be to the specific source of the anisotropy. In this respect it is useful to note that the gravity calculation involves only the coupling of the string to the background metric. This means that any anisotropy that gives rise to a qualitatively similar metric (and no Neveu-Schwarz B-field) will yield qualitatively similar results for the jet quenching parameter irrespectively of the form of the rest of supergravity fields.

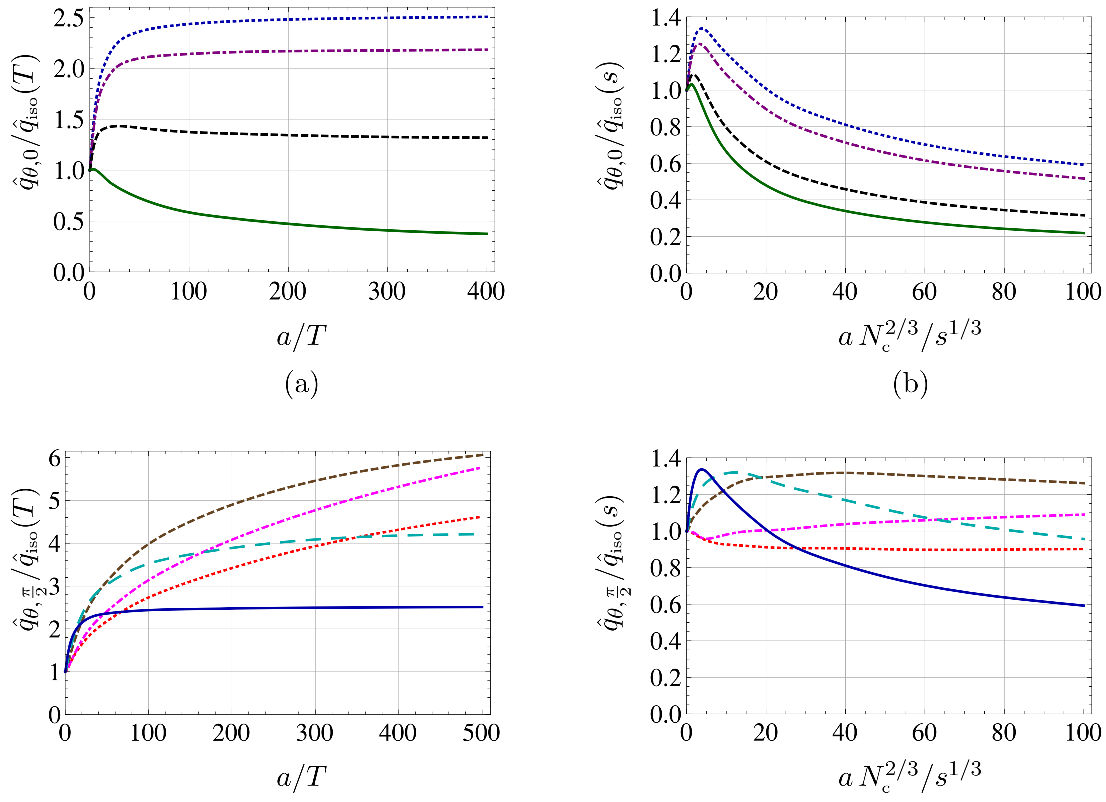

(a) (b)

(c) (d)

Figure 6. Jet quenching parameter for a quark moving along an arbitrary direction in the xz-plane, associated to momentum broadening along the transverse y-direction (top) or within the xz-plane (bottom). In (a) and (b) the angle between the direction of motion and the longitudinal z-direction is (from top to bottom) $\theta = 0, \pi/6, \pi/3, \pi/2$, whereas the correspondence in (c) and (d) is $\theta = 5\pi/12$ (brown, dashed), $49\pi/100$ (magenta, dotted-dashed), $\pi/2$ (red, dotted), $\pi/3$ (cyan, coarsely dashed), and 0 (blue, continuous). $\hat{q}_{\theta\varphi}$ and a are plotted in the appropriate units to facilitate comparison with the isotropic result for a plasma at the same temperature (left), or at the same entropy density (right). The isotropic result is given in eqs. (3.17) and (3.18).

For small enough an anisotropy the jet quenching parameter $\hat{q}_{\theta,\varphi}$ is always larger than that in an isotropic plasma at the same temperature (but different entropy density), regardless of the directions of motion and of momentum broadening. This feature is difficult to appreciate in figures 4(a), 5(a), 6(a) and 6(c) because of the scale in the horizontal axis, but it can be clearly seen in figure 7(a). Increasing the anisotropy, $\hat{q}_{\theta,\varphi}$ remains larger than the isotropic value except in a small region close to the $(\theta, \varphi) = (\pi/2, 0)$ corner, which we recall corresponds to the momentum broadening along the y-direction experienced by a quark propagating along the x-axis. This region is most clearly shown in figure 9(a), in which we have plotted the curves along which $\hat{q}_{\theta,\varphi} = \hat{q}_{\rm iso}(T)$, i.e. the intersections between the two surfaces shown in each of the plots in figure 7. We see that the two regions separated by these curves depend mildly on the value of a/T, which varies by more than two orders of magnitude between the magenta, dashed curve ($a/T = 12.2$) and the black, dotted curve ($a/T = 3380$).

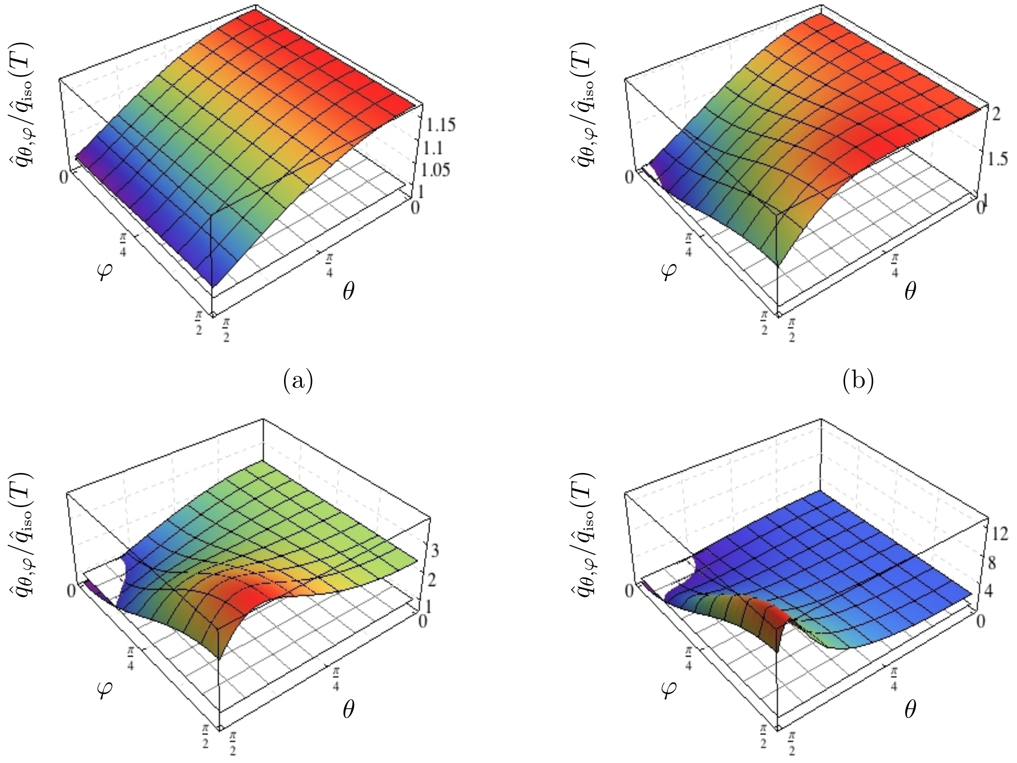

(a) (b)

(c) (d)

Figure 7. Jet quenching parameter for a quark moving along an arbitrary direction within the xz-plane as a function of the angles θ and φ and for anisotropies $a/T = 1.38$ (a), 12.2 (b), 86 (c), 3380 (d). $\hat{q}_{\theta,\varphi}$ is plotted in the appropriate units to facilitate comparison with the isotropic result for a plasma at the same temperature. The isotropic result is given in eq. (3.17).

Another interesting feature of the comparison at equal temperature is that, at small a/T, $\hat{q}_{\theta,\varphi}$ is larger for $\theta \simeq 0$, whereas for large a/T the situation gets inverted and $\hat{q}_{\theta,\varphi}$ becomes larger for $\theta \simeq \pi/2$ (except in the small region close to the $(\theta, \varphi) = (\pi/2, 0)$ corner). In other words, at small a/T the momentum broadening is larger for quarks propagating along the beam axis z, whereas at large a/T it is larger for quarks propagating in the transverse plane (unless the momentum broadening is measured very close to the orthogonal direction within the transverse plane). Finally, we see that in most of the region where $\hat{q}_{\theta,\varphi} > \hat{q}_{\rm iso}(T)$, the value of the anisotropic jet quenching parameter increases with a/T. This can be seen by noting the scales in the vertical axes in the plots of figure 7, as well as from the slices at constant values of θ and φ shown in figures 4(a), 5(a), 6(a) and 6(c).

In contrast, if the comparison is made between plasmas at equal entropy densities (but different temperatures), then the anisotropic jet quenching parameter can be either smaller or larger than its isotropic counterpart for any value of the entropy density, as seen in figure 8. As most clearly shown in figure 9(b), for small $aN_{\rm c}^{2/3}/s^{1/3}$ the anisotropic jet quenching parameter is greater than the isotropic one except in a small region close to

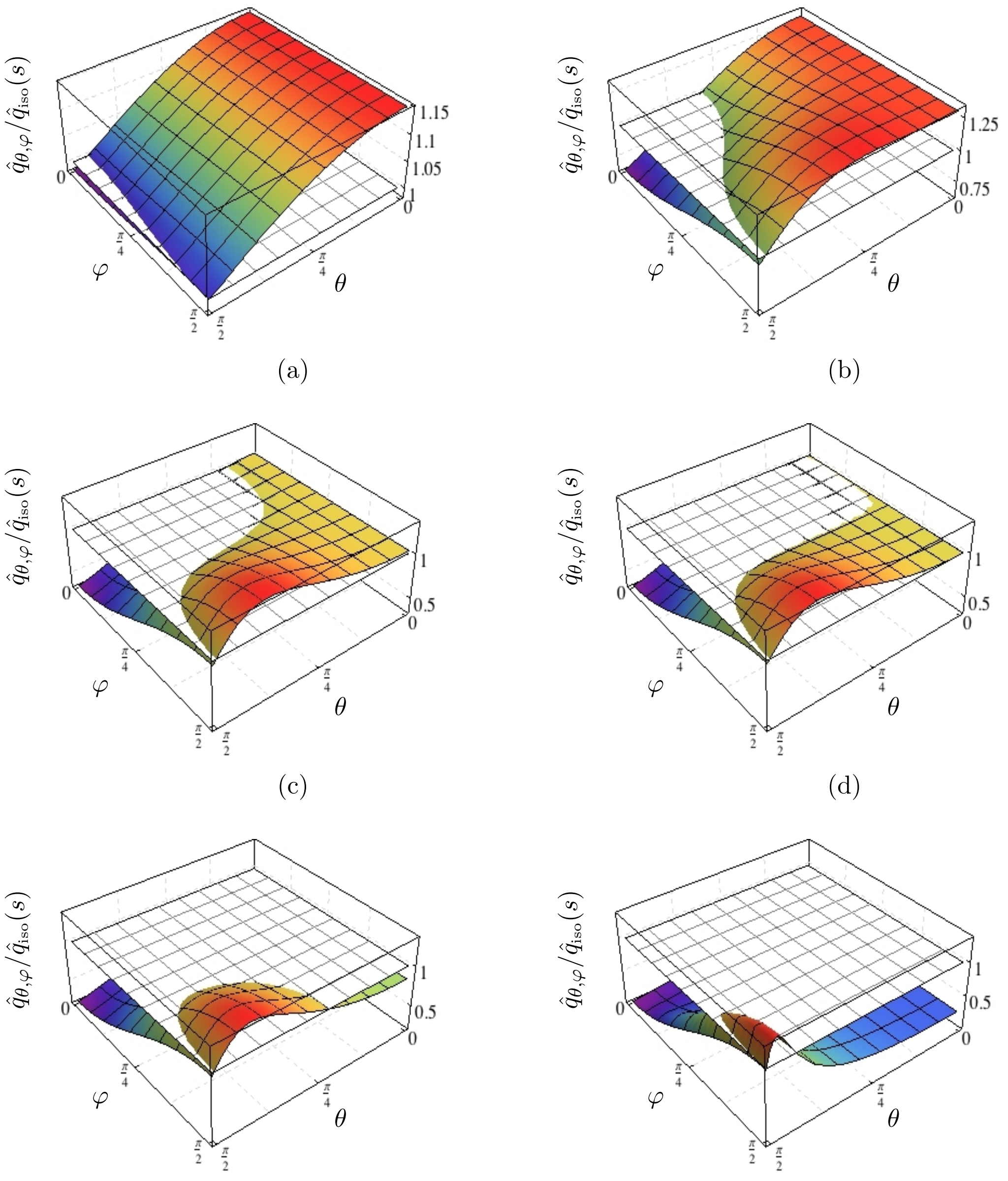

(a) (b) (c) (d) (e) (f)

Figure 8. Jet quenching parameter for a quark moving along an arbitrary direction within the xz-plane as a function of the angles θ and φ and for anisotropies $aN_{\mathrm{c}}^{2/3}/s^{1/3} = 0.80$ (a), 6.24 (b), 18.2 (c), 20.2 (d), 35.5 (e), 928 (f). $\hat{q}_{\theta,\varphi}$ is plotted in the appropriate units to facilitate comparison with the isotropic result for a plasma at the same entropy density. The isotropic result is given in eq. (3.18).

$\theta = \pi/2$, i.e. for all quarks except those propagating close to the transverse plane. This situation gets progressively inverted as $aN_{\mathrm{c}}^{2/3}/s^{1/3}$ increases, until for large $aN_{\mathrm{c}}^{2/3}/s^{1/3}$ the anisotropic $\hat{q}_{\theta,\varphi}$ is only larger than $\hat{q}_{\mathrm{iso}}(s)$ near the $(\theta,\varphi) = (\pi/2, \pi/2)$ corner, which we recall corresponds to the momentum broadening along the z-direction experienced by

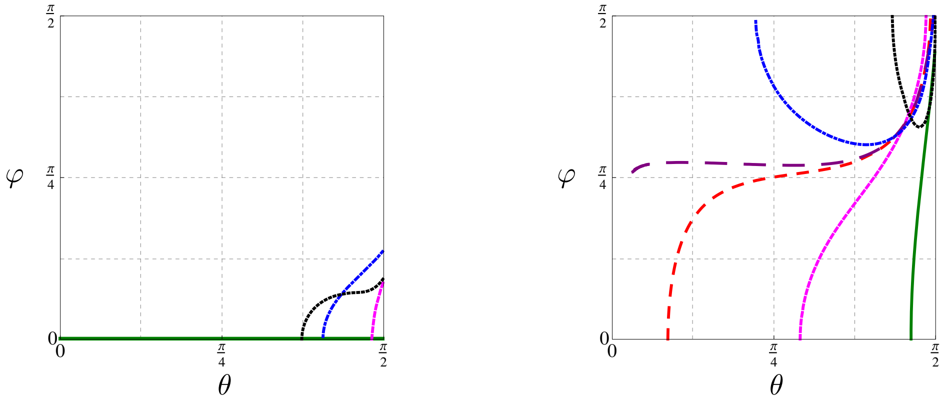

(a) (b)

Figure 9. Above (below) these curves in the (θ, φ) plane the jet quenching $\hat{q}_{\theta,\varphi}$ of the anisotropic plasma is larger (smaller) than the jet quenching of an isotropic plasma at the same temperature (a) or at the same entropy density (b). In (a) the curves correspond to $a/T = 1.38$ (green, solid), 12.2 (magenta, dashed), 86 (blue, dot-dashed) and 3380 (black, dotted). In (b) they correspond to $aN_c^{2/3}/s^{1/3} = 0.80$ (solid, green), 6.24 (magenta, dashed), 18.2 (red, coarsely dashed), 20.2 (purple, very coarsely dashed), 35.5 (blue, dot-dashed) and 928 (black, dotted).

a quark propagating along the x-direction. Thus we see that when the two plasmas are compared at equal entropy densities, the regions where the anisotropic jet quenching is larger or smaller than the isotropic one depend strongly on the value of the entropy density.

Also in contrast with the equal-temperature case, at equal entropy densities the value of the jet quenching parameter for almost all orientations of the directions of motion and of momentum broadening decreases as $aN_c^{2/3}/s^{1/3}$ increases. This can be seen from the scale in the vertical axes of figure 8, as well as from the slices at constant values of θ and φ shown in figures 4(b), 5(b), 6(b) and 6(d).

One feature that the equal-entropy results share with the equal-temperature ones is that, at small $aN_c^{2/3}/s^{1/3}$, $\hat{q}_{\theta,\varphi}$ is larger for $\theta \simeq 0$, whereas for large $aN_c^{2/3}/s^{1/3}$ the situation gets inverted and $\hat{q}_{\theta,\varphi}$ becomes larger for $\theta \simeq \pi/2$ (except in the small region close to the $(\theta, \varphi) = (\pi/2, 0)$ corner). This agreement is of course expected, since the normalizations $\hat{q}_{\text{iso}}(T)$ or $\hat{q}_{\text{iso}}(s)$ cancel out when comparing the values of $\hat{q}_{\theta,\varphi}$ for different values of θ, φ at constant values of T or s.

We will now compare our results to the results for the momentum broadening in the real-world QGP in the presence of anisotropies [29–32].[1] This comparison should be interpreted with caution because the sources of anisotropy in the QGP created in a heavy ion collision and in our system are different, and for this reason we will limit our comparison to qualitative features of the results. In the QGP the anisotropy is dynamical in the sense that it is due to the initial distribution of particles in momentum space, which will evolve in time and eventually become isotropic. In contrast, in our case the anisotropy is due

---

[1] Refs. [33, 34] considered an explicitly time-dependent situation, so we will not attempt a comparison with their results.

to an external source that keeps the system in an equilibrium anisotropic state that will not evolve in time. We hope that, nevertheless, our system might provide a good toy model for processes whose characteristic time scale is sufficiently shorter than the time scale controlling the time evolution of the QGP.

The most interesting case to consider in the context of heavy ion collisions is that of a quark propagating within the transverse plane, which we discussed in section 3.2. In this case the momentum broadening along the beam axis, $\hat{q}_{\rm L}$, and along the transverse plane, $\hat{q}_\perp$, will generically differ. Refs. [29–31] compared these quantities to their isotropic counterpart in a plasma at the same temperature. They found that $\hat{q}_{\rm L} \gtrsim \hat{q}_{\rm iso} > \hat{q}_\perp$, i.e. that the momentum broadening along the beam axis increases slightly in the presence of anisotropy, whereas the momentum broadening in the transverse plane decreases more significantly. These effects become stronger as the anisotropy grows. These results were suggested as a possible explanation of the asymmetric broadening of jet profiles in the plane of pseudorapidity (η) and azimuthal angle (ϕ) [28, 35–38].

The calculations in refs. [29–31] rely on the existence of quasi-particles in the plasma. In contrast, our strongly coupled model possess no quasi-particle excitations. In this model we find that the ordering is indeed $\hat{q}_{\rm L} > \hat{q}_{\rm iso} > \hat{q}_\perp$ for $a/T \gtrsim 6.35$, but for smaller anisotropies we find that $\hat{q}_{\rm L} > \hat{q}_\perp > \hat{q}_{\rm iso}$. The latter region is not clearly seen in figure 5(a) because of the scale in the horizontal axis, but it is illustrated in figure 7(a), where we see that at $a/T = 1.38$ we have $\hat{q}_{\theta,\varphi} > \hat{q}_{\rm iso}$ for all θ, φ. Note that $a/T \gtrsim 6.35$ is a sizable anisotropy, since the transition between the two limiting behaviours of the entropy density shown in figure 2 takes place around $a/T \simeq 3.7$.

Another difference is that, even for $a/T \gtrsim 6.35$, the most significant effect of the anisotropy is actually on $\hat{q}_{\rm L}$, whose increase with a/T is faster than the decrease of $\hat{q}_\perp$, as seen in figure 5(a). The momentum broadening at an intermediate angle φ with respect to the transverse plane is given by eq. (3.30), and this can be smaller or larger than the isotropic value. To illustrate this in figure 10 we have plotted a curve in the $(a/T, \varphi)$ plane below (above) which the anisotropic jet quenching parameter is larger (smaller) than its counterpart in an isotropic plasma at the same temperature. Finally, we note from figure 5(b) that, if the comparison is made at equal entropy densities, then the ordering we find is $\hat{q}_{\rm iso} > \hat{q}_{\rm L} > \hat{q}_\perp$ for all values of $aN_{\rm c}^{2/3}/s^{1/3}$, and moreover the most significant effect in this case is the fast decrease of $\hat{q}_\perp$ as $aN_{\rm c}^{2/3}/s^{1/3}$ increases.

We close by emphasizing one general conclusion of our analysis, namely the fact that whether the jet quenching parameter increases or decreases with respect to its isotropic value depends sensitively on whether the comparison is made at equal temperatures but different entropy densities, or viceversa. This contrasts with our recent calculation of the drag force in the same system [39]. In that case the comparison between the anisotropic and the isotropic plasmas was relatively insensitive to whether it was done at equal temperatures or at equal entropy densities. This discrepancy is not surprising. The momentum broadening and the drag force are related to each other in the limit $v \to 0$ by the fluctuation-dissipation theorem (see e.g. [40–42] for a discussion in the context of AdS/CFT). However, we have considered the ultra-relativistic limit $v = 1$, in which case there is a priori no relation between the momentum broadening and the drag force.

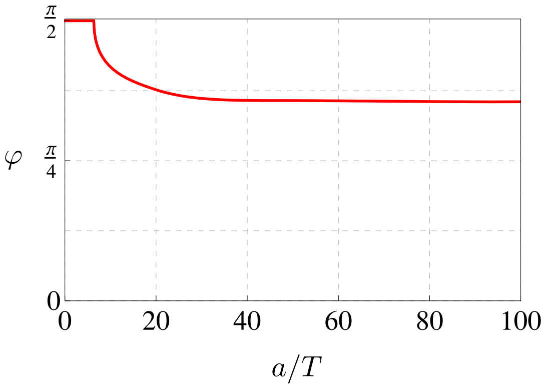

Figure 10. Below (above) this curve in the $(a/T, \varphi)$ plane the jet quenching parameter $\hat{q}_{x\varphi}$ of the anisotropic plasma is larger (smaller) than the jet quenching of the isotropic plasma at the same temperature.

Acknowledgments

It is a pleasure to thank Mauricio Martinez, and specially Jorge Casalderrey-Solana, for helpful discussions. MC is supported by a postdoctoral fellowship from Mexico's National Council of Science and Technology (CONACyT). We acknowledge financial support from 2009-SGR-168, MEC FPA2010-20807-C02-01, MEC FPA2010-20807-C02-02 and CPAN CSD2007-00042 Consolider-Ingenio 2010 (MC, DF and DM), and from DE-FG02-95ER40896 and CNPq (DT).

References

[1] STAR collaboration, J. Adams et al., *Experimental and theoretical challenges in the search for the quark gluon plasma: The STAR collaboration's critical assessment of the evidence from RHIC collisions*, *Nucl. Phys.* **A 757** (2005) 102 [`nucl-ex/0501009`] [INSPIRE].

[2] PHENIX collaboration, K. Adcox et al., *Formation of dense partonic matter in relativistic nucleus-nucleus collisions at RHIC: Experimental evaluation by the PHENIX collaboration*, *Nucl. Phys.* **A 757** (2005) 184 [`nucl-ex/0410003`] [INSPIRE].

[3] Proceedings of the *Quark Matter 2011*, May 23–28, Annecy, France (2011), published in *J. Phys.* **G 38** (2011).

[4] E. Shuryak, *Why does the quark gluon plasma at RHIC behave as a nearly ideal fluid?*, *Prog. Part. Nucl. Phys.* **53** (2004) 273 [`hep-ph/0312227`] [INSPIRE].

[5] E.V. Shuryak, *What RHIC experiments and theory tell us about properties of quark-gluon plasma?*, *Nucl. Phys.* **A 750** (2005) 64 [`hep-ph/0405066`] [INSPIRE].

[6] J.M. Maldacena, *The large-N limit of superconformal field theories and supergravity*, *Int. J. Theor. Phys.* **38** (1999) 1113 [*Adv. Theor. Math. Phys.* **2** (1998) 231] [`hep-th/9711200`] [INSPIRE].

[7] S. Gubser, I.R. Klebanov and A.M. Polyakov, *Gauge theory correlators from noncritical string theory*, *Phys. Lett.* **B 428** (1998) 105 [`hep-th/9802109`] [INSPIRE].

[8] E. Witten, *Anti-de Sitter space and holography*, *Adv. Theor. Math. Phys.* **2** (1998) 253 [hep-th/9802150] [INSPIRE].

[9] J. Casalderrey-Solana, H. Liu, D. Mateos, K. Rajagopal and U.A. Wiedemann, *Gauge/string duality, hot QCD and heavy ion collisions*, arXiv:1101.0618 [INSPIRE].

[10] W. Florkowski, *Anisotropic fluid dynamics in the early stage of relativistic heavy-ion collisions*, *Phys. Lett.* **B 668** (2008) 32 [arXiv:0806.2268] [INSPIRE].

[11] W. Florkowski and R. Ryblewski, *Dynamics of anisotropic plasma at the early stages of relativistic heavy-ion collisions*, *Acta Phys. Polon.* **B 40** (2009) 2843 [arXiv:0901.4653] [INSPIRE].

[12] R. Ryblewski and W. Florkowski, *Early anisotropic hydrodynamics and the RHIC early-thermalization and HBT puzzles*, *Phys. Rev.* **C 82** (2010) 024903 [arXiv:1004.1594] [INSPIRE].

[13] W. Florkowski and R. Ryblewski, *Highly-anisotropic and strongly-dissipative hydrodynamics for early stages of relativistic heavy-ion collisions*, *Phys. Rev.* **C 83** (2011) 034907 [arXiv:1007.0130] [INSPIRE].

[14] M. Martinez and M. Strickland, *Dissipative dynamics of highly anisotropic systems*, *Nucl. Phys.* **A 848** (2010) 183 [arXiv:1007.0889] [INSPIRE].

[15] R. Ryblewski and W. Florkowski, *Non-boost-invariant motion of dissipative and highly anisotropic fluid*, *J. Phys.* **G 38** (2011) 015104 [arXiv:1007.4662] [INSPIRE].

[16] M. Martinez and M. Strickland, *Non-boost-invariant anisotropic dynamics*, *Nucl. Phys.* **A 856** (2011) 68 [arXiv:1011.3056] [INSPIRE].

[17] R. Ryblewski and W. Florkowski, *Highly anisotropic hydrodynamics — Discussion of the model assumptions and forms of the initial conditions*, *Acta Phys. Polon.* **B 42** (2011) 115 [arXiv:1011.6213] [INSPIRE].

[18] R. Ryblewski and W. Florkowski, *Highly-anisotropic and strongly-dissipative hydrodynamics with transverse expansion*, *Eur. Phys. J.* **C 71** (2011) 1761 [arXiv:1103.1260] [INSPIRE].

[19] D. Mateos and D. Trancanelli, *The anisotropic $N = 4$ super Yang-Mills plasma and its instabilities*, *Phys. Rev. Lett.* **107** (2011) 101601 [arXiv:1105.3472] [INSPIRE].

[20] D. Mateos and D. Trancanelli, *Thermodynamics and instabilities of a strongly coupled anisotropic plasma*, *JHEP* **07** (2011) 054 [arXiv:1106.1637] [INSPIRE].

[21] K. Bitaghsir Fadafan, B. Pourhassan and J. Sadeghi, *Calculating the jet-quenching parameter in STU background*, *Eur. Phys. J.* **C 71** (2011) 1785 [arXiv:1005.1368] [INSPIRE].

[22] J. Sadeghi and B. Pourhassan, *Jet-quenching of the rotating heavy meson in a $\mathcal{N} = 4$ SYM plasma in presence of a constant electric field*, *Int. J. Theor. Phys.* **50** (2011) 2305 [arXiv:1001.0706] [INSPIRE].

[23] D. Giataganas, *Probing strongly coupled anisotropic plasma*, *JHEP* **07** (2012) 031 [arXiv:1202.4436] [INSPIRE].

[24] T. Azeyanagi, W. Li and T. Takayanagi, *On string theory duals of Lifshitz-like fixed points*, *JHEP* **06** (2009) 084 [arXiv:0905.0688] [INSPIRE].

[25] H. Liu, K. Rajagopal and U.A. Wiedemann, *Calculating the jet quenching parameter from AdS/CFT*, *Phys. Rev. Lett.* **97** (2006) 182301 [hep-ph/0605178] [INSPIRE].

[26] H. Liu, K. Rajagopal and U.A. Wiedemann, *Wilson loops in heavy ion collisions and their calculation in AdS/CFT*, *JHEP* **03** (2007) 066 [hep-ph/0612168] [INSPIRE].

[27] F. D'Eramo, H. Liu and K. Rajagopal, *Transverse momentum broadening and the jet quenching parameter, redux*, *Phys. Rev.* **D 84** (2011) 065015 [`arXiv:1006.1367`] [INSPIRE].

[28] R. Baier, Y.L. Dokshitzer, A.H. Mueller, S. Peigne and D. Schiff, *Radiative energy loss and p_T broadening of high-energy partons in nuclei*, *Nucl. Phys.* **B 484** (1997) 265 [`hep-ph/9608322`] [INSPIRE].

[29] P. Romatschke, *Momentum broadening in an anisotropic plasma*, *Phys. Rev.* **C 75** (2007) 014901 [`hep-ph/0607327`] [INSPIRE].

[30] A. Dumitru, Y. Nara, B. Schenke and M. Strickland, *Jet broadening in unstable non-abelian plasmas*, *Phys. Rev.* **C 78** (2008) 024909 [`arXiv:0710.1223`] [INSPIRE].

[31] B. Schenke, A. Dumitru, Y. Nara and M. Strickland, *QGP collective effects and jet transport*, *J. Phys.* **G 35** (2008) 104109 [`arXiv:0804.4557`] [INSPIRE].

[32] R. Baier and Y. Mehtar-Tani, *Jet quenching and broadening: the transport coefficient q-hat in an anisotropic plasma*, *Phys. Rev.* **C 78** (2008) 064906 [`arXiv:0806.0954`] [INSPIRE].

[33] A. Majumder, B. Müller and S. Mrowczynski, *Momentum broadening of a fast parton in a perturbative quark-gluon plasma*, *Phys. Rev.* **D 80** (2009) 125020 [`arXiv:0903.3683`] [INSPIRE].

[34] S. Mrowczynski, *On the dynamics of unstable quark-gluon plasma*, *Acta Phys. Polon. Supp.* **3** (2010) 639 [`arXiv:0911.0022`] [INSPIRE].

[35] P. Jacobs, *Jets in nuclear collisions: Status and perspective*, *Eur. Phys. J.* **C 43** (2005) 467 [`nucl-ex/0503022`] [INSPIRE].

[36] STAR collaboration, F. Wang, *Measurement of jet modification at RHIC*, *J. Phys.* **G 30** (2004) S1299 [`nucl-ex/0404010`] [INSPIRE].

[37] STAR collaboration, J. Adams et al., *Distributions of charged hadrons associated with high transverse momentum particles in pp and Au + Au collisions at $s_{NN}^{1/2} = 200\,GeV$*, *Phys. Rev. Lett.* **95** (2005) 152301 [`nucl-ex/0501016`] [INSPIRE].

[38] J. Putschke, *Intra-jet correlations of high-p_T hadrons from STAR*, *J. Phys.* **G 34** (2007) S679 [`nucl-ex/0701074`] [INSPIRE].

[39] M. Chernicoff, D. Fernandez, D. Mateos and D. Trancanelli, *Drag force in a strongly coupled anisotropic plasma*, `arXiv:1202.3696` [INSPIRE].

[40] C. Herzog, A. Karch, P. Kovtun, C. Kozcaz and L. Yaffe, *Energy loss of a heavy quark moving through $N = 4$ supersymmetric Yang-Mills plasma*, *JHEP* **07** (2006) 013 [`hep-th/0605158`] [INSPIRE].

[41] J. Casalderrey-Solana and D. Teaney, *Heavy quark diffusion in strongly coupled $N = 4$ Yang-Mills*, *Phys. Rev.* **D 74** (2006) 085012 [`hep-ph/0605199`] [INSPIRE].

[42] J. Casalderrey-Solana and D. Teaney, *Transverse momentum broadening of a fast quark in a $N = 4$ Yang-Mills plasma*, *JHEP* **04** (2007) 039 [`hep-th/0701123`] [INSPIRE].

3.3 Screening length of mesons

This section contains the publication:

- M. Chernicoff, D. Fernandez, D. Mateos and D. Trancanelli, "Quarkonium dissociation by anisotropy,"

  JHEP **1301** (2013) 170, `arXiv:1208.2672 [hep-th]`.

Published for SISSA by Springer

Received: *August 20, 2012*
Revised: *December 16, 2012*
Accepted: *December 26, 2012*
Published: *January 28, 2013*

Quarkonium dissociation by anisotropy

Mariano Chernicoff,[a] **Daniel Fernández,**[b] **David Mateos**[b,c] **and Diego Trancanelli**[d,e]

[a] *Department of Applied Mathematics and Theoretical Physics, Centre for Mathematical Sciences,*
Wilberforce Road, Cambridge, CB3 0WA, U.K.
[b] *Departament de Física Fonamental & Institut de Ciències del Cosmos (ICC),*
Universitat de Barcelona (UB),
Martí i Franquès 1, E-08028 Barcelona, Spain
[c] *Institució Catalana de Recerca i Estudis Avançats (ICREA),*
Passeig Lluís Companys 23, E-08010, Barcelona, Spain
[d] *Instituto de Física, Universidade de São Paulo,*
05314-970 São Paulo, Brazil
[e] *Department of Physics, University of Wisconsin,*
Madison, WI 53706, U.S.A.

E-mail: `M.Chernicoff@damtp.cam.ac.uk`, `daniel@ffn.ub.edu`, `dmateos@icrea.cat`, `dtrancan@fma.if.usp.br`

Abstract: We compute the screening length for quarkonium mesons moving through an anisotropic, strongly coupled $\mathcal{N} = 4$ super Yang-Mills plasma by means of its gravity dual. We present the results for arbitrary velocities and orientations of the mesons, as well as for arbitrary values of the anisotropy. The anisotropic screening length can be larger or smaller than the isotropic one, and this depends on whether the comparison is made at equal temperatures or at equal entropy densities. For generic motion we find that: (i) mesons dissociate above a certain critical value of the anisotropy, even at zero temperature; (ii) there is a limiting velocity for mesons in the plasma, even at zero temperature; (iii) in the ultra-relativistic limit the screening length scales as $(1 - v^2)^\epsilon$ with $\epsilon = 1/2$, in contrast with the isotropic result $\epsilon = 1/4$.

Keywords: Gauge-gravity correspondence, Holography and quark-gluon plasmas

ArXiv ePrint: 1208.2672

doi:10.1007/JHEP01(2013)170

Contents

1 Introduction

A remarkable conclusion from the experiments at the Relativistic Heavy Ion Collider (RHIC) [1, 2] and at the Large Hadron Collider (LHC) (see the contributions on elliptic flow at the LHC in [3]) is that the quark-gluon plasma (QGP) does not behave as a weakly coupled gas of quarks and gluons, but rather as a strongly coupled fluid [4, 5]. This places limitations on the applicability of perturbative methods. The lattice formulation of Quantum Chromodynamics (QCD) is also of limited utility, since for example it is not well suited for studying real-time phenomena. This has provided a strong motivation for understanding the dynamics of strongly coupled non-Abelian plasmas through the gauge/string duality [6–8] (see [9] for a recent review of applications to the QGP). In general, a necessary requirement for the string description to be tractable is that the plasma be infinitely strongly coupled, $\lambda = g_{\rm YM}^2 N_{\rm c} \to \infty$. Of course, the real-world QGP is not infinitely strongly coupled, and its dynamics involves a complex combination of both weak and strong coupling physics that depend on the possibly multiple scales that characterize the process of interest. The motivation for studying string models is that they provide examples in which explicit calculations can be performed from first principles at strong coupling, in particular in the real-time domain. The hope is then that, by understanding the weak and the strong coupling limits, one may be able to bracket the dynamics of the real-world QGP, which lies somewhere in between.

During the initial stage after the collision the plasma is far from equilibrium, and after a certain time a hydrodynamic description becomes applicable. If one thinks of hydrodynamics as a gradient expansion around a locally isotropic system, it is somewhat surprising that the hydrodynamic description actually becomes applicable when the longitudinal and transverse pressures are still significantly different. This can be explicitly seen, for example, in holographic descriptions [10–13] in which gravity provides a valid description all the way from the far-from-equilibrium phase to the locally isotropic phase, across the intermediate hydrodynamic-but-still-anisotropic phase. Thus, during most of the time that viscous hydrodynamics is applied, the plasma created in a heavy ion collision is anisotropic, with the level of anisotropy in fact increasing as one approaches the edge of the system. The fact that the range of time and space over which the QGP is anisotropic is larger than traditionally assumed has provided additional motivation for the study of anisotropic plasmas.

In this paper we will investigate the effect of an intrinsic anisotropy on the screening length between a quark-antiquark pair in a strongly coupled plasma. As we will review below, the plasma is static because it is held in anisotropic equilibrium by an external force [14, 15]. We will discuss all the caveats in more detail below, but we emphasize from the beginning that there are several reasons why, in terms of potential extrapolations to the real-world QGP, our results must be interpreted with caution. First, the sources of anisotropy in the QGP created in a heavy ion collision and in our system are different. In the QGP the anisotropy is dynamical in the sense that it is due to the initial distribution of particles in momentum space, which will evolve in time and eventually become isotropic. In contrast, in our case the anisotropy is due to an external source that keeps the system in an equilibrium anisotropic state that will not evolve in time. Nevertheless, we hope that our system might provide a good toy model for processes whose characteristic time scale is sufficiently shorter than the time scale controlling the evolution of a dynamical plasma.

The second caveat concerns the fact that, even in an static situation, different external sources can be chosen to hold the plasma in equilibrium, so one may wonder to what extent the results depend on this choice. We will provide a partial answer to this question in section 7, where we will explain that our qualitative results, for example the ultrarelativistic limit, do not depend on the details of our solution but only on a few general features. Nevertheless, it would still be very interesting to compute the same observables in other strongly coupled, static, anisotropic plasmas. Only then a general picture would emerge that would allow one, for example, to understand which observables are robust, in the sense that they are truly insensitive to the way in which the plasma is held in anisotropic equilibrium, and which ones are model-dependent. Obviously it is the first type of observables that have a better chance of being relevant for the real-world QGP. Our paper should be regarded as a first step in this general program.

We will consider the screening length in the case in which the quark-antiquark pair is at rest in the plasma as well as the case in which it is moving through the plasma. For this purpose we will examine a string with both endpoints on the boundary of an asymptotically

AdS spacetime [14, 15] that is dual to an anisotropic $\mathcal{N}=4$ super Yang-Mills plasma. The gravity solution possesses an anisotropic horizon, it is completely regular on and outside the horizon, and it is solidly embedded in type IIB string theory. For these reasons it provides an ideal toy model in which questions about anisotropic effects at strong coupling can be addressed from first principles. For the particular case of a quark-antiquark pair at rest, the screening length has also been computed [16] in a different model [17] of a strongly coupled, anisotropic plasma. The results exhibit some differences with respect to those presented here. While this may indicate some model dependence of the screening length, it is important to note that the solution of [17] possesses a naked singularity. Although this is a rather benign singularity, its presence introduces a certain amount of ambiguity in the calculations, which can only be performed by prescribing somewhat ad hoc boundary conditions at the singularity. In any case, this discussion is another indication that it would be interesting to compute the screening length in a larger class of models in order to ascertain which of its features are model-independent.

To avoid any possible confusion, we clarify from the beginning that the quarks and antiquarks that we will consider are infinitely massive, i.e. the bound states that we will consider are the analogue of heavy quarkonium mesons in QCD. Thus, the reader should always have the word 'quarkonium' in mind despite the fact that we will often refer to these states simply as 'mesons', 'heavy mesons', 'quark-antiquark bound states', 'dipoles', etc. This is specially relevant in the ultra-relativistic limit of the screening length, to which we will pay particular attention since it can be determined analytically. We emphasize that our results correspond to sending the quark and antiquark masses to infinity first, and then sending $v \to 1$. In particular, this means that in any future attempt to connect our results to the phenomenology of the QGP, this connection can only be made to the phenomenology of heavy quarkonium moving through the plasma.

The screening length for quarkonium mesons at rest in the anisotropic plasma of [14, 15] has been previously studied in [16, 18]. Our section 4 has some overlap with these references and, wherever they overlap, our results agree with theirs. Other physical properties of the anisotropic plasma that have been calculated include its shear viscosity [19, 20], the drag force on a heavy quark [18, 21], the jet quenching parameter [16, 18, 22], and the energy lost by a rotating quark [23]. The phase diagram of the zero-coupling version of the model considered in [14, 15] has been studied in [24]. Dissociation of baryons in the isotropic $\mathcal{N}=4$ plasma has been analyzed in [25].

2 Gravity solution

The type IIB supergravity solution of [14, 15] in the string frame takes the form

$$ds^2 = \frac{L^2}{u^2}\left(-\mathcal{F}\mathcal{B}\,dt^2 + dx^2 + dy^2 + \mathcal{H}dz^2 + \frac{du^2}{\mathcal{F}}\right) + L^2 e^{\frac{1}{2}\phi} d\Omega_5^2, \tag{2.1}$$

$$\chi = az\,, \qquad \phi = \phi(u)\,, \tag{2.2}$$

where χ and ϕ are the axion and the dilaton, respectively, and (t, x, y, z) are the gauge theory coordinates. Since there is rotational invariance in the xy-directions, we will refer

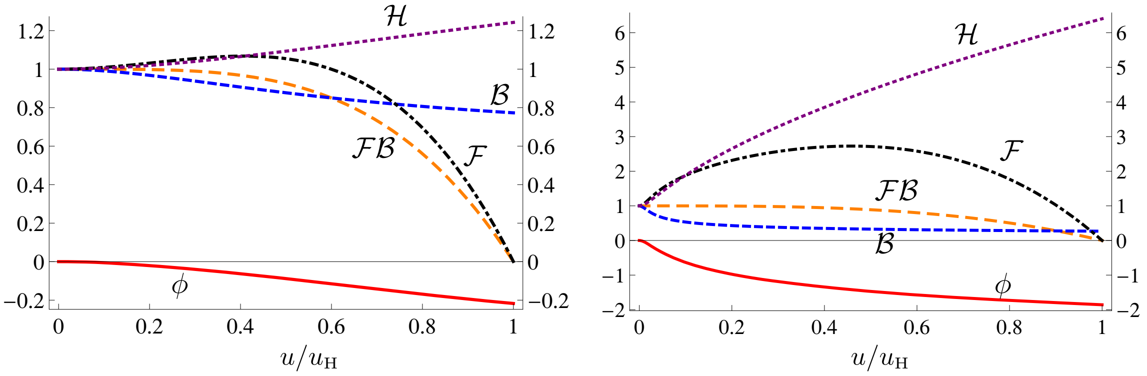

Figure 1. Metric functions for $a/T \simeq 4.4$ (left) and $a/T \simeq 86$ (right).

to these as the transverse directions, and to z as the longitudinal direction. $\mathcal{F}, \mathcal{B}$ and $\mathcal{H}$ are functions of the holographic radial coordinate u that were determined numerically in [14, 15]. Their form for two values of a/T is plotted in figure 1. The horizon lies at $u = u_{\mathrm{H}}$, where $\mathcal{F} = 0$, and the boundary at $u = 0$, where $\mathcal{F} = \mathcal{B} = \mathcal{H} = 1$ and $\phi = 0$. The metric near the boundary asymptotes to $AdS_5 \times S^5$. Note that the axion is linear in the z-coordinate. The proportionality constant a has dimensions of mass and is a measure of the anisotropy. The axion profile is dual in the gauge theory to a position-dependent theta parameter of the form $\theta \propto z$. This acts as an isotropy-breaking external source that forces the system into an anisotropic equilibrium state.

If $a = 0$ then the solution reduces to the isotropic black D3-brane solution dual to the isotropic $\mathcal{N} = 4$ theory at finite temperature. In this case

$$\mathcal{B} = \mathcal{H} = 1\,, \qquad \chi = \phi = 0\,, \qquad \mathcal{F} = 1 - \frac{u^4}{u_{\mathrm{H}}^4}\,, \qquad u_{\mathrm{H}} = \frac{1}{\pi T} \tag{2.3}$$

and the entropy density takes the form

$$s_{\mathrm{iso}} = \frac{\pi^2}{2} N_{\mathrm{c}}^2 T^3\,. \tag{2.4}$$

Figure 2 shows the entropy density per unit 3-volume in the xyz-directions of the anisotropic plasma as a function of the dimensionless ratio a/T, normalized to the entropy density of the isotropic plasma at the same temperature. At small a/T the entropy density scales as in the isotropic case, whereas at large a/T it scales as [14, 15, 26]

$$s = c_{\mathrm{ent}} N_{\mathrm{c}}^2 a^{1/3} T^{8/3}\,, \qquad\qquad [a/T \gg 1] \tag{2.5}$$

where c_{ent} is a constant that can be determined numerically. The transition between the two asymptotic behaviors of the entropy density takes place at $a/T \simeq 3.7$.

For later use we list here the near-boundary behavior of the different functions that determine the solution (2.2):

$$\mathcal{F} = 1 + \frac{11}{24} a^2 u^2 + \left(\mathcal{F}_4 + \frac{7}{12} a^4 \log u \right) u^4 + O(u^6)\,,$$

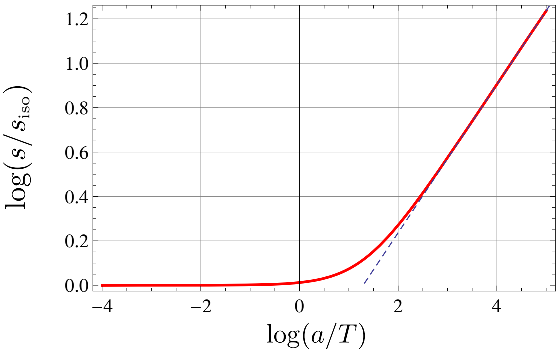

Figure 2. Log-log plot of the entropy density per unit 3-volume in the xyz-directions as a function of a/T, with $s_{\rm iso}$ defined as in eq. (2.4). The dashed blue line is a straight line with slope 1/3.

$$\begin{aligned} \mathcal{B} &= 1 - \frac{11}{24}a^2u^2 + \left(\mathcal{B}_4 - \frac{7}{12}a^4 \log u\right) u^4 + O(u^6)\,, \\ \mathcal{H} &= 1 + \frac{1}{4}a^2u^2 - \left(\frac{2}{7}\mathcal{B}_4 - \frac{5}{4032}a^4 - \frac{1}{6}a^4 \log u\right) u^4 + O(u^6)\,. \end{aligned} \tag{2.6}$$

The coefficients $\mathcal{F}_4$ and $\mathcal{B}_4$ depend on a and T and are known analytically in the limits of low, and high temperature and numerically for intermediate regimes [15].

A feature of the solution (2.2) that played an important role in the analysis of [14, 15] is the presence of a conformal anomaly. Its origin lies in the fact that diffeomorphism invariance in the radial direction u gets broken in the process of renormalization of the on-shell supergravity action. In the gauge theory this means that scale invariance is broken by the renormalization process. One manifestation of the anomaly is the fact that, unlike the entropy density, other thermodynamic quantities do not depend solely on the ratio a/T but on a and T separately. Fortunately, this will not be the case for the screening length, as we will see below.

To facilitate a (rough) comparison of the anisotropy in our system to that in other anisotropic plasmas it is useful to consider the ratio

$$\alpha = \frac{4E + P_\perp - P_{\rm L}}{3Ts}\,, \tag{2.7}$$

where E is the energy density and $P_\perp, P_{\rm L}$ are the transverse and longitudinal pressures, respectively. In addition to being dimensionless, this ratio has the virtue that it does not depend on a and T separately, but only on the combination a/T. For the isotropic $\mathcal{N}=4$ super Yang-Mills plasma $\alpha = 1$, whereas for $0 < a/T \lesssim 20$ the ratio is well approximated by the expression

$$\alpha \simeq 1 - 0.0036 \left(\frac{a}{T}\right)^2 - 0.000072 \left(\frac{a}{T}\right)^4\,, \tag{2.8}$$

as shown in figure 3.

At various points we will refer to the limit $T = 0$ of the anisotropic plasma. The zero-temperature version of the solution (2.2) was found in [26]. In this case the string-frame metric exhibits a naked curvature singularity deep in the infra-red, and the

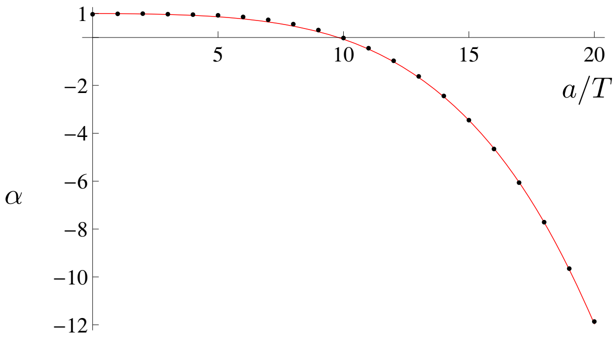

Figure 3. Ratio (2.7) as a function of a/T. The blue dots are the actual values of the ratio, and the red curve is the fit (2.8).

Einstein-frame metric exhibits infinite tidal forces [27, 28]. However, we emphasize that, for any finite temperature, the singularity is hidden behind the horizon and the solution is completely regular on and outside the horizon, exhibiting no pathologies of any type. Thus we will think of the $T = 0$ results as those obtained by taking the limit $T \to 0$ of the finite-temperature results. Moreover, regulating the infra-red geometry in this or any other way is actually unnecessary for most of the physics of quarkonium dissociation. The reason is that, as we will see, in the limit in which a/T becomes large the penetration depth into the AdS bulk of the string that is dual to the quarkonium meson becomes very small. As a result, the dissociation is entirely controlled by the metric near the boundary, which is insensitive to the infra-red behavior described above.

3 Preliminaries

In this paper we define the screening length L_s as the separation between a quark and an antiquark such that for $\ell < L_s$ ($\ell > L_s$) it is energetically favorable for the quark-antiquark pair to be bound (unbound) [29, 30]. Obviously this satisfies $L_s \leq L_{\text{max}}$, where L_{max} is the maximum separation L_{max} for which a bound quark-antiquark solution exists. We will determine L_s by comparing the action $S(\ell)$ of the bound pair, which is a function of the quark-antiquark separation ℓ, to the action S_{unbound} of the unbound system, i.e. by computing:

$$\Delta S(\ell) = S(\ell) - S_{\text{unbound}} \,. \tag{3.1}$$

The screening length is the maximum value of ℓ for which ΔS is positive (since we will work in Lorentzian signature). This may correspond to the value of ℓ at which ΔS crosses zero, in which case $L_s < L_{\text{max}}$, or the maximum value of ℓ for which a bound state exists, in which case $L_s = L_{\text{max}}$. In the Euclidean version of our calculations, this criterion corresponds to determining which configuration has the lowest free energy, which is therefore the configuration that is thermodynamically preferred. As shown in figure 4, for a meson moving through the isotropic plasma (2.3) one has $L_s < L_{\text{max}}$ for $v < v_{\text{trans}}$, whereas for $v > v_{\text{trans}}$ one finds that $L_s = L_{\text{max}}$, where $v_{\text{trans}} \simeq 0.45$ is the transition velocity between the two behaviors [31–33]. These qualitative features extend to the anisotropic case, as we have

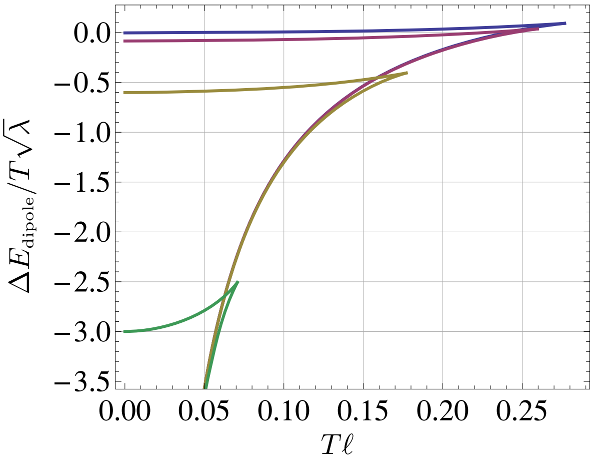

Figure 4. Energy difference, as defined in (3.2), between a bound and an unbound quark-antiquark pair moving through the isotropic plasma (2.3) with velocities (from the rightmost curve to the leftmost curve) $v = 0, 0.35, 0.85, 0.996$. The dipole is oriented orthogonally to its velocity. For $v < v_{\text{trans}}$ one has $L_s < L_{\text{max}}$, whereas for $v > v_{\text{trans}}$ one finds $L = L_{\text{max}}$, where $v_{\text{trans}} \simeq 0.45$ is the transition velocity between the two behaviors. At $v = 0$ the screening length and the maximum separation are $L_{\text{s}} \simeq 0.24/T$ and $L_{\text{max}} \simeq 0.27/T$, respectively.

illustrated in figure 5. The transition velocity decreases with the anisotropy, so for large a/T one has $L_s = L_{\text{max}}$ except for very low velocities. Similarly, if the ultra-relativistic limit $v \to 1$ is taken at fixed a and T, then obviously $v > v_{\text{trans}}$ and again $L_s = L_{\text{max}}$.

All our calculations will be done in the rest frame of the quark-antiquark pair, to which we will refer as the dipole rest frame. Since any observable can be easily translated between this frame and the plasma rest frame, we will speak interchangeably of 'mesons in a plasma wind' and of 'mesons in motion in the plasma'. We emphasize however that all the physical quantities that we will present, e.g. the screening length, are computed in the dipole rest frame.

The actions are scalar quantities, so $\Delta S_{\text{dipole}} = \Delta S_{\text{plasma}}$. Moreover, in the dipole rest frame we have

$$\Delta S_{\text{dipole}} = -\mathcal{T} \Delta E_{\text{dipole}} \,, \tag{3.2}$$

since the dipole is static in its own rest frame. In this expression E_{dipole} is the energy (as opposed to the free energy) of the configuration and $\mathcal{T} = \int dt$ is the length of the integration region in time. Thus we see that our criterion, which is based on comparing the actions, can also be thought of as a comparison between the energies of the bound and the unbound configurations in the dipole rest frame.

We will see that the ultraviolet divergences in the string action associated to integrating all the way to the boundary of AdS cancel out in the difference (3.1), and neither the bound nor the unbound actions possess infrared divergences associated to integrating all the way down to the horizon. This can be verified explicitly and it also follows from their relation to the energy in the rest frame of the dipole: while the energy of the unbound string pair possesses an infrared logarithmic divergence in the plasma rest frame [34], no such divergence is present in the dipole rest frame (see e.g. the discussion in [33]).

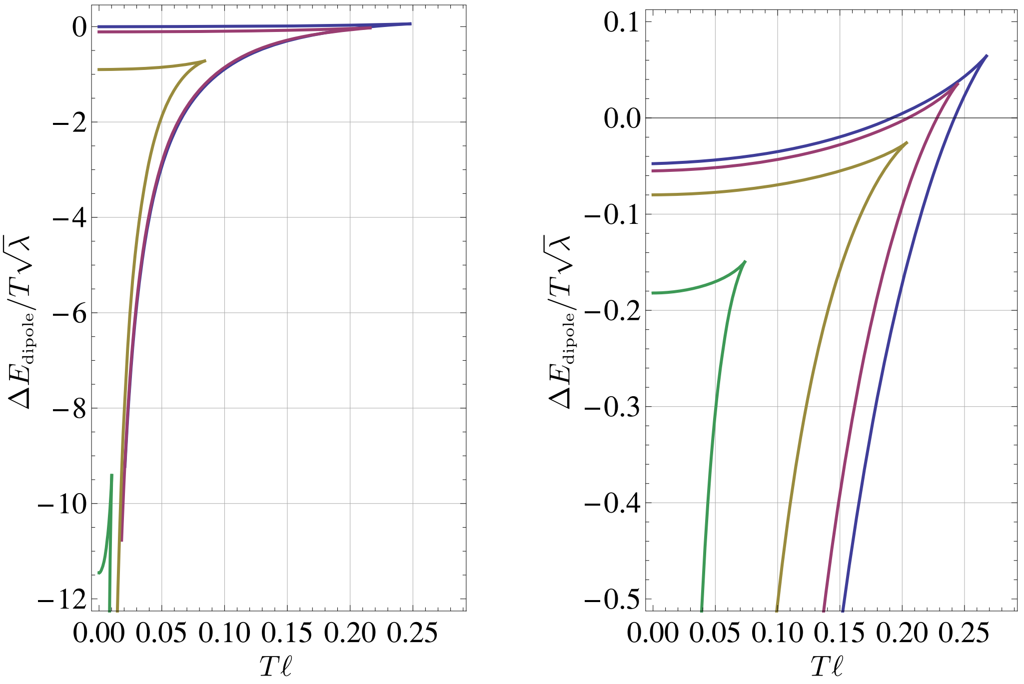

Figure 5. Energy difference in an anisotropic plasma, as defined in (3.2), between a bound and an unbound quark-antiquark pair oriented along the transverse direction x and moving along the anisotropic direction z. All the curves on the left correspond to $a/T = 12.2$ and different velocities (from the rightmost curve to the leftmost curve) $v = 0, 0.35, 0.85, 0.996$. All the curves on the right correspond to the same velocity $v = 0.25$ and different anisotropies (from the rightmost curve to the leftmost curve) $a/T = 0, 6.5, 43, 744$. For these anisotropies the corresponding transition velocities are respectively given by $v_{\rm trans} = 0.45, 0.29, 0.19, 0.11$.

4 Static dipole in an anisotropic plasma

In an anisotropic plasma the screening length depends on the relative orientation between the dipole and the anisotropic direction z. Given the rotational symmetry in the xy-plane we assume without loss of generality that the dipole lies in the xz-plane, at an angle θ with the z-axis. We thus choose the static gauge $t = \tau, \sigma = u$ and specify the string embedding as

$$x \to \sin\theta\, x(u)\,, \qquad z \to \cos\theta\, z(u)\,. \tag{4.1}$$

The string action takes the form

$$S = -\frac{L^2}{2\pi\alpha'}\, 2 \int dt \int_0^{u_{\rm max}} du \frac{1}{u^2}\sqrt{\mathcal{B}\left(1 + \mathcal{F}\mathcal{H}\cos^2\theta\, z'^2 + \mathcal{F}\sin^2\theta\, x'^2\right)}\,, \tag{4.2}$$

where the 2 comes from the two branches of the string and $u_{\rm max}$ will be determined below. The conserved momenta associated to translation invariance in the x, z directions are given by

$$\Pi_x = \frac{1}{\sin\theta}\frac{\partial\mathcal{L}}{\partial x'} = \frac{\mathcal{B}\mathcal{F}\sin\theta\, x'}{u^2\sqrt{\mathcal{B}\left(1+\mathcal{F}\mathcal{H}\cos^2\theta\, z'^2+\mathcal{F}\sin^2\theta\, x'^2\right)}}\,, \tag{4.3}$$

$$\Pi_z = \frac{1}{\cos\theta}\frac{\partial\mathcal{L}}{\partial z'} = \frac{\mathcal{B}\mathcal{F}\mathcal{H}\cos\theta\, z'}{u^2\sqrt{\mathcal{B}\left(1+\mathcal{F}\mathcal{H}\cos^2\theta\, z'^2+\mathcal{F}\sin^2\theta\, x'^2\right)}}\,. \tag{4.4}$$

Inverting these relations we find

$$x' = \frac{\sqrt{\mathcal{H}}\csc\theta\, u^2\,\Pi_x}{\sqrt{\mathcal{F}}\sqrt{\mathcal{B}\mathcal{F}\mathcal{H}-u^4\left(\Pi_z^2+\mathcal{H}\,\Pi_x^2\right)}}\,, \qquad z' = \frac{\sec\theta\, u^2\,\Pi_z}{\sqrt{\mathcal{F}\mathcal{H}}\sqrt{\mathcal{B}\mathcal{F}\mathcal{H}-u^4\left(\Pi_z^2+\mathcal{H}\,\Pi_x^2\right)}}\,. \tag{4.5}$$

Substituting back in the action we arrive at

$$S = -\frac{L^2}{2\pi\alpha'}\,2\int dt\int_0^{u_{\rm max}} du\frac{1}{u^2}\frac{\mathcal{B}\sqrt{\mathcal{F}\mathcal{H}}}{\sqrt{\mathcal{B}\mathcal{F}\mathcal{H}-u^4\left(\Pi_z^2+\mathcal{H}\,\Pi_x^2\right)}}\,. \tag{4.6}$$

For a U-shaped string describing a bound quark-antiquark pair the turning point $u_{\rm max}$ is determined in terms of the momenta by the condition that $x'(u_{\rm max}) = z'(u_{\rm max}) \to \infty$. This happens if $u_{\rm max} = u_{\rm H}$, in which case $\mathcal{F}(u_{\rm max}) = 0$, or if

$$\mathcal{B}\mathcal{F}\mathcal{H} - u^4\left(\Pi_z^2+\mathcal{H}\,\Pi_x^2\right)\big|_{u_{\rm max}} = 0\,. \tag{4.7}$$

The first possibility is not physically relevant because the second possibility is always realized first, meaning that the string turns around at $u_{\rm max} < u_{\rm H}$, before reaching the horizon. The only exception is the case $\Pi_x = \Pi_z = 0$, but this corresponds to $x' = z' = 0$, namely to an unbound pair of strings that descend from the boundary straight down to the horizon.

The momenta are determined by the boundary conditions that require the string endpoints to lie a distance ℓ apart from each other:

$$\frac{\ell}{2} = \int_0^{u_{\rm max}} du\, x' = \int_0^{u_{\rm max}} du\, z'\,. \tag{4.8}$$

These two equations, together with (4.7), can be solved numerically to express the momenta and $u_{\rm max}$ in terms of ℓ. In this way the on-shell action (4.6) for a bound pair becomes a function of ℓ alone. In order to determine L_s we subtract from this action the action of a static, unbound quark-antiquark pair, which is described by two straight strings hanging down from the boundary to the horizon. The action of this unbound pair is equal to (4.6) with the momenta set to zero and the range of integration extended down to the horizon:

$$S_{\rm unbound} = -\frac{L^2}{2\pi\alpha'}\,2\int dt\int_0^{u_{\rm H}} du\frac{\sqrt{\mathcal{B}}}{u^2}\,. \tag{4.9}$$

We obtain the screening length by numerically determining the value of ℓ at which the difference $S(\ell) - S_{\rm unbound}$ crosses zero, since in the static case we always have $L_s < L_{\rm max}$. The result for this difference as a function of ℓ in the isotropic plasma [29, 30] described by eq. (2.3) is plotted in figure 4, from which we see that the screening length is

$$L_{\rm iso}(T) \simeq \frac{0.24}{T} \qquad \text{[static dipole]}\,. \tag{4.10}$$

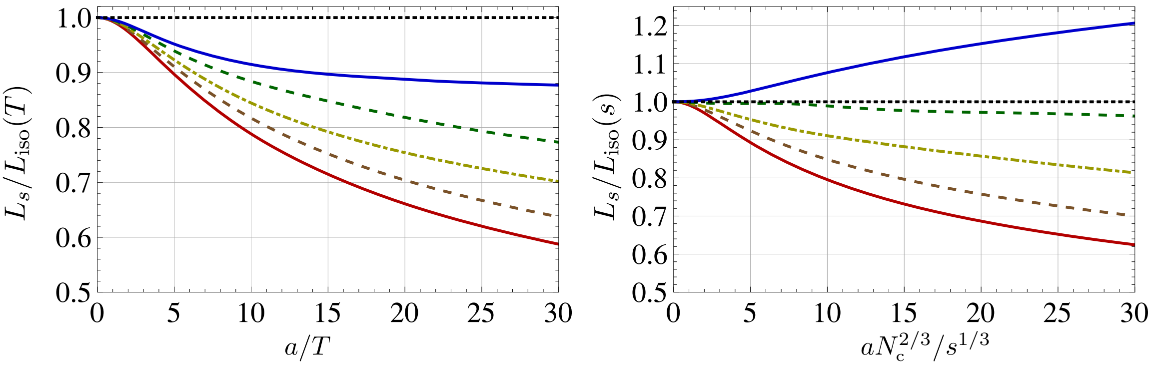

Figure 6. Screening length as a function of the anisotropy for a static quark-antiquark dipole lying at an angle with the z-direction (from top to bottom on the right-hand side of the plot) $\theta = \pi/2, \pi/3, \pi/4, \pi/6, 0$. The screening length is plotted in the appropriate units to facilitate comparison with the isotropic result for a plasma at the same temperature (left), or at the same entropy density (right). The isotropic result is given in eqs. (4.10) and (4.11).

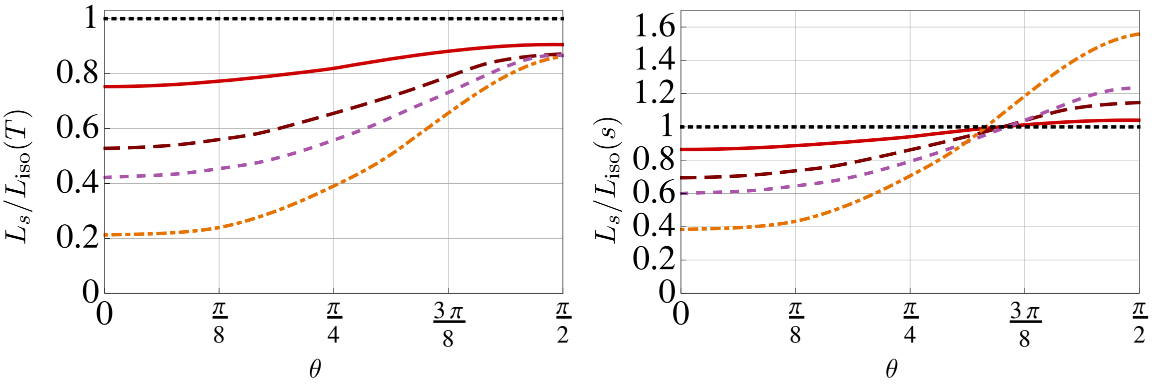

Figure 7. Screening length for a quark-antiquark dipole lying at an angle θ with the z-direction for anisotropies $a/T = 12.2$ (red, solid), 42.6 (maroon, coarsely dashed), 86 (violet, dashed), 744 (orange, dot-dashed). The corresponding values in units of the entropy density are (in the same order) $aN_c^{2/3}/s^{1/3} = 6.2, 19, 35, 242$. The screening length is plotted in the appropriate units to facilitate comparison with the isotropic result for a plasma at the same temperature (left), or at the same entropy density (right). The isotropic result is given in eqs. (4.10) and (4.11).

The scaling with the temperature is expected on dimensional grounds. In the isotropic case the temperature and the entropy density are related simply through (2.4), so this result can be recast as

$$L_{\text{iso}}(s) \simeq 0.24 \left(\frac{\pi^2 N_c^2}{2s} \right)^{1/3} \qquad \text{[static dipole]}\,, \qquad (4.11)$$

which will be useful later.

The results in the anisotropic case are plotted in figures 6 and 7. Figure 6 shows the screening length, for several orientations of the dipole, as a function of the anisotropy measured in units of the temperature (left) and the entropy density (right). The reason for working with both normalizations is that we wish to compare the screening length in the anisotropic plasma to that in the isotropic plasma, and this can be done at least in two different ways: the two plasmas can be taken to have the same temperatures but different entropy densities, or the same entropy densities but different temperatures. Figure 7 shows the screening length as a function of the dipole orientation for several values of the anisotropy.

We see from figure 6(left) that L_s decreases monotonically as a increases, for any dipole orientation, if the temperature is kept fixed. We also see from figure 7(left) that this effect is more pronounced for a dipole oriented along the anisotropic direction. In contrast, the behavior of the screening length at constant entropy density depends on the dipole's orientation, as shown in figures 6(right) and 7(right). For dipole's aligned sufficiently close to the anisotropic direction the screening length decreases with the anisotropy, whereas for orientations sufficiently close to the transverse plane the screening length increases with the anisotropy.

5 Dipole in an anisotropic plasma wind

In this section we will consider a static quark-antiquark pair in an anisotropic plasma that is moving with constant velocity with respect to the dipole — a dipole in an 'anisotropic plasma wind'. We will pay particular attention to the ultra-relativistic limit, which can be understood analytically.[1] This limit, together with the static results from section 4, will allow us to understand qualitatively the results at any velocity $0 < v < 1$.

We will first rewrite the solution (2.2) in a boosted frame, and then place a dipole in it — see figure 8. Given the rotational symmetry in the xy-plane we assume that the boost velocity is contained in the xz-plane, and that it lies at an angle θ_v with the z-axis. Thus we first rotate to a new coordinate system defined through

$$\begin{aligned} t &= \tilde{t}\,, \\ x &= \tilde{z}\,\sin\theta_v + \tilde{x}\,\cos\theta_v\,, \\ y &= \tilde{y}\,, \\ z &= \tilde{z}\,\cos\theta_v - \tilde{x}\,\sin\theta_v\,, \end{aligned} \tag{5.1}$$

and then perform a boost along the $\tilde{z}$-direction by setting

$$\begin{aligned} \tilde{t} &= \gamma\left(t' - v\,z'\right)\,, \\ \tilde{x} &= x'\,, \\ \tilde{y} &= y'\,, \\ \tilde{z} &= \gamma\left(-v\,t' + z'\right)\,, \end{aligned} \tag{5.2}$$

where $\gamma = 1/\sqrt{1-v^2}$ is the usual Lorentz factor. Below we will consider a dipole with an arbitrary orientation with respect to both the velocity of the plasma and the anisotropic

---

[1] We recall that we first send the quark mass to infinity and then $v \to 1$ (see section 1).

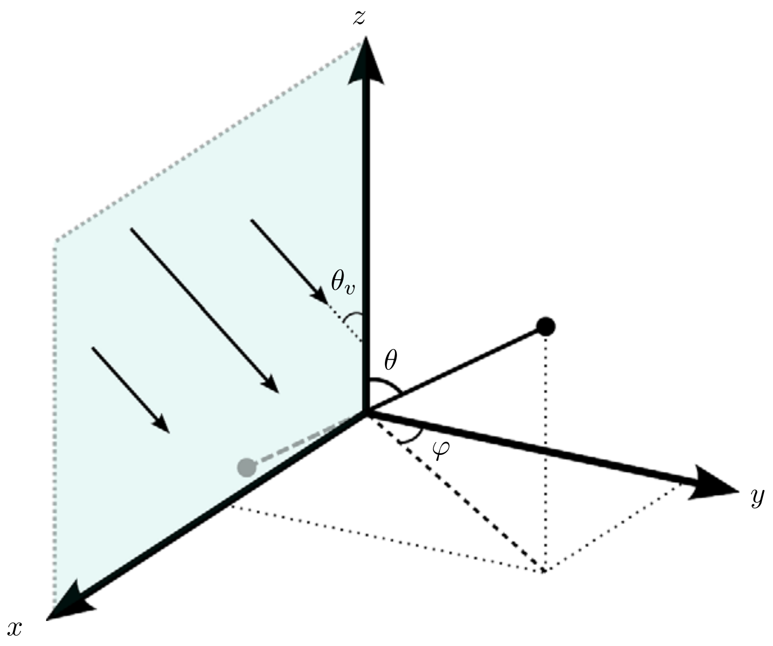

Figure 8. Orientation of the dipole in an anisotropic plasma wind. The wind's velocity lies in the original xz-plane (before the boost (5.2)) at an angle θ_v with respect to the anisotropic direction z. The quark lies at angles $\vec{q} = (x, y, z) = \frac{\ell}{2}(\sin\theta\sin\varphi, \sin\theta\cos\varphi, \cos\theta)$ with respect to the relabeled directions (after the boost (5.2)), and the antiquark lies at $-\vec{q}$.

direction z — see figure 8. We parametrize the orientation of the dipole by two angles θ, φ so that the quark lies at

$$\vec{q} = (x', y', z') = \frac{\ell}{2}(\sin\theta\sin\varphi, \sin\theta\cos\varphi, \cos\theta) \tag{5.3}$$

and the antiquark lies at $-\vec{q}$.

For notational simplicity, below we will drop the primes in the final set of coordinates. To avoid confusion, we emphasize that the direction θ_v of the plasma wind is always measured with respect to the original (x, y, z) axes, i.e. before the rotation and the boost above. In particular, motion within (outside) the transverse plane refers to a dipole in a plasma wind with $\theta_v = \pi/2$ ($\theta_v \neq \pi/2$). In contrast, the orientation of the dipole is measured with respect to the final set of coordinates (x', y', z'). However, if instead of specifying the dipole's orientation through a pair (θ, φ) we specify it by saying that the dipole is aligned with the x-, y- or z-directions, then we are referring to the original directions. Just as an illustration, consider the case of a plasma wind blowing along the original x-direction, i.e. a plasma wind with $\theta_v = \pi/2$. Then we see from (5.1) and (5.2) that $(x, z) \sim (z', x')$. Thus in this case by 'a dipole oriented along the x-direction' we mean a dipole with $\theta = 0$.

After dropping the primes from the final set of coordinates in (5.2) the five-dimensional part of the metric (2.2) takes the form

$$ds^2 = \frac{L^2}{u^2}\left(-g_{tt}dt^2 + g_{xx}dx^2 + dy^2 + g_{zz}dz^2 + g_{tx}dt\,dx + g_{tz}dt\,dz + g_{xz}dx\,dz + \frac{du^2}{\mathcal{F}}\right), \tag{5.4}$$

where

$$
\begin{aligned}
g_{tt} &= \frac{\mathcal{BF} - v^2(\sin^2\theta_v + \mathcal{H}\cos^2\theta_v)}{1-v^2}\,, && (5.5)\\
g_{xx} &= \cos^2\theta_v + \mathcal{H}\sin^2\theta_v\,, && (5.6)\\
g_{zz} &= \frac{\sin^2\theta_v + \mathcal{H}\cos^2\theta_v - v^2\mathcal{BF}}{1-v^2}\,, && (5.7)\\
g_{tx} &= \frac{(\mathcal{H}-1)v}{\sqrt{1-v^2}}\sin(2\theta_v)\,, && (5.8)\\
g_{tz} &= \frac{2v(\mathcal{BF} - \sin^2\theta_v - \mathcal{H}\cos^2\theta_v)}{1-v^2}\,, && (5.9)\\
g_{xz} &= \frac{1-\mathcal{H}}{\sqrt{1-v^2}}\sin(2\theta_v)\,. && (5.10)
\end{aligned}
$$

In order to determine the screening length for a generic velocity we need to compare the actions of a bound and an unbound quark-antiquark pair, as in the static case of section 4. However, in the ultra-relativistic this is not strictly necessary because $L_s = L_{\text{max}}$ (see section 3). In other words, in this limit we only need to determine the maximum possible quark-antiquark separation for which a bound state exists. Nevertheless, for completeness we will briefly present the analysis of the unbound configuration. Each of the strings in the unbound pair is one of the trailing strings studied in [21], so the reader is referred to this reference for additional details. Note, however, that [21] worked in the plasma rest frame. Here we will work in the dipole's rest and focus on the ultra-relativistic limit.

5.1 Unbound quark-antiquark pair

As in section 4 we fix the static gauge $t = \tau$, $\sigma = u$, and specify the embedding of the unbound string as

$$x \to x(u)\,, \qquad z \to z(u)\,. \tag{5.11}$$

The embedding in the y-direction is simply $y = 0$ because of rotational symmetry in the xy-plane and because the string is unbound. As we will see below, in the case of a bound string (dipole) the boundary conditions will generically imply a non-trivial embedding $y(u)$.

The action for the unbound string reads

$$S_{\text{unbound}} = -\frac{L^2}{2\pi\alpha'}\,2\int dt \int_0^{u_{\text{H}}} du\,\frac{1}{u^2}\sqrt{\mathcal{F}^{-1}K_0 + K_{xx}x'^2 + K_{zz}z'^2 + K_{xz}x'z'}\,, \tag{5.12}$$

where

$$
\begin{aligned}
K_0 &= g_{tt}\,,\\
K_{xx} &= \frac{\mathcal{BF}(\cos^2\theta_v + \mathcal{H}\sin^2\theta_v) - \mathcal{H}v^2}{1-v^2}\,,\\
K_{zz} &= \mathcal{BF}\left(\sin^2\theta_v + \mathcal{H}\cos^2\theta_v\right)\,,\\
K_{xz} &= \frac{\mathcal{BF}(1-\mathcal{H})}{\sqrt{1-v^2}}\sin(2\theta_v)\,. && (5.13)
\end{aligned}
$$

Introducing the conjugate momenta

$$\Pi_x = \frac{\partial \mathcal{L}_{\text{unbound}}}{\partial x'} \,, \qquad \Pi_z = \frac{\partial \mathcal{L}_{\text{unbound}}}{\partial z'} \tag{5.14}$$

and solving for x', z' we find

$$x' = \frac{u^2}{\mathcal{F}\sqrt{\mathcal{B}\mathcal{H}}} \frac{N_x}{\sqrt{D}} \,, \qquad z' = \frac{u^2}{\mathcal{F}\sqrt{\mathcal{B}\mathcal{H}}} \frac{N_z}{\sqrt{D}} \,, \tag{5.15}$$

where

$$\begin{aligned} N_x &= K_{zz}\Pi_x - \frac{1}{2}K_{xz}\Pi_z \,, \\ N_z &= -\frac{1}{2}K_{xz}\Pi_x + K_{xx}\Pi_z \,, \\ D &= \mathcal{B}\mathcal{H}\mathcal{F}K_0 - u^4 \left(K_{zz}\Pi_x^2 + K_{xx}\Pi_z^2 - K_{xz}\Pi_x\Pi_z \right) . \end{aligned} \tag{5.16}$$

Substituting into the action we arrive at

$$S_{\text{unbound}} = -\frac{L^2}{2\pi\alpha'} \, 2 \int dt \int_0^{u_{\text{H}}} du \, \frac{\sqrt{\mathcal{B}\mathcal{H}}K_0}{u^2\sqrt{D}} \,. \tag{5.17}$$

The momenta are determined by the condition that (5.15) remain real for a string that extends all the way from the boundary to the horizon. Following [21] we analyze this condition by noting that D can be rewritten as

$$D = \frac{2u^4}{K_{xz}} N_x N_z - b\Big[\Pi_x\Pi_z - c\Big]\Big[\mathcal{B}\mathcal{F} - v^2(\sin^2\theta_v + \mathcal{H}\cos^2\theta_v)\Big] \tag{5.18}$$

where

$$b = \frac{\mathcal{H}u^4}{(1-\mathcal{H})\sqrt{1-v^2}\,\sin\theta_v\cos\theta_v} \,, \qquad c = \frac{\mathcal{B}\mathcal{F}(1-\mathcal{H})\sin\theta_v\cos\theta_v}{u^4\sqrt{1-v^2}} \,. \tag{5.19}$$

As in [21] we must require that the zeros of the second summand in (5.18) coincide with one another and with those of N_x and N_z. One of the zeros of the second summand occurs at a critical value $u = u_c$ such that

$$\mathcal{B}_c\,\mathcal{F}_c - d_c\,v^2 = 0 \,, \qquad d_c \equiv \mathcal{H}_c\cos^2\theta_v + \sin^2\theta_v \,, \tag{5.20}$$

where $\mathcal{B}_c = \mathcal{B}(u_c)$, etc. At this point we have

$$N_x N_z|_{u_c} = \frac{v^4\cos\theta_v\sin\theta_v}{\sqrt{1-v^2}}(\mathcal{H}_c - 1)\,d_c\left[d_c\Pi_x + \frac{(\mathcal{H}_c-1)\cos\theta_v\sin\theta_v}{\sqrt{1-v^2}}\,\Pi_z\right]^2 . \tag{5.21}$$

Noting that $\mathcal{H}_c > 1$ and that $K_{xz} < 0$, we see that D would be negative at u_c unless the momenta are related through

$$\Pi_x = \frac{(1-\mathcal{H}_c)\cos\theta_v\sin\theta_v}{d_c\sqrt{1-v^2}}\,\Pi_z \,. \tag{5.22}$$

Assuming this relation and requiring that the other zero in the second summand of (5.18) coincide with u_c yields

$$\Pi_z^2 = \frac{\mathcal{B}_c \mathcal{F}_c \, d_c}{u_c^4} \,, \qquad \Pi_x^2 = \frac{\mathcal{B}_c \mathcal{F}_c (\mathcal{H}_c - 1)^2 \cos^2\theta_v \sin^2\theta_v}{u_c^4 (1-v^2) d_c} \,. \tag{5.23}$$

Note that Π_z does not vanish for any value of θ_v, whereas Π_x vanishes if $\theta_v = 0, \pi/2$. The reason is that for these two particular orientations the plasma wind blows along the original z- or x-directions and the string orients itself with the corresponding axis [21]. As a consequence, the momentum along the orthogonal axis vanishes. However, the changes of coordinates (5.1) and (5.2) always relabel the direction of motion as z, so after these changes the non-vanishing momentum is labelled Π_z irrespectively of whether $\theta_v = 0$ or $\theta_v = \pi/2$.

We will analyze in detail the ultra-relativistic limit. This is facilitated by explicitly distinguishing the case of motion outside the transverse plane ($\theta_v \neq \pi/2$) and motion within the transverse plane ($\theta_v = \pi/2$).

5.1.1 Ultra-relativistic motion outside the transverse plane

In the ultra-relativistic limit u_c approaches the boundary, i.e. $u_c \to 0$, and we can use the near-boundary expansion (2.6) to determine it. The condition (5.20) yields in this limit [21]

$$u_{\mathrm{c}}^2 \simeq \frac{4(1-v^2)}{a^2 \cos^2\theta_v} \qquad\qquad [\theta_v \neq \pi/2] \,, \tag{5.24}$$

which when substituted in (5.23) gives the momenta

$$\Pi_z^2 \simeq \frac{a^4 \cos^4\theta_v}{16(1-v^2)^2} \,, \qquad \Pi_x^2 \simeq \frac{a^4 \cos^2\theta_v \sin^2\theta_v}{16(1-v^2)} \,. \tag{5.25}$$

In these expressions we have ignored subleading terms in an expansion in $1-v^2$, for example we have set $v \simeq 1$, $\mathcal{H}_c \simeq 1$, etc. Note that in this expansion Π_x is subleading with respect to Π_z.

For later use we must evaluate how S_{unbound} scales with $1-v^2$ in the limit $v \to 1$. For this purpose we split the integration region, and hence the action (5.17), as

$$S_{\text{unbound}} = S_{\text{unbound}}^{(1)} + S_{\text{unbound}}^{(2)} \,, \tag{5.26}$$

where $S_{\text{unbound}}^{(1)}$ is the action with the integral in u ranging between 0 and u_c, and $S_{\text{unbound}}^{(2)}$ is the action with the integral in u ranging between u_c and u_{H}. The reason for this separation is that in the first interval u is small and hence we will be able to use the near-boundary expressions (2.6), (5.24) and (5.25). In order to exhibit the dependence on $1-v^2$ of $S_{\text{unbound}}^{(1)}$ explicitly, it is convenient to work with a rescaled variable r which remains finite in the $v \to 1$ limit, defined though

$$u = r\sqrt{1-v^2} \,, \qquad u_c = r_c \sqrt{1-v^2} \,. \tag{5.27}$$

In terms of this variable we get

$$S_{\text{unbound}}^{(1)} = -\frac{L^2}{2\pi\alpha'} \frac{2}{\sqrt{1-v^2}} \int dt \int_0^{r_c} dr \, \frac{1 - \frac{1}{4}a^2 r^2 \cos^2\theta_v + \ldots}{r^2 \sqrt{1 - \frac{1}{4}a^2 r^2 \cos^2\theta_v - \frac{1}{16}a^4 r^4 \cos^4\theta_v + \ldots}} \,. \tag{5.28}$$

The divergence near $r = 0$ will cancel out with that in the action for the bound string. The integrand is smooth across $r = r_c$. The crucial point is that the result is $O\left[(1-v^2)^{-1/2}\right]$ in the counting in powers of $1-v^2$, and we will find this same scaling in the bound string action (see below). In contrast, $S^{(2)}_{\text{unbound}}$ scales as $1-v^2$ in the ultra-relativistic limit. The reason is that u is not small in units of $1-v^2$ in the corresponding region of integration, so all the dependence comes from the fact that the action (5.17) scales as $1/\Pi_z \sim 1-v^2$ in this region.

5.1.2 Ultra-relativistic motion within the transverse plane

In this case $\theta_v = \pi/2$ and hence we see from (5.23) that $\Pi_x = 0$. The condition (5.20) now gives [21]

$$u_c^2 \simeq \sqrt{\frac{1-v^2}{C}}\,, \tag{5.29}$$

where

$$C = \frac{121}{576}a^4 - \mathcal{F}_4 - \mathcal{B}_4\,, \tag{5.30}$$

and we recall that $\mathcal{F}_4, \mathcal{B}_4$ are the coefficients that enter the near-boundary expansion (2.6). Substituting (5.29) into (5.23) and dropping subleading terms as before we obtain the momentum in the z-direction (recall that this corresponds to the original x-direction):

$$\Pi_z \simeq \frac{1}{u_c^2} = \sqrt{\frac{C}{1-v^2}}\,. \tag{5.31}$$

It is now convenient to work with a rescaled radial coordinate r defined through

$$u = r(1-v^2)^{1/4}\,. \tag{5.32}$$

Splitting the unbound string action as before, we find

$$S^{(1)}_{\text{unbound}} = -\frac{L^2}{2\pi\alpha'}\frac{2}{(1-v^2)^{1/4}}\int dt \int_0^{r_c} dr\, \frac{1-Cr^4+\ldots}{r^2\sqrt{1-2Cr^4+\ldots}}\,. \tag{5.33}$$

Again, the divergence near $r = 0$ will cancel out with that in the action for the bound string, which will also be of $O\left[(1-v^2)^{-1/4}\right]$ in the counting in powers of $1-v^2$ (see below). In contrast, $S^{(2)}_{\text{unbound}}$ scales as $1/\Pi_x \sim \sqrt{1-v^2}$ in the ultra-relativistic limit, and is therefore subleading.

In summary, we find that in the ultra-relativistic limit

$$S_{\text{unbound}} = \begin{cases} O\left[(1-v^2)^{-1/2}\right] \text{ if } \theta_v \neq \pi/2 & \text{[outside the transverse plane]} \\[2ex] O\left[(1-v^2)^{-1/4}\right] \text{ if } \theta_v = \pi/2 & \text{[within the transverse plane]}\,. \end{cases} \tag{5.34}$$

5.2 Bound quark-antiquark pair

We now consider a dipole with an arbitrary orientation with respect to both the velocity of the plasma and the anisotropic direction z — see figure 8. As before we fix the static gauge $\tau = t, \sigma = u$ and specify the string embedding via three functions $(x(u), y(u), z(u))$ subject to the boundary conditions

$$\frac{\ell}{2}\sin\theta\sin\varphi = \int_0^{u_{\max}} x'du\,,$$

$$
\begin{aligned}
\frac{\ell}{2}\sin\theta\cos\varphi &= \int_0^{u_{\max}} y' du\,, \\
\frac{\ell}{2}\cos\theta &= \int_0^{u_{\max}} z' du\,,
\end{aligned}
\tag{5.35}
$$

where $u_{\max}$ is the turning point of the U-shaped string. The integral in the action of the bound string extends only up to this point and now includes a term proportional to y'^2:

$$
S = -\frac{L^2}{2\pi\alpha'}\,2\int dt \int_0^{u_{\max}} du\,\frac{1}{u^2}\sqrt{\mathcal{F}^{-1}K_0 + K_{xx}x'^2 + K_{yy}y'^2 + K_{zz}z'^2 + K_{xz}x'z'}\,. \tag{5.36}
$$

All the K's were defined in (5.13) except for K_{yy}, which is given by

$$
K_{yy} = \frac{\mathcal{BF} - v^2(\sin^2\theta_v + \mathcal{H}\cos^2\theta_v)}{1-v^2}\,. \tag{5.37}
$$

The momenta are defined as

$$
\Pi_x = \frac{\partial\mathcal{L}}{\partial x'}\,, \qquad \Pi_y = \frac{\partial\mathcal{L}}{\partial y'}\,, \qquad \Pi_z = \frac{\partial\mathcal{L}}{\partial z'}\,. \tag{5.38}
$$

Inverting these equations we get

$$
\begin{aligned}
x' &= \frac{u^2}{\mathcal{F}\sqrt{\mathcal{BH}}\sqrt{D}}\left(K_{zz}\Pi_x - \frac{1}{2}K_{xz}\Pi_z\right)\,, \\
y' &= \frac{u^2\sqrt{\mathcal{BH}}}{\sqrt{D}}\Pi_y\,, \\
z' &= \frac{u^2}{\mathcal{F}\sqrt{\mathcal{BH}}\sqrt{D}}\left(-\frac{1}{2}K_{xz}\Pi_x + K_{xx}\Pi_z\right)\,,
\end{aligned}
\tag{5.39}
$$

where

$$
D = \mathcal{BHF}K_0 - u^4\left(K_{zz}\,\Pi_x^2 + \mathcal{BFH}\,\Pi_y^2 + K_{xx}\,\Pi_z^2 - K_{xz}\,\Pi_x\Pi_z\right)\,. \tag{5.40}
$$

Substituting these expressions into the action (5.36) we get

$$
S = -\frac{L^2}{2\pi\alpha'}\,2\int dt \int_0^{u_{\max}} du\,\frac{\sqrt{\mathcal{BH}}K_0}{u^2\sqrt{D}}\,. \tag{5.41}
$$

As in the case of the unbound string, we will now distinguish between the cases of motion outside and within the transverse plane, focusing on the ultra-relativistic limit.

5.2.1 Ultra-relativistic motion outside the transverse plane

The turn-around point $u_{\max}$ is defined by the condition $D(u_{\max}) = 0$. In the ultra-relativistic limit we expect that this point approaches the boundary for the string solution of interest, as in the isotropic case. Thus in this limit $u_{\max}$ can be determined by using the near-boundary expansions of the metric functions (2.6).

In the limit $u \to 0$ we find the following expansions:

$$
K_{zz} \simeq 1 + \frac{a^2u^2\cos^2\theta_v}{4} + \cdots\,, \tag{5.42}
$$

$$
\begin{aligned}
K_{xz} &\simeq 0 - \frac{a^2u^2\sin\theta_v\cos\theta_v}{2\sqrt{1-v^2}} + \cdots\,, && (5.43)\\
K_{xx} &\simeq 1 - \frac{a^2u^2\cos^2\theta_v}{4(1-v^2)} + \cdots\,, && (5.44)
\end{aligned}
$$

from which it follows that

$$
D \simeq 1 - \frac{a^2u^2\cos^2\theta_v}{4(1-v^2)} - u^4(\Pi_x^2+\Pi_y^2+\Pi_z^2) + \cdots\,. \tag{5.45}
$$

Similarly, the boundary conditions (5.35) take the form

$$
\begin{aligned}
\frac{\ell}{2}\sin\theta\sin\varphi &\simeq \int_0^{u_{\max}} du\,\frac{u^2}{\sqrt{D}}\,\Pi_x + \cdots\,, && (5.46)\\
\frac{\ell}{2}\sin\theta\cos\varphi &\simeq \int_0^{u_{\max}} du\,\frac{u^2}{\sqrt{D}}\,\Pi_y + \cdots\,,\\
\frac{\ell}{2}\cos\theta &\simeq \int_0^{u_{\max}} du\,\frac{u^2}{\sqrt{D}}\left(1-\frac{a^2u^2\cos^2\theta_v}{4(1-v^2)}\right)\Pi_z + \cdots\,,
\end{aligned}
$$

In the ultra-relativistic limit, all the terms that we have omitted in the equations above, in particular in (5.45) and (5.47), are subleading with respect to the terms that we have retained provided the radial coordinate and the momenta scale as

$$
u = r\sqrt{1-v^2}\,, \qquad \Pi_i = \frac{p_i}{1-v^2}\,, \tag{5.47}
$$

where r and p_i are kept fixed in the limit $v\to 1$. In terms of these rescaled variables (5.47) the boundary conditions (5.47) take the form

$$
\begin{aligned}
\frac{\ell}{2}\sin\theta\sin\varphi &\simeq \sqrt{1-v^2}\,p_x\,\mathcal{I}_2(p,\theta_v)\,,\\
\frac{\ell}{2}\sin\theta\cos\varphi &\simeq \sqrt{1-v^2}\,p_y\,\mathcal{I}_2(p,\theta_v)\,,\\
\frac{\ell}{2}\cos\theta &\simeq \sqrt{1-v^2}\,p_z\left(\mathcal{I}_2(p,\theta_v) - \frac{a^2\cos^2\theta_v}{4}\mathcal{I}_4(p,\theta_v)\right)\,, && (5.48)
\end{aligned}
$$

where the integral

$$
\mathcal{I}_n(p,\theta_v) \equiv \int_0^{r_{\max}} dr\,\frac{r^n}{\sqrt{1-\frac{a^2r^2}{4}\cos^2\theta_v - r^4(p_x^2+p_y^2+p_z^2)}} \tag{5.49}
$$

is of $O(1)$ in the counting in powers in $(1-v^2)$, and is finite if $n\geq 0$. Further noting that

$$
K_0 = 1 - \frac{a^2u^2\cos^2\theta_v}{4(1-v^2)} + O(u^4) \simeq 1 - \frac{a^2r^2\cos^2\theta_v}{4}\,, \tag{5.50}
$$

we see that the bound action scales as

$$
S \simeq -\frac{L^2}{2\pi\alpha'}\frac{2}{\sqrt{1-v^2}}\left(\mathcal{I}_{-2}(p,\theta_v) - \frac{a^2\cos^2\theta_v}{4}\mathcal{I}_0(p,\theta_v)\right)\int dt\,. \tag{5.51}
$$

Since both this bound action and the unbound action (5.28) scale as $(1-v^2)^{-1/2}$, the divergence at $r=0$ in the bound action coming from the $\mathcal{I}_{-2}(p,\theta_v)$ integral would exactly cancel that in the unbound action in the difference (3.1). Moreover, by comparing the two actions we would conclude that the momenta p_i introduced in (5.47) are indeed of $O(1)$ in the counting in powers of $(1-v^2)$ in the ultra-relativistic limit. It would then follow that the integrals $\mathcal{I}_n(p,\theta_v)$ are also of $O(1)$, and therefore that the screening length scales as $L_s \sim (1-v^2)^{1/2}$ in the ultra-relativistic limit. However, as explained below (5.10), in the ultra-relativistic $L_s = L_{\rm max}$ is simply the maximum possible separation between a bound quark-antiquark pair, so it can be determined by maximizing ℓ in (5.48) with respect to the momenta. Since the integrals are bounded from above for any value of the p_i, and the maximum is v-independent, it follows that $L_s = L_{\rm max} \sim (1-v^2)^{1/2}$.

5.2.2 Ultra-relativistic motion within the transverse plane

In this case $\theta_v = \pi/2$ and the expansions of D and of the boundary conditions (5.35) become

$$D \simeq 1 - \frac{Cu^4}{1-v^2} - u^4(\Pi_x^2 + \Pi_y^2 + \Pi_z^2) + \cdots \tag{5.52}$$

and

$$\begin{aligned}
\frac{\ell}{2}\sin\theta\sin\varphi &\simeq \int_0^{u_{\rm max}} du\, u^2 \frac{\Pi_x}{\sqrt{1-\frac{Cu^4}{1-v^2} - u^4(\Pi_x^2+\Pi_y^2+\Pi_z^2)}} + \cdots\,, \\
\frac{\ell}{2}\sin\theta\cos\varphi &\simeq \int_0^{u_{\rm max}} du\, u^2 \frac{\Pi_y}{\sqrt{1-\frac{Cu^4}{1-v^2} - u^4(\Pi_x^2+\Pi_y^2+\Pi_z^2)}} + \cdots\,, \\
\frac{\ell}{2}\cos\theta &\simeq \int_0^{u_{\rm max}} du\, u^2 \frac{\left(1-\frac{Cu^4}{1-v^2}\right)\Pi_z}{\sqrt{1-\frac{Cu^4}{1-v^2} - u^4(\Pi_x^2+\Pi_y^2+\Pi_z^2)}} + \cdots\,,
\end{aligned}$$

where C was defined in (5.30). As in the previous section, in the ultra-relativistic limit all the terms that we have omitted in the equations above are subleading with respect to the terms that we have retained provided the radial coordinate and the momenta scale in this case as

$$u = r(1-v^2)^{1/4}\,, \qquad \Pi_i = \frac{p_i}{\sqrt{1-v^2}}\,, \tag{5.53}$$

where r and p_i are kept fixed in the limit $v \to 1$. In terms of the rescaled variables the boundary conditions (5.53) become

$$\begin{aligned}
\frac{\ell}{2}\sin\theta\sin\varphi &\simeq (1-v^2)^{1/4}\, p_x\, \mathcal{J}_2(p)\,, \\
\frac{\ell}{2}\sin\theta\cos\varphi &\simeq (1-v^2)^{1/4}\, p_y\, \mathcal{J}_2(p)\,, \\
\frac{\ell}{2}\cos\theta &\simeq (1-v^2)^{1/4}\, p_z\, \left(\mathcal{J}_2(p) - C\mathcal{J}_6(p)\right)\,,
\end{aligned} \tag{5.54}$$

where the integral

$$\mathcal{J}_n(p) = \int_0^{r_{\text{max}}} dr \, \frac{r^n}{\sqrt{1 - r^4(C + p_x^2 + p_y^2 + p_z^2)}} \tag{5.55}$$

is of $O(1)$ in the counting in powers in $(1 - v^2)$, and is finite if $n \geq 0$. Further noting that

$$K_0 = 1 - \frac{C}{1 - v^2} u^4 + O(u^6) \simeq 1 - C r^4 \,, \tag{5.56}$$

we see that the bound action becomes

$$S \simeq -\frac{L^2}{2\pi\alpha'} \frac{2}{(1 - v^2)^{1/4}} \Big(\mathcal{J}_{-2}(p) - C \mathcal{J}_2(p) \Big) \int dt \,. \tag{5.57}$$

Since both this bound action and the unbound action (5.33) scale as $(1 - v^2)^{-1/4}$, the divergence at $r = 0$ in the bound action coming from the $\mathcal{J}_{-2}(p)$ integral would exactly cancel that in the unbound action in the difference (3.1). Moreover, by comparing the two actions we would conclude that the momenta p_i introduced in (5.53) are indeed of $O(1)$ in the counting in powers of $(1 - v^2)$ in the ultra-relativistic limit. It would then follow that the integrals $\mathcal{J}_n(p)$ are also of $O(1)$, and therefore that the screening length scales as $L_s \sim (1 - v^2)^{1/4}$ in the ultra-relativistic limit. However, as explained below (5.10), in the ultra-relativistic $L_s = L_{\text{max}}$ is simply the maximum possible separation between a bound quark-antiquark pair, so it can be determined by maximizing ℓ in (5.54) with respect to the momenta. Since the integrals are bounded from above for any value of the p_i, and the maximum is v-independent, it follows that $L_s = L_{\text{max}} \sim (1 - v^2)^{1/4}$.

In summary, we conclude that in the dipole rest frame the screening length scales in the ultra-relativistic limit as

$$L_s \sim \begin{cases} (1 - v^2)^{1/2} \text{ if } \ \theta_v \neq \pi/2 & \text{[motion outside the transverse plane]} \\ \\ (1 - v^2)^{1/4} \text{ if } \ \theta_v = \pi/2 & \text{[motion within the transverse plane]} \end{cases} \tag{5.58}$$

irrespectively of the dipole orientation.

5.3 Isotropic limit

The results above reduce to the isotropic result of ref. [31, 32] in the limit $a \to 0$. This limit is most easily recovered from the results for motion within the transverse plane, since some of the terms in the expansions in section 5.2.1 vanish if $a = 0$, thus invalidating the analysis. In contrast, setting $a = 0$ in section 5.2.2 boils down to simply setting C to its isotropic value, which from (5.30) and (2.3) is

$$C = -\mathcal{F}_4 = \frac{1}{u_{\text{H}}^4} = \pi^4 T^4 \,. \tag{5.59}$$

Since the value of C does not affect the ultra-relativistic scaling of the screening length, we recover the scaling

$$L_{\text{iso}} \sim (1 - v^2)^{1/4} \qquad \text{[isotropic plasma]} \tag{5.60}$$

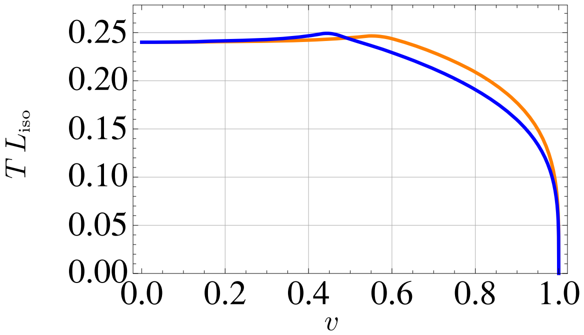

Figure 9. Screening length for a dipole moving through an isotropic plasma in a direction orthogonal (top, blue curve) or parallel (bottom, orange curve) to its orientation.

found in the isotropic case by the authors of [31, 32]. As in the anisotropic case, the ultra-relativistic scaling of the screening length is independent of the dipole's orientation. In fact, even for $v < 1$, the isotropic screening length depends only mildly on the dipole's orientation, as shown in figure 9.

5.4 Numerical results for generic velocities

Away from the ultra-relativistic limit the screening length must be obtained numerically. For this reason we have focused on a few representative cases, namely those in which both the direction of the plasma wind and the dipole's orientation are aligned with one of the original x, y, or z axes. Given the rotational symmetry in the xy-plane, there are only five inequivalent cases to consider, because if the wind 'blows' in the z-direction then orienting the dipole along x or y gives identical physics. In each case, we plot the screening length both as a function of the velocity v for different degrees of anisotropy a, and also as a function of the degree of anisotropy for different values of the velocity. In each case the result can be qualitatively understood combining the static results from section 4 and the ultra-relativistic behavior derived analytically in section 5. We recall that in all cases below, by 'a dipole oriented along x, y or z' we are referring to the original directions before the rotation (5.1) and the boost (5.2).

Wind along z and dipole along z. The numerical results are shown in figures 10 and 11. The curves in figure 10 start at $v = 0$ with the same value as the $\theta = 0$ static result shown in figure 7, and that they vanish as $(1 - v^2)^{1/4}$ in the limit $v \to 1$, in agreement with (5.58)(top line) and (5.60). The screening length decreases with the anisotropy, irrespectively of whether T or s are kept fixed.

Wind along z and dipole along x. The numerical results are shown in figures 12 and 13. We see that the curves in figure 12 start at $v = 0$ with the same value as the $\theta = \pi/2$ static result shown in figure 7, and that they vanish as $(1 - v^2)^{1/4}$ in the limit $v \to 1$, in agreement with (5.58)(top line) and (5.60). In this case the screening length decreases with the anisotropy for any velocity provided the temperature is kept fixed. The

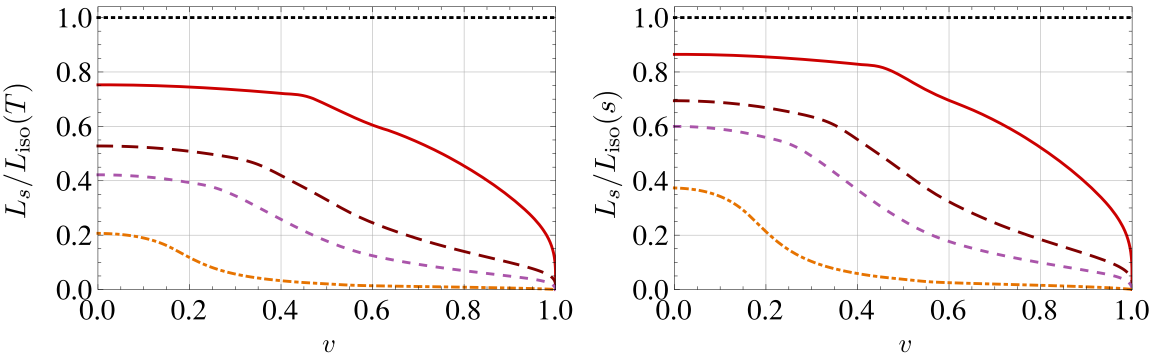

Figure 10. Screening length for a plasma wind along the z-direction and a dipole oriented along the z-direction, for four different values of the anisotropy (from top to bottom) $a/T = 12.2, 42.6, 86, 744$. The corresponding values in units of the entropy density are (in the same order) $aN_c^{2/3}/s^{1/3} = 6.2, 19, 35, 242$. The screening length is plotted in the appropriate units to facilitate comparison with the isotropic result for a plasma at the same temperature (left), or at the same entropy density (right). The isotropic result is plotted in figure 9, and its ultra-relativistic behavior is given in eq. (5.60). At $v = 0$ the curves agree with the $\theta = 0$ values in figure 7. As $v \to 1$ they vanish as $(1 - v^2)^{1/4}$, in agreement with (5.58)(top line) and (5.60).

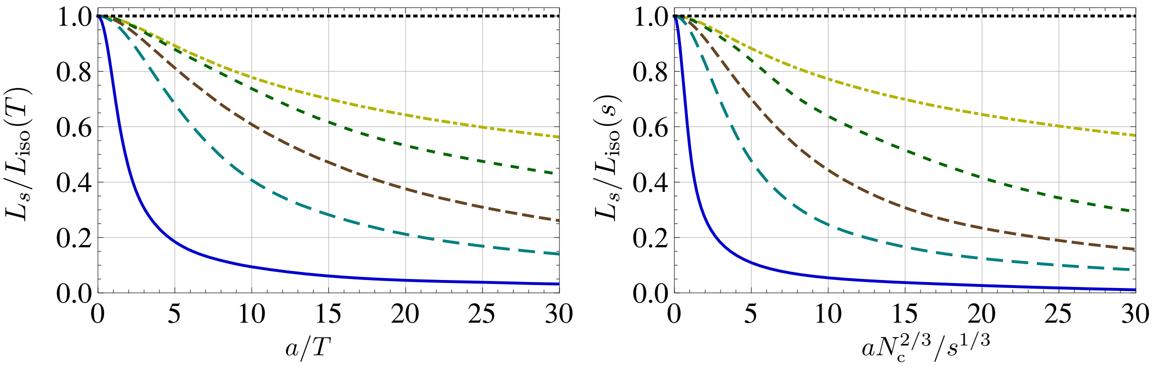

Figure 11. Screening length for a plasma wind along the z-direction and a dipole oriented along the z-direction, at five different velocities (from top to bottom) $v = 0.25, 0.5, 0.7, 0.9, 0.9995$. The screening length is plotted in the appropriate units to facilitate comparison with the isotropic result for a plasma at the same temperature (left), or at the same entropy density (right). The isotropic result is plotted in figure 9, and its ultra-relativistic behavior is given in eq. (5.60).

same behavior is found at constant entropy density for high enough velocities, whereas for low velocities the screening length at constant s actually increases with a.

Wind along x and dipole along x. The numerical results are shown in figures 14 and 15. The curves in figure 14 start at $v = 0$ with the same value as the $\theta = \pi/2$ static result shown in figure 7, and that they approach a finite, non-zero value as $v \to 1$, in agreement with (5.58)(bottom line) and (5.60). As in previous cases, the screening length decreases with the anisotropy for any velocity provided the temperature is kept fixed. The opposite behavior is found at constant s.

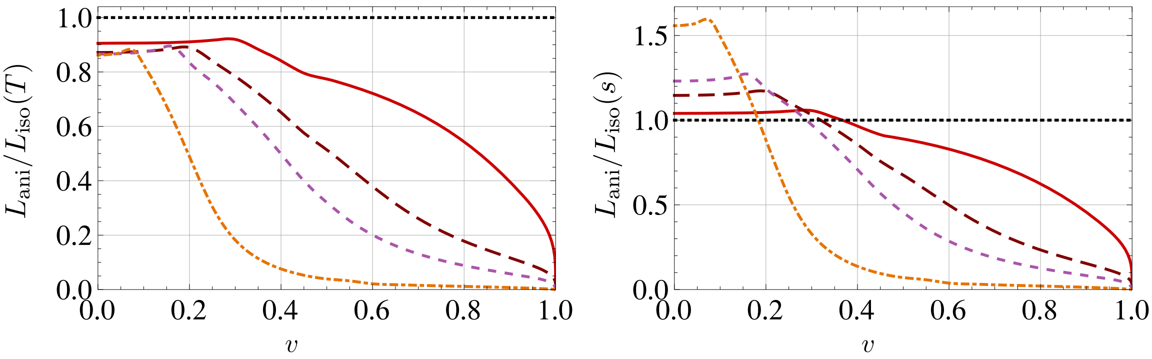

Figure 12. Screening length for a plasma wind along the z-direction and a dipole oriented along the x-direction, for four different values of the anisotropy $a/T = 12.2$ (red, solid), 42.6 (maroon, coarsely dashed), 86 (violet, dashed), 744 (orange, dot-dashed). The corresponding values in units of the entropy density are (in the same order) $aN_c^{2/3}/s^{1/3} = 6.2, 19, 35, 242$. The screening length is plotted in the appropriate units to facilitate comparison with the isotropic result for a plasma at the same temperature (left), or at the same entropy density (right). The isotropic result is plotted in figure 9, and its ultra-relativistic behavior is given in eq. (5.60). At $v = 0$ the curves agree with the $\theta = \pi/2$ values in figure 7. As $v \to 1$ they vanish as $(1-v^2)^{1/4}$, in agreement with (5.58)(top line) and (5.60).

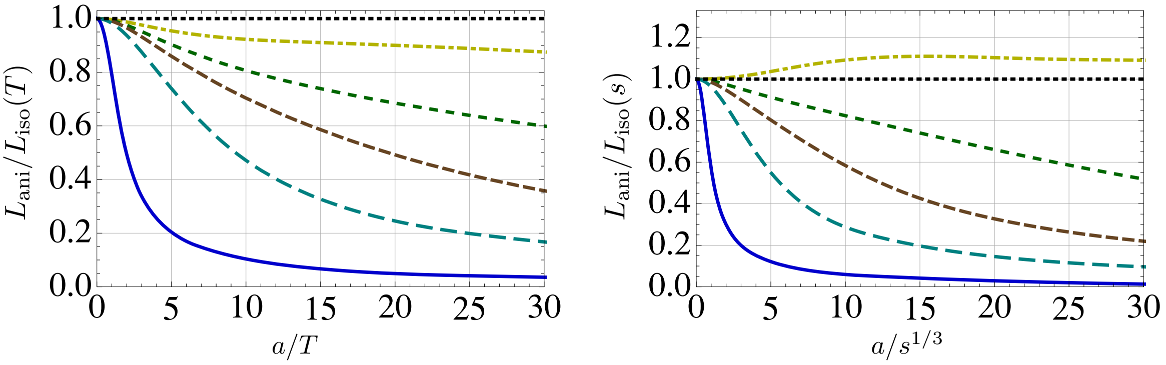

Figure 13. Screening length for a plasma wind along the z-direction and a dipole oriented along the x-direction, at five different velocities (from top to bottom) $v = 0.25, 0.5, 0.7, 0.9, 0.9995$. The screening length is plotted in the appropriate units to facilitate comparison with the isotropic result for a plasma at the same temperature (left), or at the same entropy density (right). The isotropic result is plotted in figure 9, and its ultra-relativistic behavior is given in eq. (5.60).

Wind along x and dipole along y. The numerical results are shown in figures 16 and 17. We see that the curves in figure 16 start at $v = 0$ with the same value as the $\theta = \pi/2$ static result shown in figure 7, and that they approach a finite, non-zero value as $v \to 1$, in agreement with (5.58)(bottom line) and (5.60). The qualitative behavior in as in the case of motion and orientation along x.

Wind along x and dipole along z. The numerical results are shown in figures 18 and 19. We see that the curves in figure 18 start at $v = 0$ with the same value as the $\theta = 0$ static result shown in figure 7, and that they approach a finite, non-zero value as

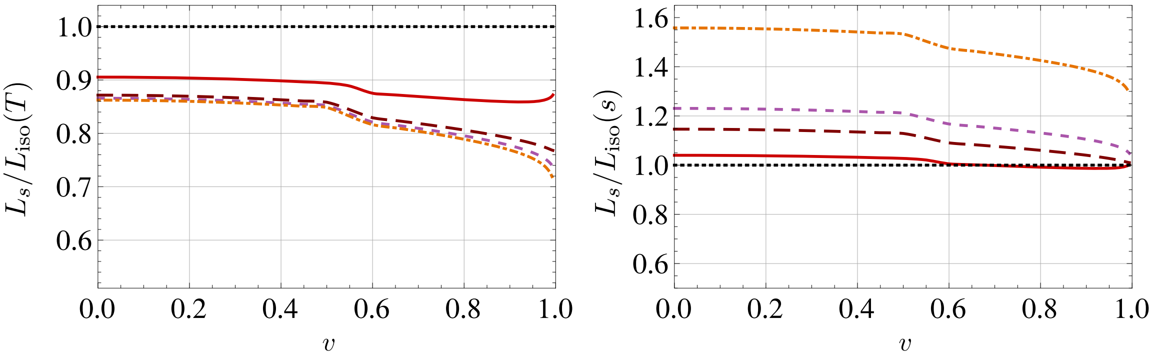

Figure 14. Screening length for a plasma wind along the x-direction and a dipole oriented along the x-direction, for four different values of the anisotropy (from top to bottom) $a/T = 12.2, 42.6, 86, 744$. The corresponding values in units of the entropy density are (in the same order) $aN_c^{2/3}/s^{1/3} = 6.2, 19, 35, 242$. The screening length is plotted in the appropriate units to facilitate comparison with the isotropic result for a plasma at the same temperature (left), or at the same entropy density (right). The isotropic result is plotted in figure 9, and its ultra-relativistic behavior is given in eq. (5.60). At $v = 0$ the curves agree with the $\theta = \pi/2$ values in figure 7. As $v \to 1$ they approach a finite, non-zero value, in agreement with (5.58)(bottom line) and (5.60).

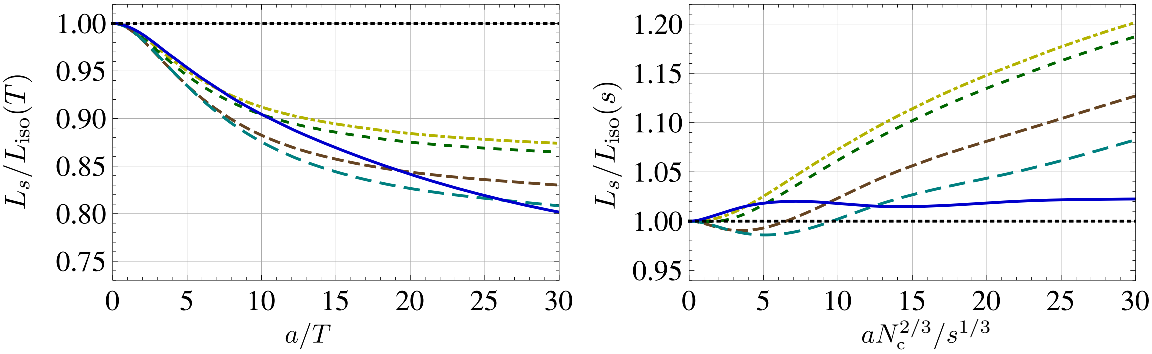

Figure 15. Screening length for a plasma wind along the x-direction and a dipole oriented along the x-direction, at five different velocities v =0.25 (yellow, dot-dashed), 0.5 (green, short dashed), 0.7 (brown, medium dashed), 0.9 (cyan, long dashed), 0.9995 (blue, solid). The screening length is plotted in the appropriate units to facilitate comparison with the isotropic result for a plasma at the same temperature (left), or at the same entropy density (right). The isotropic result is plotted in figure 9, and its ultra-relativistic behavior is given in eq. (5.60).

$v \to 1$, in agreement with (5.58)(bottom line) and (5.60). The screening length decreases with the anisotropy for any velocity provided the temperature is kept fixed. The same is true at large anisotropies if the entropy density is kept fixed.

6 Dissociation temperature and dissociation anisotropy

In previous sections we have focused on computing the screening length in an anisotropic plasma, $L_s(T,a)$, and on comparing it to its isotropic counterpart $L_{\rm iso} = L_s(T,0)$. The

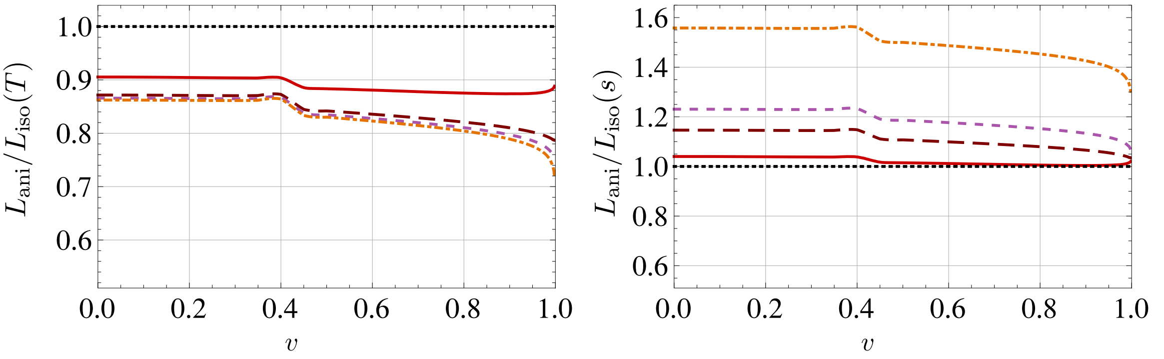

Figure 16. Screening length for a plasma wind along the x-direction and a dipole oriented along the y-direction, for four different values of the anisotropy $a/T = 12.2$ (red, solid), 42.6 (maroon, coarsely dashed), 86 (violet, dashed), 744 (orange, dot-dashed). The corresponding values in units of the entropy density are (in the same order) $aN_{\rm c}^{2/3}/s^{1/3} = 6.2, 19, 35, 242$. The screening length is plotted in the appropriate units to facilitate comparison with the isotropic result for a plasma at the same temperature (left), or at the same entropy density (right). The isotropic result is plotted in figure 9, and its ultra-relativistic behavior is given in eq. (5.60). At $v = 0$ the curves agree with the $\theta = \pi/2$ values in figure 7. As $v \to 1$ they approach a finite, non-zero value, in agreement with (5.58)(bottom line) and (5.60).

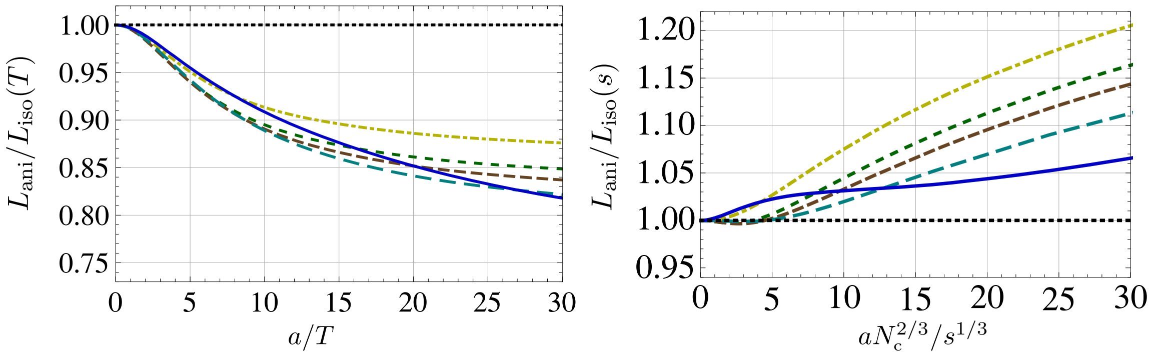

Figure 17. Screening length for a plasma wind along the x-direction and a dipole oriented along the y-direction, at five different velocities v =0.25 (yellow, dot-dashed), 0.5 (green, short dashed), 0.7 (brown, medium dashed), 0.9 (cyan, long dashed), 0.9995 (blue, solid). The screening length is plotted in the appropriate units to facilitate comparison with the isotropic result for a plasma at the same temperature (left), or at the same entropy density (right). The isotropic result is plotted in figure 9, and its ultra-relativistic behavior is given in eq. (5.60).

screening length characterizes the dissociation of a quark-antiquark pair for fixed T and a: a pair separated a distance $\ell < L_s$ forms a bound state, but if ℓ is increased above L_s then the bound state dissociates. Similarly, one may define a dissociation temperature $T_{\rm diss}(a, \ell)$ that characterizes the dissociation of a quark-antiquark pair of fixed size ℓ in a plasma with a given degree of anisotropy a: for $T < T_{\rm diss}$ the pair forms a bound state, but if T is increased above $T_{\rm diss}$ then the bound state dissociates. Analogously, one may define a dissociation anisotropy $a_{\rm diss}(T, \ell)$ such that a bound state forms for $a < a_{\rm diss}$ but

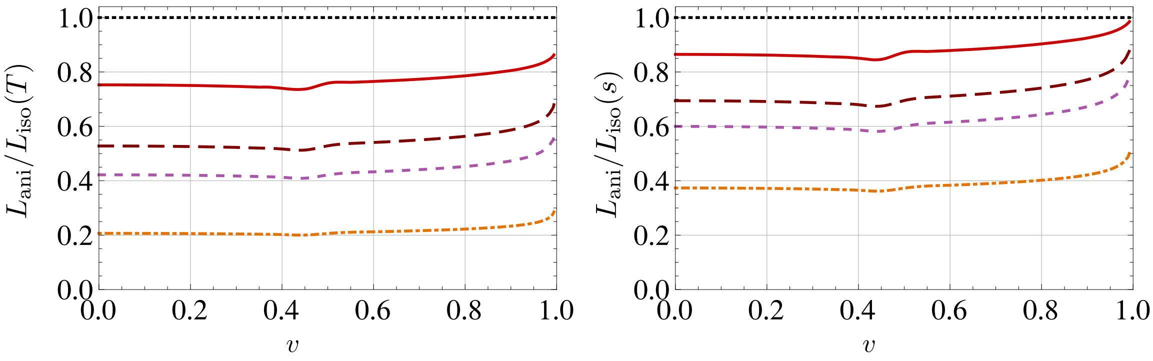

Figure 18. Screening length for a plasma wind along the x-direction and a dipole oriented along the z-direction, for four different values of the anisotropy (from top to bottom) $a/T = 12.2,\, 42.6,\, 86,\, 744$. The corresponding values in units of the entropy density are (in the same order) $aN_{\rm c}^{2/3}/s^{1/3} = 6.2, 19, 35, 242$. The screening length is plotted in the appropriate units to facilitate comparison with the isotropic result for a plasma at the same temperature (left), or at the same entropy density (right). The isotropic result is plotted in figure 9, and its ultra-relativistic behavior is given in eq. (5.60). At $v = 0$ the curves agree with the $\theta = 0$ values in figure 7. As $v \to 1$ they approach a finite, non-zero value, in agreement with (5.58)(bottom line) and (5.60).

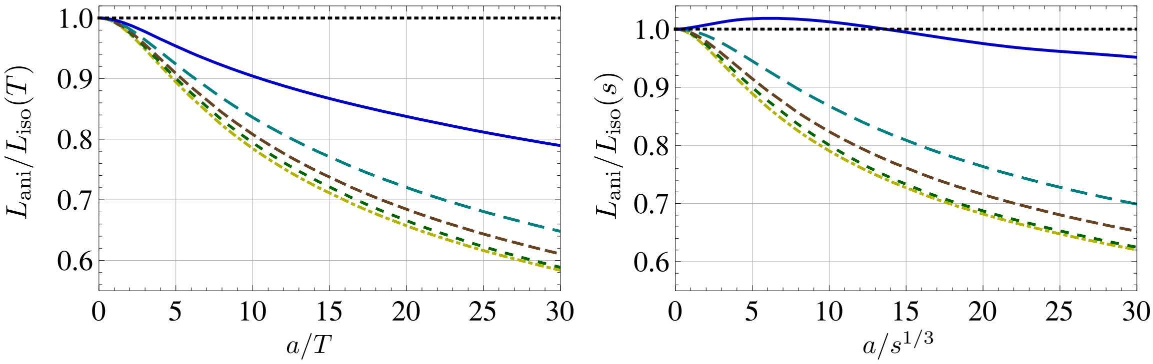

Figure 19. Screening length for a plasma wind along the x-direction and a dipole oriented along the z-direction, at five different velocities (from bottom to top) $v = 0.25, 0.5, 0.7, 0.9, 0.9995$. The screening length is plotted in the appropriate units to facilitate comparison with the isotropic result for a plasma at the same temperature (left), or at the same entropy density (right). The isotropic result is plotted in figure 9, and its ultra-relativistic behavior is given in eq. (5.60).

not for $a > a_{\rm diss}$. It is useful to think of the three-dimensional space parametrized by (T, a, ℓ) as divided in two disconnected regions by a two-dimensional surface: in one region quark-antiquark pairs bind together, while in the other one they do not. The functions $L_s(T, a)$, $T_{\rm diss}(a, \ell)$ and $a_{\rm diss}(T, \ell)$ are then simply different parametrizations of the dividing surface. It is therefore clear that if a triplet (T, a, ℓ) lies on the dividing surface then

$$TL_s(a,T) = T_{\rm diss}(a,\ell)\ell\,, \qquad aL_s(T,a) = a_{\rm diss}(T,\ell)\ell\,, \qquad \text{etc.} \tag{6.1}$$

In this section we will focus on the qualitative form of $T_{\rm diss}$ and $a_{\rm diss}$. As we will see, most of the analysis follows from the asymptotic behavior of the screening length for

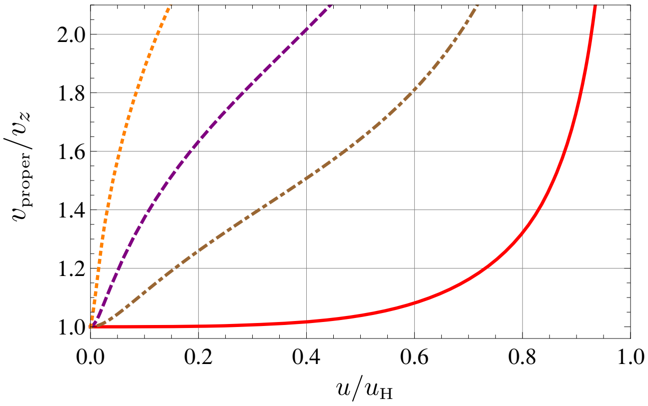

Figure 20. Proper velocity in the z-direction at a position u away from the boundary, as defined in (6.2), for different values of a/T. From right to left, $a/T = 1.38, 33, 86, 249$.

$a \gg T$. This means that, at the qualitative level, most of the results that we will obtain would also apply if we were to replace the temperature by the entropy density as one of our variables. The reason is that, by virtue of (2.5), the limit $a \gg T$ corresponds to the limit $a \gg s^{1/3}$ and vice versa. In addition, we will see that for generic dipole's orientations and velocities, the large-anisotropy limit is entirely controlled by the near-boundary behavior of the metric at $O(u^2)$, which depends solely on a and is therefore completely insensitive to the values of the temperature or of the entropy density.

The key point in the large-a analysis is the requirement that no point on the string can move faster than the local speed of light in the bulk. Consider a meson moving with a velocity v that has a non-zero component v_z along the z-direction. Then we see from (2.2) that the proper velocity along this direction of a point on the string sitting at a value u of the radial coordinate is

$$v_{\rm proper}(u) = v_z \sqrt{-\frac{g_{zz}(u)}{g_{tt}(u)}} = v_z \sqrt{\frac{\mathcal{H}(u)}{\mathcal{F}(u)\mathcal{B}(u)}}\,. \tag{6.2}$$

The function $\mathcal{H}(u)$ increases monotonically from the boundary to the horizon, and is does so more steeply as a/T increases, as illustrated in figure 1. The combination $\mathcal{F}(u)\mathcal{B}(u)$ has the opposite behavior, as expected from the fact that gravity is attractive: it decreases monotonically from the boundary to the horizon. In the isotropic case $\mathcal{H} = 1$ and $\mathcal{FB}$ decreases more steeply as T increases. This is thus the first hint that increasing the anisotropy has an effect similar to increasing the temperature: both make $v_{\rm proper}(u)$ a more steeply increasing function away from the boundary. We have illustrated the effect of the anisotropy in figure 20, where we see that $v_{\rm proper}/v_z$ becomes a steeper function of u as a/T increases.

It follows that, for fixed $v_z \neq 0$, there is a maximum value of $u_{\rm max}$ beyond which $v_{\rm proper}$ becomes superluminal, so no string solution can penetrate to $u > u_{\rm max}$. As we will corroborate numerically, this upper bound on $u_{\rm max}$ translates into an upper bound on L_s. Moreover, $u_{\rm max}$ decreases as a/T increases. This means that for sufficiently large anisotropies we can use the near-boundary expansions (2.6) in order to determine L_s, in analogy to what we did in the ultra-relativistic limit. As in that case, for $v_z \neq 0$ the analysis is controlled by the $O(u^2)$ terms in (2.6). The key point is that these terms depend on a but not on T, so by dimensional analysis it follows that $u_{\text{max}} \sim a^{-1}$ and $L_s \sim a^{-1}$ in the limit $a/T \gg 1$. This limit can be understood as $a \to \infty$ at fixed T, or as $T \to 0$ at fixed a. We thus conclude that, even at $T = 0$, a generic meson will dissociate for a sufficiently large anisotropy a_{diss}.

Mesons at rest and mesons whose velocity is exactly aligned with the transverse plane constitute an exception to the argument above, since in this case $v_z = 0$ and their physics is mostly insensitive to the function $\mathcal{H}(u)$ which characterizes the anisotropic direction. Therefore in this case we expect that u_{max} and L_s will remain finite as we send $a \to \infty$ at fixed T, and hence that dimensional analysis will imply $L_s \sim T^{-1}$.

In summary, the heuristic argument above suggests that in the limit $a/T \gg 1$ we should have

$$L_s(T,a) \sim \begin{cases} \text{const.} \times T^{-1} & \text{if the meson is static or in motion within the transverse plane,} \\ & \\ \text{const.} \times a^{-1} & \text{otherwise.} \end{cases} \tag{6.3}$$

The constants may depend on all the dimensionless parameters such as the velocity and the dipole's orientation. We will refer to the behavior in the second line as 'generic' and to that in the first line as 'non-generic', since the latter only applies if the velocity is exactly zero or if the motion is exactly aligned with the transverse plane. The generic behavior is of course consistent with the analysis of section 5.2.1. Indeed, we saw in that section that for motion outside the transverse plane the ultra-relativistic behavior of L_s is entirely controlled by the $O(u^2)$ terms in the metric, which depend on a but not on T.

Figure 21 shows our numerical results for u_{max}, in units of T^{-1} and a^{-1}, as a function of a/T, for the five physically distinct cases discussed in section 5.4. From the continuous, magenta curves in the first two rows we see that u_{max} goes to zero at large a/T in the cases of motion along z, irrespectively of the dipole's orientation. In contrast, we see that u_{max} does not go zero for a static meson (dashed, blue curves) or for a meson moving along the x-direction (continuous, magenta curves in the last three rows).

Recalling that the isotropic screening length is of the form $L_{\text{iso}} \propto 1/T$, we see that the quantity plotted on the vertical axes in figures 6, 11, 13, 15, 17 and 19 is precisely proportional to $TL_s(T,a)$. However, the asymptotic behavior (6.3) is not apparent in these plots because in most cases the horizontal axes do not extend to high enough values of a/T. For this reason we have illustrated the two possible asymptotic behaviors of L_s in figure 22, where we have extended the horizontal axes to larger values of a/T. We see from the continuous, magenta curves in the first two rows that $L_s \sim 1/a$ for motion along the z-direction. For motion within the transverse plane we see from the same curves in the last three rows that $L_s \sim 1/T$. This approximate scaling relation seems to hold quite precisely for a dipole oriented within the transverse plane (3rd and 4th rows), whereas for a dipole oriented in the z-direction the product TL_s seems to retain a slight (perhaps logarithmic) dependence on a/T at large a/T. We can draw similar conclusions from the dashed, blue curves in the figure, which correspond to static mesons. We see that for mesons oriented within the transverse plane (2nd, 3rd and 4th rows) the relation $TL_s \sim$ constant holds

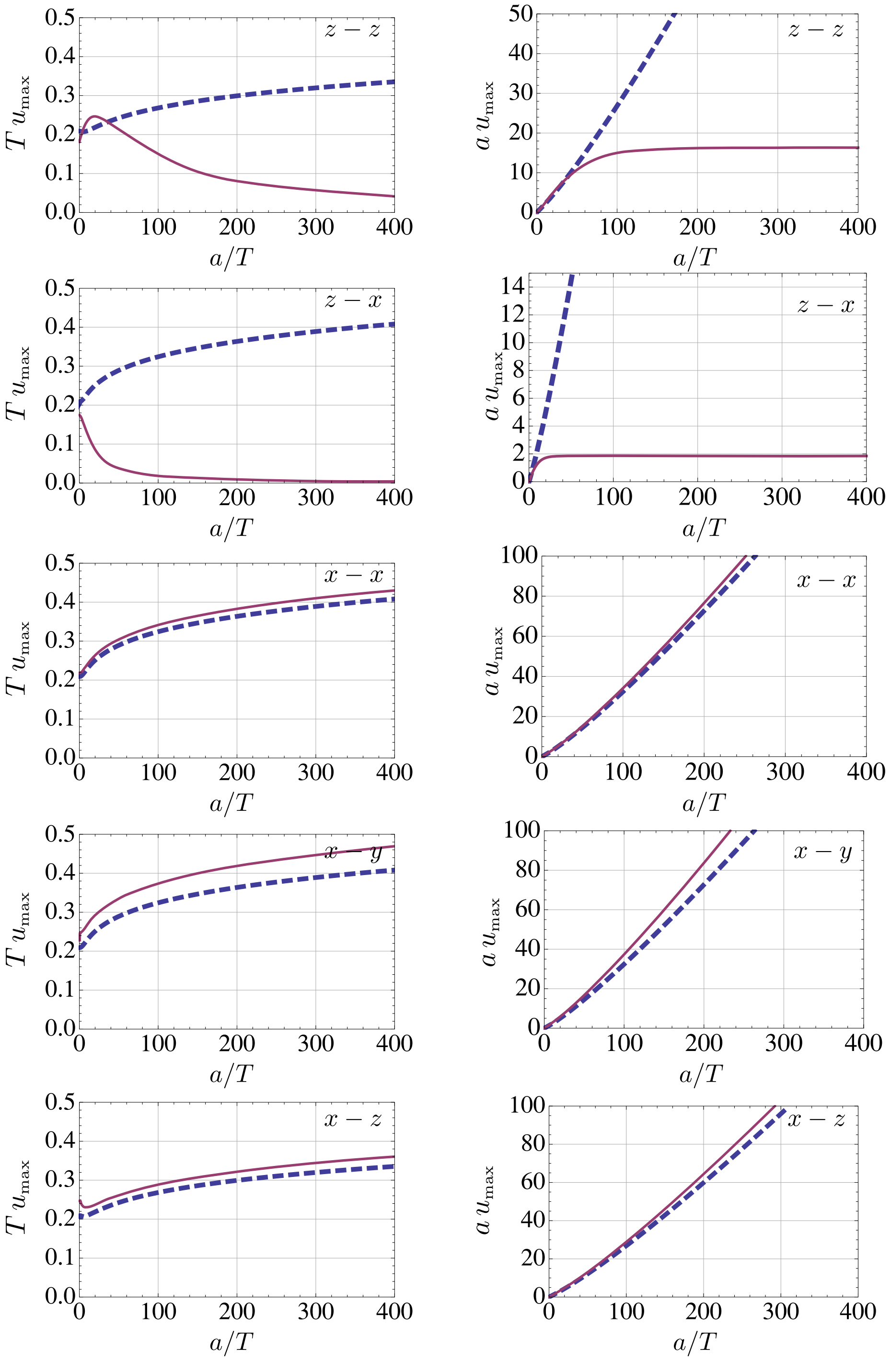

Figure 21. Value of $u_{\max}$ in units of $1/T$ (left) or $1/a$ (right), as a function of the ratio a/T, for a dipole at rest (dashed, blue curve) and for a dipole moving with $v = 0.45$ (continuous, magenta curve). The first letter on the top right corner of each plot indicates the direction of motion, and the second one indicates the orientation of the dipole.

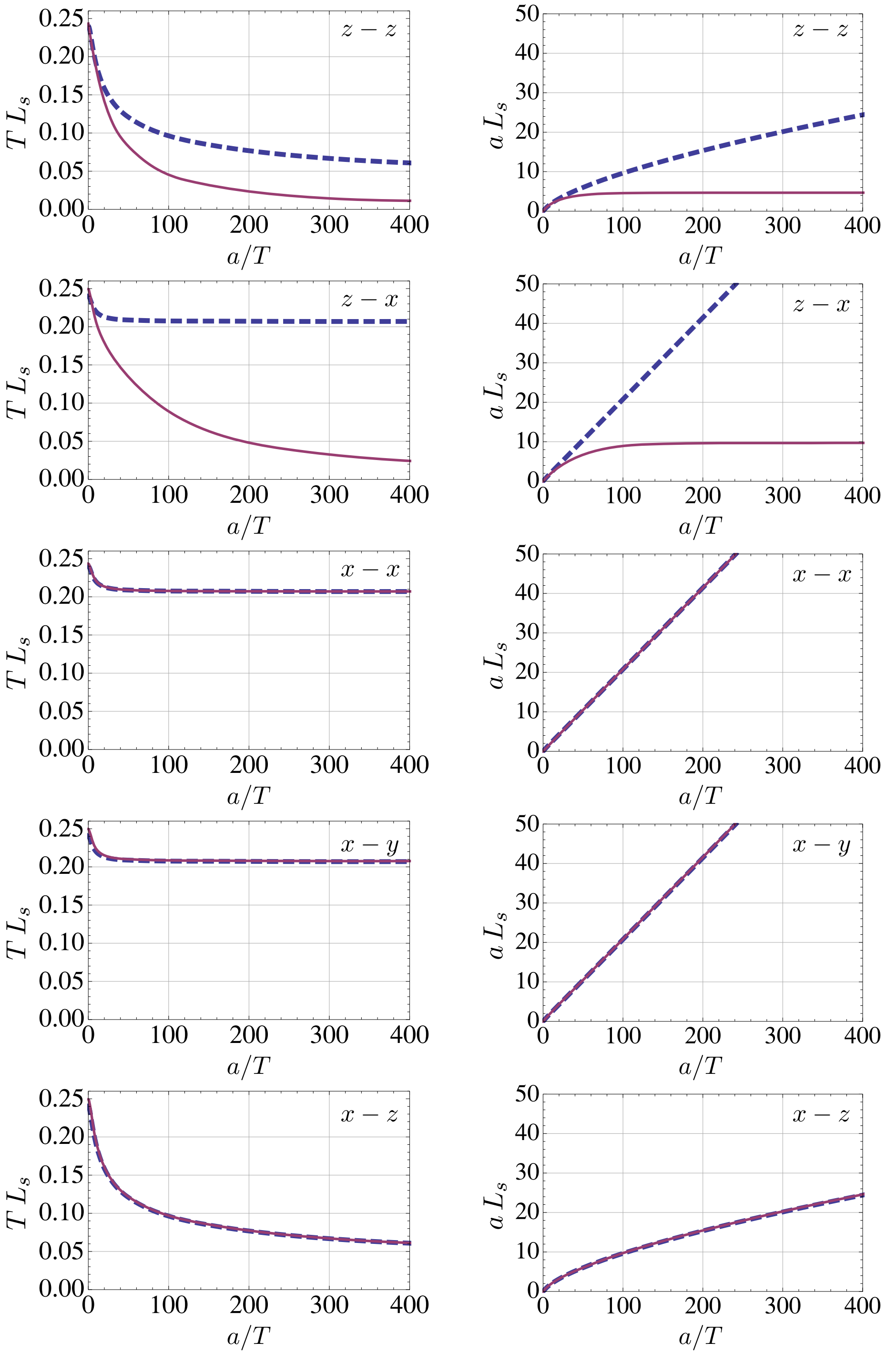

Figure 22. Screening length in units of $1/T$ (left) or $1/a$ (right), as a function of the ratio a/T, for a dipole at rest (dashed, blue curve) and for a dipole moving with $v = 0.45$ (continuous, magenta curve). The first letter on the top right corner of each plot indicates the direction of motion, and the second one indicates the orientation of the dipole.

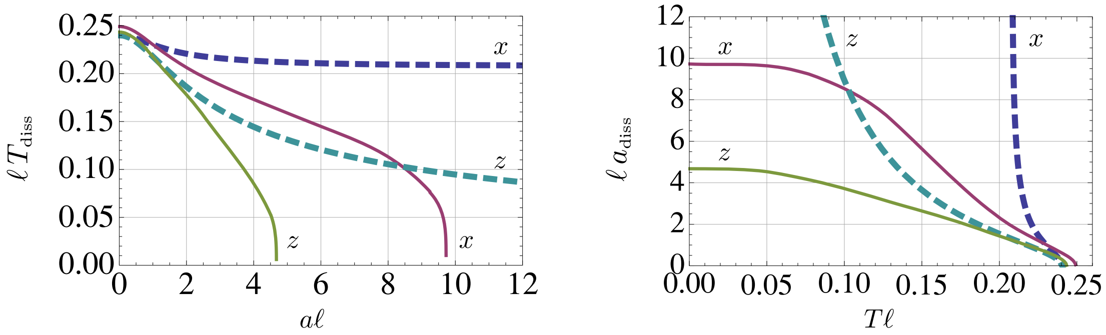

Figure 23. Dissociation temperature (left) $T_{\mathrm{diss}}(a,\ell) = \ell^{-1} f(a\ell)$ and dissociation anisotropy (right) $a_{\mathrm{diss}}(T,\ell) = \ell^{-1} g(T\ell)$ for a dipole at rest (dashed curves) and for a dipole moving along the z-direction with $v = 0.45$ (continuous curves). The orientation of the dipole is indicated by a letter next to each curve.

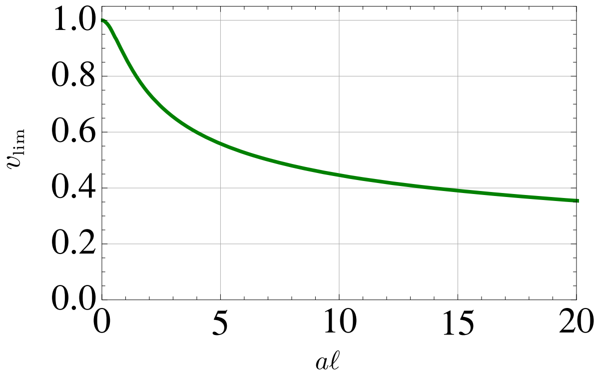

Figure 24. Limiting velocity, for fixed anisotropy and $T = 0$, beyond which a meson oriented along the x-direction and moving along the z-direction will dissociate.

quite precisely, whereas for mesons oriented in the z-direction (1st and 5th rows) there seems to be some slight residual dependence on a/T at large a/T.

Combining the two plots on the left and the right columns of figure 22 we can eliminate a/T and obtain TL_s as a function of aL_s and vice versa. Recalling (6.1) we see that we can interpret the result in the first case as $T_{\mathrm{diss}}(a,\ell) = \ell^{-1} f(a\ell)$, whereas in the second case we get $a_{\mathrm{diss}}(T,\ell) = \ell^{-1} g(T\ell)$. The functions f and g are the curves shown in figure 23(left) and figure 23(right), respectively. The right plot is of course the mirror image along a 45 degree line of the left plot. We see in figure 23(left) that the dissociation temperature decreases monotonically with increasing anisotropy and vanishes at $a\ell \simeq 9.75$ (for the chosen velocity and orientation). On the right plot this corresponds to the dissociation anisotropy at zero temperature. As anticipated above, even at zero temperature, a generic meson of size ℓ will dissociate if the anisotropy is increased above $a_{\mathrm{diss}}(T=0,\ell) \propto 1/\ell$. The proportionality constant in this relation is a decreasing function of the meson velocity in the plasma. This implies that for a fixed anisotropy there is a limiting velocity v_{lim} above which a meson will dissociate, even at zero temperature. The form of $v_{\mathrm{lim}}(a\ell)$ for $T = 0$ is plotted in figure 24.

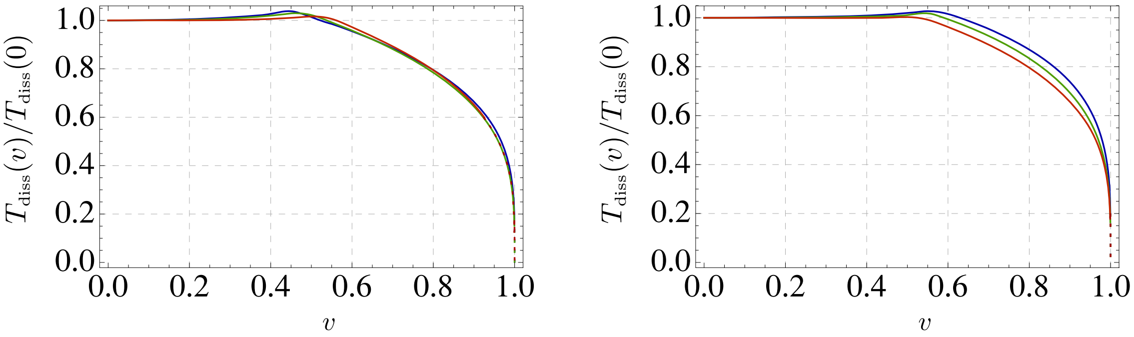

Figure 25. Dissociation temperature for a meson moving along the x-direction and oriented along the z-direction (left) or along the x-direction (right). Each curve corresponds to a fixed value of the product $a\ell = 0$ (blue curve), 1.4 (green curve), 25 (red curve).

The existence of a limiting velocity for quarkonium mesons is well known in a strongly coupled isotropic plasma [35, 36], in which case the dissociation at $v = v_{\text{lim}}$ is caused by the temperature. What we see here is that in our anisotropic plasma this behavior persists as $T \to 0$ for generic motion. In this limit it is the anisotropy that is responsible for the dissociation. In the case of ultra-relativistic motion the relation between a_{diss} or T_{diss} and v_{lim} can be obtained by combining the scalings (5.58) and (6.3). For generic motion these relations yield

$$a_{\text{diss}}(T,\ell) \sim \frac{1}{\ell}(1-v_{\text{lim}}^2)^{1/2}\,, \qquad [a \gg T\,, v_{\text{lim}} \lesssim 1] \tag{6.4}$$

whereas for motion within the transverse plane we obtain

$$T_{\text{diss}}(a,\ell) \sim \frac{1}{\ell}(1-v_{\text{lim}}^2)^{1/4}\,. \qquad [a \gg T\,, v_{\text{lim}} \lesssim 1] \tag{6.5}$$

The scaling (6.5) agrees with the isotropic result [31, 32] and illustrates the fact that, for motion within the transverse plane, the limiting velocity in our anisotropic plasma approaches unity as $T \to 0$. This behavior is the same for a meson at rest, as illustrated in figure 23, where we see that a sufficiently small meson will remain bound in the plasma for any value of the anisotropy provided the plasma is cold enough. In fact, the form of the dissociation temperature for all anisotropies and all velocities within the transverse plane is qualitatively analogous to that of the isotropic case, as shown in figure 25. The fact that the curves in this figure approximately overlap one another signals that the dependence of the dissociation temperature on v and $a\ell$ can be approximately factorized over the entire range $0 \leq v \leq 1$.

In contrast, for generic motion we saw above that the limiting velocity is subluminal even at $T = 0$, $v_{\text{lim}}(T=0, a\ell) < 1$. Increasing the temperature simply decreases the value of the limiting velocity, $v_{\text{lim}}(T\ell, a\ell) < v_{\text{lim}}(T=0, a\ell)$. Turning these statements around we see that, at a fixed anisotropy, the dissociation temperature is a decreasing function of the velocity that vanishes at $v = v_{\text{lim}}(T=0, a\ell)$. This is illustrated in figure 26, where we see that $v_{\text{lim}}(T=0, a\ell)$ decreases as the anisotropy increases, in agreement with figure 24. In

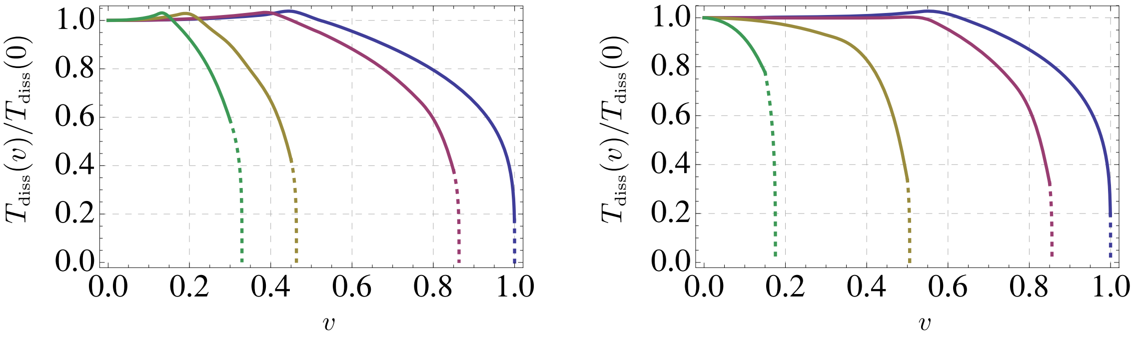

Figure 26. Dissociation temperature for a meson moving along the z-direction and oriented along the x-direction (left) or along the z-direction (right). Each curve corresponds to a fixed value of the product $a\ell$. From right to left, $a\ell = 0, 1, 5.4, 25$.

order to facilitate comparison with the isotropic results of [31–33], in figure 26 we have chosen to normalize the dissociation temperature by its value at $v = 0$ instead of by the dipole's size ℓ. Our numerical results suggest that as v approaches $v_{\rm lim}$ the dissociation temperature may vanish as

$$\frac{T_{\rm diss}(v, a\ell)}{T_{\rm diss}(0, a\ell)} \sim \left(v_{\rm lim}^2 - v^2\right)^{\varepsilon} . \tag{6.6}$$

In this equation $v_{\rm lim} = v_{\rm lim}(T = 0, a\ell)$ and $\varepsilon = \varepsilon(a\ell) > 0$ is an anisotropy-dependent exponent. Unfortunately, the limit $v \to v_{\rm lim}$ is difficult to analyze numerically, so our results are not precise enough to allow us to establish (6.6) unambiguously. To emphasize this point, in figure 26 we have plotted as discontinuous the part of the curves between the last two data points. The last point lies on the horizontal axis at $(v, T) = (v_{\rm lim}, 0)$, and the penultimate point lies at a certain height at $(v \lesssim v_{\rm lim}, T > 0)$. Since this last bit of the curves is an interpolation between these data points, it is difficult to establish whether the slopes of the curves diverge as they meet the horizontal axis, as would be implied by the scaling (6.6). Presumably, this scaling could be verified or falsified analytically by including the first correction in T/a to the scaling in the second line of (6.3).

7 Discussion

We have considered an anisotropic $\mathcal{N} = 4$ SYM plasma in which the x, y directions are rotationally symmetric, but the z-direction is not. In the context of heavy ion collisions the latter would correspond to the beam direction, and the former to the transverse plane. The screening length of a quarkonium meson in motion in the plasma depends on the relative orientation between these directions, on the one hand, and the direction of motion of the meson and its orientation, on the other. This dependence can be parametrized by three angles $(\theta_v, \theta, \varphi)$, as shown in figure 8. We have determined the screening length for the most general geometric parameters and for any anisotropy. Our results are valid in the strong-coupling, large-N_c limit, since we have obtained them by means of the gravity dual [14, 15] of the anisotropic $\mathcal{N} = 4$ plasma. The anisotropy is induced by a position-dependent theta term in the gauge theory, or equivalently by a position-dependent axion on the gravity side. One may therefore wonder how sensitive the conclusions may be to the specific source of the anisotropy. In this respect it is useful to note that the gravity calculation involves only the coupling of the string to the background metric. This means that any anisotropy that gives rise to a qualitatively similar metric (and no Neveu-Schwarz B-field) will yield qualitatively similar results for the screening length, irrespectively of the form of the rest of supergravity fields.

An example of a rather robust conclusion is the ultra-relativistic behavior[2] of the screening length (5.58), which for motion not exactly aligned with the transverse plane is $L_s \sim (1-v^2)^{1/2}$. The $1/2$ exponent contrasts with the $1/4$ isotropic result [31, 32], and follows from the fact that the near-boundary fall-off of the metric (2.2) takes the schematic form

$$g_{\mu\nu} = \frac{L^2}{u^2}\left(\eta_{\mu\nu} + u^2 g^{(2)}_{\mu\nu} + u^4 g^{(4)}_{\mu\nu} + \cdots\right) . \tag{7.1}$$

As v grows closer and closer to 1 the point of maximum penetration of the string into the bulk, $u_{\rm max}$, moves closer and closer to the AdS boundary at $u=0$. As a consequence, the physics in this limit is solely controlled by the near-boundary behavior of the metric. For generic motion the behavior is in fact governed by the $O(u^2)$ terms alone, and a simple scaling argument then leads to the $1/2$ exponent above. In the isotropic case the $O(u^2)$ terms are absent and the same scaling argument leads to the $1/4$ exponent.

In fact, a similar reasoning allowed us to determine the large-anisotropy limit. Since the metric component $g_{zz} \propto \mathcal{H}(u)$ grows as one moves from the boundary to the horizon, a subluminal velocity of the meson at the boundary would eventually translate into a superluminal proper velocity (6.2) at a sufficiently large value of u.[3] This sets an upper limit on the maximum penetration length $u_{\rm max}$ of the string into the bulk and hence on L_s. Moreover, g_{zz} becomes steeper as a/T increases, so in the limit $a/T \gg 1$ the point $u_{\rm max}$ approaches the AdS boundary (unless the motion is aligned with the transverse plane), just as in the ultra-relativistic limit. In this limit the physics is again controlled by the $O(u^2)$ terms in the metric, which depend on a but not on T. Therefore dimensional analysis implies that $L_s = \text{const.} \times a^{-1}$, were the proportionality 'constant' is a decreasing function of the velocity. This led us to one of our main conclusions: even in the limit $T \to 0$, a generic meson of size ℓ will dissociate at some high enough anisotropy $a_{\rm diss} \sim \ell^{-1}$. Similarly, for fixed a and T, even if $T=0$, a generic meson will dissociate if its velocity exceeds a limiting velocity $v_{\rm lim}(a,T) < 1$, as shown in figure 24 for $T=0$. As explained in section 6, the conclusions in this paragraph would remain unchanged if we worked at constant entropy density instead of at constant temperature, since in the limit $a \gg s^{1/3}$ the physics would again be controlled only by the $O(u^2)$ terms in the metric.

The above discussion makes it clear that, at the qualitative level, much of the physics depends only on a few features of the solution: the presence of the $g^{(2)}_{\mu\nu}$ term in the near-boundary expansion of the metric, the fact that the metric (7.1) be non-boost-invariant at order u^2 (i.e. that $g^{(2)}_{\mu\nu}$ not be proportional to $\eta_{\mu\nu}$), and the fact that g_{zz} increases as

---

[2] We recall that we first send the quark mass to infinity and then $v \to 1$ (see section 1).

[3] Note that the overall conformal factor $1/u^2$ in (2.2) plays no role in this argument, since it cancels out in the ratio (6.2).

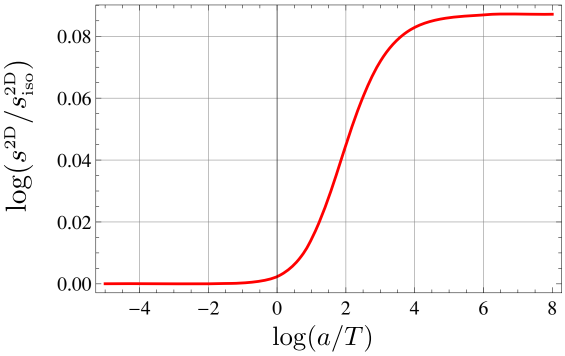

Figure 27. Log-log plot of the entropy density per unit 2-area in the xy-directions on a constant-z slice as a function of a/T, normalized to the isotropic result $s^{2D}_{\rm iso} = \frac{\pi}{2} N_c^2 T^2$.

a function of both u and a/T.[4] The second condition is necessary because otherwise the physics of a meson in motion would be equivalent to that of a meson at rest, and we have seen that the latter is very similar to that of a meson in an isotropic plasma. The third condition ensures that $u_{\rm max}$ moves close to the boundary as a/T increases. Note that adding temperature to an otherwise boost-invariant metric will only affect $g^{(4)}_{\mu\nu}$, and thus this is not enough to make $g^{(2)}_{\mu\nu}$ non-boost-invariant. This conclusion is consistent with the fact that $g^{(2)}_{\mu\nu}$ is only a function of the external sources which the theory is coupled to.

From the gauge theory viewpoint, some heuristic intuition can be gained by recalling that the anisotropy is induced by dissolving along the z-direction objects that extend along the xy-directions [14, 15, 26]. The number density of such objects along the z-direction, dn/dz, is proportional to a. On the gravity side these are D7-branes that wrap the five-sphere in the metric (2.2), extend along the xy-directions, and are homogeneously distributed in the z-direction. Increasing a has a large effect on the entropy density per unit 3-volume in the xyz-directions, in the sense that $s/T^3 \to \infty$ as $a/T \to \infty$, as shown in figure 2. In contrast, the entropy density per unit 2-area in the xy-directions on a constant-z slice, s^{2D}/T^2, approaches a constant in the limit $a/T \to \infty$. This is illustrated in figure 27, which is based on our numerical calculations, but it can also be proven analytically following the argument in section 2.5 of ref. [26]. In view of these differences, it is perhaps not surprising that the anisotropy has the largest effect on the physics of mesons moving along the z-direction, and the smallest effect on the physics of mesons moving within the transverse plane. Mesons at rest are also more sensitive to the anisotropy if they extend along the z-direction than if they are contained within the transverse plane. Presumably, the correct intuition behind this physics is that moving against the D7-branes is harder than moving along them.

We close with a few comments on existing weak-coupling results on the physics of quarkonium dissociation in the real-world QGP. In the isotropic case the velocity dependence of the heavy quark potential has been studied using perturbative and effective field theory methods, see e.g. [37–40]. These analyses include modifications of both the

---

[4] Again, up to possible overall conformal factors.

real and imaginary parts of the potential, which are related to screening and to the thermal width of the states, respectively. They find that meson dissociation at non-zero velocity results form a complex interplay between the real and the imaginary parts of the potential. However, the general trend that seems to emerge is that screening effects increase with the velocity, while the width of the states decreases. The behavior of the real part is thus in qualitative agreement with the isotropic limit of our results. However, the extraction of a screening length from these analyses is not immediate due to the fact that the real part of the potential is not approximately Yukawa-like [39, 40], in contrast with the holographic result. In any case, an interesting consequence of the dominance of the real part of the potential is that, at sufficiently high velocities, dissociation is caused by screening rather than by Landau damping [39, 40]. In the holographic framework, the thermal widths of our mesons could presumably be computed along the lines of [41].

To the best of our knowledge no results at non-zero velocity exist in the presence of anisotropies, so in this case we will limit ourselves to the static situation. We emphasize though that any comparison between these results and ours should be interpreted with caution, because the sources of anisotropy in the QGP created in a heavy ion collision and in our system are different. In the QGP the anisotropy is dynamical in the sense that it is due to the initial distribution of particles in momentum space, which will evolve in time and eventually become isotropic. In contrast, in our case the anisotropy is due to an external source that keeps the system in an equilibrium anisotropic state that will not evolve in time. We hope that, nevertheless, our system might provide a good toy model for processes whose characteristic time scale is sufficiently shorter than the time scale controlling the time evolution of the QGP.

A general conclusion of refs. [42–44] is that, if the comparison between the anisotropic plasma and its isotropic counterpart is made at equal temperatures, then the screening length increases with the anisotropy. This effect occurs for dipoles oriented both along and orthogonally to the anisotropic direction, but it is more pronounced for dipoles along the anisotropic direction. The dependence on the anisotropy in these weak-coupling results is the opposite of what we find in our strongly coupled plasma. In our case the screening length in the anisotropic plasma is smaller than in its isotropic counterpart if both plasmas are taken to have the same temperature, as shown in figure 6(left). We also find that the effect is more pronounced for dipoles extending along the anisotropic direction, as illustrated in figure 7(left).

Refs. [44, 45] argued that if the comparison between the anisotropic and the isotropic plasmas is made at equal entropy densities, then the physics of quarkonium dissociation exhibits little or no sensitivity to the value of the anisotropy. This is again in contrast to our results since, as shown in figure 6(right) and figure 7(right), the screening length in this case is just as sensitive to the anisotropy as in the equal-temperature comparison. The difference in the equal-entropy case is simply that the screening length may increase or decrease with the anisotropy depending on the dipole's orientation.

Acknowledgments

It is a pleasure to thank M. Strickland for helpful discussions. MC is supported by a postdoctoral fellowship from Mexico's National Council of Science and Technology (CONACyT). We acknowledge financial support from 2009-SGR-168, MEC FPA2010-20807-C02-01, MEC FPA2010-20807-C02-02 and CPAN CSD2007-00042 Consolider-Ingenio 2010 (MC, DF and DM), and from DE-FG02-95ER40896 and CNPq (DT).

References

[1] STAR collaboration, J. Adams et al., *Experimental and theoretical challenges in the search for the quark gluon plasma: the STAR collaboration's critical assessment of the evidence from RHIC collisions*, Nucl. Phys. **A 757** (2005) 102 [`nucl-ex/0501009`] [INSPIRE].

[2] PHENIX collaboration, K. Adcox et al., *Formation of dense partonic matter in relativistic nucleus-nucleus collisions at RHIC: experimental evaluation by the PHENIX collaboration*, Nucl. Phys. **A 757** (2005) 184 [`nucl-ex/0410003`] [INSPIRE].

[3] *Proceedings of Quark Matter* 2011, J. Phys. **G 38** (2011).

[4] E. Shuryak, *Why does the quark gluon plasma at RHIC behave as a nearly ideal fluid?*, Prog. Part. Nucl. Phys. **53** (2004) 273 [`hep-ph/0312227`] [INSPIRE].

[5] E.V. Shuryak, *What RHIC experiments and theory tell us about properties of quark-gluon plasma?*, Nucl. Phys. **A 750** (2005) 64 [`hep-ph/0405066`] [INSPIRE].

[6] J.M. Maldacena, *The large-N limit of superconformal field theories and supergravity*, *Adv. Theor. Math. Phys.* **2** (1998) 231 [Int. J. Theor. Phys. **38** (1999) 1113] [`hep-th/9711200`] [INSPIRE].

[7] S. Gubser, I.R. Klebanov and A.M. Polyakov, *Gauge theory correlators from noncritical string theory*, Phys. Lett. **B 428** (1998) 105 [`hep-th/9802109`] [INSPIRE].

[8] E. Witten, *Anti-de Sitter space and holography*, *Adv. Theor. Math. Phys.* **2** (1998) 253 [`hep-th/9802150`] [INSPIRE].

[9] J. Casalderrey-Solana, H. Liu, D. Mateos, K. Rajagopal and U.A. Wiedemann, *Gauge/string duality, hot QCD and heavy ion collisions*, `arXiv:1101.0618` [INSPIRE].

[10] P.M. Chesler and L.G. Yaffe, *Boost invariant flow, black hole formation and far-from-equilibrium dynamics in $N = 4$ supersymmetric Yang-Mills theory*, Phys. Rev. **D 82** (2010) 026006 [`arXiv:0906.4426`] [INSPIRE].

[11] P.M. Chesler and L.G. Yaffe, *Holography and colliding gravitational shock waves in asymptotically AdS_5 spacetime*, Phys. Rev. Lett. **106** (2011) 021601 [`arXiv:1011.3562`] [INSPIRE].

[12] M.P. Heller, R.A. Janik and P. Witaszczyk, *The characteristics of thermalization of boost-invariant plasma from holography*, Phys. Rev. Lett. **108** (2012) 201602 [`arXiv:1103.3452`] [INSPIRE].

[13] M.P. Heller, R.A. Janik and P. Witaszczyk, *A numerical relativity approach to the initial value problem in asymptotically anti-de Sitter spacetime for plasma thermalization — an ADM formulation*, Phys. Rev. **D 85** (2012) 126002 [`arXiv:1203.0755`] [INSPIRE].

[14] D. Mateos and D. Trancanelli, *The anisotropic $N = 4$ super Yang-Mills plasma and its instabilities*, *Phys. Rev. Lett.* **107** (2011) 101601 [`arXiv:1105.3472`] [INSPIRE].

[15] D. Mateos and D. Trancanelli, *Thermodynamics and instabilities of a strongly coupled anisotropic plasma*, *JHEP* **07** (2011) 054 [`arXiv:1106.1637`] [INSPIRE].

[16] A. Rebhan and D. Steineder, *Probing two holographic models of strongly coupled anisotropic plasma*, *JHEP* **08** (2012) 020 [`arXiv:1205.4684`] [INSPIRE].

[17] R.A. Janik and P. Witaszczyk, *Towards the description of anisotropic plasma at strong coupling*, *JHEP* **09** (2008) 026 [`arXiv:0806.2141`] [INSPIRE].

[18] D. Giataganas, *Probing strongly coupled anisotropic plasma*, *JHEP* **07** (2012) 031 [`arXiv:1202.4436`] [INSPIRE].

[19] A. Rebhan and D. Steineder, *Violation of the holographic viscosity bound in a strongly coupled anisotropic plasma*, *Phys. Rev. Lett.* **108** (2012) 021601 [`arXiv:1110.6825`] [INSPIRE].

[20] K.A. Mamo, *Holographic RG flow of the shear viscosity to entropy density ratio in strongly coupled anisotropic plasma*, *JHEP* **10** (2012) 070 [`arXiv:1205.1797`] [INSPIRE].

[21] M. Chernicoff, D. Fernandez, D. Mateos and D. Trancanelli, *Drag force in a strongly coupled anisotropic plasma*, *JHEP* **08** (2012) 100 [`arXiv:1202.3696`] [INSPIRE].

[22] M. Chernicoff, D. Fernandez, D. Mateos and D. Trancanelli, *Jet quenching in a strongly coupled anisotropic plasma*, *JHEP* **08** (2012) 041 [`arXiv:1203.0561`] [INSPIRE].

[23] K.B. Fadafan and H. Soltanpanahi, *Energy loss in a strongly coupled anisotropic plasma*, *JHEP* **10** (2012) 085 [`arXiv:1206.2271`] [INSPIRE].

[24] A. Gynther, A. Rebhan and D. Steineder, *Thermodynamics and phase diagram of anisotropic Chern-Simons deformed gauge theories*, *JHEP* **10** (2012) 012 [`arXiv:1207.6283`] [INSPIRE].

[25] C. Krishnan, *Baryon dissociation in a strongly coupled plasma*, *JHEP* **12** (2008) 019 [`arXiv:0809.5143`] [INSPIRE].

[26] T. Azeyanagi, W. Li and T. Takayanagi, *On string theory duals of Lifshitz-like fixed points*, *JHEP* **06** (2009) 084 [`arXiv:0905.0688`] [INSPIRE].

[27] S. Kachru, X. Liu and M. Mulligan, *Gravity duals of Lifshitz-like fixed points*, *Phys. Rev.* **D 78** (2008) 106005 [`arXiv:0808.1725`] [INSPIRE].

[28] K. Copsey and R. Mann, *Pathologies in asymptotically Lifshitz spacetimes*, *JHEP* **03** (2011) 039 [`arXiv:1011.3502`] [INSPIRE].

[29] S.-J. Rey, S. Theisen and J.-T. Yee, *Wilson-Polyakov loop at finite temperature in large-N gauge theory and anti-de Sitter supergravity*, *Nucl. Phys.* **B 527** (1998) 171 [`hep-th/9803135`] [INSPIRE].

[30] A. Brandhuber, N. Itzhaki, J. Sonnenschein and S. Yankielowicz, *Wilson loops in the large-N limit at finite temperature*, *Phys. Lett.* **B 434** (1998) 36 [`hep-th/9803137`] [INSPIRE].

[31] H. Liu, K. Rajagopal and U.A. Wiedemann, *An AdS/CFT calculation of screening in a hot wind*, *Phys. Rev. Lett.* **98** (2007) 182301 [`hep-ph/0607062`] [INSPIRE].

[32] H. Liu, K. Rajagopal and U.A. Wiedemann, *Wilson loops in heavy ion collisions and their calculation in AdS/CFT*, *JHEP* **03** (2007) 066 [`hep-ph/0612168`] [INSPIRE].

[33] M. Chernicoff, J.A. Garcia and A. Guijosa, *The energy of a moving quark-antiquark pair in an $N = 4$ SYM plasma*, *JHEP* **09** (2006) 068 [`hep-th/0607089`] [INSPIRE].

[34] C. Herzog, A. Karch, P. Kovtun, C. Kozcaz and L. Yaffe, *Energy loss of a heavy quark moving through $N = 4$ supersymmetric Yang-Mills plasma*, *JHEP* **07** (2006) 013 [`hep-th/0605158`] [INSPIRE].

[35] D. Mateos, R.C. Myers and R.M. Thomson, *Thermodynamics of the brane*, *JHEP* **05** (2007) 067 [`hep-th/0701132`] [INSPIRE].

[36] Q.J. Ejaz, T. Faulkner, H. Liu, K. Rajagopal and U.A. Wiedemann, *A limiting velocity for quarkonium propagation in a strongly coupled plasma via AdS/CFT*, *JHEP* **04** (2008) 089 [`arXiv:0712.0590`] [INSPIRE].

[37] T. Song, Y. Park, S.H. Lee and C.-Y. Wong, *The thermal width of heavy quarkonia moving in quark gluon plasma*, *Phys. Lett.* **B 659** (2008) 621 [`arXiv:0709.0794`] [INSPIRE].

[38] F. Dominguez and B. Wu, *On dissociation of heavy mesons in a hot quark-gluon plasma*, *Nucl. Phys.* **A 818** (2009) 246 [`arXiv:0811.1058`] [INSPIRE].

[39] M.A. Escobedo, J. Soto and M. Mannarelli, *Non-relativistic bound states in a moving thermal bath*, *Phys. Rev.* **D 84** (2011) 016008 [`arXiv:1105.1249`] [INSPIRE].

[40] M.A. Escobedo, *Non-relativistic bound states in a moving thermal bath*, http://quark.phy.bnl.gov/www/rhic2/talks_qprogram/moving.pdf, Physik-Department T30f, Technische Universität München, Munich Germany June 15 2011.

[41] T. Faulkner and H. Liu, *Meson widths from string worldsheet instantons*, *Phys. Lett.* **B 673** (2009) 161 [`arXiv:0807.0063`] [INSPIRE].

[42] A. Dumitru, Y. Guo and M. Strickland, *The heavy-quark potential in an anisotropic (viscous) plasma*, *Phys. Lett.* **B 662** (2008) 37 [`arXiv:0711.4722`] [INSPIRE].

[43] A. Dumitru, Y. Guo, A. Mócsy and M. Strickland, *Quarkonium states in an anisotropic QCD plasma*, *Phys. Rev.* **D 79** (2009) 054019 [`arXiv:0901.1998`] [INSPIRE].

[44] Y. Burnier, M. Laine and M. Vepsäläinen, *Quarkonium dissociation in the presence of a small momentum space anisotropy*, *Phys. Lett.* **B 678** (2009) 86 [`arXiv:0903.3467`] [INSPIRE].

[45] O. Philipsen and M. Tassler, *On quarkonium in an anisotropic quark gluon plasma*, `arXiv:0908.1746` [INSPIRE].

Chapter 4

An analysis of transport phenomena in p-wave superfluids

This chapter contains the publication:

- J. Erdmenger, D. Fernandez, and H. Zeller,
“New Transport Properties of Anisotropic Holographic Superfluids,”
JHEP **1304** (2013) 049, `arXiv:1212.4838 [hep-th]`.

Published for SISSA by Springer

Received: *January 28, 2013*
Accepted: *March 20, 2013*
Published: *April 8, 2013*

New transport properties of anisotropic holographic superfluids

Johanna Erdmenger,[a] **Daniel Fernández**[b] **and Hansjörg Zeller**[a]

[a] *Max-Planck-Institut für Physik (Werner-Heisenberg-Institut),*
Föhringer Ring 6, 80805 München, Germany
[b] *Departament de Física Fonamental & Institut de Ciències del Cosmos (ICC),*
Universitat de Barcelona (UB), Martí i Franquès 1, E-08028 Barcelona, Spain

E-mail: `jke@mppmu.mpg.de`, `daniel@ffn.ub.edu`, `zeller@mppmu.mpg.de`

Abstract: We complete the analysis of transport phenomena in p-wave superfluids within gauge/gravity duality, using the SU(2) Einstein-Yang-Mills model with backreaction. In particular, we analyze the fluctuation modes of helicity zero in addition to the helicity one and two modes studied earlier. We compute a further transport coefficient, associated to the first normal stress difference, not previously considered in the holographic context. In the unbroken phase this is related to a minimally coupled scalar on the gravity side. Moreover we find transport phenomena related to the thermoelectric and piezoelectric effects, in particular in the direction of the condensate, as well as the flexoelectric effect. These are similar to phenomena observed in condensed matter systems.

Keywords: Gauge-gravity correspondence, AdS-CFT Correspondence, Black Holes, Holography and condensed matter physics (AdS/CMT)

ArXiv ePrint: 1212.4838

doi:10.1007/JHEP04(2013)049

Contents

1 Introduction

Gauge/gravity duality has become a valuable tool for gaining insight into the physics of many different strongly coupled theories and, in particular, is being used to successfully describe their hydrodynamical behavior, with the prospect of making contact with systems found in nature. Recently, many new features within hydrodynamics have been discovered using gauge/gravity duality: For instance, the importance of anomalies for relativistic hydrodynamics as applied to quark-gluon plasma first appeared in the context of gauge/gravity duality [1, 2]. Subsequently, in [3–7] and [8, 9] it has been realized by thermal field theory computations and from general hydrodynamics arguments that anomalies induce modifications in the constitutive relations of relativistic hydrodynamics. Moreover, in [10–12] chiral anomalies have been shown to give rise to non-dissipative transport coefficients. Anisotropy has been included by considering the backreacted holographic p-wave superfluid (see below) and by means of a position-dependent theta-term, leading to several interesting effects [13–15]. A common feature of these systems is that the breaking of symmetries brings about a richer structure to the theory, so that new phenomena are unveiled.

A very suitable system to study anisotropic hydrodynamics is the holographic backreacted p-wave superfluid, in which the rotational symmetry is broken by a vector condensate which may be interpreted as a vector meson. This system has been studied in [16–21]. It involves a finite SU(2) charge density or isospin density. In the present article we present the study of the remaining hydrodynamic modes that were not accounted for in [19] and describe the corresponding new transport properties.

In [18, 19], the helicity two and one fluctuations have been analyzed. It has been found that the helicity one modes lead to contributions to the viscosity tensor whose ratio with the entropy density is non-universal at leading order in the 't Hooft coupling and N. These contributions are temperature dependent and satisfy the viscosity bound, $\eta/s \geq 1/4\pi$. This is in contrast to the θ-term model of [14] where the usual viscosity bound [22–24] is violated [25]. This happens already for Einstein gravity, violations of the bound by Gauss-Bonnet terms have been studied in [26].

The Einstein-Yang-Mills model may also be used as a starting point to derive similar universal relations, such as the holographic realization of Homes' law [27] of condensed matter physics. Furthermore when considering finite SU(2) magnetic fields, the system admits more than one possible solution (or state), but similarly to the holographic superfluid at finite SU(2) density, only one is physically realized, determined by the lowest free energy. A magnetic field generates an Abrikosov lattice [28] in a superconductor, which becomes the preferred state if the magnetic field is sufficiently large.

The Einstein-Yang-Mills system we consider in this publication is motivated by the D3/D7 setup [29], which allows for temperature and matter in the fundamental representation to be added to the system. Holographically, the Hawking temperature of a black hole geometry coincides with the temperature T of the dual thermal field theory. A chemical potential μ can also be introduced by placing a non-vanishing boundary condition upon the bulk gauge field. Given these ingredients, it is possible to do thermodynamics, since each solution labeled with T/μ describes a different thermal state of the dual field theory.

In this paper we consider a superfluid generated by a finite SU(2) density (for an extensive study of this background see [16, 19]). In this case, the temperature determines the preferred state, i.e. at some critical value T_c the system undergoes a phase transition between the normal ($T > T_c$) and superfluid ($T < T_c$) states. We will be interested in the superfluid phase and study its transport properties. To do so, we consider fluctuations in a backreacted holographic p-wave superfluid theory defined in an AdS$_5$ geometry with an

SU(2) Yang-Mills gauge field. The boundary condition that fixes the chemical potential,

$$\lim_{r\to\infty} A_t = \mu \,, \tag{1.1}$$

breaks explicitly this SU(2) symmetry, leaving a $\mathrm{U}(1)_3$ gauge symmetry. Depending on the values of μ, the system may present a superfluid or a normal phase, with the order of the phase transition being controlled by a parameter α, which on the gravity side measures the effect of the gauge fields onto the geometry. The superfluid state is thermodynamically preferred at low temperatures compared to the chemical potential, and the transition to this phase is characterised by the formation of a vector condensate $\langle \mathcal{J}_1^x \rangle$, as opposed to the case of an s-wave superfluid, in which a scalar field condenses. The vector condensate designates a particular direction both in momentum and flavor space, and as a consequence the spatial rotational SO(3) symmetry and the $\mathrm{U}(1)_3$ symmetry are spontaneously broken. Schematically, this process can be represented as

$$\begin{aligned} \mathrm{SU}(2) \xrightarrow[\text{Expl.B}]{} \mathrm{U}(1)_3 &\xrightarrow[\text{SSB}]{} \mathbb{Z}_2 \,, \\ \mathrm{SO}(3) &\xrightarrow[\text{SSB}]{} \mathrm{SO}(2) \,. \end{aligned} \tag{1.2}$$

This is an example of spontaneous breaking of continuous symmetries in gauge/gravity duality (first achieved in [30]) to construct holographic superfluids or superconductors. This technique was initially developed by breaking Abelian symmetries [31, 32] and later adapted to p-wave superconductors/superfluids [33] as in the case at hand, giving rise to the first string theory embeddings of these constructions [34–36].

We present an analysis of the perturbations of the spacetime metric, $h_{\mu\nu}$, and of the Yang-Mills field, a_μ^a, about the Einstein-Yang-Mills model in AdS_5. Due to the breaking of the spatial rotational symmetry, these fluctuations can be grouped according to their transformation behavior under the remaining SO(2) rotational symmetry around the x-axis. In this paper, we present the fluctuations which transform as scalars under this group. Vector and tensor fluctuations have been studied in [18, 19]. To make the equations tractable, we set the spatial momentum $\vec{k} = 0$. This simplification leads to an additional $\mathbb{Z}_2$ symmetry under which the scalar fluctuations can be characterized further. We end up with two distinct blocks, the first of which contains, among others, the gauge field fluctuation a_x^3 and the metric fluctuation h_{tx}, and the second one the diagonal metric fluctuations, a_x^1 and a_x^2.

From the field theory point of view, the corresponding correlation functions are related to the thermoelectric effect which correlates charge and heat transport in the direction of the condensate, since a_x^3 can be identified with an electric field in the x direction and h_{tx} with a temperature gradient in the x direction. This effect was studied for holographic s-wave superfluids [32, 37] and for p-wave superfluids in the transverse directions [19], but to our knowledge, this is the first time this effect has been calculated with backreaction and in the direction of the condensate.

The second block contains, among others, the diagonal metric fluctuations $h_{xx} - h_{yy}$ and the gauge field fluctuations a_x^1 and a_x^2. A field theoretic description of the corresponding

Green's functions is not fully addressed in this paper and is left for future work. However, we know that some of the modes in this block are related to the transport coefficients in the viscosity tensor η^{ijkl}. In general, the viscosities of a system are encoded in a rank four tensor η^{ijkl} which in the most general case has 21 independent components. Due to the symmetries of the system at hand, we are left with five independent components of the tensor η^{ijkl} [38, 39], two of which are shear viscosities, η_{xy} and η_{yz}, that were addressed in [19]. Two of the remaining components are bulk viscosities and can be set to zero using the tracelessness condition for the conformal energy-momentum tensor, leaving one free transport coefficient, denoted by λ. While η and ζ measure the response of the system to deformations due to shear or normal stress, λ is related to the normal stress difference that is induced by an anisotropic strain. Our holographic computation shows that in the zero frequency limit, the ratio of λ to the entropy density is finite. Moreover, in the normal phase it turns into the shear viscosity of the isotropic fluid, which we simply denote by η. Therefore it acquires a fixed value given by the well-known

$$\frac{\eta}{s} = \frac{1}{4\pi} \,. \tag{1.3}$$

Note that we normalized λ in a way that at the phase transition it matches η. In the broken phase we see a temperature dependence and the resulting curve does not fall below $1/(4\pi)$ for any backreaction parameter α and for any temperature.

Since we have completed our analysis of all fluctuation modes in the p-wave system, let us now summarize them, as well as the transport phenomena they correspond to:

1. h_{yz} (helicity two) is related to the shear viscosity η_{yz} which for all values of T takes the universal value $\eta/s = 1/4\pi$ (see [19]),
2. $h_{x\perp}$ (helicity one) is related to the shear viscosity $\eta_{x\perp}$ which shows a temperature dependence in the broken phase (see [19]),
3. The coupling between $a_\perp^\pm = a_\perp^1 \pm i a_\perp^2$ (helicity one) and $h_{x\perp}$ leads to an effect which is similar to the flexoelectric effect known from crystals (see [19]),
4. $a_\perp^3$ is related to the "electrical" conductivity $\sigma^{\perp\perp}$ (helicity one), and its coupling to $h_{t\perp}$ (helicity one) is related to the so called thermoelectric effect transverse to the condensate (see [19]),
5. $\Phi_4 \sim a_x^3$ (helicity zero) is related to the "electrical" conductivity σ^{xx}, and its coupling to h_{tx} (helicity zero) gives the thermoelectric effect in the direction of the condensate (see section 4),
6. $\Phi_3 \sim h_{xx} - h_{yy}$ (helicity zero) is related to the transport coefficient λ found in the viscosity tensor η^{ijkl} and its coupling to $\Phi_\pm \sim a_x^\pm$ (helicity zero) shows a behaviour similar to the piezoelectric effect (see section 4).

We see that the study of fluctuations in a backreacted holographic p-wave superfluid provides a rich structure of different effects which by using the fluctuation-dissipation theorem may be related to well-known transport phenomena in other areas of physics.

The paper is organized as follows: In section 2, we recapitulate the backreacted holographic p-wave superfluid. In section 3, the scalar fluctuations (helicity zero) and the corresponding Green's functions on the gravity side are presented. The following section 4 contains our results for the transport properties of the superfluid and an approach to interpreting them from a hydrodynamical point of view. In 5 we present our conclusions. Many of the technical details are collected in the appendices: In A, we discuss the necessary holographic renormalization, in B we specify the physical fields of the system, in C we review the numerical procedure to deal with the coupled equations of motion, and finally some general remarks on anisotropic fluids are given in D.

2 Holographic setup and equilibrium

The setup used in this paper was already described in [16, 19]. Therefore, here we give a brief review of its most important properties. We consider SU(2) Einstein-Yang-Mills theory in $(4+1)$-dimensional asymptotically AdS space. The action is

$$S = \int \mathrm{d}^5 x \, \sqrt{-g} \left[\frac{1}{2\kappa_5^2} (R - \Lambda) - \frac{1}{4\hat{g}^2} F^a_{MN} F^{aMN} \right] + S_{\text{bdy}} \,, \tag{2.1}$$

where κ_5 is the five-dimensional gravitational constant, $\Lambda = -\frac{12}{L^2}$ is the cosmological constant (with L being the AdS radius), and $\hat{g}$ is the Yang-Mills coupling constant. It is convenient to define

$$\alpha \equiv \frac{\kappa_5}{\hat{g}} \,, \tag{2.2}$$

which measures the strength of the backreaction. The SU(2) field strength F^a_{MN} is defined by

$$F^a_{MN} = \partial_M A^a_N - \partial_N A^a_M + \epsilon^{abc} A^b_M A^c_N \,, \tag{2.3}$$

where capital Latin letter indices run over $\{t, x, y, z, r\}$, with r being the AdS radial coordinate, and ϵ^{abc} is the totally antisymmetric tensor with $\epsilon^{123} = +1$. The A^a_M are the components of the matrix-valued Yang-Mills gauge field $A = A^a_M \tau^a dx^M$, where the τ^a are the SU(2) generators, related to the Pauli matrices by $\tau^a = \sigma^a / 2\mathrm{i}$. Finally, the S_{bdy} term includes boundary terms, namely the Gibbons-Hawking boundary term as well as counterterms required for the on-shell action to be finite, that will be discussed below. It does not affect the equations of motion.

The Einstein and Yang-Mills equations derived from the above action are

$$R_{MN} + \frac{4}{L^2} g_{MN} = \kappa_5^2 \left(T_{MN} - \frac{1}{3} T_P{}^P g_{MN} \right) \,, \tag{2.4}$$

$$\nabla_M F^{aMN} = -\epsilon^{abc} A^b_M F^{cMN} \,, \tag{2.5}$$

where the Yang-Mills stress-energy tensor T_{MN} is

$$T_{MN} = \frac{1}{\hat{g}^2} \left(F^a_{PM} F^{aP}{}_N - \frac{1}{4} g_{MN} F^a_{PQ} F^{aPQ} \right) \,. \tag{2.6}$$

To solve this equations, we use the following ansätze for the gauge field and the metric, which can be motivated from symmetry considerations [16, 33]

$$A = \phi(r)\tau^3 \mathrm{d}t + w(r)\tau^1 \mathrm{d}x \,, \tag{2.7}$$

$$\mathrm{d}s^2 = -N(r)\sigma(r)^2 \mathrm{d}t^2 + \frac{1}{N(r)}\mathrm{d}r^2 + r^2 f(r)^{-4}\mathrm{d}x^2 + r^2 f(r)^2\left(\mathrm{d}y^2 + \mathrm{d}z^2\right) \,, \tag{2.8}$$

where $N(r) \equiv -\frac{2m(r)}{r^2} + \frac{r^2}{L^2}$. The AdS boundary is at $r \to \infty$ and for our black hole solutions we denote the position of the horizon as r_h.

This ansatz is compatible with the well-known AdS Reissner-Nordström solution, where $w(r) = 0$ for all values of r. This solution features $w(r) = 0$, so it preserves the SO(3) symmetry and corresponds to the normal phase of the system. There is a second solution with non-vanishing $w(r)$, which can only be computed numerically. The second solution breaks the rotational SO(3) symmetry and describes the condensed superfluid phase. Due to our choice of boundary conditions, this breaking occurs spontaneously. For completeness, we state here the coefficients of the expansion at the horizon (in terms of $(r/r_h - 1)^n$),

$$\left\{\phi_1^h, \sigma_0^h, w_0^h, f_0^h\right\} \,, \tag{2.9}$$

being $\phi_0^h = 0$ in order for A to be well defined as a one-form [40], and of the expansion at the boundary (in terms of $(r_h/r)^{2n}$),

$$\left\{\mu, \phi_1^b, m_0^b, w_1^b, f_2^b\right\} \,. \tag{2.10}$$

Note that $w_0^b = 0$, otherwise the SO(3) would be broken explicitly instead of spontaneously. Besides, we can fix the metric to have asymptotic AdS boundary conditions, so that $\sigma_0^b = f_0^b = 1$. The fields can be made dimensionless through $m(r) \to r_h^4 m(r)$, $\phi(r) \to r_h \phi(r)$ and $w(r) \to r_h w(r)$, while $f(r)$ and $\sigma(r)$ are already dimensionless.

In terms of these coefficients we can express the different field theory quantities, such as temperature and entropy density, given by

$$T = \frac{\sigma_0^h}{12\pi}\left(12 - \alpha^2 \frac{(\phi_1^h)^2}{\sigma_0^{h\,2}}\right) r_h \,, \qquad s = \frac{2\pi}{\kappa_5^2} r_h^3 \,. \tag{2.11}$$

The field theory expectation values of the dual operators of the different fields are directly related to the expansion coefficients. For the charge density and the condensate we have

$$\langle \mathcal{J}_3^t \rangle = -\frac{2\alpha^2}{\kappa_5^2} r_h^3 \, \phi_1^b \,, \qquad \langle \mathcal{J}_1^x \rangle = \frac{2\alpha^2}{\kappa_5^2} r_h^3 \, w_1^b \,, \tag{2.12}$$

and for the energy-momentum tensor [41, 42] they are

$$\langle \mathcal{T}_{tt} \rangle = \frac{3r_h^4}{\kappa_5^2} m_0^b \,, \quad \langle \mathcal{T}_{xx} \rangle = \frac{r_h^4}{\kappa_5^2}\left(m_0^b - 8f_2^b\right) \,, \quad \langle \mathcal{T}_{yy} \rangle = \langle \mathcal{T}_{zz} \rangle = \frac{r_h^4}{\kappa_5^2}\left(m_0^b + 4f_2^b\right) \,. \tag{2.13}$$

In [16] it was found that the value of the Yang-Mills coupling constant α determines if the phase transition is second order ($\alpha \leq \alpha_c = 0.365$) or first order ($\alpha > \alpha_c = 0.365$).

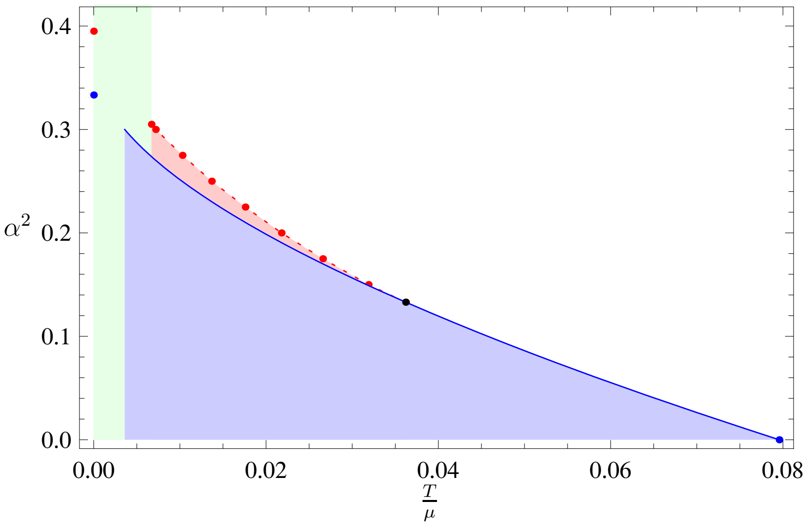

Figure 1. This diagram shows the dependence of the order of the phase transition on α^2 and T_c/μ. For a description of the plot see the text. This figure is taken from [19].

The quantitative dependence of the critical temperature on the parameter α is given in figure 1. The broken phase is thermodynamically preferred in the blue and red regions, while in the white region the ground state is the Reissner-Nordström black hole. The phase transition from the white to the blue region is second order, while the one from the white to the red region is first order. The black dot determines the critical point where the order of the phase transition changes. In the green region the numerics are unstable. At zero temperature, the data may be obtained analytically as described in [21, 43].

3 Perturbations about equilibrium

In this section we study the response of the holographic p-wave superfluid under small perturbations. This analysis is necessary to ultimately compute the transport coefficients of the system. On the gravity side, the perturbations are given by fluctuations of the metric $h_{MN}(x^\mu, r)$ and the gauge field $a^a_M(x^\mu, r)$. Thus we are studying a total of 14 physical modes: 5 coming from the massless graviton in 5 dimensions and 3×3 from the massless vectors in five dimensions. Due to time and spatial translation invariance in the Minkowski directions, the fluctuations can be decomposed in a Fourier decomposition as

$$\begin{aligned} h_{MN}(x^\mu, r) &= \int \frac{\mathrm{d}^4 k}{(2\pi)^4} \mathrm{e}^{\mathrm{i}k_\mu x^\mu}\, \hat{h}_{MN}(k^\mu, r)\,, \\ a^a_M(x^\mu, r) &= \int \frac{\mathrm{d}^4 k}{(2\pi)^4} \mathrm{e}^{\mathrm{i}k_\mu x^\mu}\, \hat{a}^a_M(k^\mu, r)\,. \end{aligned} \tag{3.1}$$

To simplify notations, we drop the hat on the transformed fields which we use from now on if not stated otherwise.

3.1 Characterization of fluctuations and gauge fixing

In general, we would have to introduce two spatial momenta: one longitudinal to the direction of the condensate, $k_{\|}$, and another one perpendicular to it, $k_{\perp}$. Thus, $k^{\mu} = (\omega, k_{\|}, k_{\perp}, 0)$. But introducing a momentum perpendicular to the condensate breaks the remaining rotational symmetry SO(2) down the discrete $\mathbb{Z}_2$ parity transformation $P_{\perp}$: $k_{\perp} \to -k_{\perp}$, $x_{\perp} \to -x_{\perp}$. This leads to a mixing of most of the fields making the problem of solving the corresponding differential equations unmanageable. Thus we do not study this case further in this paper. However, a momentum exclusively in the direction longitudinal to the condensate, or zero spatial momentum, preserves the SO(2) rotational symmetry such that we can classify the fluctuations according to their transformation under the SO(2) symmetry (see table 1). The modes of different helicity decouple from each other. The momentum longitudinal to the condensate, however, breaks the longitudinal parity invariance $P_{\|}$. In this paper we will set this spatial momentum to zero as well. Therefore, we can classify the modes further by their behaviour under the longitudinal parity transformation $P_{\|}$. Under this transformation the helicity 0 fields are divided into two blocks, the first block contains h_{tx}, a_x^3, a_t^1 and a_t^2 and the second one h_{tt}, h_{xx}, $h_{yy} + h_{zz}$, a_x^1, a_x^2 and a_t^3.

In order to obtain the physical modes of the system we have to fix the gauge freedom. We choose a gauge where $a_r^a \equiv 0$ and $h_{Mr} \equiv 0$ such that the equations of motion for these fields become constraints. These constraints fix the unphysical fluctuations in each helicity sector and allow only the physical modes to fluctuate. The physical modes may be constructed by enforcing them to be invariant under the residual gauge transformations, $\delta a_r^a = 0$ and $\delta h_{Mr} = 0$ (see appendix B). Thus, the physical fields we define are given in terms of the fluctuations, and classified as (from here on we set $k_{\|} = k$)

$$\begin{aligned} &\text{helicity two:} \quad && \Xi = g^{yy} h_{yz},\ \ h_{yy} - h_{zz}\,, \\ &\text{helicity one:} \quad && \Psi = g^{yy}(\omega h_{xy} + k h_{ty});\ \ a_y^a\,, \end{aligned} \tag{3.2}$$

and for helicity zero:

$$\begin{aligned} \Phi_1 = {}& a_x^1 - \frac{\mathrm{i}k}{\phi} a_t^2 + \frac{k^2}{w\phi} a_t^3 + \frac{k\omega}{w\phi} a_x^3 + \frac{kw}{\omega}\xi_{tx} - \\ & - \frac{k^2 f^4 N w \sigma^2}{2r^2\omega^2}\xi_t + \frac{k^2 f^5 w^2 \sigma\phi\left(\sigma N' + 2N\sigma'\right) - 2r^2\omega^2 f\left(w\phi w' + k^2\phi'\right)}{4r\omega^2 w\phi\left(f + rf'\right)}\xi_y, \\ \Phi_2 = {}& a_x^2 + \frac{\mathrm{i}\left(-k^2 + w^2\right)}{\omega w} a_t^3 - \\ & - \frac{\mathrm{i}k}{w} a_x^3 - \frac{\mathrm{i}w\phi}{2\omega}\xi_t + \frac{\mathrm{i}rf\left(w^2\phi\left(\sigma N' + 2N\sigma'\right) + 2N\left(k^2 - w^2\right)\sigma\phi'\right)}{4\omega N w\sigma\left(f + rf'\right)}\xi_y, \\ \Phi_3 = {}& \xi_x + \frac{2k}{\omega}\xi_{tx} - \frac{k^2 f^4 N\sigma^2}{r^2\omega^2}\xi_t + \frac{4r^2\omega^2 f' - 2r\omega^2 f + k^2 f^5\sigma\left(\sigma N' + 2N\sigma'\right)}{2r\omega^2\left(f + rf'\right)}\xi_y, \\ \Phi_4 = {}& a_x^3 + \frac{k}{\omega} a_t^3 - \frac{w\phi}{\omega^2 - \phi^2} a_t^1 - \frac{\mathrm{i}\omega w}{\omega^2 - \phi^2} a_t^2 + \frac{w^2\phi}{\omega^2 - \phi^2}\xi_{tx} - \\ & - \frac{k f^4 N w^2 \sigma^2 \phi}{2r^2\omega\left(\omega^2 - \phi^2\right)}\xi_t + \frac{kf\left(f^4 w^2\sigma\phi\left(\sigma N' + 2N\sigma'\right) + 2r^2\left(-\omega^2 + \phi^2\right)\phi'\right)}{4r\omega\left(\omega^2 - \phi^2\right)\left(f + rf'\right)}\xi_y, \end{aligned} \tag{3.3}$$

	dynamical fields	constraints	# physical modes
helicity 2	$h_{yz}, h_{yy} - h_{zz}$	none	2
helicity 1	$h_{ty}, h_{xy}; a^a_y$	h_{yr}	4
	$h_{tz}, h_{xz}; a^a_z$	h_{zr}	4
helicity 0	$h_{tt}, h_{xx}, h_{yy} + h_{zz}, h_{xt}; a^a_t, a^a_x$	$h_{tr}, h_{xr}, h_{rr}; a^a_r$	4

Table 1. Classifications of the fluctuations according to their transformation under the little group SO(2). The constraints are given by the equations of motion for the fields which are set to zero due the fixing of the gauge freedom: $a^a_r \equiv 0$ and $h_{rM} \equiv 0$. The number of physical modes is obtained by the number of dynamical fields minus the number of constraints. Due to SO(2) invariance the fields in the first and second line of the helicity one fields can be identified.

with

$$\xi_y = g^{yy} h_{yy}, \qquad \xi_x = g^{xx} h_{xx}, \qquad \xi_t = g^{tt} h_{tt}, \qquad \xi_{tx} = g^{xx} h_{tx}. \tag{3.4}$$

First we look at the asymptotic behavior of the helicity zero physical fields in terms of the asymptotic form of the background (2.10) and the fluctuation fields (A.5). The physical fields are chosen so that each one can be identified at the boundary with a fluctuation field, or a combination of them. In fact, in this limit they asymptote to

$$\begin{aligned}
\Phi_1(\omega, r) &\longrightarrow \left(a^1_x\right)^b_0, \\
\Phi_2(\omega, r) &\longrightarrow \left(a^2_x\right)^b_0, \\
\Phi_3(\omega, r) &\longrightarrow (\xi_x)^b_0 - (\xi_y)^b_0, \\
\Phi_4(\omega, r) &\longrightarrow \left(a^3_x\right)^b_0.
\end{aligned} \tag{3.5}$$

Note that this computation was done in the $\vec{k} = 0$ limit, since this is the relevant limit for this paper. The resulting correlators from the helicity zero modes will be written in terms of this physical fields.

3.2 Equations of motion, on-shell action and correlators

In the following we will focus on the response exclusively due to time dependent perturbations, i. e. $k^\mu = (\omega, 0, 0, 0)$. In this case in addition to the SO(2) symmetry, $P_\parallel$ parity is conserved which allows us to decouple some of the physical modes in the different helicity blocks. In this section we obtain the retarded Green's functions G of the gauge theory corresponding to the stress-energy tensor $T^{\mu\nu}$ and the currents J^μ_a, defined as two point functions, as in

$$\begin{aligned}
G^{\mu\nu,\rho\sigma}(k) &= -\mathrm{i}\int \mathrm{d}t\mathrm{d}^3x\, \mathrm{e}^{-\mathrm{i}k_\mu x^\mu}\, \theta(t)\langle[T^{\mu\nu}(t,\vec{x}), T^{\rho\sigma}(0,0)]\rangle, \\
G^{\mu,\nu}_{a,b}(k) &= -\mathrm{i}\int \mathrm{d}t\mathrm{d}^3x\, \mathrm{e}^{-\mathrm{i}k_\mu x^\mu}\, \theta(t)\langle[J^\mu_a(t,\vec{x}), J^\nu_b(0,0)]\rangle, \\
G^{\mu\nu\rho}_{\ \ \ a}(k) &= -\mathrm{i}\int \mathrm{d}t\mathrm{d}^3x\, \mathrm{e}^{-\mathrm{i}k_\mu x^\mu}\, \theta(t)\langle[T^{\mu\nu}(t,\vec{x}), J^\rho_a(0,0)]\rangle, \\
G^{\rho\mu\nu}_a(k) &= -\mathrm{i}\int \mathrm{d}t\mathrm{d}^3x\, \mathrm{e}^{-\mathrm{i}k_\mu x^\mu}\, \theta(t)\langle[J^\rho_a(t,\vec{x}), T^{\mu\nu}(0,0)]\rangle.
\end{aligned} \tag{3.6}$$

Here $T^{\mu\nu}$ and J^{μ}_{a} are respectively the full stress-energy tensor and current, which include the equilibrium parts of section 2, $\langle \mathcal{T}^{\mu\nu} \rangle$ and $\langle \mathcal{J}^{\mu}_{a} \rangle$, as well as the corresponding dissipative parts which arise due to the introduction of fluctuations in our model.

We use the methods developed in the context of gauge-string duality to extract these Green's functions. First we determine the on-shell action at the boundary of the asymptotically AdS space from which we can easily read of the Green's functions using the recipe described in the seminal paper [44] and its generalisation to the case of operator mixing (c.f. [45]).

We refer the reader to [19] for the treatment of the helicity one and two modes. Here we present the analysis of the helicity zero fluctuations.

3.2.1 Helicity zero modes

The equations of motion corresponding to these fluctuations are very lengthy, therefore, to guarantee readability, we omit them here. They can be derived by expanding the action (2.1) up to second order in the fluctuations and varying it with respect to the corresponding fields.

Due to the parity symmetry $P_{\parallel}$ in the $k = 0$ case the modes split into two blocks, one transforming oddly (block 1) the other evenly (block 2) under $P_{\parallel}$.

Block 1 — Parity odd. The first block is composed by the modes $\{a^1_t, a^2_t, a^3_x, \xi_{tx}\}$. The contribution of these modes to the on-shell action is[1]

$$\begin{aligned}\tilde{S}^{\text{on-shell}}_{\text{hel.0, bl.1}} = \frac{1}{\kappa_5^2} \int \frac{\mathrm{d}^4 k}{(2\pi)^4} \Bigg\{ & \frac{r^5}{4 f^4 \sigma} \xi_{tx} {\xi_{tx}}' + \frac{r^3 \alpha^2}{2\sigma} \left(a^1_t {a^1_t}' + a^2_t {a^2_t}' \right) - \frac{r \alpha^2 f^4 N \sigma}{2} a^3_x {a^3_x}' \\ & + \frac{3 r^4}{2 f^4 \sigma} {\xi_{tx}}^2 - \frac{r^3 \alpha^2}{2\sigma} \xi_{tx} \left(w' a^1_t + \phi' a^3_x \right) \Bigg\} \Bigg|_{r = r_{\text{bdy}}} ,\end{aligned} \tag{3.7}$$

which is divergent as we send $r_{\text{bdy}} \to \infty$. The divergence can be cured via holographic renormalization, i.e. the addition of covariant boundary counterterms that cancel the divergences without affecting the equations of motion (see appendix A). To obtain the boundary action we plug the field expansions at r_{bdy} into equation (3.7). Since we have four fields satisfying four second order differential equations and three constraints (coming from setting h_{xr}, a^1_r, a^2_r to zero) we are left with a total of five ($8 - 3 = 5$) independent parameters at the boundary, $\{(a^1_t)^b_0, (a^2_t)^b_0, (a^3_x)^b_0, (a^3_x)^b_1, (\xi_{tx})^b_0\}$ (see (A.6)). There is some freedom in choosing the undetermined coefficients, however the present choice is convenient for the later use of the gauge/gravity dictionary. We express the renormalized on-shell action at

---

[1] Here and in other similar expressions ahead, the products are to be understood as evaluated on opposite values of the frequency, as is natural for a Lagrangian written in Fourier space. For instance, $\xi_{tx}\, a^1_t$ would actually be $\xi_{tx}(-\omega, r)\, a^1_t(\omega, r)$.

the boundary in terms of these coefficients[2],

$$S^{\text{on-shell}}_{\text{hel.0, bl.1}} = \frac{r_h^4}{\kappa_5^2} \int \frac{\mathrm{d}^4k}{(2\pi)^4} \left\{ \frac{\alpha^2\mu\phi_1^b}{\omega^2-\mu^2} \left(a_t^1\right)_0^{b\,2} + \frac{\alpha^2\mu\phi_1^b}{\omega^2-\mu^2} \left(a_t^2\right)_0^{b\,2} - \frac{\alpha^2\omega^2}{4} \left(a_x^3\right)_0^{b\,2} \right. \\ - \frac{3}{2} m_0^b (\xi_{tx})_0^{b\,2} + \frac{2\mathrm{i}\alpha^2\omega\phi_1^b}{\omega^2-\mu^2} \left(a_t^1\right)_0^b \left(a_t^2\right)_0^b + \frac{\alpha^2\mu w_1^b}{\omega^2-\mu^2} \left(a_t^1\right)_0^b \left(a_x^3\right)_0^b \\ \left. - \frac{\mathrm{i}\alpha^2\omega w_1^b}{\omega^2-\mu^2} \left(a_t^2\right)_0^b \left(a_x^3\right)_0^b + \alpha^2 \left(a_x^3\right)_0^b \left(a_x^3\right)_1^b + 2\alpha^2\phi_1^b \left(a_x^3\right)_0^b (\xi_{tx})_0^b \right\} . \tag{3.8}$$

As we discuss in appendix B, there is a residual gauge freedom left, which has to be taken into account to obtain physically sensible observables. Using the gauge transformations given in (B.11) for $\vec{k} = 0$ and setting $K_t = K_r = \Lambda_0^3 = 0$, since they do not affect the fields discussed in this block, we obtain the unique linear combination (up to an overall scaling discussed in the previous paragraph)

$$\Phi_4 = a_x^3 + w \frac{\mathrm{i}\omega a_t^2 + \phi a_t^1 - w\phi\xi_{tx}}{\phi^2 - \omega^2} \tag{3.9}$$

Following [33], we rewrite the boundary action (3.8) in terms of gauge-equivalent fields, which guarantees that our solutions are gauge invariant. The set of allowed transformations is parametrized by three coefficients. The gauge equivalents to the fields which solve the equations of motion and constraints are

$$\begin{aligned} a_t^1 &\to \alpha_0 a_t^1 - \mathrm{i}\omega\Lambda_0^1 - \phi\Lambda_0^2 - \mathrm{i}\omega w K_x \,, \\ a_t^2 &\to \alpha_0 a_t^2 - \mathrm{i}\omega\Lambda_0^2 + \phi\Lambda_0^1 \,, \\ a_x^3 &\to \alpha_0 a_x^3 + w\Lambda_0^2 \,, \\ \xi_{tx} &\to \alpha_0 \xi_{tx} - \mathrm{i}\omega K_x \,. \end{aligned} \tag{3.10}$$

Note that we also took an overall multiplicative scaling factor into account. This can be included because different solutions of the equations of motion are related by a rescaling of the fields. These expressions give a relation, parametrized by four coefficients $\{\alpha_0, \Lambda_0^1, \Lambda_0^2, K_x\}$, between different sets of classical solutions which are equivalent.

In order to compute the two-point functions as derivatives of the classical action, we will follow the directions given in [33], which instructs us to prescribe the value of the perturbations at the boundary, respectively defined as $\{\beta_t^1, \beta_t^2, \beta_x^3, \beta_{tx}\}$, in terms of the gauge-equivalent quantities defined in (3.10). Those are

$$\begin{aligned} \beta_t^1 &= \alpha_0 \left(a_t^1\right)_0^b - \mathrm{i}\omega\Lambda_0^1 - \phi_0^b\Lambda_0^2 - \mathrm{i}\omega w K_x \,, \\ \beta_t^2 &= \alpha_0 \left(a_t^2\right)_0^b - \mathrm{i}\omega\Lambda_0^2 + \phi_0^b\Lambda_0^1 \,, \\ \beta_x^3 &= \alpha_0 \left(a_x^3\right)_0^b \,, \\ \beta_{tx} &= \alpha_0 \left(\xi_{tx}\right)_0^b - \mathrm{i}\omega K_x \,. \end{aligned} \tag{3.11}$$

---

[2] All fields in the following boundary action are dimensionless, i.e. we pulled out r_h. Wherever the context allows, we are sloppy with the notation and do not give the dimensionless fields new names.

The four coefficients of the gauge transformation can be chosen so that the fields asymptote to these vales. Thus, we are effectively fixing the gauge, because the gauge freedom is "absorbed" in the freedom of choosing the boundary values. Then, we rewrite the boundary action (3.8) in terms of the β_i and obtain

$$S^{\text{on-shell}}_{\text{hel.0, bl.1}} = \frac{r_h^4}{\kappa_5^2} \int \frac{\mathrm{d}^4 k}{(2\pi)^4} \begin{pmatrix} \beta_t^{1*} & \beta_t^{2*} & \beta_x^{3*} & \beta_{tx}^* \end{pmatrix} \mathcal{G}_{(1)}(\omega) \begin{pmatrix} \beta_t^1 \\ \beta_t^2 \\ \beta_x^3 \\ \beta_{tx} \end{pmatrix} , \tag{3.12}$$

where $\mathcal{G}_{(1)}$ is the Green's function matrix of this block, which relates the response of the system to field fluctuations a_t^1, a_t^2, a_x^3 and h_{tx}. Note that, following our convention, the fields on the left row vector are evaluated in $-\omega$ and the fields on the right column vector are in ω. Next, by taking derivatives $\partial^2/\partial\beta^*(-\omega)\partial\beta(\omega)$ of the action above we obtain

$$\begin{pmatrix} \langle J_1^t \rangle(\omega) \\ \langle J_2^t \rangle(\omega) \\ \langle J_3^x \rangle(\omega) \\ \langle T^{tx} \rangle(\omega) \end{pmatrix} = \begin{pmatrix} \frac{\delta S^{\text{on-shell}}_{\text{helicity 0}}}{\delta\left(a_t^1\right)_0^b(-\omega)} \\ \frac{\delta S^{\text{on-shell}}_{\text{helicity 0}}}{\delta\left(a_t^2\right)_0^b(-\omega)} \\ \frac{\delta S^{\text{on-shell}}_{\text{helicity 0}}}{\delta(\Phi_4)_0^b(-\omega)} \\ \frac{\delta S^{\text{on-shell}}_{\text{helicity 0}}}{\delta\left(\xi_{tx}\right)_0^b(-\omega)} \end{pmatrix} = \begin{pmatrix} G^{t,t}_{1,1}(\omega) & G^{t,t}_{1,2}(\omega) & G^{t,x}_{1,3}(\omega) & G^{t\ tx}_{1}(\omega) \\ G^{t,t}_{2,1}(\omega) & G^{t,t}_{2,2}(\omega) & G^{t,x}_{2,3}(\omega) & G^{t\ tx}_{2}(\omega) \\ G^{x,t}_{3,1}(\omega) & G^{x,t}_{3,2}(\omega) & G^{x,x}_{3,3}(\omega) & G^{x\,tx}_{3}(\omega) \\ G^{tx\,t}{}_{1}(\omega) & G^{tx\,t}{}_{2}(\omega) & G^{tx\,x}{}_{3}(\omega) & G^{tx,tx}(\omega) \end{pmatrix} \begin{pmatrix} \left(a_t^1\right)_0^b(\omega) \\ \left(a_t^2\right)_0^b(\omega) \\ (\Phi_4)_0^b(\omega) \\ \left(\xi_{tx}\right)_0^b(\omega) \end{pmatrix} ,$$

which explicitly written in terms of the field theory expectation values is

$$\mathcal{G}_{(1)}(\omega) = \begin{pmatrix} \frac{\mu}{\mu^2-\omega^2}\langle \mathcal{J}_3^t \rangle & \frac{\mathrm{i}\omega}{\mu^2-\omega^2}\langle \mathcal{J}_3^t \rangle & \frac{-\mu}{\mu^2-\omega^2}\langle \mathcal{J}_1^x \rangle & 0 \\ \frac{-\mathrm{i}\omega}{\mu^2-\omega^2}\langle \mathcal{J}_3^t \rangle & \frac{\mu}{\mu^2-\omega^2}\langle \mathcal{J}_3^t \rangle & \frac{\mathrm{i}\omega}{\mu^2-\omega^2}\langle \mathcal{J}_1^x \rangle & 0 \\ \frac{-\mu}{\mu^2-\omega^2}\langle \mathcal{J}_1^x \rangle & \frac{-\mathrm{i}\omega}{\mu^2-\omega^2}\langle \mathcal{J}_1^x \rangle & G^{x,x}_{3,3}(\omega) & -\langle \mathcal{J}_3^t \rangle \\ 0 & 0 & -\langle \mathcal{J}_3^t \rangle & -\langle \mathcal{T}_{tt} \rangle \end{pmatrix} , \tag{3.13}$$

where we already included a factor of 2 coming from the prescription developed in [44] for real-time correlators. Note that using the prescription above we automatically get the correlator which includes the physical field Φ_4 instead of a_x^3 as it is pointed out in [33].

The matrix is completely determined by the background solution near the boundary, except for one entry, the one corresponding to the two-point correlator of Φ_4, which in terms of the parity odd helicity zero modes reads

$$G^{x,x}_{3,3}(\omega) = -\frac{1}{2}\alpha^2\omega^2 + \frac{2\,\alpha^2}{(a_x^3)_0^b} \left[\left(a_x^3\right)_1^b + w_1^b \frac{\mu\left(a_t^1\right)_0^b + i\omega\left(a_t^2\right)_0^b}{\mu^2-\omega^2} \right] . \tag{3.14}$$

Rewriting this correlator in terms of the physical field we obtain

$$G^{x,x}_{3,3}(\omega) = -\alpha^2 \left(r^3 \frac{\Phi_4'(r)}{\Phi_4(r)}\bigg|_{r=r_{\text{bdy}}} + \text{ counter terms} \right) \tag{3.15}$$

showing that all entries of $\mathcal{G}_{(1)}$ are gauge invariant.

To compute this correlator we have to numerically integrate the equations of motion and constraint equations of this block. Since we choose infalling conditions at the horizon, we fix four of the eight independent coefficients. And out of the remaining four coefficients, three are fixed by the constraint equations, leaving us with one free parameter. This parameter corresponds to the overall scaling of the physical field and is related to α_0 in (3.10) and (3.11). Since the correlators are defined by ratios of the boundary values, this parameter is scaled out and we can just set it to one. From the solution of the numerical integration, we read off the boundary values of the fields and plug them into (3.14) to obtain the Green's functions. The results are presented in section 4, together with a qualitative analysis of the thermoelectric effect associated to these correlators.

Block 2 — Parity even. The second block is composed by the modes $\{a_t^3, a_x^2, a_x^1, \xi_t, \xi_y, \xi_x\}$, which combine to form three physical fields. The combinations we chose were defined in (3.3), and in this section we are taking $\vec{k} = 0$, in which case they reduce to

$$\begin{aligned}
\Phi_1 &= a_x^1 - \frac{f w'}{2\left(f + r f'\right)}\xi_y\,, \\
\Phi_2 &= a_x^2 + \frac{\mathrm{i}w}{\omega}a_t^3 - \frac{\mathrm{i}w\phi}{2\omega}\xi_t + \frac{\mathrm{i}r f w\left(2\phi N\sigma' + \phi N'\sigma - 2\phi' N\sigma\right)}{4\omega N\sigma\left(f + r f'\right)}\xi_y \\
\Phi_3 &= \xi_x + \frac{2 r f' - f}{f + r f'}\xi_y\,,
\end{aligned} \tag{3.16}$$

The contribution of this second block of helicity zero modes to the on-shell action is

$$\begin{aligned}
\tilde{S}^{\text{on-shell}}_{\text{hel.0, bl.2}} = \frac{1}{\kappa_5^2}\int\frac{\mathrm{d}^4k}{(2\pi)^4}\Bigg\{&\frac{r^3 N\sigma}{4}\xi_y{\xi_y}' - \frac{r\alpha^2 f^4 N\sigma}{2}\left(a_x^1{a_x^1}' + a_x^2{a_x^2}'\right) + \frac{r^3\alpha^2}{2\sigma}a_t^3{a_t^3}' \\
&- \frac{3r^2 N\sigma}{8}{\xi_t}^2 - \frac{r^2}{8f}\left(2fN\sigma + \frac{fr\sigma N'}{2} + fNr\sigma' + 2Nr\sigma f'\right){\xi_x}^2 \\
&+ \frac{r^3 N\sigma}{4}\xi_y\left({\xi_t}' + {\xi_x}'\right) + \frac{r^2}{4f}\left(5fN\sigma - rN\sigma f' + \frac{rf\sigma N'}{2} + rfN\sigma'\right)\xi_y\xi_t \\
&+ \frac{r^3 N\sigma}{4}\left(\xi_t + \xi_x\right){\xi_y}' + \frac{r^2}{2f}\left(2fN\sigma + \frac{rN\sigma f'}{2} + \frac{rf\sigma N'}{2} + rfN\sigma'\right)\xi_y\xi_x \\
&+ \frac{r^3 N\sigma}{8}\left(\xi_t{\xi_x}' + \xi_x{\xi_t}'\right) + \frac{r^2}{8f}\left(5fN\sigma + 2rN\sigma f' + \frac{rf\sigma N'}{2} + rfN\sigma'\right)\xi_t\xi_x \\
&- \frac{r\alpha^2 f^4 N\sigma w'}{4}a_x^1\left(\xi_t - \xi_x + 2\xi_y\right) - \frac{r^3\alpha^2\phi'}{4\sigma}a_t^3\left(\xi_t - \xi_x - 2\xi_y\right)\Bigg\}\Bigg|_{r=r_{\text{bdy}}}\,,
\end{aligned} \tag{3.17}$$

which again is divergent. The renormalized on-shell action is derived and presented in the appendix, see (A.15).

Since we have six fields determined by second order differential equations and three constraints, we end up with twelve $(12 - 3 = 9)$ undetermined coefficients of the boundary expansion, in terms of which the expression above is written. They are

$$\left\{\left(a_t^3\right)_0^b, \left(a_x^2\right)_0^b, \left(a_x^2\right)_1^b, \left(a_x^1\right)_0^b, \left(a_x^1\right)_1^b, \left(\xi_t\right)_0^b, \left(\xi_y\right)_0^b, \left(\xi_y\right)_2^b, \left(\xi_x\right)_0^b\right\}\,. \tag{3.18}$$

Notice that six of them (the ones with subscript 0) coincide with the boundary values of the fields. The other three are higher-order coefficients. They are undetermined since the boundary expansion does not know about the boundary conditions set on the horizon (i. e. that they must satisfy an infalling condition at the horizon). Actually when integrating the equations these coefficients are fixed by the boundary values we choose at the horizon. However, how the expansion coefficients at the boundary depend on the coefficients at the horizon cannot be addressed analytically, since in the bulk we can only solve the equations of motion numerically and this dependence is precisely determined by the behaviour of the fields in the bulk.

As in the previous case, the Green's functions cannot be extracted directly from (3.17) because there is a residual gauge freedom left under which the fluctuation fields are not invariant. To fix the gauge freedom, we can apply again the formalism used before to derive the gauge-equivalent solutions. In this case, we have to look for the restricted set of gauge transformations and rescalings that keeps unaffected the perturbations of the first block. This set is parametrized by six coefficients $\{\alpha_0^i, \Lambda_0^3, K_t, K_r\}$, with $i = 1, 2, 3$, and gives the gauge-equivalents of a solution, which are

$$\begin{aligned}
a_t^3 &\to \alpha_0 a_t^3 - \mathrm{i}\omega\Lambda_0^3 + \mathrm{i}\omega\phi K_t + \left(\sqrt{N}\phi' - \omega^2(\phi A - C_\phi)\right) K_r \,, \\
a_x^2 &\to \alpha_0 a_x^2 - w\Lambda_0^3 - \mathrm{i}\omega w C_\phi K_r \,, \\
a_x^1 &\to \alpha_0 a_x^1 + \sqrt{N} w' K_r \,, \\
\xi_t &\to \alpha_0 \xi_t + 2\mathrm{i}\omega K_t + \left(\frac{\sigma N' + 2N\sigma'}{\sqrt{N}\sigma} - 2\omega^2 A\right) K_r \,, \\
\xi_y &\to \alpha_0 \xi_y + \frac{2\sqrt{N}\,(f + rf')}{rf} K_r \,, \\
\xi_x &\to \alpha_0 \xi_x + \frac{2\sqrt{N}\,(f - 2rf')}{rf} K_r \,;
\end{aligned} \tag{3.19}$$

where A, C_ϕ are defined in (B.7). We do not explicitly write the 3 independent scale factors out, rather we use a general scaling α_0. As will be explained later, the 3 independent scale parameters are related to the freedom of choosing the value for 3 of the fields at the horizon. However, due to the complicated mixing of the fields in the bulk it is not known how this translates into the scaling at the boundary. Following the steps of [33], we would now proceed by prescribing the values of the perturbations at the boundary $\{\beta_t^3, \beta_x^2, \beta_x^1, \beta_t, \beta_y, \beta_x\}$ by evaluating the asymptotic behavior of the gauge transformations, that we find is given by

$$\begin{aligned}
\beta_t^3 &= \left(a_t^3\right)_0^b - \mathrm{i}\omega\Lambda_0^3 + \mathrm{i}\omega\phi_0^b K_t \,, \\
\beta_x^2 &= \left(a_x^2\right)_0^b \,, \\
\beta_x^1 &= \left(a_x^1\right)_0^b \,, \\
\beta_t &= (\xi_t)_0^b + 2K_r + 2\mathrm{i}\omega K_t \,, \\
\beta_y &= (\xi_y)_0^b + 2K_r \,, \\
\beta_x &= (\xi_x)_0^b + 2K_r \,.
\end{aligned} \tag{3.20}$$

Since we do not know how the scale parameters enter the above equations, we have to alter our approach in deriving the action in terms of the physical fields.

We parametrize the fluctuations in such a way that each physical mode asymptotes (see equation (3.5)) to the boundary value of a fluctuation field. For this reason, from here on we will work with

$$\xi_p(\omega, r) = \xi_x(\omega, r) + \xi_y(\omega, r) \,, \qquad \xi_m(\omega, r) = \xi_x(\omega, r) - \xi_y(\omega, r) \,. \tag{3.21}$$

In addition, we perform a rotation of the a_x^1, a_x^2 into

$$a_x^+(\omega, r) = a_x^1(\omega, r) + \mathrm{i}\, a_x^2(\omega, r) \,, \qquad a_x^-(\omega, r) = a_x^1(\omega, r) - \mathrm{i}\, a_x^2(\omega, r) \,. \tag{3.22}$$

Accordingly, we rotate the corresponding physical fields into $\Phi_\pm = \Phi_1 \pm \mathrm{i}\ \Phi_2$, so that their respective boundary values coincide with those of $a_x^\pm$. This parametrization is more convenient, since the a_x^+ and a_x^- fields transform under the fundamental representation of the unbroken $\mathrm{U}(1)_3$. That is, they behave in a similar fashion as electrically charged vector mesons do under the $\mathrm{U}(1)_{\mathrm{em}}$. To make contact with the unbroken phase, we keep the parametrization also in the broken phase. Notice that these fields are conjugate of one another: $(a^\pm(\omega))^* = a^\mp(-\omega)$.

Next, we will invert the definitions (3.16) and solve for the selected fluctuation fields $\varphi_{\mathrm{I}} = \{a_x^\pm, \xi_m\}$ in terms of the corresponding physical fields $\Phi_{\mathrm{I}} = \{\Phi_\pm, \Phi_3\}$. The idea is to replace these three fields and write the on-shell action in terms of the physical fields of this block along with the remaining fluctuations $\varphi_i = \{a_t^3, \xi_t, \xi_p\}$. This can be seen as a change to a more convenient basis, which guarantees that the resulting correlators are free of gauge ambiguity.

We perform the replacement in (3.17) and in the corresponding counterterms (appendix A.2). In terms of the expansion coefficients of the physical fields at the boundary we obtain the on-shell action

$$\begin{aligned}
S^{\text{on-shell}}_{\text{hel.0, bl.2}} = \frac{r_h^4}{\kappa_5^2} \int \frac{\mathrm{d}^4 k}{(2\pi)^4} \Bigg\{ & \frac{\alpha^2}{2} \left[(\Phi_+)_0^b\, (\Phi_-)_1^b + (\Phi_-)_0^b\, (\Phi_+)_1^b \right] \\
& + \frac{1}{3}\, (\Phi_3)_0^b\, (\Phi_3)_2^b - \frac{1}{4} \alpha^2\, (\mu + \omega)^2\, (\Phi_+)_0^b\, (\Phi_-)_0^b \\
& + \frac{2\mu - \omega}{12\omega} \alpha^2 w_1^b \left[(\Phi_+)_0^b\, (\Phi_3)_0^b + (\Phi_3)_0^b\, (\Phi_-)_0^b \right] - \left(\frac{\omega^4}{64} + \frac{5 f_2^b}{3} + \frac{19 m_0^b}{96} \right) (\Phi_3)_0^{b\,2} \\
& + \frac{\alpha^2 w_1^b}{\omega} \left[(\Phi_-)_0^b - (\Phi_+)_0^b \right] \left(a_t^3 \right)_0^b + \left(f_2^b + \frac{m_0^b}{16} \right) (\Phi_3)_0^b \left[3\, (\xi_p)_0^b - 2\, (\xi_t)_0^b \right] \\
& + \frac{\mu - \omega}{4\omega} \alpha^2 w_1^b \left[\left((\xi_p)_0^b - 2\, (\xi_t)_0^b \right) (\Phi_+)_0^b + (\Phi_-)_0^b \left((\xi_p)_0^b - 2\, (\xi_t)_0^b \right) \right] \\
& + \frac{m_0^b}{32} \left[12 (\xi_t)_0^{b\,2} - 9 (\xi_p)_0^{b\,2} + 12\, (\xi_p)_0^b\, (\xi_t)_0^b \right] \Bigg\} \Bigg|_{r = r_{\mathrm{bdy}}}
\end{aligned} \tag{3.23}$$

The fields in this action are defined by equation (3.5) and (3.21) and below equation (3.22). This new action (including the φ_i part), when written in terms of the block 2 perturbation modes, coincides exactly with what we have in (A.15).

The part involving the physical fields only can schematically be written as

$$S^{\text{on-shell}}_{\text{hel.0, bl.2}} = \frac{r_h^4}{\kappa_5^2} \int \frac{\mathrm{d}^4 k}{(2\pi)^4} \left[\Phi^*_{\mathrm{I}}(-\omega, r) A(k,r)_{\mathrm{IJ}} \partial_r \Phi_{\mathrm{J}}(\omega, r) + \Phi^*_{\mathrm{I}}(-\omega, r) B(k,r)_{\mathrm{IJ}} \Phi_{\mathrm{J}}(\omega, r)\right]_{r=r_b} ,$$

where the derivatives $\partial_r \Phi_{\mathrm{I}}$ evaluated at the boundary absorb the higher-order coefficients of the expansions (see (3.18)), in the same way that the $\Phi_{\mathrm{I}}(r_b)$ absorb the boundary values of the replaced fields. Of the matrices A, B; we only need to know their asymptotic values at the cutoff r_{bdy}, which are given by

$$A(\omega, r_{\text{bdy}}) = \begin{pmatrix} -\frac{1}{4}\alpha^2 r^3_{\text{bdy}} & 0 & 0 \\ 0 & -\frac{1}{4}\alpha^2 r^3_{\text{bdy}} & 0 \\ 0 & 0 & -\frac{1}{12} r^5_{\text{bdy}} \end{pmatrix} , \tag{3.24}$$

and

$$B(\omega, r_{\text{bdy}}) = \begin{pmatrix} \frac{1}{4}\alpha^2 \left(\mu - \omega\right)^2 \log\left(\frac{r_h}{r}\right) & 0 & -\frac{2\mu+\omega}{24\omega}\alpha^2 w_1^b \\ 0 & \frac{1}{4}\alpha^2 \left(\mu + \omega\right)^2 \log\left(\frac{r_h}{r}\right) & \frac{2\mu-\omega}{24\omega}\alpha^2 w_1^b \\ -\frac{2\mu+\omega}{24\omega}\alpha^2 w_1^b & \frac{2\mu-\omega}{24\omega}\alpha^2 w_1^b & B_{33}(\omega, r_{\text{bdy}}) \end{pmatrix} , \tag{3.25}$$

with $B_{33}(\omega, r) = \frac{1}{96}\left[-4\omega^2 r^2 + 2\omega^4 \log\left(\frac{r_h}{r}\right) - 160 f_2^b - 19 m_0^b\right]$.

At this point we refer the reader to [45] for a prescription to calculate the Green's functions in systems where the operators mix. In appendix C, we discuss this prescription in more detail and show how it can be generalized to our case.

The matrices A, B are the ones used to perform the numerical calculations described there, and the rest of the terms in (3.23) give directly the Green's functions. In fact the matrix of Green's functions of this block may be written as

$$\begin{pmatrix} \langle J_3^t \rangle(\omega) \\ \langle J_+^x \rangle(\omega) \\ \langle J_-^x \rangle(\omega) \\ \langle \frac{1}{2}\left(T^{xx} - 2T^{\perp\perp}\right)\rangle(\omega) \\ \langle \frac{1}{2}\left(T^{xx} + 2T^{\perp\perp}\right)\rangle(\omega) \\ \langle T^{tt} \rangle(\omega) \end{pmatrix} = \begin{pmatrix} \frac{\delta S^{\text{on-shell}}_{\text{helicity 0}}}{\delta\left(a_t^3\right)_0^b(-\omega)} \\ \frac{\delta S^{\text{on-shell}}_{\text{helicity 0}}}{\delta(\Phi_+{}^*)_0^b(-\omega)} \\ \frac{\delta S^{\text{on-shell}}_{\text{helicity 0}}}{\delta(\Phi_-{}^*)_0^b(-\omega)} \\ \frac{\delta S^{\text{on-shell}}_{\text{helicity 0}}}{\delta\left(\Phi_3\right)_0^b(-\omega)} \\ \frac{\delta S^{\text{on-shell}}_{\text{helicity 0}}}{\delta\left(\xi_p\right)_0^b(-\omega)} \\ \frac{\delta S^{\text{on-shell}}_{\text{helicity 0}}}{\delta\left(\xi_t\right)_0^b(-\omega)} \end{pmatrix} = \mathcal{G}_{(2)}(\omega) \begin{pmatrix} \left(a_t^3\right)_0^b(\omega) \\ (\Phi_+)_0^b(\omega) \\ (\Phi_-)_0^b(\omega) \\ \left(\Phi_3\right)_0^b(\omega) \\ \left(\xi_p\right)_0^b(\omega) \\ \left(\xi_t\right)_0^b(\omega) \end{pmatrix} , \tag{3.26}$$

where the entries are denoted by

$$\mathcal{G}_{(2)}(\omega) = \begin{pmatrix} G^{t,t}_{3,3}(\omega) & G^{t,x}_{3,+}(\omega) & G^{t,x}_{3,-}(\omega) & G^{t\ m}_{3}(\omega) & G^{t\ p}_{3}(\omega) & G^{t\ t}_{3}(\omega) \\ G^{x,t}_{+,3}(\omega) & G^{x,x}_{+,+}(\omega) & G^{x,x}_{+,-}(\omega) & G^{x\ m}_{+}(\omega) & G^{x\ p}_{+}(\omega) & G^{x\ t}_{+}(\omega) \\ G^{x,t}_{-,3}(\omega) & G^{x,x}_{-,+}(\omega) & G^{x,x}_{-,-}(\omega) & G^{xm}_{-}(\omega) & G^{xp}_{-}(\omega) & G^{xt}_{-}(\omega) \\ G^{mt}{}_{3}(\omega) & G^{mx}{}_{+}(\omega) & G^{mx}{}_{-}(\omega) & G^{m,m}(\omega) & G^{m,p}(\omega) & G^{m,t}(\omega) \\ G^{pt}{}_{3}(\omega) & G^{px}{}_{+}(\omega) & G^{px}{}_{-}(\omega) & G^{p,m}(\omega) & G^{p,p}(\omega) & G^{p,t}(\omega) \\ G^{tt}{}_{3}(\omega) & G^{tx}{}_{+}(\omega) & G^{tx}{}_{-}(\omega) & G^{t,m}(\omega) & G^{t,p}(\omega) & G^{t,t}(\omega) \end{pmatrix} \tag{3.27}$$

and we find that they are given by $\mathcal{G}_{(2)}(\omega) =$

$$\begin{pmatrix} 0 & -\frac{1}{2\omega}\langle\mathcal{J}_1^x\rangle & \frac{1}{2\omega}\langle\mathcal{J}_1^x\rangle & 0 & 0 & 0 \\ \frac{1}{2\omega}\langle\mathcal{J}_1^x\rangle & G^{x,x}_{+,+}(\omega) & G^{x,x}_{+,-}(\omega) & G^{x\,m}_{+}(\omega) & -\frac{\mu+\omega}{8\omega}\langle\mathcal{J}_1^x\rangle & \frac{\mu+\omega}{4\omega}\langle\mathcal{J}_1^x\rangle \\ -\frac{1}{2\omega}\langle\mathcal{J}_1^x\rangle & G^{x,x}_{-,+}(\omega) & G^{x,x}_{-,-}(\omega) & G^{x\,m}_{-}(\omega) & \frac{\mu-\omega}{8\omega}\langle\mathcal{J}_1^x\rangle & -\frac{\mu-\omega}{4\omega}\langle\mathcal{J}_1^x\rangle \\ 0 & G^{m\,x}_{\ \ +}(\omega) & G^{m\,x}_{\ \ -}(\omega) & G^{m,m}(\omega) & \frac{3}{16}\left(\langle\mathcal{T}_{tt}\rangle - 2\langle\mathcal{T}_{xx}\rangle\right) & -\frac{1}{8}\left(\langle\mathcal{T}_{tt}\rangle - 2\langle\mathcal{T}_{xx}\rangle\right) \\ 0 & \frac{\mu-\omega}{8\omega}\langle\mathcal{J}_1^x\rangle & -\frac{\mu+\omega}{8\omega}\langle\mathcal{J}_1^x\rangle & \frac{3}{16}\left(\langle\mathcal{T}_{tt}\rangle - 2\langle\mathcal{T}_{xx}\rangle\right) & -\frac{3}{16}\langle\mathcal{T}_{tt}\rangle & \frac{1}{8}\langle\mathcal{T}_{tt}\rangle \\ 0 & -\frac{\mu-\omega}{4\omega}\langle\mathcal{J}_1^x\rangle & \frac{\mu+\omega}{4\omega}\langle\mathcal{J}_1^x\rangle & -\frac{1}{8}\left(\langle\mathcal{T}_{tt}\rangle - 2\langle\mathcal{T}_{xx}\rangle\right) & \frac{1}{8}\langle\mathcal{T}_{tt}\rangle & \frac{1}{4}\langle\mathcal{T}_{tt}\rangle \end{pmatrix}.$$

Now some comments are in order explaining the expectation values of equation (3.26) and the notation we use. Regarding the former, we derive $\langle\frac{1}{2}\left(T^{xx} - 2T^{\perp\perp}\right)\rangle$ and $\langle\frac{1}{2}\left(T^{xx} + 2T^{\perp\perp}\right)\rangle$ in appendix D and furthermore use that $T^{yy} = T^{zz}$. Regarding the notation, note that the index m is related to Φ_3 field, since $(\Phi_3)_0^b = (\xi_m)_0^b$. Furthermore the $\substack{x \\ \pm}$ indices are related to the Φ_+ and Φ_- fields. Here all entries are functions of the background, except for the sector containing the physical fields and their couplings, which has to be computed numerically. As before, to do so we choose infalling boundary conditions at the horizon which leaves us with six of the former twelve free parameters. From the six left, three are fixed by the constraint equations. The value of the three remaining coefficients just scale the solutions and since we compute ratios of the boundary values it does not matter which value we choose for them. Note that a more detailed explanation of the numerical procedure we apply is described in appendix C. This part of $\mathcal{G}_{(2)}$ describes the dynamics of this block, and it is related holographically to several interesting properties of the superfluid phase, as we describe in the next section.

4 Transport properties

In this section we extract the transport properties of the holographic p-wave superfluid from the correlation functions presented in the previous section. We split our analysis into distinct transport phenomena.

4.1 Thermoelectric effect parallel to the condensate

We start by presenting the thermoelectric effect parallel to the condensate, i.e. we look at charge transport and temperature gradients in the x direction. This is related to the first block of helicity zero states we presented in section 3.2.1. Furthermore our results are in agreement with [33] for the non-backreacted case.

The thermoelectric effect describes the simultaneous transport of charge and heat (or energy). This means that an electric field not only leads to a current, but also to a heat flux and, conversely, a temperature gradient leads to an electric current in addition to a heat flux. In holographic systems, this effect was already observed in s-wave superfluids (see e.g. [31, 37, 46]) or in the p-wave superfluid component transverse to the condensate [19]. However, in the case at hand, we have a slight complication due to a further coupling of the a_t^1 and a_t^2 fields to the a_x^3 and to the h_{tx} metric component (see section 3.2.1).

A straightforward calculation (see [37]) shows that $\nabla_x T$ is related to the g_{tt} component of the metric through the change in the period of the Euclidean time. The change can be done in a way that δg_{tt} becomes pure gauge provided a complementary change is done for A^3_x and g_{tx}. It is customary to fix the gauge requesting δg_{tt} to vanish, and allowing for δA^3_x and δg_{tx} only. On the other hand, E_x receives an additional contribution from the vector potential, $i\omega\,(\Phi_4)^b_0$. The combined effect is so that we define the electric field and temperature gradient

$$\begin{aligned} E_x &= \mathrm{i}\omega\left[(\Phi_4)^b_0 + \mu\,(\xi_{tx})^b_0\right] ,\\ -\frac{\nabla_x T}{T} &= \mathrm{i}\omega\,(\xi_{tx})^b_0 \,. \end{aligned} \tag{4.1}$$

This modes source the charge current J^x in direction of the condensate and the heat flux $Q^x = T^{tx} - \mu J^x$, respectively. The relation of these currents to the corresponding electrical field and temperature gradient defines the conductivity matrix

$$\begin{pmatrix} \langle J^x\rangle \\ \langle Q^x\rangle \end{pmatrix} = \begin{pmatrix} \sigma^{xx} & T\alpha^{xx} \\ T\alpha^{xx} & T\bar{\kappa}^{xx} \end{pmatrix} \begin{pmatrix} E_x \\ -(\nabla_x T)/T \end{pmatrix} . \tag{4.2}$$

Comparing this matrix to the lower right corner of the one in (3.13), we can identify the electric, thermal and thermoelectric conductivities, which are related to the retarded Green's functions by

$$\begin{aligned} \sigma^{xx} &= -\frac{\mathrm{i}}{\omega} G^{x,x}_{3,3} \,,\\ T\alpha^{xx} &= -\frac{\mathrm{i}}{\omega}\left(G^{x\,tx}_3 - \mu G^{x,x}_{3,3}\right) = \frac{\mathrm{i}}{\omega}\langle \mathcal{J}^t_3\rangle - \mu\sigma^{xx} \,,\\ T\bar{\kappa}^{xx} &= -\frac{\mathrm{i}}{\omega}\left(G^{tx,tx} - 2\mu G^{x\,tx}_3 + \mu^2 G^{x,x}_{3,3}\right) = \frac{\mathrm{i}}{\omega}\left(\langle \mathcal{T}_{tt}\rangle - 2\mu\langle \mathcal{J}^t_3\rangle\right) + \mu^2\sigma^{xx} \,. \end{aligned} \tag{4.3}$$

The conductivity in direction of the condensate σ^{xx} has been calculated numerically. The results are shown in figures 2 and 3 for $\alpha = 0.316 < \alpha_c$. The results for other values of α do not show any significant qualitative difference, therefore we do not show them in this paper.

The rest of the matrix (3.13) shows the response of the system due to the a^1_t, a^2_t fluctuations. This is a manifestation of the fact that the equations of motion of the gauge field fluctuations are coupled. Therefore, if a temperature gradient excites one of these modes, the other two will respond, and their response is dictated by the coefficients of the matrix. In [33], the a^1_t, a^2_t fluctuation fields are interpreted as generating a rotation of the charge density in direction $\langle J^t_1\rangle$ and $\langle J^t_2\rangle$, however without changing its magnitude.

The complete transport matrix of this block then reads

$$\begin{pmatrix} \langle J^t_1\rangle \\ \langle J^t_2\rangle \\ \langle J^x\rangle \\ \langle Q^x\rangle \end{pmatrix} = \begin{pmatrix} \sigma^{t,t}_{1,1} & \sigma^{t,t}_{1,2} & \sigma^{t,x}_{1,3} & -\mu\sigma^{t,x}_{1,3} \\ \sigma^{t,t}_{2,1} & \sigma^{t,t}_{2,2} & \sigma^{t,x}_{2,3} & -\mu\sigma^{t,x}_{2,3} \\ \sigma^{x,t}_{3,1} & \sigma^{x,t}_{3,2} & \sigma^{xx} & T\alpha^{xx} \\ -\mu\sigma^{x,t}_{3,1} & -\mu\sigma^{x,t}_{3,2} & T\alpha^{xx} & T\bar{\kappa}^{xx} \end{pmatrix} \begin{pmatrix} i\omega a^1_t \\ i\omega a^2_t \\ E_x \\ -\frac{\nabla_x T}{T} \end{pmatrix} , \tag{4.4}$$

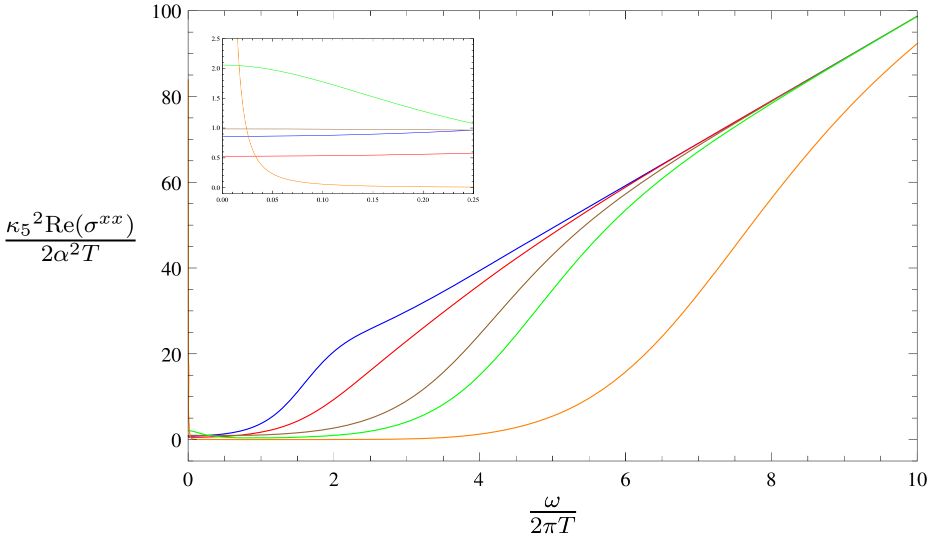

Figure 2. Real part of the conductivity $\mathrm{Re}(\sigma^{xx})$ over the frequency $\omega/(2\pi T)$ for $\alpha = 0.316$. The color coding is as follows: blue $T = 1.63T_c$, red $T = 0.98T_c$, brown $T = 0.88T_c$, green $T = 0.78T_c$, orange $T = 0.50T_c$. There is a delta peak at strictly $\omega = 0$, not noticeable in this figure, as dictated by the sum rule (the area below the curves has to be the same for any T).

where each of the transport coefficients is simply related to the corresponding Green's function by $\sigma = -\mathrm{i}G/\omega$. We will now focus on the electric conductivity σ^{xx}, the others can be obtained from it.

The fact that the longitudinal conductivity σ^{xx} has a different behavior than that of the component transverse to the condensate $\sigma^{\perp\perp}$ (c.f. [19]) in the broken phase is an effect of the breaking of rotational symmetry.

Let us discuss the similarities and differences between σ^{xx} and $\sigma^{\perp\perp}$ (for a discussion of $\sigma^{\perp\perp}$ see [19]). The curve of the real part of σ^{xx} (figure 2) shows the correct [47] asymptotic behaviour for large frequencies, i. e. the real part is proportional to the frequency for all temperatures. More precisely, for $\omega \gg T$ we have

$$\frac{\kappa_5{}^2\mathrm{Re}(\sigma^{xx})}{2\alpha^2 T} \to \pi^2 \frac{\omega}{2\pi T}\,. \tag{4.5}$$

We expect this behavior on dimensional grounds, and as a consequence of the conformal symmetry in our system.[3] On the other hand, for decreasing frequencies we see that the conductivity decreases until nearly vanishing. This sharp decrease is a known feature of superconductors. It is present for all temperatures, not only for $T < T_c$. However, for smaller temperatures the decrease takes place at larger values of ω. It is by far not as sharp as in $\sigma^{\perp\perp}$, and furthermore there are some qualitative differences: The bump before decreasing is absent for σ^{xx} - the asymptotic value for large frequencies is approached by the curves with smaller temperature from below, rather than from above, as opposed to the perpendicular case. Besides, up to numerical inaccuracy the conductivities do not seem to vanish for any frequency, for temperatures above $0.5T_c$. In comparison, the transverse

---

[3] There is no lattice spacing which would spoil the high frequency behavior.

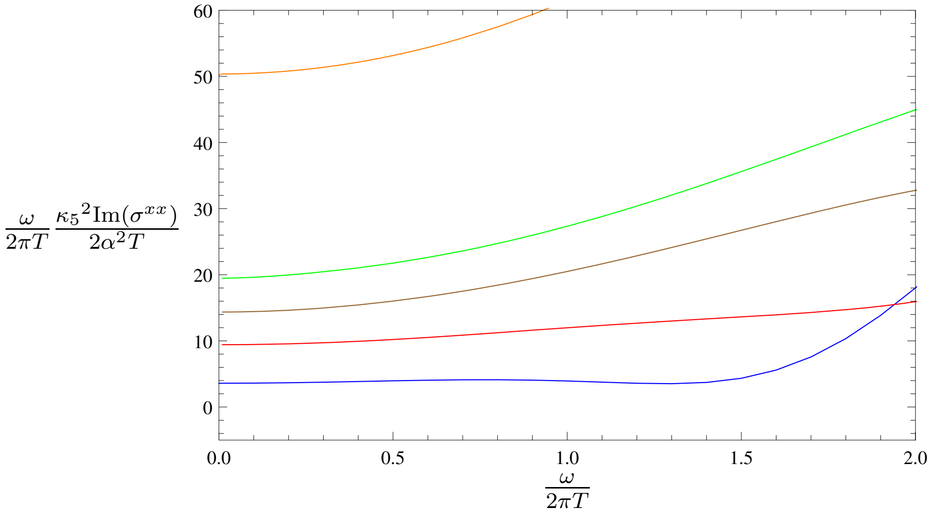

Figure 3. Imaginary part of the conductivity times the frequency, $\omega\mathrm{Im}(\sigma^{xx})$ over the frequency $\omega/(2\pi T)$ for $\alpha = 0.316$. The color coding is as follows: blue $T = 1.63T_c$, red $T = 0.98T_c$, brown $T = 0.88T_c$, green $T = 0.78T_c$, orange $T = 0.50T_c$. The curves tend to a constant value as $\omega \to 0$, which indicates the presence of a pole at the origin. This is related to the delta peak in the real part of σ^{xx}.

conductivity has a far stronger temperature suppression in the gapped region. However, below $0.5T_c$ the situation seems to change dramatically as is explained in the next section.

The real part of σ^{xx}, as opposed to the perpendicular case, increases again for small but finite frequencies and reaches a finite value in the $\omega \to 0$ limit, as seen in the zoomed region of figure 2. This increase in the real part in the zero frequency limit is due to a quasinormal mode which moves up the imaginary axis in the complex frequency plane (see the blue arrow in figure 6) and seems to reach the origin $\omega = 0$ at temperatures slightly above $0.5T_c$. The increase we see towards the $\omega \to 0$ limit comes from the projection of the quasinormal mode onto the real frequency axis. Note that this bump increases with decreasing temperature. Unfortunately it is challenging to compute the exact temperature when the mode arrives at the origin, since we have to rely on numerical calculations. Nevertheless, for temperatures below $0.5T_c$ it appears that a pole is formed and at the same time the real part of the conductivity is more strongly suppressed at finite small frequencies in comparison to cases of temperatures above $0.5T_c$ (see the green and orange curve in zoomed region of figure 2). It seems that somewhere around $0.5T_c$, due to the quasinormal mode at the origin, the conductivity behavior in the direction of the condensate changes. It would be interesting to understand this effect from a field theoretic point of view, we leave this for future work.

Due to the pole in the imaginary part of the conductivity (see figure 3) and the Kramers-Kronig relation [32] we know that at $\omega = 0$ the real part must have a delta peak. There are two main contributions to the prefactor of this delta peak, which change with temperature, and they come from the pole at the origin of the imaginary part, expressed as

$$\omega\,\mathrm{Im}\,(\sigma^{xx}) \simeq A_{\mathrm{D}}(\alpha, T) + A_s^x(\alpha)\left(1 - \frac{T}{T_c}\right) . \tag{4.6}$$

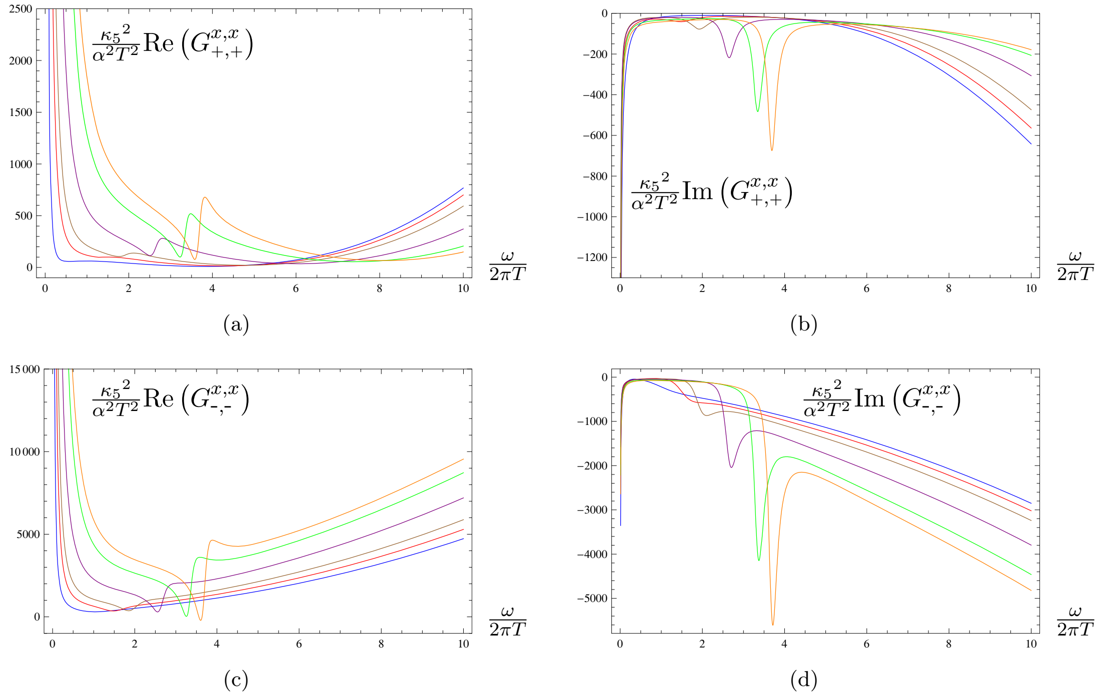

(a) (b)

(c) (d)

Figure 4. These plots show the real and imaginary part of the correlators $G^{x,x}_{\pm,\pm}$ versus the reduced frequency $\omega/(2\pi T)$ for $\alpha = 0.316$ at different temperatures: blue $T = 0.98T_c$, red $T = 0.88T_c$, brown $T = 0.78T_c$, purple $T = 0.62T_c$, green $T = 0.50T_c$, orange $T = 0.46T_c$.

This is reminiscent of the perpendicular case (c.f. [19]). In fact, similarly the first contribution A_{D} is a consequence of translational invariance at all temperatures, specifically for temperatures above T_c. The other contribution, A_s^x, appears when temperatures decrease below T_c. This prefactor is expected to be connected to the superfluid density, however it differs from the corresponding factor in the transverse case.

The properties of the two components of the conductivities we state here are very similar to the ones found in the non-backreacted case (see [33]). Therefore corrections due to the backreaction seem to be rather small.

4.2 Viscosities and flavour transport coefficients

The second block of coupled modes transforming as scalars under the SO(2) symmetry includes the fields a_x^1, a_x^2, a_t^3, $\xi_t = g^{tt}h_{tt}$, $\xi_x = g^{xx}h_{xx}$ and $\xi_y = g^{yy}h_{yy}$. Similarly to the first block, these fields form 3 physical modes, Φ_1, Φ_2 and Φ_3 (see (3.3)). It turns out that it is more sensible to consider this fields in terms of $\Phi_\pm = \Phi_1 \pm i\Phi_2$, since they transform fundamentally under the $\mathrm{U}(1)_3$ in the unbroken phase.

4.2.1 Piezoelectric effect

The transport properties presented in this section show similarities to an effect known as piezoelectric effect[4] found in crystals [39]. This effect describes the generation of an

---

[4] A similar effect, the flexoelectric effect, is related to the helicity one modes, see [19].

electric current due to the squeezing and/or elongation of a crystal, or the generation of a mechanical strain due to an external electric field. A coupling between a normal stress difference and (flavour) currents that resembles this effect is found in this block. Note that the piezoelectric effect was already found in the context of black branes in [48].

In simple terms, there is an interaction analogous to the one of the first block, between

$$\begin{pmatrix} \langle J^x_\pm \rangle \\ \langle T^{xx}, T^{\perp\perp}, T^{tt} \rangle \end{pmatrix} \longleftrightarrow \begin{pmatrix} a^\pm_x \\ h_{xx}, h_{\perp\perp}, h_{tt} \end{pmatrix} . \tag{4.7}$$

The broken phase is characterized by a condensate $\langle J^x_1 \rangle$. The $a^\pm_x$ fluctuate around this background value and the system reacts by working against this perturbations by changing the diagonal stress-energy tensor components $\langle T^{xx} \rangle$, $\langle T^{\perp\perp} \rangle$ and $\langle T^{tt} \rangle$. The converse case, where we fluctuate about equilibrium values of the stress-energy tensor and look at the response of the currents $\langle J^x_1 \rangle$ works in a similar fashion. Note that this is not the only response of the system to these fluctuations. However, in this section we are interested exactly in the coupling between different modes. In the field theory this may be related to an electric current being affected by, or generating, mechanical stress (Piezoelectric effect). Finally, the transport coefficients "measure" the strength of the response of the system, i.e. how do the expectation values change with respect to the original values when they are perturbed.

In figures 4 and 5 we plot the real and imaginary part of $G^{x,x}_{\pm,\pm}$ and $G^{x,x}_{\pm,\mp}$ over the reduced frequency $\omega/(2\pi T)$, for several values of the temperature, or equivalently of the chemical potential μ. We find the symmetry relations

$$\begin{aligned} G^{x,x}_{-,-}(\omega) &= G^{x,x}_{+,+}(-\omega)^* , \qquad & G^{x,x}_{+,-}(\omega) &= G^{x,x}_{-,+}(-\omega)^* , \\ G^{x,x}_{-,-}(\omega) &= G^{x,x}_{+,+}(-\omega)^* , \qquad & G^{x,x}_{+,-}(\omega) &= G^{x,x}_{-,+}(-\omega)^* , \end{aligned}$$

as we did in the study of helicity one modes [19]. This was expected from the fact that $(\Phi_+(\omega))^* = \Phi_-(-\omega)$, $(\Phi_-(\omega))^* = \Phi_+(-\omega)$ and $(\Phi_3(\omega))^* = \Phi_3(-\omega)^*$.

In figure 7 we plot the $G^{m\,x}_{\pm}$, whose imaginary parts are identical to those of $G^{x\,m}_{\pm}$, and whose real parts are similar, except for small frequencies compared to the temperature.

Notice that many of the curves in figures 4–7 show a pole at $\omega = 0$. To understand why, remember that the formation of $\langle J^x_1 \rangle$ selects a preferred direction in flavor space, spontaneously breaking the SO(3) and U(1)$_3$ symmetries. As a consequence of this, the a^2_x field becomes one of the three massless Goldstone modes arising from the spontaneous symmetry breaking. This common pole reflects the formation of this Goldstone mode, since it is included in the fields $\Phi_\pm$, which are involved in all of the correlators presented here. When plotting the quasinormal modes in the complex frequency plane we also see this pole at the origin, so that for $T > T_c$ they asymptote to the origin of the frequency place $\omega = 0$. In fact, although it is not apparent in figures 5 and 7, the correlators vanish completely in the unbroken phase $T > T_c$, since in this limit the equations of motion of the bulk fields decouple.

Another common feature of our results is the appearance of a rich structure for the correlators in the broken phase, including the formation of a bump located on the same

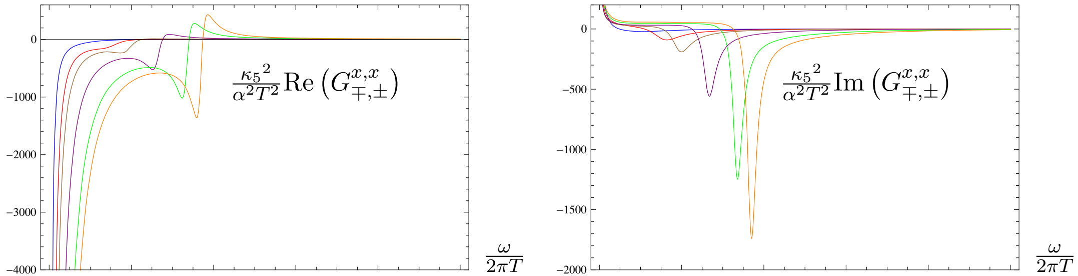

(a) (b)

Figure 5. These plots show the real and imaginary part of the correlator $G^{x,x}_{+,-}$, or equivalently $G^{x,x}_{-,+}$, versus the reduced frequency $\omega/(2\pi T)$ for $\alpha = 0.316$ at different temperatures: blue $T = 0.98T_c$, red $T = 0.88T_c$, brown $T = 0.78T_c$, purple $T = 0.62T_c$, green $T = 0.50T_c$, orange $T = 0.46T_c$.

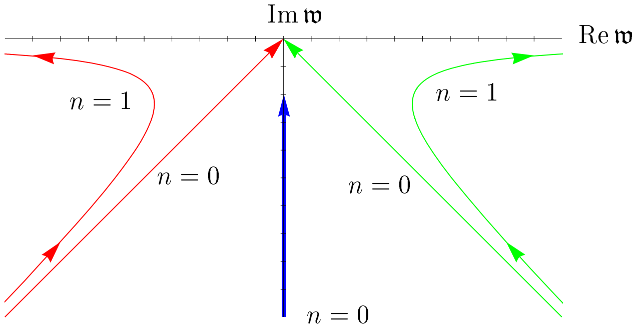

Figure 6. This figure, taken from [34], shows the different quasinormal modes in the D3/D7 system in the complex frequency plane. Here $\mathfrak{w} = \omega/(2\pi T)$. The red and green curves show the modes of the fluctuations which correspond to $\Phi_\pm$ in our setup and the blue curve corresponds to our Φ_4. It is interesting to see that the backreaction and the bottom up approach we pursue in the system at hand behave in a very similar fashion as the D3/D7 probe setup. Note however, that there is one difference: due to the backreaction and consequently the rotational symmetry breaking in the superfluid phase, the $a_y^\pm$ decouple from the $\Phi_\pm$, contrary to what happens in the D3/D7 mode. Moreover, we only see the red and green modes in the $\Phi_\pm$ sector and not in the $a_y^\pm$ sector (see [19] for a treatment of this modes).

value of the frequency for all of them. These bumps come from higher quasinormal excitations. With decreasing temperature, they move in the direction of smaller values of the negative imaginary parts and larger real parts of the frequencies. Therefore they become more accentuated with decreasing temperature. Nevertheless the quasinormal modes stay in the lower half complex frequency plane for all the temperatures we were able to check numerically. We will leave it for future work to investigate their behavior at finite spatial momentum and zero temperature. Note that their behavior is very similar to the one found in the D3/D7 model in [34] (see figure 6). Following [34], these bumps may be interpreted as bound states, e.g. mesons. However, since we do not have a precise knowledge of the the field theory side, this interpretation should be treated with care. We cannot say much more at this stage, without having the exact formulation of the hydrodynamics dual to this gravitational setup.

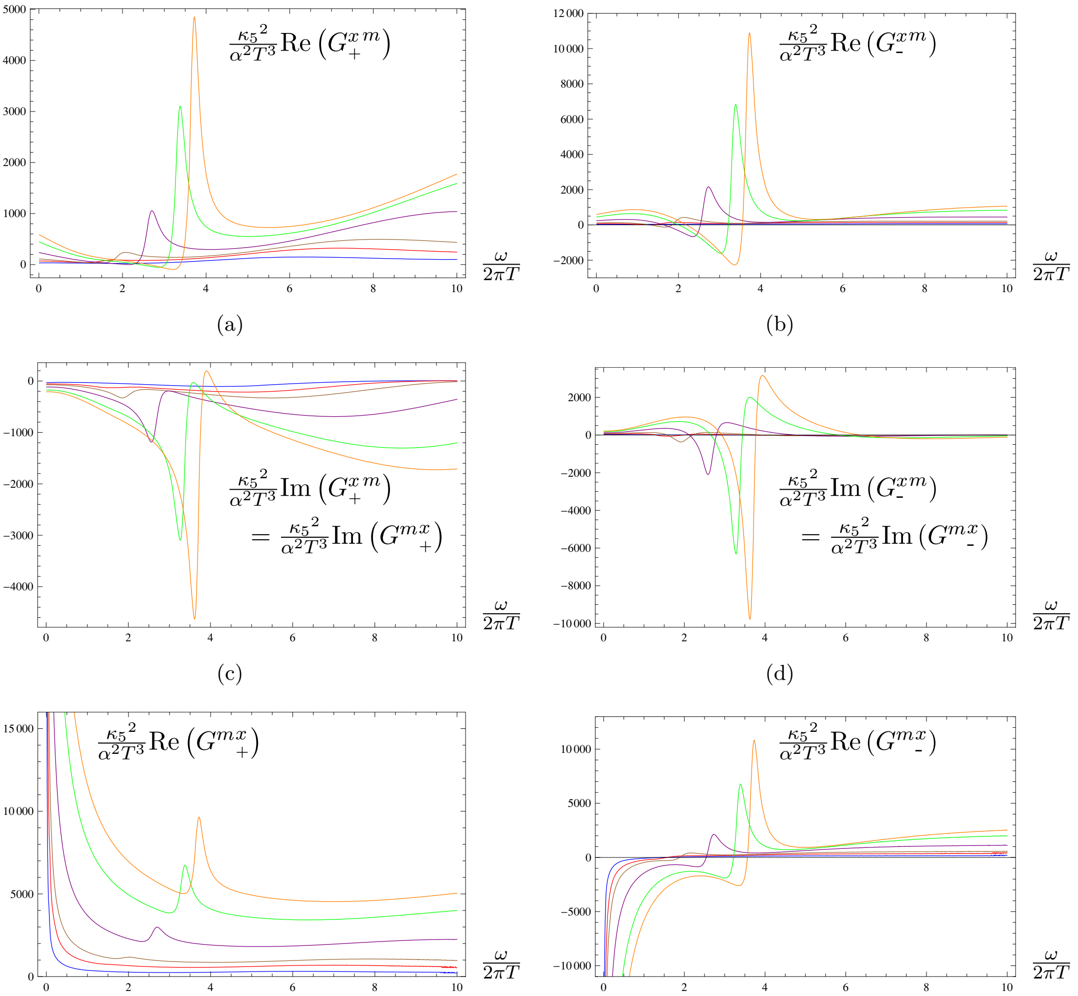

(a) (b)

(c) (d)

(e) (f)

Figure 7. These plots show the real and imaginary part of the correlators $G^{x\ m}_{\pm}$ versus the reduced frequency $\omega/(2\pi T)$ for $\alpha = 0.316$ at different temperatures: blue $T = 0.98T_c$, red $T = 0.88T_c$, brown $T = 0.78T_c$, purple $T = 0.62T_c$, green $T = 0.50T_c$, orange $T = 0.46T_c$. We are not showing $G^{m x}_{\ \ \pm}$ because their imaginary parts are identical. Their real parts, however, show a different low frequency behaviour.

The Green's functions $G^{x,x}_{\pm,\pm}$ (c.f. figure 4) seem to have different asymptotic values, however this is just a consequence of the small frequency range displayed here. Actually, they do asymptote to the same value for all temperatures in the limit of large frequencies. However this veils the interesting details at low frequency, therefore we do not show it here. Nevertheless, the large frequency limit is proportional to ω^2, in agreement with the underlying CFT.

Finally, note that the real parts of $G^{x\ m}_{\pm}$ and $G^{m x}_{\ \ \pm}$ are not symmetric to each other. In the latter one we see poles in the $\omega \to 0$ limit. This poles are due to the fact that in the $G^{m x}_{\ \ \pm}$ case we are dividing by the boundary value of $\Phi_{\pm}$, which contains the (massless) Goldstone mode a_x^2 and therefore vanishes at $\omega = 0$, whereas in the $G^{x\ m}_{\pm}$ case we divide by the boundary value of Φ_3, whose quasinormal mode is not located at the origin.

In the next subsection we look at $G^{m,m}$, the Green's function generated by Φ_3.

4.2.2 Transport coefficient associated to a normal stress difference

In the presence of anisotropy, besides the two shear viscosities η_{yz} and η_{xy}, there are three other coefficients. But in a conformal fluid, two of them, ζ_x and ζ_y, vanish due to the tracelessness condition of the energy-momentum tensor in conformal theories. The remaining nonzero component, λ, is related to the normal stress difference as discussed below.

In the $\omega \to 0$ limit the imaginary part of the two-point function of Φ_3 asymptotes to a finite value different from zero, see figure 8. We can relate this Green's function to the transport coefficient λ (see appendix D), i. e.

$$\lambda = \lim_{\omega \to 0} \frac{3}{2\omega} \operatorname{Im} G^{m,m}(\omega)\,. \tag{4.8}$$

As discussed in appendix D there is no λ in the isotropic phase. However, the corresponding transport coefficient in the unbroken phase is just the shear viscosity η (compare equations (D.5) and (D.6)). Therefore we can match λ to η at the phase transition. In the following we show that the Green's function of Φ_3 in the isotropic case gives the correct value of η.

If we consider perturbations around a background with unbroken SO(3) symmetry, i. e. with zero $w(r)$, then the physical field Φ_3 decouples from the other fields. Inserting the analytic solution of the AdS Reissner-Nordström black hole,

$$\mathrm{d}s^2 = -N(r)\mathrm{d}t^2 + \frac{1}{N(r)}\mathrm{d}r^2 + r^2\left(\mathrm{d}x^2 + \mathrm{d}y^2 + \mathrm{d}z^2\right)\,, \tag{4.9}$$

its equation of motion can simply be written as

$$\frac{\omega^2 r^3}{N(r)}\Phi_3 + \left[r^3 N(r)\Phi_3'\right]' = 0\,, \tag{4.10}$$

where $N(r) = r^2 - \frac{2m_0}{r^2} + \frac{2\alpha^2 q^2}{3r^4}$. This is the equation of motion of a minimally coupled scalar, thus we can apply the procedure developed in [24] to derive the value of the corresponding transport coefficient. The relevant part of the boundary action in the unbroken case for this mode is

$$S^{\text{on-shell}}_{\Phi_3} = \frac{r_h^4}{\kappa_5^2}\int \frac{\mathrm{d}^4k}{(2\pi)^4}\left[-\frac{r^5}{12}\Phi_3^*(\omega,r)\partial_r\Phi_3(\omega,r) + B_{33}(k,r)\Phi_3^*(\omega,r)\Phi_3(\omega,r)\right]_{r=r_b} \tag{4.11}$$

with $B_{33}(\omega,r) = \frac{1}{96}\left[-4\omega^2 r^2 + 2\omega^4\log\left(\frac{r_h}{r}\right) - 19m_0^b\right]$ and m_0^b defined as in the AdS Reissner-Nordström solution. Using the result of [24] and the Kubo formula (4.8),[5] we obtain for this particular case the viscosity coefficient

$$\frac{\eta}{s} = \frac{1}{4\pi}\,, \tag{4.12}$$

where s is the entropy density. This is the expected value for the shear viscosity in the isotropic phase.

---

[5] Just interchange η with λ, since λ is normalized in a way to match η at the phase transition.

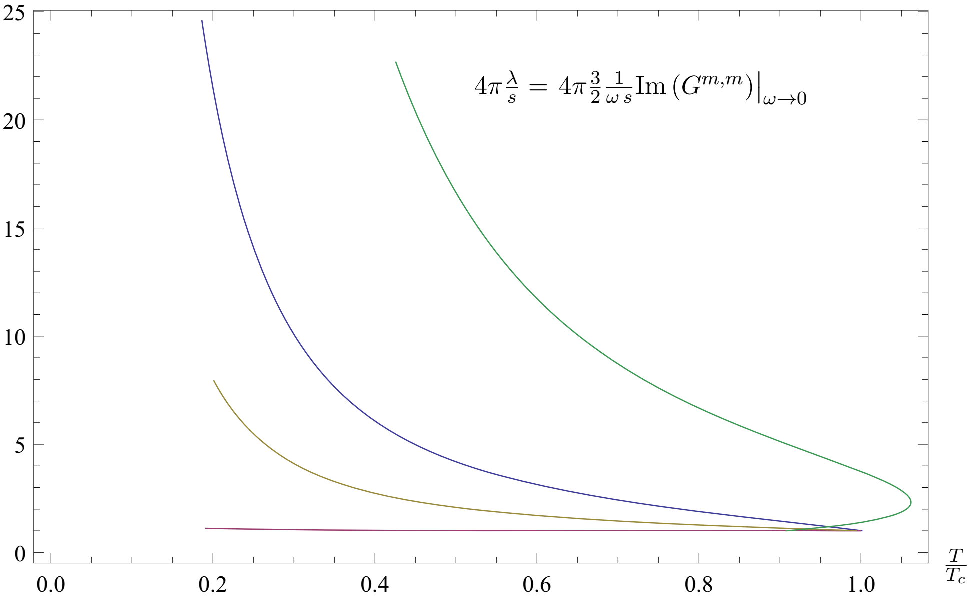

Figure 8. We plot $\frac{\lambda}{s}$ over the temperature T/T_c for $\alpha = 0.032$ (red), $\alpha = 0.224$ (yellow), $\alpha = 0.316$ (blue) and $\alpha = 0.447$ (green). Note that $\alpha = 0.447 > \alpha_c$ and therefore the phase transition is first order leading to multiple values near the phase transition. All curves tend to $1/(4\pi)$ at T_c, since in the unbroken phase λ corresponds to the isotropic shear viscosity η.

As stated above λ is the transport coefficient related to the normal stress difference, that is, the difference of the diagonal components of the stress tensor, $\langle\frac{1}{2}\left(T^{xx} - 2T^{\perp\perp}\right)\rangle$. Generically, whenever a incompressible material is squeezed between two surfaces by applying normal stresses, it will tend to expand along the directions parallel to these surfaces (e.g. normal radial squeezing on a cylinder is expected to lengthen its shape on the vertical direction).

In our setup, a positive strain difference $(\Phi_3)_0^b \sim \left(h_{xx} - \frac{1}{2}\left(h_{yy} + h_{zz}\right)\right)_0^b$,[6] corresponds to a deformation that enlarges a direction $\vec{n}$, which results in the formation of a squeezing normal stress in the perpendicular direction to $\vec{n}$, which translates into a positive $\langle T_{xx} - 2T_{\perp\perp}\rangle$. Therefore, one expects to have a positive coefficient λ. An experimental consequence of this behavior of the coefficient would be that, if the fluid is inside a recipient and a spinning rod is placed in it, the fluid would be expelled outwards more noticeably in the superfluid phase, climbing up the walls of the recipient.

5 Conclusion

We have considered a holographic p-wave superfluid within SU(2) Einstein-Yang-Mills theory, in which the formation of the condensate spontaneously breaks the rotation symmetry, selecting a preferred direction x and keeping transverse isotropy in the y, z-plane. This

---

[6] Note that we do not differentiate between h_{yy} and h_{zz}, since both are related via the SO(2) symmetry. Therefore, we get $\frac{1}{2}\left(h_{yy} + h_{zz}\right) = h_{\perp\perp}$.

remaining SO(2) symmetry group allows us to classify the perturbations about equilibrium according to their transformation properties, into three different helicity sectors. In this paper we have focused on the helicity zero states and studied their transport properties. Due to $\mathbb{Z}_2$ parity, the helicity zero sector splits into two blocks. In the first block, we obtain the thermoelectric conductivity in the direction parallel to the condensate, whereas the second block allows us to study the piezoelectric effect and transport properties related to the normal stress difference. These are interesting new phenomena which are due to the anisotropy in our system.

We see that the thermoelectric conductivity displays some differences with respect to the transverse case (i. e. the helicity one fluctuations), despite being qualitatively similar. In particular, the temperature suppression in the broken phase is much lighter in the presented longitudinal case for temperatures above around $0.5T_c$. For temperatures below the temperature suppression of the real part a finite small frequencies increases dramatically and we see a pole at $\omega = 0$. This is due to a quasinormal mode traveling up the imaginary axis of the complex frequency plane. At around $0.5T_c$ this mode arrives at the origin and stays there.

On the other hand, in the parity even block we find a behavior reminiscent of the piezoelectric effect. Furthermore we see bumps in the correlators of this sector, which seem to be related to the generation of bound states.

In the zero frequency limit, we find a non-zero value for the two-point function of the diagonal metric fluctuations, which is related by a Kubo formula to a component of the viscosity tensor, denoted by λ. Since λ has the same dimensions as a shear viscosity we investigate its behavior by taking its ratio with respect to the entropy density s. We find that in the broken case λ/s is temperature dependent, whereas in the unbroken phase it turns into the isotropic shear viscosity $\eta/s = 1/(4\pi)$ for all temperatures $T > T_c$. The ratio λ/s does not fall below the $1/(4\pi)$ for all temperatures and all values of the backreaction parameter α. The physical interpretation of this coefficient is the effect that an anisotropic strain has over the normal stress difference, $\frac{1}{2}\langle T_{xx} - 2T_{\perp\perp}\rangle$.

We have determined the coefficients associated to these effects for generic values of the frequency and the temperature. Our results are valid as an effective description of the transport properties near the critical temperature T_c, where scale invariance is approached and simple models of AdS/CFT can be applied.

For further progress, a detailed analysis of the hydrodynamics of anisotropic superfluids is desirable to give a further interpretation to our study. In addition, it would be interesting to perform an analysis at finite spatial momentum, which would allow us to investigate the dispersion relations of the normalizable modes [49] and to check if there are instabilities similar to the ones found in [50, 51].

Acknowledgments

We are grateful to Patrick Kerner and Amos Yarom for discussions. DF acknowledges financial support from 2009-SGR-168, MEC FPA2010-20807-C02-01, MEC FPA2010-20807-C02-02, CPAN CSD2007-00042 Consolider-Ingenio 2010, and ERC StG 306605 HoloLHC.

DF is thankful to D. Mateos, J. Casalderrey-Solana, A. Buchel, C. Manuel, J. M. Pons, J. Tarrío and M.A. Valle for discussions, as well as to the Max Planck Institute for Physics in Munich and to Perimeter Institute for Theoretical Physics for hospitality during the initial and final stages of this work, respectively. This work was supported in part by *The Cluster of Excellence for Fundamental Physics - Origin and Structure of the Universe*.

A Holographic renormalization

The boundary part S_{ct} of the action (2.1) does not have any influence on the equations of motion, but it must ensure that the action is finite on-shell. It includes the Gibbons-Hawking boundary term and some additional terms that will constitute the counterterm action S_{ct}, needed to cancel out any divergences that may appear. Thus, the full action is written as

$$S = \frac{1}{2\kappa_5^2} \int \mathrm{d}^5x \sqrt{-g} \left[R - \Lambda - \frac{\alpha^2}{2} F^a_{MN} F^{aMN} \right] + \frac{1}{\kappa_5^2} \int \mathrm{d}^4x \sqrt{-\gamma}\, K + S_{ct}, \tag{A.1}$$

where K is the trace of the extrinsic curvature.

We will follow the lead of the references [52, 53] to perform the holographic renormalization and obtain the counterterm action.

A.1 Asymptotic behavior

In this section we look at the behavior of the fluctuation fields $\{F(r)\}$ at the horizon and at the boundary. Eventually we will want to calculate real-time retarded Green's functions [44, 54], therefore at the horizon, besides regularity,[7] we have to fulfill the incoming boundary condition. For this purpose the ansatz we plug in for the behavior of the fields near the horizon is

$$F(r)\big|_{r\to r_H} = \epsilon_h^\beta \sum_{i\geq 0} F_i^h \epsilon_h^i \,, \tag{A.2}$$

where $\epsilon_h = r/r_h - 1$, into the equations of motion of the fluctuation fields. It turns out that, as expected, we obtain two possibilities for β, namely

$$\beta = \pm \mathrm{i} \frac{\omega}{4\pi T}, \tag{A.3}$$

with T being the temperature defined in equation (2.11). As said before, we choose the solution with the "$-$" sign which corresponds to the incoming boundary condition. The other solution represents the outgoing boundary condition.

On the other hand, our ansatz at the boundary is similar to the one used for the background calculation in section 2. However, here we have to add a logarithmic term to get a consistent solution (c.f. [52]). Therefore we use

$$F(r)\big|_{r\to r_{\mathrm{bdy}}} = \sum_{i\geq 0} \left(F_i^b + \frac{1}{2} \hat{F}_i^b \ln \epsilon_b \right) \epsilon_b^i \,, \tag{A.4}$$

where $\epsilon_b = (r_h/r)^2$ is the expansion parameter.

---

[7] The condition $\phi(r_H) = 0$ at the horizon guarantees regularity. Even with all fluctuations switched on, there is no need for any further constraint.

Let us now use the above expansions for the helicity zero states (the expressions for the helicity one and two states can be found in [19]). In this case, the equations of motion for the fluctuation fields can be distributed into two blocks. In the first block, we have 5 independent expansion coefficients at the boundary (8 free parameters from the 4 second order differential equations minus 3 free parameters due to the constraints). We choose them to be $\left(\xi_{tx}\right)_0^b$, $\left(a_t^1\right)_0^b$, $\left(a_t^2\right)_0^b$, $\left(a_x^3\right)_0^b$ and $\left(a_x^3\right)_1^b$. At the horizon, we already halved the independent parameters by choosing the incoming boundary condition. From the remaining 4 parameters, we can get rid of 3 by using the constraint equations. Therefore, we are left with just one free parameter at the horizon.

We can perform similar considerations for the second block. Here we have also 3 constraints, but we are dealing with 6 fields, each with its corresponding second order differential equation. Therefore at the boundary we have $12-3=9$ independent parameters, namely $\left(\xi_y\right)_0^b$, $\left(\xi_x\right)_0^b$, $\left(\xi_t\right)_0^b$, $\left(a_x^1\right)_0^b$, $\left(a_x^2\right)_0^b$, $\left(a_t^3\right)_0^b$, $\left(a_x^1\right)_1^b$, $\left(a_x^2\right)_1^b$ and $\left(\xi_y\right)_2^b$. At the horizon, as before, we already fixed 6 free parameters by choosing the incoming boundary condition. There are $6-3=3$ free parameters that give a fully determined system.

Now we will state the first few non-vanishing terms of the expansion at the boundary of the different fields, because we will need them later on to determine divergences in the on-shell action and to calculate the Green's functions. The explicit form of these expansions is

$$\begin{aligned}
\xi_y &= \left(\xi_y\right)_0^b + \omega^2 \frac{\left(\xi_y\right)_0^b - \left(\xi_x\right)_0^b}{12}\epsilon_b + \left(\left(\xi_y\right)_2^b - \frac{1}{96}\omega^4 \left[\left(\xi_y\right)_0^b - \left(\xi_x\right)_0^b \right] \log\epsilon_b \right) \epsilon_b^2 + \mathcal{O}(\epsilon_b^3)\,,\\
\xi_x &= \left(\xi_x\right)_0^b + \omega^2 \frac{\left(\xi_x\right)_0^b - \left(\xi_y\right)_0^b}{6}\epsilon_b + \left(\ldots - \frac{1}{48}\omega^4 \left[\left(\xi_x\right)_0^b - \left(\xi_y\right)_0^b \right] \log\epsilon_b \right) \epsilon_b^2 + \mathcal{O}(\epsilon_b^3)\,,\\
\xi^t &= \left(\xi_t\right)_0^b + \omega^2 \frac{2\left(\xi_y\right)_0^b + \left(\xi_x\right)_0^b}{6}\epsilon_b + \mathcal{O}(\epsilon_b^2)\,,\\
a_x^1 &= \left(a_x^1\right)_0^b + \left(\left(a_x^1\right)_1^b - \frac{1}{4}\left[\left(\mu^2+\omega^2\right)\left(a_x^1\right)_0^b - 2\mathrm{i}\mu\omega\left(a_x^2\right)_0^b \right] \log\epsilon_b \right)\epsilon_b + \mathcal{O}(\epsilon_b^2)\,,\\
a_x^2 &= \left(a_x^2\right)_0^b + \left(\left(a_x^2\right)_1^b - \frac{1}{4}\left[\left(\mu^2+\omega^2\right)\left(a_x^2\right)_0^b + 2\mathrm{i}\mu\omega\left(a_x^1\right)_0^b \right] \log\epsilon_b \right)\epsilon_b + \mathcal{O}(\epsilon_b^2)\,,\\
a_t^3 &= \left(a_t^3\right)_0^b + \left(-\frac{\mathrm{i}}{\omega}\left(a_x^2\right)_0^b w_1^b - \frac{1}{2}\left[2\left(\xi_y\right)_0^b + \left(\xi_x\right)_0^b - \left(\xi_t\right)_0^b \right]\phi_1^b \right)\epsilon_b + \mathcal{O}(\epsilon_b^2)\,;
\end{aligned} \tag{A.5}$$

for the fields of the second block, and

$$\begin{aligned}
a_t^1 &= \left(a_t^1\right)_0^b + \frac{\left[\omega^2\left(\xi_{tx}\right)_0^b - \left(a_x^3\right)_0^b\mu - \left(\xi_{tx}\right)_0^b\mu^2\right]w_1^b - \left[\left(a_t^1\right)_0^b\mu + \mathrm{i}\omega\left(a_t^2\right)_0^b\right]\phi_1^b}{\omega^2-\mu^2}\epsilon_b + \mathcal{O}(\epsilon_b^2)\,,\\
a_t^2 &= \left(a_t^2\right)_0^b + \frac{-\mathrm{i}\omega\left(a_x^3\right)_0^b w_1^b + \left[\left(a_t^2\right)_0^b\mu - \mathrm{i}\omega\left(a_t^1\right)_0^b\right]\phi_1^b}{\mu^2-\omega^2}\epsilon_b + \frac{\mathrm{i}\omega\left(a_x^3\right)_0^b w_1^b}{8}\epsilon_b^2 + \mathcal{O}(\epsilon_b^3)\,,\\
a_x^3 &= \left(a_x^3\right)_0^b + \left(\left(a_x^3\right)_1^b - \frac{1}{4}\omega^2\left(a_x^3\right)_0^b\log\epsilon_b \right)\epsilon_b + \mathcal{O}(\epsilon_b^2)\,,\\
\xi_{tx} &= \left(\xi_{tx}\right)_0^b - \alpha^2\left(a_x^3\right)_0^b\phi_1^b\epsilon_b + \mathcal{O}(\epsilon_b^3)\,;
\end{aligned} \tag{A.6}$$

for the first block. Note that $\mu \equiv \phi_0^b$, ϕ_1^b and w_1^b are the expansion coefficients of $\phi(r)$ and $w(r)$ at the boundary.

We do not state the expansions at the horizon, since the explicit form is quite lengthy and does not provide additional information to equation (A.2).

A.2 Counterterms

By plugging the expansions (A.6) into (3.7) and (3.17), we obtain the non-renormalized on-shell action, $S_{\text{on-shell}} = \frac{1}{\kappa_5^2}\int \frac{\mathrm{d}^4k}{(2\pi)^4}\,\mathcal{L}_{r_b}$, where the integrand $\mathcal{L}_{r_b}$ is written in terms of the free parameters of the previous expansions as

$$\begin{aligned}
\frac{\mathcal{L}_{r_b}}{r_h^4} &= \frac{\alpha^2\mu\phi_1^b}{\omega^2-\mu^2}\left(a_t^1\right)_0^{b\,2} + \frac{\alpha^2\mu\phi_1^b}{\omega^2-\mu^2}\left(a_t^2\right)_0^{b\,2} - \frac{\alpha^2\omega^2}{4}\left(1+\log\epsilon_b\right)\left(a_x^3\right)_0^{b\,2} \\
&+ \left(\frac{3}{2\epsilon_b^2} - 6f_2^b\right)\left(\xi_{tx}\right)_0^{b\,2} + \frac{2i\alpha^2\omega\phi_1^b}{\omega^2-\mu^2}\left(a_t^1\right)_0^b\left(a_t^2\right)_0^b + \frac{\alpha^2\mu w_1^b}{\omega^2-\mu^2}\left(a_t^1\right)_0^b\left(a_x^3\right)_0^b \\
&- \frac{i\alpha^2\omega w_1^b}{\omega^2-\mu^2}\left(a_t^2\right)_0^b\left(a_x^3\right)_0^b + \alpha^2\left(a_x^3\right)_0^b\left(a_x^3\right)_1^b - \alpha^2\phi_1^b\left(a_x^3\right)_0^b\left(\xi_{tx}\right)_0^b \\
&+ \left(-\frac{3}{8\epsilon_b^2} - \frac{\omega^2}{8\epsilon_b} - \frac{7\omega^4}{192} - f_2^b + \frac{5m_0^b}{4} + \frac{\omega^4}{48}\log\epsilon_b\right)\left(\xi_x\right)_0^{b\,2} + \left(-\frac{3}{8\epsilon_b^2} + \frac{3m_0^b}{4}\right)\left(\xi_t\right)_0^{b\,2} \\
&+ \left(\frac{\omega^2}{8\epsilon_b} - \frac{13\omega^4}{192} + \frac{\omega^4}{48}\log\epsilon_b\right)\left(\xi_y\right)_0^{b\,2} - \frac{\alpha^2\left(\mu^2+\omega^2\right)}{4}\left(1+\log\epsilon_b\right)\left[\left(a_x^1\right)_0^{b\,2} + \left(a_x^2\right)_0^{b\,2}\right] \\
&+ 2\left(\xi_y\right)_2^b\left[\left(\xi_x\right)_0^b - \left(\xi_y\right)_0^b\right] + \left(\frac{3}{2\epsilon_b^2} + \frac{3\omega^2}{4\epsilon_b} + \frac{\omega^4}{96} + f_2^b + m_0^b - \frac{\omega^4}{24}\log\epsilon_b\right)\left(\xi_y\right)_0^b\left(\xi_x\right)_0^b \\
&+ \left(\frac{3}{2\epsilon_b^2} - \frac{\omega^2}{4\epsilon_b} - f_2^b - 4m_0^b\right)\left(\xi_y\right)_0^b\left(\xi_t\right)_0^b + \left(\frac{3}{4\epsilon_b^2} - \frac{\omega^2}{8\epsilon_b} + f_2^b - 2m_0^b\right)\left(\xi_x\right)_0^b\left(\xi_t\right)_0^b \\
&+ \frac{\alpha^2 w_1^b}{2}\left(a_x^1\right)_0^b\left[2\left(\xi_y\right)_0^b + \left(\xi_x\right)_0^b - \left(\xi_t\right)_0^b\right] - \frac{i\alpha^2\mu w_1^b}{\omega}\left(a_x^2\right)_0^b\left[\left(\xi_x\right)_0^b - \left(\xi_t\right)_0^b\right] \\
&+ \alpha^2\left(a_x^1\right)_0^b\left(a_x^1\right)_1^b + \left(1 + i\alpha^2\mu\omega\log\epsilon_b\right)\left(a_x^1\right)_0^b\left(a_x^2\right)_0^b + \alpha^2\left(a_x^2\right)_0^b\left(a_x^2\right)_1^b \\
&- \frac{i\alpha^2 w_1^b}{\omega}\left(a_x^2\right)_0^b\left(a_t^3\right)_0^b\Bigg|_{r=r_{\text{bdy}}} . \qquad \text{(A.7)}
\end{aligned}$$

This is evaluated at the boundary, where $\epsilon_b = (r_h/r_{\text{bdy}})^2 = 0$, so any higher order terms vanish. And we have changed to momentum space, so that in each product of expansion parameters in this expression, the first one has always to be understood as evaluated on $-\omega$ and the second on ω, e.g. on the first term we have $\left(a_t^1\right)_0^b(-\omega)\left(a_t^1\right)_0^b(\omega)$. Therefore, note that the order in which they are multiplied matters.

The terms that have to be considered for the counterterms are the ones in (A.7) with explicit ϵ_b dependence, since those are the ones responsible for the divergences

$$\begin{aligned}
\frac{\mathcal{L}_{r_b}^{\text{Div}}}{r_h^4} &= \frac{1}{\epsilon_b^2}\left[\frac{3}{2}\left(\xi_{tx}\right)_0^{b\,2} + \frac{3}{8}\left(-\left(\xi_x\right)_0^{b\,2} - \left(\xi_t\right)_0^{b\,2} + 4\left(\xi_y\right)_0^b\left(\xi_x\right)_0^b + 4\left(\xi_y\right)_0^b\left(\xi_t\right)_0^b + 2\left(\xi_x\right)_0^b\left(\xi_t\right)_0^b\right)\right] \\
&\quad + \frac{1}{\epsilon_b}\frac{\omega^2}{8}\left[\left(\xi_y\right)_0^{b\,2} - \left(\xi_x\right)_0^{b\,2} + 6\left(\xi_y\right)_0^b\left(\xi_x\right)_0^b - 2\left(\xi_y\right)_0^b\left(\xi_t\right)_0^b - \left(\xi_x\right)_0^b\left(\xi_t\right)_0^b\right] \\
&\quad + \log\epsilon_b\left[-\frac{\alpha^2\omega^2}{4}\left(a_x^3\right)_0^{b\,2} + \frac{\omega^4}{48}\left(\left(\xi_y\right)_0^{b\,2} + \left(\xi_x\right)_0^{b\,2} - 2\left(\xi_y\right)_0^b\left(\xi_x\right)_0^b\right)\right. \\
&\qquad\qquad \left. - \frac{\alpha^2\left(\mu^2-\omega^2\right)}{4}\left(\left(a_x^1\right)_0^{b\,2} + \left(a_x^2\right)_0^{b\,2}\right) + \mathrm{i}\alpha^2\mu\omega\left(a_x^1\right)_0^b\left(a_x^2\right)_0^b\right] . \qquad \text{(A.8)}
\end{aligned}$$

For the construction of the counterterms, first we need to define the induced metric $\gamma_{\mu\nu}$ on the $r = r_{\text{bdy}}$ plane,

$$\gamma_{\mu\nu} = \frac{\partial x^M}{\partial \tilde{x}^\mu} \frac{\partial x^N}{\partial \tilde{x}^\nu} g_{MN}(r) \bigg|_{r=r_{\text{bdy}}} , \tag{A.9}$$

resulting in

$$\mathrm{d}s^2_{r_{\text{bdy}}} = -N(r_{\text{bdy}})\sigma(r_{\text{bdy}})^2 \mathrm{d}t^2 + \frac{r^2_{\text{bdy}}}{f(r_{\text{bdy}})^4} \mathrm{d}x^2 + r^2_{\text{bdy}} f(r_{\text{bdy}})^2 (\mathrm{d}y^2 + \mathrm{d}z^2). \tag{A.10}$$

Note that the expansion of the determinant of the induced metric for $r \gg 1$ is divergent and is given by

$$\begin{aligned}
\sqrt{-\gamma}\bigg|_{r\gg 1} = r^4 \bigg[\frac{1}{2} (\xi_{tx})^{b\,2}_0 - \frac{1}{8} \Big((\xi_x)^{b\,2}_0 + (\xi_t)^{b\,2}_0 - 4\,(\xi_y)^b_0\,(\xi_x)^b_0 \\
- 4\,(\xi_y)^b_0\,(\xi_t)^b_0 - 2\,(\xi_x)^b_0\,(\xi_t)^b_0 \Big) \bigg] \\
+ \frac{\omega^2 r^2}{24} \Big[2(\xi_y)^{b\,2}_0 - (\xi_x)^{b\,2}_0 + 8\,(\xi_y)^b_0\,(\xi_x)^b_0 - 2\,(\xi_y)^b_0\,(\xi_t)^b_0 - (\xi_x)^b_0\,(\xi_t)^b_0 \Big] \\
+ \frac{\omega^4}{48} \log\frac{1}{r} \Big[(\xi_y)^{b\,2}_0 + (\xi_x)^{b\,2}_0 - 2\,(\xi_y)^b_0\,(\xi_x)^b_0 \Big] \\
+ (\xi_y)^b_2 \Big((\xi_x)^b_0 - (\xi_y)^b_0 \Big) - \frac{\omega^4}{288} \Big(7(\xi_y)^{b\,2}_0 + 4(\xi_x)^{b\,2}_0 - 2\,(\xi_y)^b_0\,(\xi_x)^b_0 \Big) \\
- 2 f^b_2 (\xi_{tx})^{b\,2}_0 - f^b_2 \Big((\xi_x)^{b\,2}_0 - (\xi_y)^b_0\,(\xi_x)^b_0 + (\xi_y)^b_0\,(\xi_t)^b_0 - (\xi_x)^b_0\,(\xi_t)^b_0 \Big) \\
+ \frac{m^b_0}{2} (\xi_{tx})^{b\,2}_0 + \frac{m^b_0}{8} \Big(5(\xi_x)^{b\,2}_0 + (\xi_t)^{b\,2}_0 + 4\,(\xi_y)^b_0\,(\xi_x)^b_0 \\
- 12\,(\xi_y)^b_0\,(\xi_t)^b_0 - 6\,(\xi_x)^b_0\,(\xi_t)^b_0 \Big) \\
- \alpha^2 \phi^b_1 \left(a^3_x\right)^b_0 (\xi_{tx})^b_0 + \frac{\alpha^2 w^b_1}{2} \Big((\xi_x)^b_0 - (\xi_t)^b_0 \Big) \left(\left(a^1_x\right)^b_0 - \frac{\mathrm{i}\mu}{\omega} \left(a^2_x\right)^b_0 \right) .
\end{aligned} \tag{A.11}$$

We will use these divergences to cancel out the ones we find in the non-renormalized action, together with other counterterms that have to be considered. It is not necessary to rigorously derive the covariant counterterms here in this work. By looking at the ones that B. Sahoo and H.-U. Yee calculated in [53], we get an idea of how they should look like; namely, some combinations of $R[\gamma]$, $R_{\mu\nu}[\gamma]$ and $F^a_{\mu\nu}$ (i.e. the Ricci scalar and Ricci tensor on the induced surface, and the field strength tensor on that surface). Possible covariant combinations of the three terms are $\sqrt{-\gamma}$, $\sqrt{-\gamma}R[\gamma]$, $\sqrt{-\gamma}R[\gamma]^2$, $\sqrt{-\gamma}R^{\mu\nu}[\gamma]R_{\mu\nu}[\gamma]$ and $\sqrt{-\gamma}F^a_{\mu\nu}F^{a\mu\nu}$. The coefficients in front of them can be guessed by requiring the divergences to vanish in the complete action. Their expansions for $r \gg 1$ are

$$\begin{aligned}
\sqrt{-\gamma}R[\gamma]\Big|_{r\gg 1} &= -\frac{r^2\omega^2}{2}\left[(\xi_y)_0^{b\,2} + 2\,(\xi_y)_0^b\,(\xi_x)_0^b\right] \\
&\quad + \frac{\omega^4}{12}\left((\xi_y)_0^{b\,2} + (\xi_x)_0^{b\,2} - 2\,(\xi_y)_0^b\,(\xi_x)_0^b\right)\,, \\
\sqrt{-\gamma}R[\gamma]^2\Big|_{r\gg 1} &= \omega^4\left(4(\xi_y)_0^{b\,2} + (\xi_x)_0^{b\,2} + 4\,(\xi_y)_0^b\,(\xi_x)_0^b\right)\,, \\
\sqrt{-\gamma}R^{\mu\nu}[\gamma]R_{\mu\nu}[\gamma]\Big|_{r\gg 1} &= \frac{\omega^4}{2}\left(3(\xi_y)_0^{b\,2} + (\xi_x)_0^{b\,2} + 2\,(\xi_y)_0^b\,(\xi_x)_0^b\right)\,, \\
\sqrt{-\gamma}F^a_{\mu\nu}F^{a\mu\nu}\Big|_{r\gg 1} &= -2\omega^2\left(a_x^3\right)_0^{b\,2} - 2\left(\mu^2+\omega^2\right)\left(\left(a_x^1\right)_0^{b\,2} + \left(a_x^2\right)_0^{b\,2}\right) \\
&\quad + 8\mathrm{i}\mu\omega\left(a_x^1\right)_0^b\left(a_x^2\right)_0^b\,.
\end{aligned} \tag{A.12}$$

It can be checked that by adding the real space action

$$\begin{aligned}
S_{\mathrm{ct}} = -\frac{1}{\kappa_5^2}\int \mathrm{d}^4x\,\sqrt{-\gamma}\,\Bigg(3 + \frac{1}{4}R[\gamma] \\
+ \left[\frac{1}{48}R[\gamma]^2 - \frac{1}{16}R^{\mu\nu}[\gamma]R_{\mu\nu}[\gamma] + \frac{\alpha^2}{8}F^a_{\mu\nu}F^{a\mu\nu}\right]\log\epsilon_b\Bigg)\Bigg|_{r=r_{\mathrm{bdy}}}
\end{aligned} \tag{A.13}$$

to the action $S_{\text{on-shell}}$ (2.1) we get a divergence-free theory (up to second order in the fluctuations) for $r_{\mathrm{bdy}} \gg 1$, i.e. also the real time Green's functions are divergence-free. The renormalized $r_{\mathrm{bdy}} \gg 1$ on-shell action of the helicity 0 modes are

$$\begin{aligned}
S^{\text{on-shell}}_{\text{hel.0, bl.1}} = \frac{r_h^4}{\kappa_5^2}\int\frac{\mathrm{d}^4k}{(2\pi)^4}\Bigg\{&\frac{\alpha^2\mu\phi_1^b}{\omega^2-\mu^2}\left(a_t^1\right)_0^{b\,2} + \frac{\alpha^2\mu\phi_1^b}{\omega^2-\mu^2}\left(a_t^2\right)_0^{b\,2} - \frac{\alpha^2\omega^2}{4}\left(a_x^3\right)_0^{b\,2} \\
&- \frac{3}{2}m_0^b(\xi_{tx})_0^{b\,2} + \frac{2\mathrm{i}\alpha^2\omega\phi_1^b}{\omega^2-\mu^2}\left(a_t^1\right)_0^b\left(a_t^2\right)_0^b + \frac{\alpha^2\mu w_1^b}{\omega^2-\mu^2}\left(a_t^1\right)_0^b\left(a_x^3\right)_0^b \\
&- \frac{\mathrm{i}\alpha^2\omega w_1^b}{\omega^2-\mu^2}\left(a_t^2\right)_0^b\left(a_x^3\right)_0^b + \alpha^2\left(a_x^3\right)_0^b\left(a_x^3\right)_1^b + 2\alpha^2\phi_1^b\left(a_x^3\right)_0^b(\xi_{tx})_0^b\Bigg\}
\end{aligned} \tag{A.14}$$

and

$$\begin{aligned}
S^{\text{on-shell}}_{\text{hel.0, bl.2}} = \frac{r_h^4}{\kappa_5^2}\int\frac{\mathrm{d}^4k}{(2\pi)^4}\Bigg\{&-\frac{\omega^4}{64}(\xi_y)_0^{b\,2} - \left(\frac{\omega^4}{64} - 2f_2^b + \frac{5m_0^b}{8}\right)(\xi_x)_0^{b\,2} + \frac{3m_0^b}{8}(\xi_t)_0^{b\,2} \\
&+ \left(\frac{\omega^4}{32} - 2f_2^b - \frac{m_0^b}{2}\right)(\xi_y)_0^b\,(\xi_x)_0^b + \left(2f_2^b + \frac{m_0^b}{2}\right)(\xi_y)_0^b\,(\xi_t)_0^b \\
&- \left(2f_2^b - \frac{m_0^b}{4}\right)(\xi_x)_0^b\,(\xi_t)_0^b + (\xi_y)_2^b\left[(\xi_y)_0^b - (\xi_x)_0^b\right] \\
&- \frac{\alpha^2\left(\mu^2+\omega^2\right)}{4}\left[\left(a_x^1\right)_0^{b\,2} + \left(a_x^2\right)_0^{b\,2}\right] + \mathrm{i}\alpha^2\mu\omega\left(a_x^1\right)_0^b\left(a_x^2\right)_0^b \\
&- \frac{\mathrm{i}\alpha^2 w_1^b}{\omega}\left(a_x^2\right)_0^b\left(a_t^3\right)_0^b + \alpha^2\left[\left(a_x^1\right)_0^b\left(a_x^1\right)_1^b + \left(a_x^2\right)_0^b\left(a_x^2\right)_1^b\right] \\
&+\alpha^2 w_1^b\left(a_x^1\right)_0^b\left[(\xi_y)_0^b - (\xi_x)_0^b + (\xi_t)_0^b\right] + \frac{\mathrm{i}\alpha^2\mu w_1^b}{2\omega}\left(a_x^2\right)_0^b\left[(\xi_x)_0^b - (\xi_t)_0^b\right]\Bigg\}\,.
\end{aligned} \tag{A.15}$$

Since we have 6 fields determined by second order differential equations and 3 constraints, we end up with $12-3=9$ undetermined coefficients of the boundary expansion, in terms of which the expression above is written. They are

$$\left\{\left(a_t^3\right)_0^b, \left(a_x^2\right)_0^b, \left(a_x^2\right)_1^b, \left(a_x^1\right)_0^b, \left(a_x^1\right)_1^b, \left(\xi_t\right)_0^b, \left(\xi_y\right)_0^b, \left(\xi_y\right)_2^b, \left(\xi_x\right)_0^b\right\} . \tag{A.16}$$

B Constructing the gauge invariant fields

The gauge group of the SU(2) Einstein-Yang-Mills theory can be a subject of formal studies, as outlined in [55]. It is shown that diffeomorphism-induced transformations of the metric functions and pure Yang-Mills transformations of the Yang-Mills fields ought not to be considered separately. On general grounds, we must look for the most general combination, which can be written as

$$\begin{aligned}
\delta\mathcal{N} &= \partial_t\Sigma^t + \Sigma^i\partial_i\mathcal{N} - \mathcal{N}^i\partial_i\Sigma^t,\\
\delta N^i &= \partial_t\Sigma^i - \mathcal{N}\partial^i\Sigma^t + \Sigma^t\partial^i\mathcal{N} + \Sigma^j\partial_j\mathcal{N}^i - \mathcal{N}^j\partial_j\Sigma^i,\\
\delta g_{ij} &= \frac{\Sigma^t}{\mathcal{N}}\partial_t g_{ij} + \left(\Sigma^k - \frac{\Sigma^t\mathcal{N}^k}{\mathcal{N}}\right)\partial_k g_{ij} + 2g_{k(i}\partial_{j)}\Sigma^k - 2\frac{\Sigma^t g_{k(i}\partial_{j)}\mathcal{N}^k}{\mathcal{N}},\\
\delta A_t^a &= A_i^a\partial_t\Sigma^i + \Sigma^i\partial_i A_t^a + F_{ti}^a\frac{\Sigma^t\mathcal{N}^i}{\mathcal{N}} + \partial_t\Lambda^a + \epsilon^{abc}\Lambda^b A_t^c,\\
\delta A_i^a &= F_{ti}^a\frac{\Sigma^t}{\mathcal{N}} + F_{ij}^a\frac{\Sigma^t\mathcal{N}^j}{\mathcal{N}} + A_j^a\partial_i\Sigma^j + \Sigma^j\partial_j A_i^a + \partial_i\Lambda^a + \epsilon^{abc}\Lambda^b A_i^c\,;
\end{aligned} \tag{B.1}$$

where the $i, j, \ldots$ indices denote the spatial coordinates $\{x, y, z, r\}$ of our spacetime. The metric g_{ij} is the spatial metric and g^{ij} is its inverse, and the functions $\mathcal{N}$ and $\mathcal{N}^i$ (called lapse and shift vector respectively) are defined as

$$\mathrm{d}s^2 = g_{MN}\mathrm{d}x^M\mathrm{d}x^N = -\mathcal{N}^2\mathrm{d}t^2 + g_{ij}(\mathrm{d}x^i + \mathcal{N}^i\mathrm{d}t)(\mathrm{d}x^j + \mathcal{N}^j\mathrm{d}t). \tag{B.2}$$

A general infinitesimal gauge transformation acting on a perturbed solution is given in terms of the 8 descriptors $\{\Sigma^M, \Lambda^a\}$. We define

$$\begin{aligned}
\hat{g}_{MN} &= g_{MN} + h_{MN},\\
\hat{A}_M^a &= A_M^a + a_M^a.
\end{aligned} \tag{B.3}$$

where g_{MN} and A_M^a are the background fields of the hairy black hole solution that is considered in section 2. This part of the fields is therefore fixed, and the fluctuations h_{MN} and a_M^a are our dynamical variables. Thus, for instance the variation of the fluctuation field defined as $\xi_t = g^{tt}h_{tt}$ is given by $\delta\xi_t = g^{tt}\delta h_{tt} = g^{tt}\delta\hat{g}_{tt}$.

Furthermore, since they are considered as perturbations, they will be of the same order as the parameters Σ^M and Λ^a. This allows us to give simple expressions to their variations, which will be approximated to lowest order.

B.1 Residual gauge transformations

In section 3.1, we decided to choose a gauge where $a_r^a \equiv 0$ and $h_{Mr} \equiv 0$. This kind of gauge fixing is allowed as long as, for any given configuration, there exists a gauge transformation such that it makes these components vanish. Since there are 8 functions that categorize each possible transformation, in principle this is feasible. Here we will see that this is justified, however the gauge is not completely fixed by these choices.

We begin by defining the background metric, which corresponds to the ansatz use in section 2, so it is of the form

$$\mathrm{d}s^2 = g_{MN}\mathrm{d}x^M\mathrm{d}y^N = -c_1(r)^2\mathrm{d}t^2 + c_2(r)^2\mathrm{d}x^2 + c_3(r)^2(\mathrm{d}y^2+\mathrm{d}z^2) + c_4(r)^2\mathrm{d}r^2, \tag{B.4}$$

the only non-zero components of the background Yang-Mills field are $A_t^3 = \phi(r)$ and $A_x^1 = w(r)$, and we will be working in momentum space, i.e.

$$\begin{aligned}\Sigma^M(t,x,r) &= \int \mathrm{d}^4x\ \mathrm{e}^{ik_\mu x^\mu}\Sigma^M(\omega,k,r),\\ \Lambda^a(t,x,r) &= \int \mathrm{d}^4x\ \mathrm{e}^{ik_\mu x^\mu}\Lambda^a(\omega,k,r),\end{aligned} \tag{B.5}$$

where $k^\mu = (\omega,k,0,0)$, since in the case we are studying the rotational symmetry SO(2) is preserved so that the fluctuations can be classified.

With these assumptions, we look at the variations of the h_{Mr} components of the metric and the a_r^a components of the Yang-Mills field, under an infinitesimal gauge transformation (B.1) acting on a perturbed background solution. To first order, these are

$$\delta h_{tr} = -i\omega {c_4}^2\Sigma^r + {c_1}'\Sigma^t - c_1\partial_r\Sigma^t, \tag{B.6a}$$

$$\delta h_{xr} = ik{c_4}^2\Sigma^r + {c_2}^2\partial_r\Sigma^x, \tag{B.6b}$$

$$\delta h_{yr} = {c_3}^2\partial_r\Sigma^y, \tag{B.6c}$$

$$\delta h_{zr} = {c_3}^2\partial_r\Sigma^z, \tag{B.6d}$$

$$\delta h_{rr} = 2c_4\left({c_4}'\Sigma^r + c_4\partial_r\Sigma^r\right), \tag{B.6e}$$

$$\delta a_r^1 = w\partial_r\Sigma^x + \partial_r\Lambda^1, \tag{B.6f}$$

$$\delta a_r^2 = \partial_r\Lambda^2, \tag{B.6g}$$

$$\delta a_r^3 = -\frac{\Sigma^t}{c_1}\partial_r\phi + \partial_r\Lambda^3. \tag{B.6h}$$

It is easy to convince oneself that by choosing carefully the Σ_M and Λ^a functions, one could make the h_{Mr} and a_r^a vanish. Now the residual gauge freedom would correspond to any further transformation that, while keeping these components null, changes the rest of the dynamical variables. We will find the most general form of a residual gauge transformation.

The solutions to $\delta h_{Mr}=0, \delta a_r^a=0$ can be written in terms of 8 constants $\{K_M, \Lambda_0^a\}$ as

$$\begin{aligned}
&\Sigma^t(\omega,k,r) = -K_t c_1 - i\omega K_r c_1 A, \quad \text{with } A=\int \mathrm{d}r \frac{c_4}{{c_1}^2};\\
&\Sigma^x(\omega,k,r) = K_x - ikK_r B, \quad \text{with } B=\int \mathrm{d}r \frac{c_4}{{c_2}^2};\\
&\Sigma^y(\omega,k,r) = K_y,\\
&\Sigma^z(\omega,k,r) = K_z,\\
&\Sigma^r(\omega,k,r) = \frac{K_r}{c_4},\\
&\Lambda^1(\omega,k,r) = ikK_r C_w + \Lambda_0^1, \quad \text{with } C_w=\int \mathrm{d}r \frac{c_4 w}{{c_2}^2};\\
&\Lambda^2(\omega,k,r) = \Lambda_0^2,\\
&\Lambda^3(\omega,k,r) = -K_t\phi - i\omega K_r\left(\phi A - C_\phi\right) + \Lambda_0^3, \quad \text{with } C_\phi=\int \mathrm{d}r \frac{c_4\phi}{{c_1}^2}.
\end{aligned} \tag{B.7}$$

The physics ought to be invariant under any gauge transformation. Therefore, those dynamical fields affected by these residual gauge transformations must be unphysical. Those linear combinations with the property of being invariant constitute the physical fields.

B.2 The physical fields

The helicity two fluctuations, $\Xi = g^{yy}h_{yz}$ and $h_{yy}-h_{zz}$ are already invariant, that is,

$$\begin{aligned}
\delta\Xi = g^{yy}\delta h_{yz} &= 0,\\
\delta(h_{yy}-h_{zz}) &= 0;
\end{aligned} \tag{B.8}$$

therefore they are already physical modes. The helicity one fluctuations transform as

$$\begin{aligned}
\delta h_{xy} &= \mathrm{i}k{c_3}^2 K_y,\\
\delta h_{ty} &= -\mathrm{i}\omega {c_3}^2 K_y,\\
\delta a_y^a &= 0;
\end{aligned} \tag{B.9}$$

so that the a_y^a are physical, and the invariant combination of the other two gives the physical mode $\Psi = g^{yy}(\omega h_{xy} + k h_{ty})$. Note that the same applies to the z components, which behave exactly the same as the y components.

Now, for the helicity zero fields[8] ξ_{tx}, ξ_t, ξ_x, ξ_y, a_x^a and a_t^a, we arrange any possible physical mode Φ as a linear combination of them given by some r-dependent coefficients τ_n, so that its invariance translates into

$$\delta\Phi = \sum_{a=1}^{3}(\tau_a \delta a_x^a + \tau_{3+a}\delta a_t^a) + \tau_7\delta\xi_{tx} + \tau_8\delta\xi_t + \tau_9\delta\xi_x + \tau_{10}\delta\xi_y = 0. \tag{B.10}$$

---

[8] Where we had defined $\xi_y = g^{yy}h_{yy}$, $\xi_x = g^{xx}h_{xx}$, $\xi_t = g^{tt}h_{tt}$ and $\xi_{tx} = g^{xx}h_{tx}$ in (3.4).

Each of the variations in this expression are given by

$$\begin{aligned}
\delta\xi_{tx} &= -\mathrm{i}\omega K_x + \mathrm{i}k\frac{{c_1}^2}{{c_2}^2}K_t - \omega k\left(B + \frac{{c_1}^2}{{c_2}^2}A\right)K_r,\\
\delta\xi_t &= 2\mathrm{i}\omega K_t + \left(\frac{2{c_1}'}{c_1c_4} - 2\omega^2 A\right)K_r,\\
\delta\xi_x &= 2\mathrm{i}kK_x + \left(\frac{2{c_2}'}{c_2c_4} + 2k^2 B\right)K_r,\\
\delta\xi_y &= \frac{2{c_3}'}{c_3c_4}K_r,\\
\delta a_x^1 &= \mathrm{i}k\Lambda_0^1 + \mathrm{i}kwK_x + \left(\frac{w'}{c_4} + k^2\left(wB - C_w\right)\right)K_r,\\
\delta a_t^1 &= -\mathrm{i}\omega\Lambda_0^1 - \phi\Lambda_0^2 - \mathrm{i}\omega wK_x - \omega k\left(wB - C_w\right)K_r,\\
\delta a_x^2 &= \mathrm{i}k\Lambda_0^2 - w\Lambda_0^3 - \mathrm{i}\omega wC_\phi K_r,\\
\delta a_t^2 &= -\mathrm{i}\omega\Lambda_0^2 + \phi\Lambda_0^1 + \mathrm{i}k\phi C_w K_r,\\
\delta a_x^3 &= \mathrm{i}k\Lambda_0^3 + w\Lambda_0^2 - \mathrm{i}k\phi K_t + \omega k\left(\phi A - C_\phi\right)K_r,\\
\delta a_t^3 &= -\mathrm{i}\omega\Lambda_0^3 + \mathrm{i}\omega\phi K_t + \left(\frac{\phi'}{c_4} - \omega^2\left(\phi A - C_\phi\right)\right)K_r.
\end{aligned} \tag{B.11}$$

Plugging everything into equation (B.10) results in 6 algebraic equations, due to the fact that the variation of the physical mode must vanish for any residual transformation, that is, for any K_t, K_x, K_r, Λ_0^1, Λ_0^2, Λ_0^3. Thus, we can solve for 6 of the τ_n coefficients in terms of the other four. The solution gives the most general gauge invariant combination and it turns out to be independent of the $\{A, B, C_w, C_\phi\}$ functions.

What we call the four physical fields, Φ_i (i: $1,\ldots,4$), are chosen as a set of independent fields that generate that invariant combination. There is more than one choice, but the one we have taken is

$$\begin{aligned}
\Phi_1 = a_x^1 &- \frac{\mathrm{i}k}{\phi}a_t^2 + \frac{k^2}{w\phi}a_t^3 + \frac{k\omega}{w\phi}a_x^3 + \frac{kw}{\omega}\xi_{tx} -\\
&- \frac{k^2 f^4 N w\sigma^2}{2r^2\omega^2}\xi_t + \frac{k^2 f^5 w^2\sigma\phi\left(\sigma N' + 2N\sigma'\right) - 2r^2\omega^2 f\left(w\phi w' + k^2\phi'\right)}{4r\omega^2 w\phi\left(f + rf'\right)}\xi_y,\\
\Phi_2 = a_x^2 &+ \frac{\mathrm{i}\left(-k^2 + w^2\right)}{\omega w}a_t^3 -\\
&- \frac{\mathrm{i}k}{w}a_x^3 - \frac{\mathrm{i}w\phi}{2\omega}\xi_t + \frac{\mathrm{i}rf\left(w^2\phi\left(\sigma N' + 2N\sigma'\right) + 2N\left(k^2 - w^2\right)\sigma\phi'\right)}{4\omega N w\sigma\left(f + rf'\right)}\xi_y,\\
\Phi_3 = \xi_x &+ \frac{2k}{\omega}\xi_{tx} - \frac{k^2 f^4 N\sigma^2}{r^2\omega^2}\xi_t + \frac{4r^2\omega^2 f' - 2r\omega^2 f + k^2 f^5\sigma\left(\sigma N' + 2N\sigma'\right)}{2r\omega^2\left(f + rf'\right)}\xi_y,\\
\Phi_4 = a_x^3 &+ \frac{k}{\omega}a_t^3 - \frac{w\phi}{\omega^2 - \phi^2}a_t^1 - \frac{\mathrm{i}\omega w}{\omega^2 - \phi^2}a_t^2 + \frac{w^2\phi}{\omega^2 - \phi^2}\xi_{tx} -\\
&- \frac{kf^4 N w^2\sigma^2\phi}{2r^2\omega\left(\omega^2 - \phi^2\right)}\xi_t + \frac{kf\left(f^4 w^2\sigma\phi\left(\sigma N' + 2N\sigma'\right) + 2r^2\left(-\omega^2 + \phi^2\right)\phi'\right)}{4r\omega\left(\omega^2 - \phi^2\right)\left(f + rf'\right)}\xi_y.
\end{aligned} \tag{B.12}$$

C Numerical evaluation of Green's functions

Here we review and generalize the algorithm to evaluate Green's functions in cases when there is operator mixing [45]. The starting point of the algorithm would be a general bilinear bulk action for some fields $\Phi_{\rm I}(x^\mu, r)$ given by

$$S = \int d^dx \; dr \left[\partial_\mu \Phi_{\rm I} \; \mathcal{A}_{\rm IJ}(x,r) \; \partial^\mu \Phi_{\rm J} + \Phi_{\rm I} \; \mathcal{B}^\mu_{\rm IJ}(x,r) \; \partial_\mu \Phi_{\rm J} + \Phi_{\rm I} \; \mathcal{C}_{\rm IJ}(x,r) \; \Phi_{\rm J}\right] \tag{C.1}$$

In principle, one could be considering a perturbed background solution, as in the problem discussed in this paper, and it may be possible that there is some gauge freedom associated with those perturbation fields. In our case, that would be given by the transformation (B.11). But of course, gauge symmetry implies that the only relevant fields are the gauge-invariant combinations of the perturbations (3.3). Therefore, the most sensible strategy would be to write the action in terms of these physical degrees of freedom $\Phi_{\rm I}$, and proceed from there.

C.1 Writing action in the correct basis

Even though the action is constituted as a gauge-invariant itself, it may not be possible to express it in terms of the physical fields only. It depends on the number of fluctuation fields and the extent of the gauge freedom. Let's say, for instance, that after whatever gauge fixing, the perturbed background is described by N fields $\varphi_i(x)$ and we are left with a residual gauge freedom parametrized by M constants. Then, the set of the possible gauge invariant linear combinations of $\varphi_i(x)$ is generated by $N-M$ independent physical fields $\Phi_{\rm I}(x)$. But the part of the action that is quadratic in perturbations may be of the form

$$S = \int d^dx \; dr \left[\partial_\mu \varphi_i \; a_{ij}(x,r) \; \partial^\mu \varphi_j + \varphi_i \; b^\mu_{ij}(x,r) \; \partial_\mu \varphi_j + \varphi_i \; c_{ij}(x,r) \; \varphi_j\right] , \tag{C.2}$$

with, assuming for simplicity dependence on r only, $(2N+1)N$ coefficients $\{a_{ij}, b_{ij}, c_{ij}\}$ (Note that a and c form symmetric matrices). The only requirement upon this action is that it be invariant under any gauge transformation. This gives $2NM$ equations (one for every field or derivative of field, and for every transformation), from which some coefficients are determined, leaving $(1+2N-2M)N$ undetermined coefficients that one is free to choose. On the other hand, an action written using only physical modes $\Phi_{\rm I}$ is constructed using $2(N-M)^2 + (N-M) = (1+2N-2M)(N-M)$ coefficients. Thus, the freedom in writing a gauge-invariant action is always greater than what the $\Phi_{\rm I}$ allow for.

We conclude that in general the action will not be expressible as in (C.1). Not with the Φ_i being physical, gauge-invariant fields. The generalization of the algorithm consists in getting as close as possible to an expression of that kind, as we explain below. Our starting point, for now, will consist in taking the complete quadratic action (C.2) and forgetting about the gauge symmetry issues. Varying this action, one can obtain the equations of motion for the perturbation fields, integrate the Lagrangian by parts, insert the equations of motion to obtain the action evaluated on-shell and add the proper counterterms to cancel out any divergences. Finally, this expression can be transformed carefully into an integration in Fourier space (see [45] for a description of the procedure).

The physical fields obey a set of coupled equations of motion of their own, and each particular solution gives a vector of functions $\{\Phi_{\rm I}(x,r)\}$, such that as we approach the boundary, it asymptotes to some boundary values. It is in general possible to normalize the physical modes and to parametrize the perturbations in such a way that each boundary value of a physical mode coincides with the boundary value of one of the fluctuations,

$$\Phi_{\rm I}(k,r) \xrightarrow[r\to\infty]{} \varphi_{\rm I}(k). \tag{C.3}$$

So we can make an association one to one between the physical modes and n of the N fluctuation fields. At any other distance r, each physical mode will of course depend on the values of all the other fluctuations that are involved in its definition.

Then, the first of the instructions would be to normalize the physical modes and to choose the appropriate fluctuation modes in order to be able to make this association on the boundary. The second step is to invert the definitions of the physical modes and solve for the fluctuations $\varphi_{\rm I}(k)$ that enter in the association. The idea is to replace these fields[9] by inserting that solution into the on-shell action. In doing so, one obtains a contribution that involves only the physical modes, another one with couplings between the physical modes and the remaining fluctuations, and finally some terms given in terms of these remaining fluctuations only. That is, $S_{\rm o.s.} = S_{\rm o.s.1} + S_{\rm o.s.2}$ where[10]

$$\begin{aligned}
S_{\rm o.s.1} &= \int d^dk \left[\Phi_{\rm I}\, \mathfrak{A}(k,r)_{\rm IJ}\, \partial_r\Phi_{\rm J} + \Phi_{\rm I}\, \mathfrak{B}(k,r)_{\rm IJ}\, \Phi_{\rm J}\right]_{r=r_b}\,, \\
S_{\rm o.s.2} &= \int d^dk \big[\Phi_{\rm I}\mathfrak{a}(k,r)_{{\rm I}j}\partial_r\varphi_j + \varphi_i\mathfrak{b}(k,r)_{i{\rm J}}\partial_r\Phi_{\rm J} + \Phi_{\rm I}\mathfrak{c}(k,r)_{{\rm I}j}\varphi_j \\
&\qquad\qquad + \varphi_i\mathfrak{d}_{ij}(k,r)\partial_r\varphi_j + \varphi_i\mathfrak{e}_{ij}(k,r)\varphi_j\big]_{r=r_b}\,,
\end{aligned}$$

The associated $\varphi_{\rm I}(x)$ fields no longer enter in the action. Now let's assume that we cannot find an analytic solution to the n coupled equations of motion, which is expected except for some simple cases. Nevertheless, since this action is evaluated on the boundary r_b, a possible analytic approach would be to solve for the equations of motion on the limit $r \gg r_h$ and obtain the asymptotic expansions of the fields. As shown in the expansions of section A.1, the expanded solutions are usually not determined by the boundary values φ_0^b only. There are also some undetermined coefficients φ_p^b which can only be fixed by supplying initial conditions at a given point from which integration starts. Since these coefficients depend on the whole integration up to the boundary, they will not be solved for analytically. It is for this reason that some Green's functions can only be evaluated numerically.

A convenient position to start the integration is the horizon of the bulk geometry, because the initial conditions can be made easily at that point by demanding incoming solutions. This condition is related to the fact that we will ultimately be calculating retarded Green's functions. For convenience, let us refrain here what has been stated elsewhere in the text: The condition at the horizon halves the number of degrees of freedom and from a

---

[9] From this point on, indices $I, J, \ldots$ denote the $n = N - M$ physical modes, while indices $i, j, \ldots$ denote the $N - n$ fluctuation modes that have not been replaced.

[10] We do not state it explicitly, but each term in the next actions includes the product of a field evaluated in k and another evaluated in $-k$. This is natural for a quadratic Lagrangian written in Fourier space.

basis of $2N$ solutions (N fluctuations under second order differential equations), we end up with just N solutions. Furthermore, there are M constraints coming from the equations of motion of the gauge-fixed fields which reduce these solutions to the $n = N - M$ degrees of freedom that manifest themselves through the physical solutions and can be found by requiring invariance under residual gauge transformations. However, the analytic expanded solution obtained around the boundary knows nothing about the incoming condition at the horizon. We have only the constraints, so accordingly we are dealing with a basis of $2N - M = N + n$ solutions - that is, $N + n$ undetermined coefficients. N of them can be taken to be the boundary values φ_0^b. Therefore, the number of undetermined coefficients φ_p^b is expected to be precisely n, the same as the number of physical modes. So a numerical integration of the equations of motion of the physical fields starting at the boundary is sufficient to fix them, since we are implicitly setting n initial conditions.

The expanded on-shell action can be then divided into two terms, $S_{\text{o.s.}} = S_{\text{o.s.(I)}} + S_{\text{o.s.(II)}}$ where

$$\begin{aligned} S_{\text{o.s.(I)}} &= \int d^d x \left[\alpha_{\text{IJ}} \left(\Phi_{\text{I}}\right)_0^b \left(\Phi_{\text{J}}\right)_0^b + \beta_{\text{IJ}} \left(\Phi_{\text{I}}\right)_0^b \left(\varphi_{\text{J}}\right)_p^b + \zeta_{\text{IJ}} \left(\varphi_{\text{I}}\right)_p^b \left(\varphi_{\text{J}}\right)_p^b\right] , \\ S_{\text{o.s.(II)}} &= \int d^d x \left[\kappa_{\text{I}j} \left(\Phi_{\text{I}}\right)_0^b \left(\varphi_j\right)_0^b + \lambda_{ij} \left(\varphi_i\right)_0^b \left(\varphi_j\right)_0^b\right] , \end{aligned} \tag{C.4}$$

provided that the expansions are arranged in such a way that the n $\left(\varphi_{\text{I}}\right)_p^b$ do not cross with the $N - n$ $\left(\varphi_i\right)_0^b$, which in general can be done because the φ_p^b are fixed by integrating the equations of motion of the physical fields, which are obtained by varying the action with respect to the physical fields, and therefore the part of the action which contains the remaining fluctuations φ_i is irrelevant to them.

In this expression, remember that $\left(\Phi_{\text{I}}\right)_0^b = \left(\varphi_{\text{I}}\right)_0^b$. Now, to obtain the Green's functions, the AdS/CFT prescription instructs us to take the functional derivative of the action with respect to the boundary values of the fields [44]. The Green's functions of the fluctuations φ_i can be easily extracted from (C.4) and read

$$G^R_{ij}(k) = -\lambda_{ij}, \qquad G^R_{\text{I}j}(k) = -\kappa_{\text{I}j} \tag{C.5}$$

On the other hand, the Green's functions $G^R_{\text{IJ}}(k)$, associated to the boundary values of the physical modes cannot be extracted directly, nor can they be expressed in an analytic way. These are the most interesting Green's functions because they have physical meaning, as discussed in section 4. We have computed them numerically following the method presented in the next section.

C.2 Prescription for numerical solutions

It is tempting to establish the identifications $S_{\text{o.s.(I)}} = S_{\text{o.s.1}}$ and $S_{\text{o.s.(II)}} = S_{\text{o.s.2}}$. However, it is important to note that this is incorrect, because the equations of motion of the fluctuations are all coupled, and consequently the expansions of the $\varphi_i(k, r)$ may depend on boundary values of the replaced $\varphi_{\text{I}}(k, r)$. Thus, expanding $S_{\text{o.s.2}}$ it is possible to produce terms like the ones found in $S_{\text{o.s.(I)}}$.

In order to deal with this, an effective action $S_{\rm eff}$ can be constructed, using physical fields only, such that its expansion near the boundary reproduces exactly those undesirable terms. This effective action is to be subtracted from $S_{\rm o.s.2}$ to cancel them out, and at the same time added to $S_{\rm o.s.1}$ producing

$$S_{\rm eff}+S_{\rm o.s.1}=\int d^dk\left[\Phi_{\rm I}(-k,r)A(k,r)_{\rm IJ}\partial_r\Phi_{\rm J}(k,r)+\Phi_{\rm I}(-k,r)B(k,r)_{\rm IJ}\Phi_{\rm J}(k,r)\right]_{r=r_b}\,. \quad \text{(C.6)}$$

The matrices A, B are obtained analytically, but only their expression at the boundary is necessary. We refer to the action as "effective" because its contribution matches exactly $S_{\rm o.s.(I)}$, but it is just an artifact - we do not derive any equation of motion from it. The fields that will be inserted are solutions of the equation of motions derived from the original action.

These solutions are obtained by numerical integration, starting from some selected values of the horizon $(\Phi_{\rm I})_0^h$. In fact, this set of values determines completely the coefficients of the expansion at the boundary. We may choose n linearly independent sets $(\Phi_{\rm I})_0^{h({\rm J})}=e_{\rm I}^{({\rm J})}$, in order to obtain n linearly independent sets of boundary values. In particular, a possible choice is

$$e_{\rm I}^{(1)}=(1,0,0,\ldots)\,,\quad e_{\rm I}^{(2)}=(0,1,0,\ldots)\,,\quad \ldots\,,\quad e_{\rm I}^{(n)}=(\ldots,0,0,1)\,. \quad \text{(C.7)}$$

Alternate choices are possible. This is just the one we used because we got good numerical results (with less noise). A numerical integration can be performed for each set in order to obtain n independent solutions $\{\Phi_{\rm I}^{({\rm J})}(k,r)\}_{\rm J}$ extended in the bulk, which can be arranged in a matrix $H(k,r)$, with entries

$$H_{\rm IJ}(k,r)=\Phi_{\rm I}^{({\rm J})}(k,r). \quad \text{(C.8)}$$

Thus, the $J^{\rm th}$ solution appears as the $J^{\rm th}$ column. On the other hand, we know that when each physical field approaches the boundary, it asymptotes to the value of its associated perturbation, $(\varphi_{\rm I})_0^b\,(k)$. At any other distance or scale r, since the system of differential equations is coupled, they will in general evaluate to a linear combination of all the $\{(\varphi_{\rm J})_0^b\}_{\rm J}$, so that the set of functions can be written as

$$\Phi_{\rm I}(k,r)=F_{\rm IJ}(k,r)\,(\varphi_{\rm J})_0^b\,(k)\,. \quad \text{(C.9)}$$

In this way, all the dynamics of the fields is encoded in the solution matrix $F_{\rm IJ}(k,r)$, which has the nice property of becoming the identity at the boundary, $F_{\rm IJ}(k,r_b)=\delta_{\rm IJ}$.

Any complete set of n independent solutions to the equations of motion is enough to build the matrix F, because any solution (any one that satisfies the incoming condition at the horizon) can be written as a linear combination of them. *In particular*, the matrix $F(k,r)$ must be linearly related to $H(k,r)$ because each $I^{\rm th}$ column of F is composed by a set of solutions that asymptotes to $(\varphi_{\rm J})_0^b=0$ for all J, except for $(\varphi_{\rm I})_0^b=1$. Since at the boundary, by definition, F is the identity, the linear relation must be given by

$$F(k,r)=H(k,r)\cdot H^{-1}(k,r_b)\,. \quad \text{(C.10)}$$

This result enables us to calculate the solution matrix, which encodes the dynamics, from n numerically integrated solutions. Then, by inserting (C.9) into our on-shell action (C.6), we obtain

$$S_{\text{eff+s.o.1}} = \int d^d k \; \Phi_{\rm I}(-k,r)\mathcal{F}_{\rm IJ}(k,r)\Phi_{\rm J}(k,r)\big|_{r=r_b} \;, \tag{C.11}$$

where $\mathcal{F} = F^\dagger \; A \; \partial_r F + F^\dagger \; B \; F$. But, since this is evaluated at the boundary, where the matrix F becomes the identity and the physical fields coincide with their associated fluctuations, we might as well write

$$S_{\text{eff+s.o.1}} = \int d^d k \, (\varphi_{\rm I})^b_0 \, (-k) \left[A_{\rm IK}(k,r_b) \; \partial_r F_{\rm KJ}(k,r_b) + B_{\rm IJ}(k,r_b)\right] (\varphi_{\rm J})^b_0 \, (k) \, . \tag{C.12}$$

The Green's functions can now be directly extracted from this expression using the AdS/CFT correspondence prescription, to give

$$G^R_{\rm IJ}(k) = -A(k,r_b)H'(k,r_b)H^{-1}(k,r_b) - B(k,r_b) \; . \tag{C.13}$$

Notice that this formula reproduces the well known result for the Green's function of a decoupled equation. Here, instead of the derivative of the field, there is the matrix of derivatives. And instead of taking the ratio with the boundary value of the field, a factor given by the inverse of the matrix of solutions is included.

This completes (C.5), giving the way of calculating all the Green's functions of the problem. However, as opposed to the ones given in (C.5), these Green's functions are not determined by the background only, the solution to the equations of motion of the perturbed degrees of freedom enters through H. Their physical meaning is clearer and more important, since they correspond holographically to the correlators of the dual operators.

D General remarks on viscosity in anisotropic fluids

The concept of viscosity is linked to the internal motion of a system that causes dissipation of energy [56]. In general, we may define a general dissipation function Ξ, such that the dissipative forces that describe the internal motion are obtained from it as velocity derivatives. Typically, frictional forces are linear in velocities u^μ, which suggests that the general form of this function be quadratic in velocities.

But, for an internal motion which describes a general translation or a general rotation, the dissipation is zero. Since it describes dissipative processes only, Ξ ought to vanish for these configurations of velocities. Because of this argument, the function must depend on the velocities through the combination of gradients of velocities $u_{\mu\nu} = \frac{1}{2}\left(\nabla_\mu u_\nu + \nabla_\nu u_\mu\right)$, rather than on the velocities themselves directly. Thus, the general form is given by the sum $\Xi = \frac{1}{2}\eta^{\mu\nu\lambda\rho}u_{\mu\nu}u_{\lambda\rho}$, where the coefficients $\eta^{\mu\nu\lambda\rho}$ define the viscosity tensor [38], whose symmetries are given by

$$\eta^{\mu\nu\lambda\rho} = \eta^{\nu\mu\lambda\rho} = \eta^{\mu\nu\rho\lambda} = \eta^{\lambda\rho\mu\nu} \, . \tag{D.1}$$

The part of the stress tensor which is dissipative due to viscosity is defined by

$$\Pi^{\mu\nu} = -\frac{\partial \Xi}{\partial u_{\mu\nu}} = -\eta^{\mu\nu\lambda\rho}u_{\lambda\rho} \, . \tag{D.2}$$

In the case of a fluid in the rest frame $u^t = 1$, and in order to satisfy the Landau frame condition $u_\mu \Pi^{\mu\nu} = 0$, the stress energy tensor (and the viscosity tensor, correspondingly) must have non-zero components only in the spatial directions $i, j, \ldots = \{x, y, z\}$. In general, only 21 independent components of η_{ijkl} appear in the expressions above.

For the particular case of an isotropic fluid, the tensor can be written using only 2 independent components, which are usually parametrized by the shear viscosity η and the bulk viscosity ζ, so that the dissipative part of the stress tensor can be expressed as $\Pi^{ij} = -2\eta(u^{ij} - \frac{1}{3}\delta^{ij}u^l_l) - \zeta u^l_l \delta^{ij}$, which is a well-known result.

For a transversely isotropic fluid, there are 5 independent components in the tensor η^{ijkl}. Without loss of generality, we choose the symmetry axis to be the x-axis. The non-zero components are parametrized by

$$\begin{aligned} \eta^{xxxx} &= \zeta_x + \frac{4}{3}\lambda\,, & \eta^{yyyy} &= \eta^{zzzz} = \zeta_y + \frac{\lambda}{3} + \eta_{yz}\,, \\ \eta^{xxyy} &= \eta^{xxzz} = -\frac{2}{3}\lambda\,, & \eta^{yyzz} &= \zeta_y + \frac{\lambda}{3} - \eta_{yz}\,, \\ \eta^{yzyz} &= \eta_{yz}\,, & \eta^{xyxy} &= \eta^{xzxz} = \eta_{xy}\,. \end{aligned} \tag{D.3}$$

So that the non-zero off-diagonal components of the stress tensor are

$$\begin{aligned} \Pi^{xy} &= -2\eta_{xy}u_{xy}\,, & \Pi^{xz} &= -2\eta_{xy}u_{xz}\,, \\ \Pi^{yz} &= -2\eta_{yz}u_{yz}\,. \end{aligned} \tag{D.4}$$

In this consideration we are including only the contribution to the stress tensor due to the dissipation via viscosity, and we find the terms in the constitutive equation which depend on the velocity of the normal fluid u_μ. But in general, there would also be terms depending on the derivatives of the Nambu-Goldstone boson fields $v_\mu = \partial_\mu \varphi$ on the superfluid velocity and on the velocity of the director, which may contribute to the dissipative part of the stress tensor (the director is the vector pointing in the preferred direction).

However, these terms do not contribute to the off-diagonal components of the energy-momentum tensor because (1) a shear viscosity due to the superfluid velocity leads to a non-positive divergence of the entropy current [56, 57], and (2) no rank two tensor can be formed out of degrees of freedom of the director if the gradients of the director vanish [58]. In our case, the second argument is fulfilled since the condensate is homogeneous and the fluctuations depend on time only. Even though these degrees of freedom will generate additional transport coefficients, they do not change the shear viscosities, so we can write Kubo formulae which give the shear viscosities in terms of the stress energy correlation functions.

Let us consider a conformal fluid, so that $\zeta_x = \zeta_y = 0$ (this can easily be shown using the tracelessness condition of the stress-energy tensor,i. e. $\Pi^a{}_a = 0$, with $a = x, y, z$). The usual way to perturb a system in thermal equilibrium is to look at small perturbations of the background fields and add these sources to the action. Here we are interested in the metric fluctuations about the flat Minkowski metric,i. e. the terms of interest here that we add to the action are

$$\Pi^{xx}h_{xx} + \Pi^{yy}h_{yy} + \Pi^{zz}h_{zz} = +i\omega\frac{2}{3}\lambda\left(h_{xx} - \frac{1}{2}(h_{yy} + h_{zz})\right)^2 + i\omega\frac{\eta_{yz}}{2}(h_{yy} - h_{zz})^2\,. \tag{D.5}$$

To derive the left side we use equations (D.2) and (D.3), as well as $u_{aa} = -\frac{i\omega}{2} h_{aa}$,[11] with $a = x, y, z$. Applying the same calculation to the isotropic case we obtain

$$\begin{aligned}\Pi^{xx} h_{xx} + \Pi^{yy} h_{yy} + \Pi^{zz} h_{zz} &= +\frac{i\omega}{3}\eta\left((h_{xx}-h_{yy})^2 + (h_{xx}-h_{zz})^2 + (h_{yy}-h_{zz})^2\right) \\ &= +i\omega\frac{2}{3}\eta\left(h_{xx} - \frac{1}{2}(h_{yy}+h_{zz})\right)^2 + i\omega\frac{\eta}{2}(h_{yy}-h_{zz})^2 \,.\end{aligned} \tag{D.6}$$

We only have one shear viscosity η in the isotropic case. The purpose of the rewriting of the latter case is to show the connection to the transversely isotropic case. This rewriting shows that at the phase transition λ turns into the isotropic shear viscosity η, explaining the behavior we see in figure 8. Note that this is a computation taking place on the field theory side. Therefore the metric we need to lower and raise indices is the flat Minkowski metric.

By plugging in the components of Π^{aa} it is easy to show that the left hand side of equation (D.5) is equivalent to

$$\begin{aligned}\Pi^{xx} h_{xx} + \Pi^{yy} h_{yy} + \Pi^{zz} h_{zz} = &\frac{1}{2}\left(\Pi^{xx} - (\Pi^{yy}+\Pi^{zz})\right)\left(h_{xx} - \frac{1}{2}(h_{yy}+h_{zz})\right) \\ &+ \frac{1}{2}\left(\Pi^{xx} + (\Pi^{yy}+\Pi^{zz})\right)\left(h_{xx} + \frac{1}{2}(h_{yy}+h_{zz})\right) \\ &+ \frac{1}{2}\left(\Pi^{yy} - \Pi^{zz}\right)(h_{yy}-h_{zz}) \,.\end{aligned} \tag{D.7}$$

Applying linear response theory we obtain the Green's function for the first term in the equation above, which can be related to $G^{m,m}$ on the gravity side

$$\begin{aligned}G^{m,m}(\omega) = &\lim_{|\vec{k}|\to 0}\int \mathrm{d}t\,\mathrm{d}^3x e^{-\mathrm{i}k_\mu x^\mu}\theta(t)\times \\ &\left\langle\left[\frac{1}{2}\left(T^{xx}(t,\vec{x}) - (T^{yy}(t,\vec{x}) + T^{zz}(t,\vec{x}))\right), \frac{1}{2}\left(T^{xx}(0,0) - (T^{yy}(0,0) + T^{zz}(0,0))\right)\right]\right\rangle .\end{aligned} \tag{D.8}$$

The Kubo formula that gives the λ viscosity is

$$\lambda = \lim_{\omega\to 0}\frac{3}{2\omega}\,\mathrm{Im}\,G^{m,m}(\omega)\,. \tag{D.9}$$

Note that the Green's function of the dissipative part of the second term of (D.7) is zero therefore we only get background fields for this components of the Green's function (3.2.1). Finally the last term of (D.7) corresponds to the helicity two mode and is related to the shear viscosity η_{yz}.

References

[1] J. Erdmenger, M. Haack, M. Kaminski and A. Yarom, *Fluid dynamics of R-charged black holes*, *JHEP* **01** (2009) 055 [arXiv:0809.2488] [INSPIRE].

---

[11] Here also used the fact, that we are in the rest frame of the fluid and therefore $u^\mu = (1, 0, 0, 0)$.

[2] N. Banerjee et al., *Hydrodynamics from charged black branes*, *JHEP* **01** (2011) 094 [`arXiv:0809.2596`] [INSPIRE].

[3] R. Loganayagam, *Anomalies and the helicity of the thermal state*, `arXiv:1211.3850` [INSPIRE].

[4] R. Loganayagam and P. Surowka, *Anomaly/transport in an ideal Weyl gas*, *JHEP* **04** (2012) 097 [`arXiv:1201.2812`] [INSPIRE].

[5] D.T. Son and N. Yamamoto, *Kinetic theory with Berry curvature from quantum field theories*, `arXiv:1210.8158` [INSPIRE].

[6] J.L. Manes and M. Valle, *Parity violating gravitational response and anomalous constitutive relations*, *JHEP* **01** (2013) 008 [`arXiv:1211.0876`] [INSPIRE].

[7] D.T. Son and P. Surowka, *Hydrodynamics with triangle anomalies*, *Phys. Rev. Lett.* **103** (2009) 191601 [`arXiv:0906.5044`] [INSPIRE].

[8] K. Jensen, R. Loganayagam and A. Yarom, *Thermodynamics, gravitational anomalies and cones*, *JHEP* **02** (2013) 088 [`arXiv:1207.5824`] [INSPIRE].

[9] S. Bhattacharyya, S. Jain, S. Minwalla and T. Sharma, *Constraints on superfluid hydrodynamics from equilibrium partition functions*, *JHEP* **01** (2013) 040 [`arXiv:1206.6106`] [INSPIRE].

[10] K. Landsteiner, E. Megias and F. Pena-Benitez, *Anomalous transport from Kubo formulae*, `arXiv:1207.5808` [INSPIRE].

[11] T. Kalaydzhyan, *Chiral superfluidity of the quark-gluon plasma*, `arXiv:1208.0012` [INSPIRE].

[12] I. Gahramanov, T. Kalaydzhyan and I. Kirsch, *Anisotropic hydrodynamics, holography and the chiral magnetic effect*, *Phys. Rev.* **D 85** (2012) 126013 [`arXiv:1203.4259`] [INSPIRE].

[13] A. Gynther, A. Rebhan and D. Steineder, *Thermodynamics and phase diagram of anisotropic Chern-Simons deformed gauge theories*, *JHEP* **10** (2012) 012 [`arXiv:1207.6283`] [INSPIRE].

[14] D. Mateos and D. Trancanelli, *Thermodynamics and instabilities of a strongly coupled anisotropic plasma*, *JHEP* **07** (2011) 054 [`arXiv:1106.1637`] [INSPIRE].

[15] M. Chernicoff, D. Fernandez, D. Mateos and D. Trancanelli, *Quarkonium dissociation by anisotropy*, *JHEP* **01** (2013) 170 [`arXiv:1208.2672`] [INSPIRE].

[16] M. Ammon, J. Erdmenger, V. Grass, P. Kerner and A. O'Bannon, *On holographic p-wave superfluids with back-reaction*, *Phys. Lett.* **B 686** (2010) 192 [`arXiv:0912.3515`] [INSPIRE].

[17] M. Natsuume and M. Ohta, *The shear viscosity of holographic superfluids*, *Prog. Theor. Phys.* **124** (2010) 931 [`arXiv:1008.4142`] [INSPIRE].

[18] J. Erdmenger, P. Kerner and H. Zeller, *Non-universal shear viscosity from Einstein gravity*, *Phys. Lett.* **B 699** (2011) 301 [`arXiv:1011.5912`] [INSPIRE].

[19] J. Erdmenger, P. Kerner and H. Zeller, *Transport in anisotropic superfluids: a holographic description*, *JHEP* **01** (2012) 059 [`arXiv:1110.0007`] [INSPIRE].

[20] P. Basu and J.-H. Oh, *Analytic approaches to anisotropic holographic superfluids*, *JHEP* **07** (2012) 106 [`arXiv:1109.4592`] [INSPIRE].

[21] P. Basu, J. He, A. Mukherjee and H.-H. Shieh, *Hard-gapped holographic superconductors*, *Phys. Lett.* **B 689** (2010) 45 [`arXiv:0911.4999`] [INSPIRE].

[22] P. Kovtun, D. Son and A. Starinets, *Viscosity in strongly interacting quantum field theories from black hole physics*, *Phys. Rev. Lett.* **94** (2005) 111601 [hep-th/0405231] [INSPIRE].

[23] A. Buchel and J.T. Liu, *Universality of the shear viscosity in supergravity*, *Phys. Rev. Lett.* **93** (2004) 090602 [hep-th/0311175] [INSPIRE].

[24] N. Iqbal and H. Liu, *Universality of the hydrodynamic limit in AdS/CFT and the membrane paradigm*, *Phys. Rev.* **D 79** (2009) 025023 [arXiv:0809.3808] [INSPIRE].

[25] A. Rebhan and D. Steineder, *Violation of the holographic viscosity bound in a strongly coupled anisotropic plasma*, *Phys. Rev. Lett.* **108** (2012) 021601 [arXiv:1110.6825] [INSPIRE].

[26] A. Buchel, R.C. Myers and A. Sinha, *Beyond eta/s* $= 1/4\pi$, *JHEP* **03** (2009) 084 [arXiv:0812.2521] [INSPIRE].

[27] J. Erdmenger, P. Kerner and S. Muller, *Towards a holographic realization of Homes' law*, *JHEP* **10** (2012) 021 [arXiv:1206.5305] [INSPIRE].

[28] Y.-Y. Bu, J. Erdmenger, J.P. Shock and M. Strydom, *Magnetic field induced lattice ground states from holography*, jhep032013165 [arXiv:1210.6669] [INSPIRE].

[29] A. Karch and E. Katz, *Adding flavor to AdS/CFT*, *JHEP* **06** (2002) 043 [hep-th/0205236] [INSPIRE].

[30] S.S. Gubser, *Breaking an abelian gauge symmetry near a black hole horizon*, *Phys. Rev.* **D 78** (2008) 065034 [arXiv:0801.2977] [INSPIRE].

[31] S.A. Hartnoll, C.P. Herzog and G.T. Horowitz, *Building a holographic superconductor*, *Phys. Rev. Lett.* **101** (2008) 031601 [arXiv:0803.3295] [INSPIRE].

[32] S.A. Hartnoll, C.P. Herzog and G.T. Horowitz, *Holographic superconductors*, *JHEP* **12** (2008) 015 [arXiv:0810.1563] [INSPIRE].

[33] S.S. Gubser and S.S. Pufu, *The gravity dual of a p-wave superconductor*, *JHEP* **11** (2008) 033 [arXiv:0805.2960] [INSPIRE].

[34] M. Ammon, J. Erdmenger, M. Kaminski and P. Kerner, *Superconductivity from gauge/gravity duality with flavor*, *Phys. Lett.* **B 680** (2009) 516 [arXiv:0810.2316] [INSPIRE].

[35] P. Basu, J. He, A. Mukherjee and H.-H. Shieh, *Superconductivity from D3/D7: holographic pion superfluid*, *JHEP* **11** (2009) 070 [arXiv:0810.3970] [INSPIRE].

[36] M. Ammon, J. Erdmenger, M. Kaminski and P. Kerner, *Flavor superconductivity from gauge/gravity duality*, *JHEP* **10** (2009) 067 [arXiv:0903.1864] [INSPIRE].

[37] S.A. Hartnoll, *Lectures on holographic methods for condensed matter physics*, *Class. Quant. Grav.* **26** (2009) 224002 [arXiv:0903.3246] [INSPIRE].

[38] L.D. Landau and E.M. Lifshitz, *Course of theoretical physics. Volume 7: theory of elasticity*, Pergamon Press, Oxford U.K. (1959).

[39] P. de Gennes, *The physics of liquid crystals*, Oxford University Press, Oxford U.K. (1974).

[40] S. Kobayashi, D. Mateos, S. Matsuura, R.C. Myers and R.M. Thomson, *Holographic phase transitions at finite baryon density*, *JHEP* **02** (2007) 016 [hep-th/0611099] [INSPIRE].

[41] V. Balasubramanian and P. Kraus, *A stress tensor for Anti-de Sitter gravity*, *Commun. Math. Phys.* **208** (1999) 413 [hep-th/9902121] [INSPIRE].

[42] S. de Haro, S.N. Solodukhin and K. Skenderis, *Holographic reconstruction of space-time and renormalization in the AdS/CFT correspondence*, *Commun. Math. Phys.* **217** (2001) 595 [`hep-th/0002230`] [INSPIRE].

[43] S.S. Gubser, F.D. Rocha and A. Yarom, *Fermion correlators in non-abelian holographic superconductors*, *JHEP* **11** (2010) 085 [`arXiv:1002.4416`] [INSPIRE].

[44] D.T. Son and A.O. Starinets, *Minkowski space correlators in AdS/CFT correspondence: recipe and applications*, *JHEP* **09** (2002) 042 [`hep-th/0205051`] [INSPIRE].

[45] M. Kaminski, K. Landsteiner, J. Mas, J.P. Shock and J. Tarrio, *Holographic operator mixing and quasinormal modes on the brane*, *JHEP* **02** (2010) 021 [`arXiv:0911.3610`] [INSPIRE].

[46] C.P. Herzog, *Lectures on holographic superfluidity and superconductivity*, *J. Phys.* **A 42** (2009) 343001 [`arXiv:0904.1975`] [INSPIRE].

[47] R.C. Myers, A.O. Starinets and R.M. Thomson, *Holographic spectral functions and diffusion constants for fundamental matter*, *JHEP* **11** (2007) 091 [`arXiv:0706.0162`] [INSPIRE].

[48] J. Armas, J. Gath and N.A. Obers, *Black branes as piezoelectrics*, *Phys. Rev. Lett.* **109** (2012) 241101 [`arXiv:1209.2127`] [INSPIRE].

[49] E.I. Buchbinder and A. Buchel, *The fate of the sound and diffusion in holographic magnetic field*, *Phys. Rev.* **D 79** (2009) 046006 [`arXiv:0811.4325`] [INSPIRE].

[50] S. Nakamura, H. Ooguri and C.-S. Park, *Gravity dual of spatially modulated phase*, *Phys. Rev.* **D 81** (2010) 044018 [`arXiv:0911.0679`] [INSPIRE].

[51] H. Ooguri and C.-S. Park, *Spatially modulated phase in holographic quark-gluon plasma*, *Phys. Rev. Lett.* **106** (2011) 061601 [`arXiv:1011.4144`] [INSPIRE].

[52] K. Skenderis, *Lecture notes on holographic renormalization*, *Class. Quant. Grav.* **19** (2002) 5849 [`hep-th/0209067`] [INSPIRE].

[53] B. Sahoo and H.-U. Yee, *Electrified plasma in AdS/CFT correspondence*, *JHEP* **11** (2010) 095 [`arXiv:1004.3541`] [INSPIRE].

[54] D. Son and M.A. Stephanov, *QCD at finite isospin density*, *Phys. Rev. Lett.* **86** (2001) 592 [`hep-ph/0005225`] [INSPIRE].

[55] J. Pons, D. Salisbury and L. Shepley, *Gauge transformations in Einstein-Yang-Mills theories*, *J. Math. Phys.* **41** (2000) 5557 [`gr-qc/9912086`] [INSPIRE].

[56] L.D. Landau and E.M. Lifshitz, *Course of theoretical physics. Volume 6: fluid mechanics*, Pergamon Press, Oxford U.K. (1959).

[57] C. Pujol and D. Davesne, *Relativistic dissipative hydrodynamics with spontaneous symmetry breaking*, *Phys. Rev.* **C 67** (2003) 014901 [`hep-ph/0204355`] [INSPIRE].

[58] F.M. Leslie, *Some constitutive equations for anisotropic fluids*, *Quart. J. Mech. Appl. Math.* **19** (1966) 357.

Chapter 5

Conclusions and future directions

The search for means of putting the gauge/gravity duality to the test is an important issue that has received much attention in recent years. The phenomenological interest of Maldacena's original conjecture is rather far-fetched, but it is clear that with the appropriate adjustments, it is possible to obtain generalizations that may help resolve open questions from heavy-ion collisions or condensed matter physics. This progress is essential to find out to what extent can the qualitative conclusions derived from holographic models be trusted.

This thesis encompasses the construction of different gravitational models, with the common purpose of obtaining phenomenological predictions, in a way or another. The quantitative details of these conclusions may depend on the specific details of the particular model, so we intend to look for results that are as universal as possible. A neat example of such a prediction is contained in chapter 2. The existence of a subluminal limiting velocity for mesons in the plasma follows from simple, generic observations and leads to the Cherenkov radiation of quarkonium mesons by quarks, an effect with an estimate of the magnitude of its energy loss of the same order as other previously established mechanisms of energy loss in the plasma. Moreover, even if its effect turns out to be subdominant with respect to other mechanisms (and therefore, more unlikely to be observed), its characteristic features may still make it identifiable. However, the gravity calculation that was performed is strictly valid only in the infinite-quark energy limit, because of the linear trajectory approximation. It would be interesting to study the energy loss in the case of light quarks. To this end, black hole embeddings would need to be considered. Note that in this case no stable quark-antiquark bound states exist in the plasma, which in the string description corresponds to the fact that excitations on the brane are characterized by quasinormal modes with complex frequencies.

The gauge/gravity duality also allowed us to study the physics of a state of matter very different from the quark gluon plasma. In chapter 4, we considered Einstein-Yang-Mills theory to describe the formation of a condensate that spontaneously breaks the rotation symmetry and a $U(1)$ gauge symmetry at the same time. The dynamics of this system represents those of a p-wave superfluid. We focused on the computation of the complete set of transport coefficients. Among them, the anisotropy of the system entails interesting new phenomena, such as the piezoelectric effect and a viscosity coefficient related to the normal stress difference. The functions we computed present a rich structure, in particular a very intriguing feature of our results is the presence of bumps in some of the correlators, which seem to be related to the generation of bound states. For further progress, a detailed analysis of the hydrodynamics of anisotropic superfluids would be desirable to give a further interpretation to this study. In addition, it would be worthy to perform an analysis at finite spatial momentum, which would allow to investigate the dispersion relations of the normalizable modes and to check for instabilities.

Another contribution we did to the analysis of quark gluon plasma physics, from a holographic point of view, was the employment of a IIB supergravity solution dual to a spatially anisotropic $\mathcal{N} = 4$ SYM plasma at finite temperature to determine the effect of anisotropy over several observables. The conclusions from the calculation of chapter 3 can be summarized as follows:

i) The anisotropy can make the drag force F exerted on massive quarks moving through this plasma become arbitrarily large, except for those whose velocity is aligned transverse to the anisotropic direction. However, it can also have the opposite effect and make the drag force smaller than the corresponding isotropic value. In the ultra-relativistic limit, the drag coefficient μ (defined so that $F = \mu p$) generically increases linearly with the momentum, $\mu \propto p$. Finally, the direction of the drag force is generally misaligned with the quark velocity and the gluon cloud trailing behind the quark.

ii) The jet quenching parameter $\hat{q}$, which in an anisotropic plasma depends on the relative orientation between the anisotropic direction, the direction of motion of the parton, and the direction along which the momentum broadening is measured; can also be larger or smaller than the corresponding isotropic value. But for small enough an anisotropy, it is always larger. It is important to note that it being larger or smaller also depends on whether the comparison is made at equal temperatures or at equal entropy densities, in contrast with the results for the drag force, that were qualitatively insensitive to this.

iii) The screening length L_s of a quarkonium meson in motion in the anisotropic plasma, which depends on relative orientations between the anisotropic direction, the direction of motion of the meson and its orientation; can also be larger or smaller than the isotropic value depending on, among other things, how the comparison is made. Perhaps the most suggestive result is that there is a limiting velocity for mesons in the plasma and that they dissociate above a certain critical value of the anisotropy, even at zero temperature. In the ultra-relativistic limit, L_s scales as $(1-v^2)^\epsilon$ with $\epsilon = 1/2$, in contrast with the isotropic result $\epsilon = 1/4$.

Ultimately, this thorough analysis is a step towards a more realistic description of the plasma created in heavy ion collisions, which is anisotropic right after the collision (with the anisotropic direction being the beam direction). However, the plasma that is considered in this calculations is completely static, which may be a good approximation when looking at processes with a characteristic timescale much shorter than that of the evolution of the plasma, but it is an undesirable limitation. Including both anisotropy and time dependence would be very difficult, but it would enable us to study the process of isotropization itself. In fact, a very important open issue about this topic is understanding why the isotropization time is so short.

On the gravity side, the far-from-equilibrium evolution of the plasma corresponds to the relaxation of a far-from-equilibrium black hole, and requires solving the full nonlinear Einstein's equations. This necessarily implies using advanced numerical techniques of General Relativity. How to incorporate this techniques into the field of AdS/CFT will probably be extensively studied in the next few years.

In the end, we must keep in mind that QCD itself, and also condensed matter systems, might or might not have a dual gravitational description. Nevertheless, the gauge/gravity duality has already produced a mesmerizing connection between string theory and gauge field theories. On the quest for the ultimate theory of Nature, string theory may still help us solve puzzles that have been around for many decades.

Chapter 6

Resumen en Castellano
Summary in Spanish

1. Introducción

1.1. La dualidad gauge/cuerdas

La correspondencia AdS/CFT, o dualidad gauge/cuerdas, ha supuesto un gran avance en nuestra comprensión de la teoría de cuerdas, además de ser una herramienta muy útil para estudiar teorías cuánticas de campos fuertemente acoplados. Específicamente, la equivalencia más conocida está establecida entre la teoría $\mathcal{N} = 4$ Súper-Yang-Mills (SYM) y la teoría de cuerdas tipo IIB en el espacio $AdS_5 \times S^5$, cuya métrica es

$$ds^2 = \frac{R^2}{z^2}\left(\eta_{\mu\nu}dx^\mu dx^\nu + dz^2 + z^2 d\Omega_5^2\right) , \tag{1.1}$$

donde z es la coordenada radial extradimensional y la frontera se encuentra en $z \to 0$.

La dualidad se puede interpretar como la geometrización del flujo del grupo de renormalización (GR) de la teoría dual. Podemos visualizar la familia formada por el conjunto de teorías efectivas, parametrizada por el valor de sus acotamientos, como una sola teoría en un espaciotiempo $(4+1)$-dimensional. La idea es que la física de la región que queda debajo de $z = z'$ sería descriptible por la teoría efectiva a escala z'. Esto sugiere la identificación de la coordenada radial con la escala de energía de la teoría gauge dual. Así, la física del límite ultravioleta se transcribe a la región cerca de la frontera, y la infrarroja con la interior.

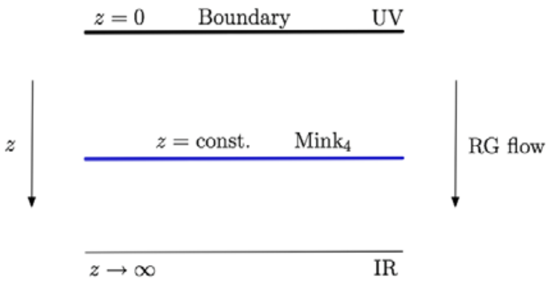

Figura 1. Esquema de la geometría de AdS.

Los parámetros de la teoría $\mathcal{N} = 4$ SYM son el acoplo g y el número de colores N_c, mientras que los de la teoría de cuerdas IIB son el acoplo de la cuerda g_s y su longitud ℓ_s, o equivalentemente se puede considerar la constante de Newton G y el radio de curvatura de AdS, R. Todos están relacionados entre sí, de manera que se tiene

$$\frac{\ell_p^8}{R^8} \propto \frac{1}{N_c^2}\,, \qquad \frac{\ell_s^2}{R^2} \propto \frac{1}{\sqrt{\lambda}}\,, \tag{1.2}$$

con $\lambda = g^2 N_c$. De aquí se deduce que el límite clásico del lado de cuerdas corresponde al límite $N_c \gg 1$, $\lambda \gg 1$ de la teoría dual.

Por otra parte, para encajar los espectros, las soluciones de un lado de la dualidad habrían de ser las imágenes de las del otro lado. Dado que en Supergravedad el acoplo está dado por el dilatón, $g_s = e^\Phi$, esto sugiere la identificación de los operadores en la teoría gauge $\mathcal{O}(x)$ con campos hiperespaciales $\Phi(x, z)$, cuyo valor de frontera $\phi(x)$ les haría de fuente:

$$S \to S + \int d^4x\ \phi(x)\mathcal{O}(x) , \tag{1.3}$$

Otra característica importante de la dualidad es que se puede trazar una correspondencia entre las simetrías globales de la teoría gauge y las simetrías gauge de la teoría de cuerdas.

Esto, a su vez, permite la identificación de algunos operadores con sus campos. El ejemplo más importante es el tensor energía-momento, cuyo campo dual es la métrica. Típicamente, las ecuaciones del movimiento de los campos son de 2º orden, así que su solución asintótica es de la forma

$$\Phi(z,k) \approx A(k)\, z^{4-\Delta} + B(k)\, z^{\Delta} \qquad \text{as } z \to 0\,. \tag{1.4}$$

La parte no normalizable $A(x)$ se convierte en el mencionado valor de frontera. La parte normalizable $B(x)$ pertenece al espacio de Hilbert de la teoría, por tanto ha de corresponder a algún estado descrito por la teoría gauge. De hecho, se puede ver que

$$\langle \mathcal{O}(x) \rangle_{A(x)} = 2(\Delta - 2) B(x)\ . \tag{1.5}$$

Así, el coeficiente del término normalizable da el valor esperado del operador asociado.

Ahora bien, la correspondencia original está muy alejada de las aplicaciones que nos interesan. Por ejemplo, la métrica (1.1) es un caso extremal. Se puede generalizar para incluir un horizonte:

$$ds^2 = \frac{R^2}{z^2}\left(-f(z)\, dt^2 + dx_1^2 + dx_2^2 + dx_3^2 + \frac{dz^2}{f(z)} + z^2 d\Omega_5^2\right)\ , \tag{1.6}$$

donde $f(z) = 1 - z^4/z_0^4$. La temperatura asociada a esta solución es $T = \frac{1}{\pi z_0}$. También se puede incorporar un potencial químico μ mediante la existencia de un campo gauge hiperespacial A_μ que satisfaga la condición de frontera $\lim\limits_{z \to 0} A_t = \mu$.

Otra modificación importante de la correspondencia original es la incorporación de N_f campos de materia que transforman en la representación fundamental del grupo de simetrías gauge. El desarrollo topológico de sus diagramas de Feynman indica que en el lado de gravedad esto requiere a la presencia de cuerdas abiertas, para lo cual es necesario introducir D-branas adicionales.

En el límite $N_\text{c} \gg N_\text{f}$, la retroacción de estas D-branas es despreciable, de forma que se pueden considerar como branas sonda. Y en el límite de baja energía, las diversas interacciones entre cuerdas abiertas y cerradas se pueden clasificar en sectores. Se recupera la simetría global de sabor $SU(N_\text{f})$ y los límites $g_s N_\text{c} \gg 1$ y $g_s N_\text{c} \ll 1$ pueden ser identificados.

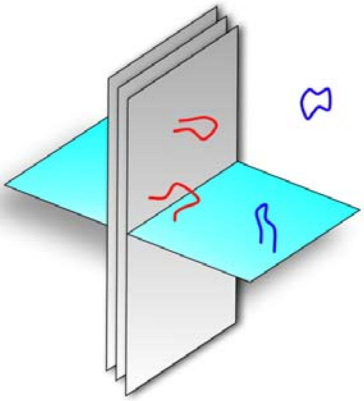

Figura 2. Representación esquemática de las D-branas sonda y cuerdas abiertas y cerradas.

1.2. Funciones de correlación

La conjetura de la dualidad se hace matemáticamente precisa a partir de la igualdad

$$Z_{\text{CFT}}\left[\phi(x)\right] = Z_{\text{string}}\left[\Phi|_{\partial AdS}(x)\right] \tag{1.7}$$

entre las funciones de partición Euclideas. Nótese que, debido a la identificación de campos y fuentes (1.3), las variables que aparecen en sendos funcionales son las mismas.

En el límite clásico, Z_{string} está determinada por la acción renormalizada del límite de Supergravedad clásica evaluada en la solución de las ecuaciones del movimiento:

$$Z_{\text{string}}[\phi] \simeq \exp\left(S^{(\text{ren})}\left[\Phi_c^{(E)}\right]\right) , \tag{1.8}$$

lo cual supone una simplificación considerable. Por contra, en el lado gauge esto se corresponde con el límite de acoplo fuerte, que supone una complicación considerable.

Los valores esperados se pueden calcular a partir de $\langle\mathcal{O}(x)\rangle_\phi = \delta S^{(\text{ren})}[\Phi_c^{(E)}]/\delta\phi(x)$, y en general con sucesivas derivadas con respecto a las fuentes asociadas, se obtienen funciones de correlación de operadores

$$\langle\mathcal{O}(x_1)\ldots\mathcal{O}(x_n)\rangle = \left.\frac{\delta^n S^{(\text{ren})}[\Phi_c^{(E)}]}{\delta\phi(x_1)\ldots\delta\phi(x_n)}\right|_{\phi=0} . \tag{1.9}$$

A partir del cálculo de los correladores se pueden obtener las funciones de Green. Se puede demostrar que una manera de computarlas es considerar perturbaciones sobre una solución clásica y observar los cambios producidos en valores esperados. La relación entre ambos es

$$\delta\langle\mathcal{O}_1(\omega,\vec{k})\rangle_{\phi_2} = G_R^{\mathcal{O}_1\mathcal{O}_2}(\omega,\vec{k})\,\phi_2(\omega,\vec{k})\,, \tag{1.10}$$

Es importante señalar que esta definición está dada en signatura Euclidea. En signatura Lorentziana, el espaciotiempo contiene un horizonte. Para tratar con esto, la prescripción consiste en poner condiciones de contorno entrantes en el horizonte: $\Phi_c(t,\vec{x}) \sim e^{-i\,\omega\,(t-z)}$.

1.3. Bucles de Wilson

Los bucles de Wilson son observables importantes en cualquier teoría gauge, por la información que contienen sobre física no perturbativa. Su valor esperado se define como[1]

$$W^r(\mathcal{C}) = \operatorname{Tr}\mathcal{P}\exp\left[i\int_{\mathcal{C}} dx^\mu\, A_\mu(x)\right] , \tag{1.11}$$

donde $\int_{\mathcal{C}}$ denota una integral a lo largo de un contorno $\mathcal{C}$, que se puede considerar como la trayectoria de un quark (un campo de la representación fundamental). En el lado de gravedad, esto corresponde al extremo de una cuerda abierta, de forma que $\mathcal{C}$ sería el borde de su hoja de universo, Σ.

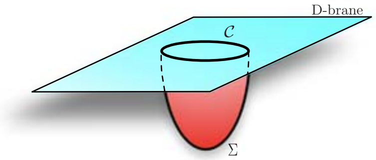

Figura 3. Hoja de universo Σ asociada al bucle de Wilson $\mathcal{C}$.

De nuevo, en el límite clásico $N_c \gg 1$, $\lambda \gg 1$ el cálculo se simplifica. $W(\mathcal{C})$ es básicamente la función de partición del quark sobre $\mathcal{C}$, por tanto se identifica como la función de partición de la Σ dual, que en este límite está determinada por $\langle W(\mathcal{C})\rangle = e^{iS(\mathcal{C})}$, donde $S(\mathcal{C})$ es la acción clásica evaluada en la solución de las ecuaciones del movimiento, que en definitiva lo que hacen es minimizar la energía. De esta forma, un cálculo que en la teoría

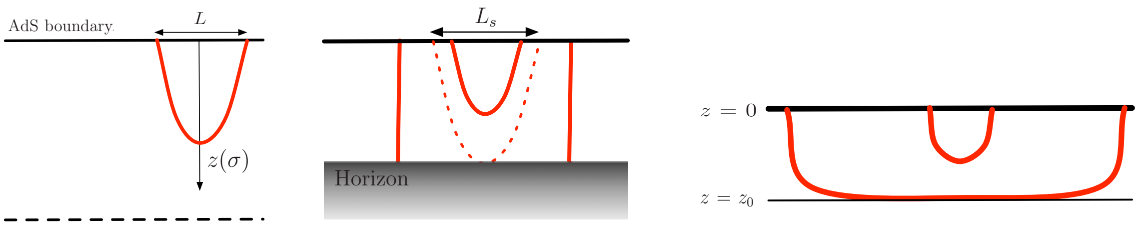

Figura 4. Cuerda asociada a un par quark-antiquark en vacío (izquierda), en un plasma a temperatura $T > 0$ (centro) y en una teoría confinante (derecha).

gauge sería cuántico y complejo se reduce básicamente a resolver una catenaria en el lado de gravedad.

De hecho, a veces la dependencia cualitativa del bucle de Wilson se puede explicar sin necesidad de cálculos. Por ejemplo, consideremos un contorno rectangular correspondiente a un par quark-antiquark estático. En este caso, $S(\mathcal{C})$ se puede entender como la energía potencial del par, $V(L)$. En AdS puro, por análisis dimensional, $V(L) \propto 1/L$. Si hay temperatura, la cuerda que cuelga de los extremos se puede partir y caer a través del horizonte. Esto sucederá para $L > L_s$ donde $L_s \sim 1/T$. Y si la teoría es confinante, lo cual se puede conseguir generalizando (1.1) a

$$ds^2 = \frac{R^2}{z^2}\left(-dt^2 + dx_1^2 + dx_2^2 + f(z)dx_3^2\right) + \frac{R^2}{z^2 f(z)}dz^2\,, \tag{1.12}$$

entonces si L es grande ($L \gg z_0$) la longitud de la cuerda es aproximable como la separación, de forma que $V(L) \sim L$. Estos razonamientos están ilustrados en la figura 4.

1.4. Criticalidad cuántica y superconductores

Los puntos críticos cuánticos, transiciones de fase a temperatura cero, se caracterizan por una invariancia de escala que evoca las versiones más simples de AdS/CFT. Además, la ausencia de cuasipartículas a acoplo fuerte hace que sean difíciles de estudiar con métodos tradicionales. La dualidad es útil por proporcionar resultados analíticos donde otros métodos no pueden. La región de aplicabilidad de los cálculos holográficos es la vecindad de la transición de fase cuántica.

Especialmente importantes son aquellos sistemas que sufren una ruptura espontánea de una simetría en la transición. Por las características que surgen a consecuencia de ello, son conocidos como superconductores y superfluídos.

La descripción gravitatoria se basa en el hecho de que (1.6) no es la única solución con temperatura, únicamente es la que es termodinámicamente favorecida. Pero la introducción de escalas adicionales, por ejemplo un potencial químico μ, puede hacer que eso cambie en alguna región del diagrama de fases, generando una transición de fase gravitatoria que se corresponde con la transición del superconductor, ya que las soluciones de gravedad se corresponden con estados de la teoría dual.

---

[1] Aquí, r es la representación del grupo de simetrías y $A_\mu(x) = A_\mu^a(x)\,T^a$.

2. Resultados Principales

2.1. Emisión Cherenkov de mesones

En el límite clásico $N_c, \lambda \to \infty$, existen dos propiedades de la dualidad que son universales, es decir, aplicables a todas las versiones conocidas de la dualidad: *i*) que la fase no confinada de la teoría gauge está descrita por la geometría de un agujero negro, y *ii*) que un número de sabores N_f finito se describe mediante la inclusión de N_f D-branas sonda.

Las D-branas se extienden en la dirección radial ($r = R^2/z$) hasta un valor mínimo, que es proporcional a la masa del quark M_q; mientras que el tamaño del agujero negro es proporcional a su temperatura T. Si $T < M_q$, las D-branas se mantienen fuera del horizonte. En esta fase, los mesones se describen por cuerdas abiertas con ambos extremos en las D-branas, cuyo espectro es discreto y abierto. Su presencia se traduce en que los mesones suficientemente pesados sobreviven al deconfinamiento.

En la fig. 5, podemos ver $\omega(q)$, la relación de dispersión (RD) de los mesones vectoriales en el plasma. Para $q \to \infty$, la RD se vuelve lineal, siendo la pendiente adquirida una velocidad límite común a todos, v_{lim}. Vemos que es subluminal, $v_{\text{lim}} < 1$, de hecho en la descripción gravitatoria se puede entender intuitivamente como la velocidad de la luz local marcada por el desplazamiento al rojo provocado por el agujero negro en la parte de abajo de las branas, que es donde se agolpa la función de onda de los mesones más energéticos, debido a la atracción gravitatoria.

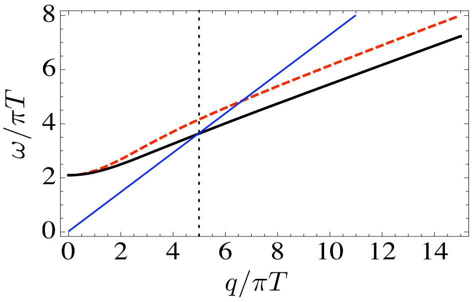

Figura 5. RD para modos transverso (negro) y longitudinal (rojo) de un mesón vectorial pesado con $v_{\text{lim}} = 0{,}35$. La línea azul corresponde a $\omega = v\, q$ con $v_{\text{lim}} < v < 1$.

Por otra parte, un quark pesado está descrito por una cuerda abierta que cuelga de las D-branas y a través del horizonte (ver fig. 6), moviéndose en dirección paralela a él.

Dos observaciones son las que conducen al efecto que nos interesa. Una es que el extremo de la cuerda está cargado bajo los campos escalares y vectoriales de las branas. En la teoría dual, el acoplo que corresponde es $\sim 1/\sqrt{N_c}$, que en el límite considerado es pequeño, de forma que la dinámica se puede aproximar hasta reducirla a una generalización simple de la electrodinámica clásica. La otra es que la velocidad del quark puede exceder la velocidad límite de los mesones, ya que el desplazamiento al rojo en su posición no es tan acentuado como en la parte de abajo de las branas.

Así pues, tenemos el análogo de una carga que se mueve en un medio dieléctrico más rápido que la velocidad de la luz en ese medio. La electrodinámica ordinaria indica que si esto pasa, la carga perderá energía por radiación Cherenkov. En este caso, el extremo de la cuerda radiará en los campos de la brana, lo cual se traduce a la teoría dual como que el quark radiará mesones (escalares y vectoriales) por Cherenkov.

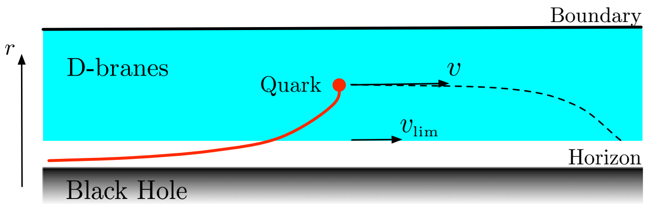

Figura 6. D-branas y cuerda abierta en la geometría del agujero negro.

Esta es la predicción, motivada mediante argumentos generales. Para realizar cálculos cuantitativos, utilizamos la teoría $SU(N_c)$ $\mathcal{N} = 4$ SYM acoplada a un sabor $N_f = 1$. En el lado de gravedad consideramos la presencia de una D7-brana sonda. Los términos de la acción del sistema brana + cuerda relevantes para el cálculo con mesones vectoriales son

$$S = -\int d^8\sigma \sqrt{-g}\, \frac{1}{4} F^{ab} F_{ab} - e \int d^8\sigma\, A_a J^a \,, \tag{2.1}$$

donde $F_{ab} = \partial_{[a} A_{b]}$, $\sigma^a = \{x^\mu, r, \Omega_3\}$ y, como se dijo más arriba, $e \sim 1/\sqrt{N_c}$, lo cual justifica despreciar términos superiores. El extremo de la cuerda es tratado como una partícula puntual y, por simplicidad, suponemos que se mueve con velocidad constante v, siguiendo una línea recta y a posición radial (y angular) constante, así que su corriente se escribe como

$$J^a = \delta^{(3)}(\vec{x} - \vec{v}t)\, \delta(r - r_0)\, \delta^{(3)}(\Omega - \Omega_0)\, (1, \vec{v}, \vec{0}, \vec{0}) \,. \tag{2.2}$$

Trabajamos con las componentes de Fourier del campo $A_\mu(\omega, q, r)$, que se desarrollan en una base de modos normalizables en la dirección radial, $\{\xi_n(q, r)\}$, que son soluciones de las ecuaciones del movimiento en ausencia de fuentes. Así realizamos una reducción del campo pentadimensional a una torre de infinitos campos tetradimensionales. La fig. 5 muestra sendas ramas inferiores de un conjunto infinito de RD, tales que la rama n-ésima daría la autofrecuencia correspondiente al coeficiente del modo n.

El ritmo de pérdida de energía se calcula como

$$\frac{dE}{dt} = -e \int d^3x\, dr\, d\Omega_3\, F_{0a} J^a = -e\, v^i\, F_{0i}(t, \vec{v}t, r_0, \Omega_0) \,, \tag{2.3}$$

y también se puede descomponer en contribuciones de cada uno de los modos de Fourier. Ahora bien, cuánto más energético es un modo, más cuesta excitarlo, de manera que las contribuciones de modos superiores a dE/dt serán despreciables. Esto es confirmado en los cálculos, ya que la ecuación del movimiento del coeficiente n-ésimo muestra un acoplo efectivo $e_{\text{eff}}(q, r_0) = e\xi_n(q, r_0)$.

El resultado numérico de un caso particular de mesones vectoriales está representado en la fig. 7. Las curvas son para diversos valores de r_0. Nótese que terminan en un valor finito de v porque el quark también tiene una velocidad límite a su altura, $v^q_{\text{lim}}(r_0)$, aunque esta sea mayor que la de los mesones. A medida que $r_0 \to 0$, la pérdida de energía crece más deprisa, mientras que esta v^q_{lim} del quark decrece.

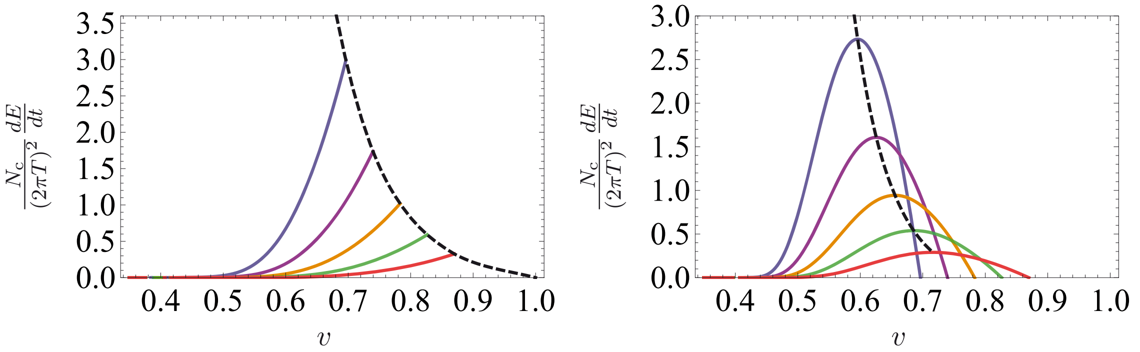

Figura 7. Ritmo de pérdida de energía hacia el modo de Fourier más bajo de mesones vectoriales (izquierda) y escalares (derecha). Las curvas corresponden a diversos valores de r_0 (valores crecientes a medida que vamos de la superior a la inferior).

En la fig. 7 se muestra el resultado análogo para mesones escalares. La principal diferencia es que curvas no crecen de manera monótona con v, sino que se anulan para la v^q_{lim} del quark. Esto se debe a que su término de acoplo, que se añadiría a (2.1) es

$$S_{\text{scalar}} \propto -\int d\tau\, \sqrt{-\dot{x}^2}\, g_{ab}\, X^a\, n^b\ , \tag{2.4}$$

y el factor $\sqrt{-\dot{x}^2} = \sqrt{-g_{00} - g_{11}v^2}$ se anula para esa velocidad.

La divergencia que observamos en la fig. 7 es un artefacto matemático, y sería cancelada por efectos físicos que no hemos tenido en cuenta, entre otros los debidos a las mencionadas aproximaciones sobre la trayectoria del quark, o simplemente efectos cuerderos para q suficientemente grande.

Esta radiación de Cherenkov mesónica es una cualidad universal de todos los plasmas con un dual de gravedad. Es concebible que también ocurra para algunos mesones de QCD. Los mesones radiados serían emitidos bajo un ángulo característico θ_c, dado por

$$\cos\,\theta_c = v_{\text{lim}}/v. \tag{2.5}$$

Este patrón de emisión es similar al de las ondas de sonido de un partón energético, la diferencia es que los mesones radiados no termalizan y por tanto no forman parte de la onda de choque hidrodinámica.

Nuestro cálculo de gravedad solo es estríctamente válido en el límite de infinita energía para el quark, así que esperamos que se aplique mejor para los quarks producidos en el LHC que en el RHIC. Una estimación burda de la magnitud de la pérdida de energía da $dE/dx \sim 2-8$ GeV/fm, lo cual se traduciría en la emisión, en el caso de J/ψ, de uno a tres mesones por fm. Esto es del mismo orden de magnitud que otros mecanismos. Pero incluso si resulta ser subdominante, hay otras características especiales que podrían hacerlo fácilmente identificable. Una es que solo ocurre cuando la velocidad supera un cierto umbral, otra es la emisión a θ_c, y finalmente que solo ocurriría dentro del rango de temperaturas en el que puede haber estados mesónicos en el plasma.

2.2. Anisotropía en plasmas fuertemente acoplados

Durante un periodo de tiempo τ_{out} inmediatamente posterior a la colisión de dos iones pesados, el sistema creado está lejos del equilibrio. Pasado un tiempo $\tau_{\text{iso}} > \tau_{\text{out}}$, se vuelve localmente isótropo. Es posible que durante este tiempo intermedio se pueda aplicar una descripción hidrodinámica intrínsicamente anisotrópica.

Para investigar qué efectos tendría esta anisotropía sobre algunos observables del plasma fuertemente acoplado que se formara en la colisión, examinamos una solución gravitatoria dual a un plasma $\mathcal{N} = 4$ SYM anisótropo. La solución empleada es estática, regular con un horizonte y encajada de manera sólida en Supergravedad tipo IIB, por lo que proporciona un buen modelo aproximado en el que hacer cálculos en detalle. Por supuesto, el tomar una anisotropía constante es una aproximación válida para escalas de tiempo apropiadamente cortas.

Dicha solución es

$$ds^2 = \frac{L^2}{u^2}\left(-\mathcal{F}\mathcal{B}\,dt^2 + dx^2 + dy^2 + \mathcal{H}dz^2 + \frac{du^2}{\mathcal{F}}\right) + L^2 e^{\frac{1}{2}\phi} d\Omega_5^2, \tag{2.6}$$

$$\chi = az\,, \qquad \phi = \phi(u)\,, \tag{2.7}$$

donde χ y ϕ son el axión y el dilatón, respectivamente. $\mathcal{F}$, $\mathcal{B}$ y $\mathcal{H}$ son funciones de la coordenada radial, que en este capítulo llamamos u. La coordenada z indica la dirección anisotrópica. La forma del axión es dual a un parámetro theta en la teoría gauge, de la forma $\theta \propto z$, que actúa como fuente externa y fuerza al sistema a estar en un equilibrio anisótropo. El grado de anisotropía está parametrizado por a.

La fuerza de arrastre. El primer observable que analizamos en este trasfondo es la fuerza de arrastre que actúa sobre un quark infinitamente masivo que se mueve a velocidad constante. Al igual que en el capítulo anterior, el quark está descrito por una cuerda que cuelga de una D7-brana, que en esta ocasión está situada en la frontera. La fuerza externa que sostiene su movimiento sería ejercida por un campo eléctrico constante en la brana.

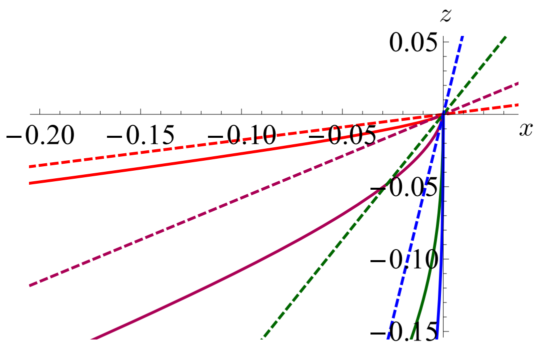

Figura 8. Proyecciones del perfil de la cuerda en el plano xz para varios ángulos. Las curvas discontinuas indican el ángulo de la velocidad.

La acción es

$$S = -\frac{1}{2\pi\alpha'}\int d^2\sigma\,\sqrt{-g} - \frac{1}{2}\int_{\partial\Sigma} d\tau F_{MN} X^M \partial_\tau X^N\,, \tag{2.8}$$

donde X^M denota las coordenadas espaciotemporales y $\partial\Sigma$ la frontera. El flujo de momento espacial a lo largo de la cuerda hacia el horizonte se obtiene de

$$\Pi_M = \frac{\partial\mathcal{L}}{\partial(\partial_\sigma X^M)}\,. \tag{2.9}$$

En la teoría dual, este momento es absorbido por el medio, y las ecuaciones que surgen de variar la acción (2.8) nos indican que la fuerza externa compensa exactamente este momento perdido.

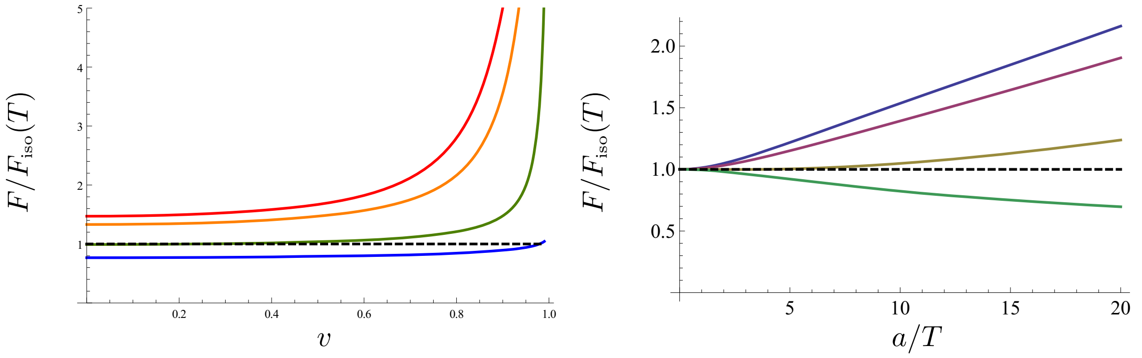

Figura 9. A la izquierda *(derecha)* vemos la fuerza de arrastre normalizada con respecto al respectivo valor isótropo a la misma temperatura como función de la velocidad v *(del cociente a/T)* para varios valores de la dirección de la velocidad φ, que varía de 0 a $\pi/2$ desde la superior a la inferior. Todas las curvas están con el mismo a/T *(la misma v).*

Consideramos un quark moviéndose en el plano xz a un ángulo φ desde el eje z. La solución de su encaje da un comportamiento como el de la fig. 8 (obtenido para $a/T = 86$). El resultado isótropo ($a = 0$) da una fuerza alineada con la velocidad:

$$\vec{F}_{\rm iso}(T) = \frac{\pi}{2}\sqrt{\lambda}\,T^2 \frac{v}{\sqrt{1-v^2}}(\sin\varphi, \cos\varphi)\,, \tag{2.10}$$

mientras que los resultados del caso anisótropo muestran una fuerza desalineada, tanto con respecto a la velocidad como al perfil de la cuerda. La comparación con respecto al caso isótropo puede hacerse considerando una solución con $a \neq 0$ pero con el mismo valor de la temperatura T, o de la densidad de entropía s. Cualitativamente, no hay diferencias notables entre un caso u otro. En la fig. 9 se hace manteniendo T constante. Además, a es una magnitud con dimensiones, por lo que se debe normalizar, ya sea considerando el cociente a/T, o $a/s^{1/3}$.

En el límite ultrarrelativista, se obtiene $F \propto 1/(1-v^2)$, o equivalentemente $F = \mu p$ con un coeficiente de arrastre $\mu \propto p$, excepto si $\varphi = \pi/2$. Este resultado depende únicamente de la presencia de un término de 2º orden $g^{(2)}_{\mu\nu}$ en el desarrollo asintótico de la métrica, que no sea proporcional a $\eta_{\mu\nu}$, por lo que se puede esperar que se mantenga para otros modelos y no únicamente para este cálculo en particular.

El parámetro de jet quenching. Para investigar el efecto de la anisotropía sobre el ensanche de momento experimentado por un partón que se mueve por el plasma, analizamos el llamado parámetro de jet quenching $\hat{q}$ para un quark ultrarrelativista. Para ello, deberemos considerar la hoja de universo de una cuerda cuyos extremos se mueven a la velocidad de la luz a lo largo de una dirección de la frontera (la dirección de propagación del quark) estando separados una distancia ℓ en la dirección perpendicular al movimiento (la dirección de ensanche del momento).

El motivo es que esta hoja de universo es dual al bucle de Wilson de la teoría gauge que sirve para extraer el valor de $\hat{q}$. Ahora bien, para hacer el cálculo dual al orden de operadores requerido, hay que considerar la solución clásica en la que se da la vuelta justo

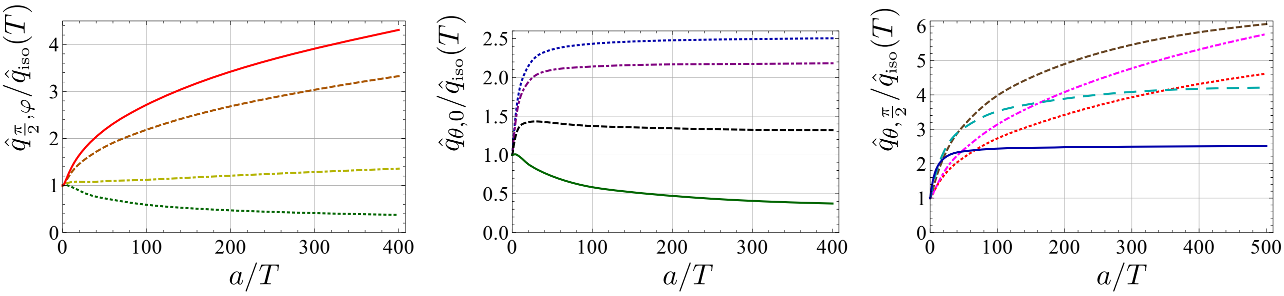

Figura 10. Parámetros de jet quenching $\hat{q}_{\pi/2,\varphi}$ (izquierda), $\hat{q}_{\theta,0}$ (centro) y $\hat{q}_{\theta,\pi/2}$ (derecha), normalizados por el correspondiente valor isótropo a la misma temperatura, para varios valores de la correspondiente coordenada angular. Los colores coincidentes se pueden identificar entre sí.

en el horizonte. Además, la solución que se da la vuelta cerca de la frontera desaparece cuando $\ell \to 0$. La acción de Nambú-Goto evaluada en una configuración como esta diverge, pero esta divergencia desaparece al considerar la diferencia con respecto a dos cuerdas separadas que cuelgan desde la frontera hasta el horizonte.

La prescripción que habremos de usar se resume en

$$e^{i2S} = \langle W^A(C) \rangle = \exp\left[-\frac{L^-\ell^2}{4\sqrt{2}}\,\hat{q}\right] , \tag{2.11}$$

donde se considera un bucle rectangular de longitud L^- a lo largo de $z^- = (t-z)/\sqrt{2}$, y ℓ a lo largo de la dirección perpendicular, y S denota la acción renormalizada por la sustracción mencionada.

En el caso isótropo $\hat{q}$ es un solo parámetro, y adquiere el valor

$$\hat{q}_{\mathrm{iso}}(T) = \frac{\pi^{3/2}\,\Gamma\left(\frac{3}{4}\right)}{\Gamma\left(\frac{5}{4}\right)}\sqrt{\lambda}\,T^3 . \tag{2.12}$$

En este caso habremos de especificar el caso particular considerado, de forma que $\hat{q}_{\theta,\varphi}$ indicaría el valor medio de la componente del momento p_φ al cuadrado adquirida por el quark al moverse en la dirección indicada por θ. Siendo $p_\varphi = p_Y \cos\varphi + p_X \sin\varphi$, es fácil ver que

$$\hat{q}_{\theta,\varphi} = \hat{q}_{\theta,0}\,\cos^2\varphi + \hat{q}_{\theta,\pi/2}\,\sin^2\varphi\,. \tag{2.13}$$

Para cada uno de estos términos, $\hat{q}_{\theta,0}$ y $\hat{q}_{\theta,\pi/2}$ se obtuvieron expresiones exactas que permiten calcularlos a partir de integrales de funcionales de $\mathcal{F}$, $\mathcal{B}$ y $\mathcal{H}$; las cuales solo se conocen númericamente. Dado que consideramos el caso más general, la dependencia respecto a la velocidad, la anisotropía y las dos orientaciones da lugar a una plétora de resultados, de los que aquí solo se da una muestra en la figura 10, que contiene diversas curvas normalizadas por el valor isótropo $\hat{q}_{\mathrm{iso}}(T)$. Es importante reseñar que en este caso sí existe una gran diferencia entre hacer la comparación con el caso isótropo a la misma temperatura o a la misma densidad de entropía.

La comparación con resultados provenientes de estudios del auténtico plasma de quarks y gluones ha de tomarse con cuidado. Para empezar, esos resultados se basan en la existencia de cuasipartículas en el plasma, mientras que nuestro modelo no posee excitaciones de cuasipartículas. En general, se encuentra que $\hat{q}_{\mathrm{L}} \gtrsim \hat{q}_{\mathrm{iso}} > \hat{q}_{\perp}$, siendo $\hat{q}_{\mathrm{L}}$ el ensanche del momento a lo largo del eje de colisión y $\hat{q}_{\perp}$ a lo largo del plano transverso. Nuestros cálculos están de acuerdo si la comparación con el caso isótropo se hace a la misma temperatura y estamos con $a/T \gtrsim 6{,}35$. En caso contrario, los resultados discrepan.

La longitud de apantallamiento. La anisotropía también tiene un efecto importante sobre la longitud de apantallamiento L_s de un par quark-antiquark en el plasma, definida como la separación a partir de la cual deja de ser favorable que se encuentren formando un estado ligado. Obviamente esto satisface $L_s \leq L_{\max}$, donde $L_{\max}$ es la máxima separación para la que dicho estado ligado existe.

La manera de determinar L_s es comparar la acción evaluada del par a distancia ℓ, con la acción del par sin ligar S_{unbound}. La longitud de apantallamiento estará dada por el máximo valor de ℓ tal que dicha diferencia es positiva. Este criterio corresponde a determinar qué configuración tiene menor energía libre, lo cual es la manera de ver cuál es termodinámicamente preferida. Nuestros cálculos están hechos en el sistema de referencia del par quark-antiquark, de manera que $\Delta S_{\mathrm{dipole}} = -\mathcal{T}\Delta E_{\mathrm{dipole}}$, donde $\mathcal{T}$ es la longitud de integración en el tiempo. Así, la cantidad termodinámica considerada puede verse como una diferencia de energías.

En la fig. 13 se muestra un ejemplo de la forma que toma la función que hay que calcular (la parte que importa es la rama de abajo). De manera análoga al caso anterior, hay que considerar una cuerda abierta con ambos extremos en la frontera, solo que en esta ocasión no se adentrará hasta el horizonte, sino que se dará la vuelta a una cierta altura radial $u_{\max} < u_{\mathrm{H}}$. Esta distancia, junto con ℓ, se da como condición de contorno para resolver el momento, que es análogo al de (2.9), y finalmente tras obtener ΔE, hacer una representación paramétrica.

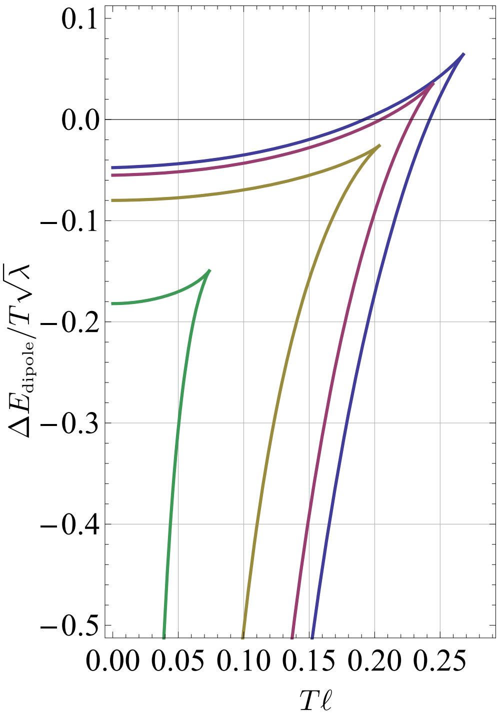

Figura 11. Diferencia de energías entre un par quark-antiquark ligado y uno desligado, para el caso de orientación en x y desplazamiento en z. Las curvas son para valores diferentes de la velocidad v.

De nuevo, la comparación con los resultados de un plasma isótropo se puede hacer a igual temperatura o densidad de entropía, y eso tiene un efecto crucial en el resultado. Por ejemplo, para el caso de un par estático, en el primer caso L_s decrece con la anisotropía en todos los casos, mientras que en el segundo caso, cuando se compara a igual densidad de entropía, L_s aumenta si la orientación del par q-$\bar{q}$ yace, o está cerca de yacer, sobre el plano transverso a la dirección anisótropa.

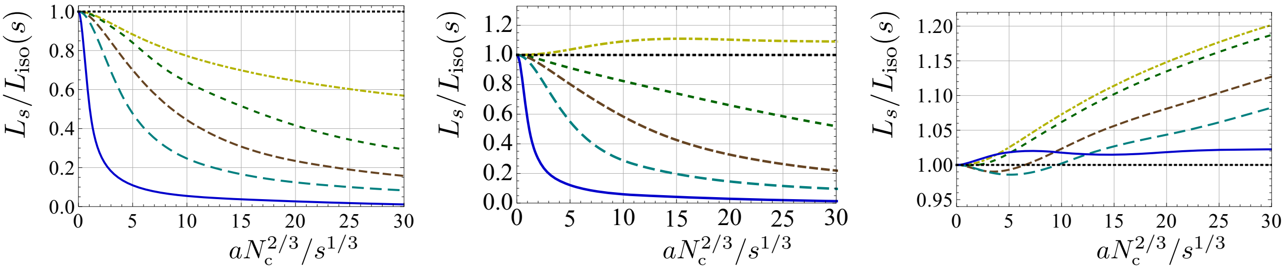

Figura 12. Longitudes de apantallamiento, normalizadas con respecto a los correspondientes valores isótropos a la misma densidad de entropía, como funciones de la anisotropía del plasma y para varios valores de la velocidad (que decrece con el nivel de punteo, siendo la línea sólida para $v = 0{,}9995$); en tres casos particulares: par q-$\bar{q}$ extendido en z y moviéndose en z paralelo a sí mismo (izquierda), par extendido en x y moviéndose en z perpendicular a sí mismo (centro), y par extendido en x y moviéndose en x, paralelo a sí mismo de nuevo (derecha). Recuérdese que z es la dirección anisótropa.

Tras estudiar el caso más general, nuestros resultados dependen de la velocidad[2] v, la anisotropía y tres orientaciones (la dirección de v, fijada por un ángulo y la orientación del par, fijada por otros dos), y además en esta ocasión no hay una relación que simplifique una de ellas como (2.13), de modo que la diversidad de resultados es aún mayor que en el apartado del jet quenching. De hecho, incluso en el caso isótropo habría dependencia respecto a un ángulo: el que forman la velocidad y la orientación del par. Es por este motivo que nos concentramos en estudiar casos particulares de orientaciones, como los que se muestran en la fig. 12.

En el límite ultrarrelativista, podemos usar las aproximaciones asintóticas de las funciones $\mathcal{F}$, $\mathcal{B}$ y $\mathcal{H}$, ya que el punto de vuelta u_{max} se acerca a la frontera (rechazamos la solución en que se acerca al horizonte por no ser física en este caso). Eso nos permite hacer un estudio analítico y averiguar cómo escala con la velocidad. Encontramos que

$$L_s \sim \begin{cases} (1-v^2)^{1/2} \text{ si } \theta_v \neq \pi/2 & \text{[movimiento fuera del plano transverso]} \\ \\ (1-v^2)^{1/4} \text{ si } \theta_v = \pi/2 & \text{[movimiento dentro del plano transverso]}\,, \end{cases} \tag{2.14}$$

sea cual sea la orientación del par.

Uno de los resultados más importantes es el hecho de que hay una L_s finita incluso a temperatura cero. Se puede hablar de una anisotropía de disociación, totalmente análoga a la temperatura de disociación, junto con la velocidad límite. De hecho, que haya una dependencia $L_s = L_s(a/T, v)$ se expresa de manera más precisa diciendo que la disociación de los mesones tendría lugar en una superficie dentro del espacio de fases formado por las variables $\{T\ell, a/T, v\}$. Si tenemos estrictamente $T = 0$ y $v = 0$, la anisotropía de disociación es, por análisis dimensional, $a_{\mathrm{diss}}(\ell) \propto 1/\ell$.

---

[2] Nótese que nos referimos a la velocidad del par, que debería entenderse como velocidad del medio, ya que el cálculo está realizado en el sistema de referencia del mesón.

2.3. Fenómenos de transporte en superfluídos de onda p

Un superfluído de onda p se caracteriza por la ruptura espontánea de una simetría rotacional y de una simetría gauge $U(1)$ al mismo tiempo, por un condensado vectorial. El modelo gravitatorio empleado para construir una descripción dual consiste en la teoría $SU(2)$ Einstein-Yang-Mills, con acción

$$S = \int d^5x \sqrt{-g} \left[\frac{1}{2\kappa_5^2} (R - \Lambda) - \frac{1}{4\hat{g}^2} F^a_{MN} F^{aMN} \right] + S_{\text{bdy}} \,, \tag{2.15}$$

donde a es el índice de sabor de $SU(2)$. Esta simetría, presente originalmente, se rompe explícitamente a $U(1)$, ya que seleccionamos el ansatz

$$A = \phi(r)\tau^3 dt + w(r)\tau^1 dx \,, \tag{2.16}$$

con un valor de frontera para $\phi(r)$, que es el potencial químico μ. Este ansatz es compatible con la solución de Reissner-Nordström en AdS, para la cual $w(r) = 0$. Sin embargo, es posible encontrar numéricamente una segunda solución con $w(r) \neq 0$. Se puede estudiar la termodinámica asociada a ambas, para ver cuál es preferida según qué valores de los parámetros consideremos. Así se construye el diagrama de fases de la figura 13.

Cada fase describe un estado diferente de la teoría dual. La región $T/\mu \ll 1$ describe la fase condensada, que manifestará propiedades de superfluídos. El esquema de ruptura de simetrías es el siguiente:

$$\begin{aligned} SU(2) \xrightarrow[\text{Expl.B}]{} U(1)_3 &\xrightarrow[\text{SSB}]{} \mathbb{Z}_2 \,, \\ SO(3) &\xrightarrow[\text{SSB}]{} SO(2) \,. \end{aligned} \tag{2.17}$$

La ruptura espontánea sucede porque $w(r)$ selecciona una dirección particular en el espacio orbital (que llamamos x) y una 'dirección' en el espacio de sabores (el índice 1). El carácter de la transición de fase depende del valor del parámetro que aparece en la acción (2.15): es de primer orden si $\alpha > \alpha_c \simeq 0{,}365$ y de segundo orden en caso contrario.

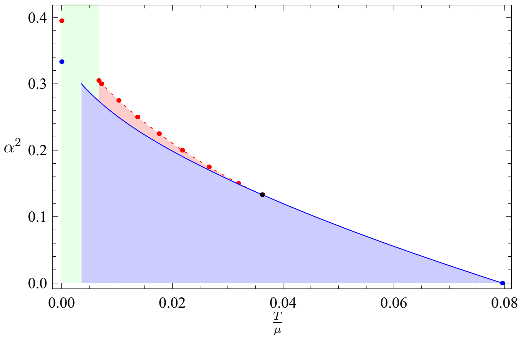

Figura 13. Diagrama de fases del sistema gravitatorio considerado. La fase condensada, con $w(r) \neq 0$, está marcada en azul.

Este es el trasfondo que perturbamos para hallar las funciones de Green de la teoría completa. Añadimos perturbaciones en torno a la solución de equilibrio y estudiamos su efecto sobre los valores esperados de los operadores asociados. Las fluctuaciones de la métrica son $h_{MN}(\omega, r)$ y las del campo gauge son $a^a_M(\omega, r)$, en representación de Fourier. No hay dependencia respecto al momento, porque lo ponemos a cero por simplicidad y porque queremos conservar el mayor número de simetrías posible para poder interpretar los resultados con más claridad. Si anulamos el momento, las ecuaciones del movimiento linearizadas para estos campos de perturbaciones se desacoplan, de manera que podemos clasificarlas en bloques y asociar a cada uno un fenómeno de la teoría dual.

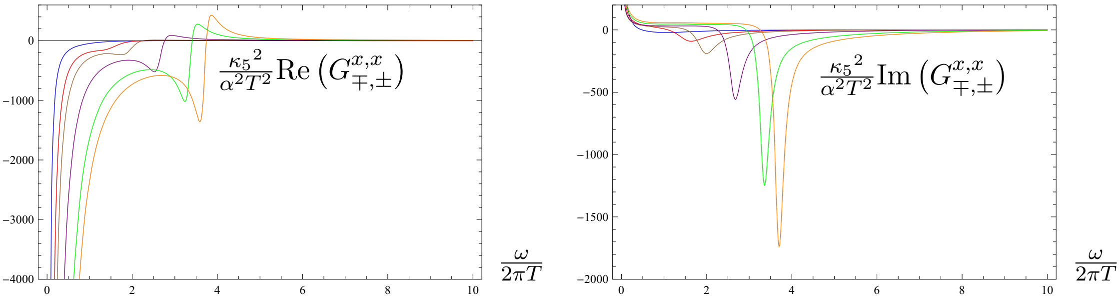

Figura 14. Partes real e imaginaria del correlador $G^{x,x}_{+,-}$, o también $G^{x,x}_{-,+}$, frente a la frecuencia reducida $\omega/(2\pi T)$ para $\alpha = 0{,}316$, y para diferentes valores de la temperatura, de forma que los picos son más marcados cuanto más baja es la temperatura.

Concretamente, la ruptura de la simetría de rotaciones deja atrás una simetría $SO(2)$, y podemos clasificar las perturbaciones por helicidades (2, 1 ó 0), atendiendo a cómo transforman bajo estas rotaciones. Centrémonos en los campos de helicidad 0, que son los que presentan una fenomenología más rica. Por ejemplo, el campo eléctrico paralelo al condensado E_x y el gradiente de temperatura $\nabla_x T$ pueden obtenerse a partir de las componentes componentes h_{tx} y a^3_x. Estos modos actúan como fuentes para la corriente eléctrica J^x y el flujo de calor $Q^x = T^{tx} - \mu J^x$, respectivamente. La relación de estas corrientes con las respectivas fluctuaciones conforma la matriz de conductividades de la teoría de respuestas lineales:

$$\begin{pmatrix} \langle J^x \rangle \\ \langle Q^x \rangle \end{pmatrix} = \begin{pmatrix} \sigma^{xx} & T\alpha^{xx} \\ T\alpha^{xx} & T\bar{\kappa}^{xx} \end{pmatrix} \begin{pmatrix} E_x \\ -(\nabla_x T)/T \end{pmatrix} . \tag{2.18}$$

Los coeficientes que obtenemos de aquí muestran un comportamiento que reconocemos como típico de un material superconductor.

Por otra parte, una interacción análoga para las componentes

$$\begin{pmatrix} \langle J^x_\pm \rangle \\ \langle T^{xx}, T^{\perp\perp}, T^{tt} \rangle \end{pmatrix} \longleftrightarrow \begin{pmatrix} a^\pm_x \\ h_{xx}, h_{\perp\perp}, h_{tt} \end{pmatrix} . \tag{2.19}$$

se puede interpretar como efecto piezoeléctrico: un fenómeno que describe la generación de corriente eléctrica debido a estrujamientos o alargamientos de un material, o la generación de deformaciones debido a la aplicación de un campo eléctrico externo. También encontramos un efecto adicional, llamado flexoeléctrico, en el que son gradientes de presión los que generan corriente eléctrica. Las funciones de Green de este bloque muestran una estructura interesante en la que se aprecia la formación de picos que son más acentuados cuanto más baja es la temperatura (ver fig. 14). Su máximo está situado sobre la misma frecuencia para todos ellos.

Por otra parte, muchos de estos correladores muestran un polo en $\omega = 0$. Esto se puede entender porque algunas componentes de las fluctuaciones, como a^2_x, se convierten en modos de Goldstone que absorben los grados de libertad de las simetrías rotas. El polo refleja su formación, al igual que el diagrama de los modos cuasinormales (ver fig. 15).

Vemos que para $T > T_c$ los modos cuasinormales asintotan al origen, $\omega = 0$. Aquí las curvas verde y roja tienen que ver con los modos $a_x^{\pm}$. Es interesante ver que aunque tenemos en cuenta la retroacción, este diagrama es muy similar al del sistema D3/D7. Los modos permanecen en la parte de abajo del plano de frecuencias complejas para todas las temperaturas que pudimos comprobar.

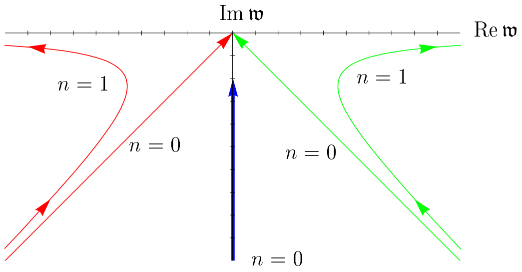

Figura 15. Esquema de los modos cuasinormales del sistema. Here $\mathfrak{w} = \omega/(2\pi T)$.

Por último, mediante formulas de Kubo, algunos de estos correladores se pueden relacionar con coeficientes de viscosidad. En presencia de anisotropía, además de las viscosidades de cizalla η_{yz} y η_{xy}, hay otros tres coeficientes, dos de los cuales se anulan si el fluido es conforme. El tercero, llamado λ, se obtiene a partir de

$$\lambda = \lim_{\omega \to 0} \frac{3}{2\omega} \operatorname{Im} G^{m,m}(\omega) \,. \tag{2.20}$$

donde

$$\begin{aligned} G^{m,m}(\omega) = \lim_{|\vec{k}| \to 0} \int dt\, d^3x e^{-ik_\mu x^\mu} \theta(t) \times \\ \left\langle \left[\frac{1}{2} \left(T^{xx}(t,\vec{x}) - (T^{yy}(t,\vec{x}) + T^{zz}(t,\vec{x})) \right), \frac{1}{2} \left(T^{xx}(0,0) - (T^{yy}(0,0) + T^{zz}(0,0)) \right) \right] \right\rangle \,. \end{aligned}$$

y está por tanto asociado a una diferencia de esfuerzos normales. Su valor respeta el confín universal: $\lambda > 1/(4\pi)$ en la fase condensada.

3. Conclusiones y direcciones futuras

Partiendo del conocido ejemplo de dualidad que involucra a la teoría $\mathcal{N} = 4$ SYM, y con los ajustes adecuados, es posible obtener generalizaciones que pudieran ayudar a resolver preguntas que siguen abiertas acerca del plasma creado en colisiones de iones pesados, o del amplio campo de la física de la materia condensada. Es importante hacer progreso en estas aplicaciones de la dualidad para saber hasta qué punto puede resultar útil.

Esta tesis recopila construcciones de diversos modelos gravitatorios que tienen el objetivo común de obtener predicciones fenomenológicas, de una u otra forma. Los detalles cuantitativos de las conclusiones que de ellos saquemos pueden depender del modelo particular empleado, así que es importante buscar resultados cualitativos que sean lo más universales posible, como es el caso de la radiación de Cherenkov mesónica. La estimación que obtenemos de este efecto nos dice que debería ser comparable a otros mecanismos de pérdida de energía previamente estudiados y, además, fácilmente reconocible por sus características especiales. Sin embargo, nuestro cálculo es solo válido para quarks pesados (estrictamente, cogemos quarks de energía infinita). Sería interesante estudiar el caso de la pérdida de energía para quarks ligeros; para lo cual, se tendría que considerar branas cuyo encaje cae a través del horizonte.

La aplicación de la dualidad al cálculo de los coeficientes de transporte de un superfluído de onda p nos ha permitido ver que la anisotropía del sistema conlleva nuevos fenómenos de gran interés, como el efecto piezoeléctrico y un coeficiente de viscosidad relacionado con la diferencia de esfuerzos normales. Las funciones de correlación obtenidas presentan una estructura muy elaborada, en particular, una característica intrigante es la presencia de bultos y/o picos en algunos correladores, que podrían estar relacionados con la aparición de estados ligados. Se necesitaría una descripción de la hidrodinámica de un superfluído de onda p para poder dar una buena interpretación a este estudio. Lamentablemente, tal formulación hidrodinámica no ha sido realizada. Además de eso, generalizar el análisis a momento finito nos permitiría estudiar las relaciones de dispersión de los modos normalizables y así buscar inestabilidades.

La inclusión de anisotropía es otra modificación respecto a la correspondencia original, que si se lleva al régimen de aplicación a física de altas energías, su estudio podría servir para, por ejemplo, averiguar porqué el tiempo de isotropización del plasma es tan pequeño. Hicimos esto mediante una solución de Supergravedad IIB dual a un plasma de $\mathcal{N} = 4$ SYM anisótropo, y llevamos a cabo un análisis muy detallado de la fuerza de arrastre de un quark, el parámetro de jet quenching y la longitud de apantallamiento de un mesón. Un análisis como este es un paso adelante hacia una descripción más realista del plasma creado en las colisiones de iones pesados. Pero una auténtica simulación incluiría dependencia temporal, además de anisotropía. El problema alcanza un nivel de dificultad considerable con esto, de modo que sería necesario emplear técnicas de gravedad numérica. Esta es claramente una dirección para el futuro cercano del estudio de aplicaciones de AdS/CFT a sistemas fuera del equilibrio.

Al final, los sistemas que queremos describir puede que no tengan una descripción dual de gravedad. Sin embargo, la conexión proporcionada por la dualidad gauge/cuerdas es de por sí sorprendente y podría ayudarnos a ganar comprensión sobre muchos problemas mientras continuamos la búsqueda de la teoría definitiva para el Universo.